

Single-molecule studies of cellulose, cellulose-binding domains,
and cellulose biosynthesis machinery

By

Mark Andrew Hilton

Dissertation
Submitted to the Faculty of the
Graduate School of Vanderbilt University
in partial fulfillment of the requirements
for the degree of

DOCTOR OF PHILOSOPHY

In

Chemical and Biomolecular Engineering

December 17, 2022

Nashville, Tennessee

Approved:

Matthew J. Lang, Ph.D.

Piran Kidambi, Ph.D.

Marija Zanic, Ph.D.

Adrian O. Olivares, Ph.D.

Copyright © 2022 Mark A Hilton
All Rights Reserved

ACKNOWLEDGMENTS

One of my favorite stories to share is how I came to Vanderbilt. I had finished my undergraduate career at Colgate and had aspirations to go to graduate school. My plan was to try to intern in any lab I could, while coaching and doing odd jobs on the side for money, in order to gain more experience before applying to programs the following year. I had previously worked summers in labs, including in Matt's lab, as an undergraduate research assistant, and I knew I wanted to pursue research. Towards the end of the summer directly after undergrad, I came to Nashville to visit family for the solar eclipse, and I decided to visit Matt's lab to say hi and see how things have been progressing. The visit must have gone well, because a week later, I received a phone call from Matt asking if I wanted to come join Vanderbilt's Chemical and Biomolecular Engineering department as a graduate student and work in his lab. I was over-the-moon excited and immediately accepted. I then asked when classes started, to which he replied, "Yesterday." Over the course of the next three days, I packed to leave Buffalo, moved down to Nashville and started classes the very next Monday, completely changing the trajectory of my life. I still look back to this moment as one of the best decisions I have ever made, and I owe a huge debt of gratitude to my advisor, Matt Lang, for taking a chance on me, for seeing my potential, and for giving me the opportunity of a lifetime. Over the course of my graduate studies, Matt has been supportive, understanding and firm. He has adamantly expressed his belief in my ability as a researcher and has held me to high expectations. Because of his mentorship, I have achieved unforeseen heights in my academic, professional, and personal lives. To Matt, thank you for choosing to advise me, nurture my curiosity, hone my skills, and prepare me for a lifetime of research, building, creation, analysis, and communication. My goal, in addition to producing the great work in this dissertation, was to be a conduit of lab knowledge and leave the lab in a better place than when I arrived. I hope I accomplished this, and I am excited to watch the future of the lab unfurl. Although our time working in the same lab may be coming to a close, I will always be a Lang Lab member.

Next, I would like to thank my family for supporting me and providing an environment that allowed me to thrive. I would not be where I am in life without any of you, and I am deeply grateful to be raised by amazing, caring, thoughtful, selfless, and loving people. To Mom and Dad, I cannot possibly thank you enough for all of the support, freedom and love over the years. You are my first and best teachers. The sacrifices you have made to provide me with the tools and experiences to be my best self are immeasurable, and I am so thankful. One thing I have learned in my time in academia is the cycle of education: students learn and become teachers, and teachers never stop

being students. I hope that one day I will be just as great of a parent, while always staying your child.

To Alex, you are one of my best friends and closest relationships. There is something very unique about sharing all stages of life with someone, and I am so glad you have been that person for me. You have supported me, advised me, and protected me. I will always value your positivity and optimism, your intelligence, and your philosophies. Although we have never much competed directly, we have always cheered each other on and pushed each other to be more than what we thought possible. This work would not be possible without your encouragement and support, to which I am very appreciative.

To Michelle, my partner, best friend, and teammate, you have supported me every step of this journey through graduate school. This dissertation is just as much your accomplishment as mine. I cannot possibly thank you enough for the innumerable hours spent listening to me vent my frustrations, providing compassion when not feeling well, and cheering me along as milestones were achieved. You have watched my career the closest and shared in every failure and success along the way. You have made all of this possible. I am so happy and grateful to share my life with you, and I would not want anyone else by my side. I love you and can't wait to marry you in just a few weeks.

To my lab mates and department friends, thank you for your support, your mentoring, your time brainstorming, your advice, your commiseration, and all of the fun you've provided. Graduate school is a unique experience, and I am happy to have you all to share it with. To Sonia, JC, Dev, Nikki and Andy, thank you for your expertise, mentorship and advice. You have built a strong foundation on which I could thrive. To Harris, you have been a great mentor, sounding board and friend. I am happy we got as much time together as we did and have learned a lot from you. To Maddie and Hannah, thank you for all of your help with assays, ideas, instruments and everything else in the lab. Your support and friendship have helped me keep pushing forward. We're in this together, and I am grateful to have shared the largest portion of my graduate career with you both. To Dan and Evan, it has been a blast watching you develop into researchers, and I thank you for your support and encouragement. To Ally and Liz, our time was short together, but I thoroughly enjoyed you both letting me mentor you. Your future is bright, and I am excited to see where it leads you.

To my committee, Professors Piran Kidambi, Marija Zanic, and Adrian Olivares, thank you for your continued support and feedback for my project. Your questions and challenges have made me a better researcher. I also want to thank our collaborators, Shishir Chundawat and Jochen Zimmer, without whom this work would not be possible.

I thank the ChBE staff for all of their work, conversations, and efforts to ensure my education and activities were possible. Felisha Baquera, Angie Pernel, Jenni Powell, Chineme Chokuba, Carol Wiley, and Mark Holmes, thank you for all of your time and support throughout the years.

I would also like to thank all of my friends, including those I have made in Nashville, those I met at Colgate, those in Buffalo, and the rest in between. You all have profoundly shaped my life experiences and who I am today. I can't wait to keep in touch and support all of you as you've all supported me.

Many individuals at Vanderbilt have provided professional mentorship and inspiration for me to develop and pursue my goals. In addition to my dissertation work, I have been heavily involved in Vanderbilt's innovation, technology transfer, and entrepreneurship ecosystem. I want to thank Bob Webster, Charleson Bell, Deanna Meador, Yesi Sevilla, George Wilson, Peter Rousos, Phil Swaney, Chris Harris, Stacie Pawlicki and others across Vanderbilt's innovation and entrepreneur landscape for their instrumental mentorship, guidance, support and challenges. I have enjoyed working with each one of you and am excited for a future of innovation.

I would like to specifically thank Marc Nabhan for embarking on entrepreneurial projects with me. We have been learning side-by-side and pushing each other to our greatest accomplishments. Thank you for being a great partner to learn, fail and succeed with. You inspire me to proceed with ambition and remind me that doing what you love makes life exhilarating and fun. I can't wait to see where we go.

To the various mental health professionals that have helped me along the way, thank you for your selflessness and investment into my wellbeing. I have overcome many tribulations with your help and have emerged as my best self. A great portion of my success is contributed to you.

Finally, to all of those whom I have not mentioned explicitly but have supported and encouraged me along the way: thank you. The culmination of human achievement is not compiled by a few individuals at discrete moments but is a continuous effort by each individual to keep moving forward. Like this dissertation, my successes are built upon the support and lives of everyone in my life.

TABLE OF CONTENTS

ACKNOWLEDGMENTS.....	III
LIST OF TABLES.....	VIII
LIST OF FIGURES.....	IX
1 Introduction.....	1
1.1 Context and Motivation	2
1.2 Biological Systems	6
1.2.1 Cellulose biopolymer.....	6
1.2.2 Cellulose degradation machinery.....	7
1.2.3 Cellulose synthesis machinery.....	9
1.3 Single-molecule Methods	12
1.3.1 Optical tweezers	13
1.3.2 Total internal reflection fluorescence (TIRF) microscopy	15
1.4 Summary.....	16
1.5 References	16
2 Cellobiohydrolase Carbohydrate Binding Module 1 from <i>Trichoderma Reesei</i> exhibits reduced binding to cellulose III and multiple binding schemes to various cellulose substrates.....	25
2.1 Summary.....	25
2.2 Introduction.....	25
2.3 Results.....	27
2.3.1 Substrate-dependent binding.....	28
2.3.2 Multiple binding regimes.....	31
2.3.3 CBM1 mutants and binding orientations	33
2.4 Discussion.....	37
2.5 Materials and Methods.....	41
2.7 References	47
3 Single-molecule mechanical and biochemical characterization of cellulose biosynthesis in the Bacterial Cellulose Synthase A-B complex from <i>Rhodobacter sphaeroides</i>	54
3.1 Summary.....	54
3.2 Introduction.....	55
3.3 Results.....	56
3.3.1 Single molecule activity of BcsAB	56
3.3.2 Temperature dependence of BcsAB.....	57
3.3.3 Biochemical dependence of BcsAB	60
3.3.4 Cyclic-di-GMP refuses dissociation	62

3.3.5 Stall force, microstructure and kinetic analysis	66
3.3.6 Cellulose stretching reveals microstructure and elasticity	75
3.3.6 Cello-oligosaccharides bind nascent cellulose strands and increase activity.....	81
3.4 Discussion.....	83
3.5 Materials and Methods.....	88
3.6 Acknowledgements	92
3.7 References	92
4 Construction of high-resolution optical tweezers with advanced drift correction.....	98
4.1 Summary.....	98
4.2 Introduction	98
4.3 Results.....	101
4.3.1 Optical path and components	101
4.3.2 Video recording	103
4.3.3 Piezo tilt mirror position calibrations	103
4.3.4 Detection position calibrations	104
4.3.5 Trap stiffness calibrations.....	107
4.3.6 Drift correction.....	110
4.3.7 Temperature control chamber	112
4.4 Discussion.....	115
4.5 Materials and Methods.....	116
4.6 Acknowledgements	117
4.7 References	117
5 Conclusions and Future Work	122
APPENDIX	126
A. Protocols	126
A.1 Buffer recipes	126
A.2 DNA tethers	130
A.3 Anti-body splitting and conjugating to DNA	132
A.4 CBM bead preparation.....	133
A.5 Anti-Digoxigenin bead preparation.....	133
A.6 Coverslip KOH etching	134
A.7 Coverslip surface passivation with PEG-silane.....	135
A.8 Cellulose aptamer bead preparation.....	135
A.9 Cellulose Solutions.....	137
A.10 CBM assay construction.....	138
A.11 BcsAB assay construction.....	139
A.12 DNA tether assay construction.....	141

LIST OF TABLES

Table	Page
2.1 Buffon needle orientation results.....	35
3.1 Comparison of biosynthesis velocities across studies	58
3.2 Comparison of various properties of both BcsAB and cellulose in the presence and absence of cello-oligosaccharides of different lengths	79
4.1 Calibration chart for different input currents on the power supply	108

LIST OF FIGURES

Figure	Page
1.1 Cellulose molecular and lattice structure.....	7
1.2 Cellobiohydrolase and its CBM	8
1.3 BcsAB complex crystal structure.....	10
1.4 Cellulose biosynthesis cycle.....	11
1.5 Optical tweezers diagram.....	13
1.6 TIRF diagram	15
2.1 XRD and FTIR spectra for cellulose allomorphs	28
2.2 Single-molecule CBM-cellulose bond rupture assay.....	29
2.3 CBM1 bond lifetimes on cellulose I and III	30
2.4 Force vs lifetime for CBM1 to cellulose I and filter paper.....	32
2.5 CBM1-cellulose bond lifetimes using Fab vs full antibody linker.....	33
2.6 CBM possible binding modes.....	34
2.7 Buffon needle approximation for CBM binding orientations	35
2.8 Bond lifetimes comparison between wtCBM1 and Y31A CBM1	36
3.2 Cellulose biosynthesis at varying temperatures	59
3.3 Biochemical controls	60
3.4 C-d-GMP controls and fluorescence	61
3.5 C-d-GMP vs c-d-GMPf bulk synthesis rates.....	62
3.6 C-d-GMP vs c-d-GMPf single-molecule synthesis rates	63
3.7 Example fluorescence traces	65
3.8 TIRF control.....	66
3.9 Kinetics analysis.....	67
3.10 Extensions and retractions	69
3.11 Cellulose vs DNA position distributions.....	69
3.12 Example traces with rapid reversible transitions	70
3.13 Histogram of observed fluctuation distances.....	71
3.14 Reversible transition analysis example	72
3.15 Variance analysis	74

3.16 Unloaded velocity	76
3.17 Single cellulose strand stretching and effects of cellohexaose hybridization	77
3.18 Persistence length and axial stiffness	78
3.19 Cellulose stretching hysteresis with cellohexaose	80
3.20 Cellohexaose and microstructure	81
3.21 BcsAB bulk activity with cellohexaose.....	82
4.1 Optical tweezers optics diagram	102
4.2 Tilt mirror steered the trap through the detection zone	104
4.3 5 th order position calibrations	105
Figure 4.4 Step detection of a fixed bead.....	106
4.5 Power spectrum calibration	108
4.6 DNA stretching control	109
Figure 4.7 Example drift correction traces.....	111
4.8 Temperature control box on the microscope.....	113
4.9 Inside the temperature control box.....	114

CHAPTER 1

Introduction

Cellulose, the most prolific biopolymer on Earth, is utilized by almost all kingdoms of life as structural scaffolding, as protective shielding or as a metabolic fuel source (1). Additionally, humanity has found seemingly innumerable functions for cellulose, such as wood in building materials, cotton for clothing, additives in paint (2) and in food (3), wound treatments (4), and renewable energy (5). The study of cellulose began just over 180 years ago when French Chemist Anselme Payen first named the fibrous plant material and discovered its chemical formula (6). As analysis techniques advanced, so did our knowledge of cellulose, its synthesis and its degradation. Size exclusion chromatography predicted the degree of polymerization of biosynthesized cellulose (7). Incorporating radioactive carbon-13 in cellulose production revealed intramolecular hydrogen bonding through Nuclear Magnetic Resonance (NMR) spectra (8). Infrared (IR) absorbance also presented intramolecular bonds (9), but Fourier-transform IR spectroscopy distinguished the differences in crystal structure between cellulose I and cellulose II (10). X-ray Crystallography particularly has advanced the knowledge of cellulose structure by identifying degrees of crystallinity and crystal unit cells for different allomorphs (11, 12). To date, cellulose's chemical and physical properties are generally understood. However, new techniques of analysis continue to uncover and address gaps in knowledge and create new potential for human advancement.

Cellulose is manufactured by biology on the scale of one hundred billion tons annually (13), and for much of history, we have taken great advantage of the many forms of cellulose without much consideration for how it was made or degraded. Cellulose biosynthesis typically accompanies photosynthetic processes, making the process one of the largest natural carbon fixation techniques. Much of cellulose synthesis studies began with the analysis of plant cell-walls, as many researchers struggled to identify and characterize cellulose synthase, the enzyme responsible for cellulose production (14). The field of cellulose synthesis study blossomed after both the discovery of the gram-negative, cellulose-secreting bacteria *Acetobacter xylinum* and the establishment of proper bacterial growth conditions to optimize cellulose production (14). Soon after, the monomer and suspected fuel source of biosynthesis was identified to be a high energy sugar, uridine diphosphate-functionalized glucose (UDP-glucose) (15). The discovery of cyclic diguanylic acid (c-di-GMP) as a signaling messenger, and later as an allosteric activator, for cellulose synthase launched an entirely new field of study as c-di-GMP regulates a large number of processes in

bacteria, including biofilm formation, motility, virulence, the cell cycle, differentiation and more (16, 17). Although the understanding of cellulose synthase is expanding rapidly, there is much that is not known.

Consequently, with such high volumes of cellulose production, it is implied that about an equal amount of cellulose is degraded each year (18). Because cellulose is one of the most physically and chemically stable biomaterials, with an estimated spontaneous decay half-life of several million years (19), life has engineered methods to enzymatically degrade cellulose back into sugar units. Processive cellobiohydrolases are key components of cellulose degradation, as they bind to and cleave cellulose strands while translocating along the polymer track (20, 21). Both bacteria and fungi digest cellulose for carbon uptake and energy production (18). Cellulolytic cocktails have been most commonly isolated from fungi secretions, specifically from *Trichoderma reesei* because of the ease of cellulase extraction (22). Much work has been done to identify the processes underlying degradation including cellulose crystallinity dependencies (23, 24), cellulose hydrolysis kinetics (25), free energy studies (21), X-ray crystallography (26), enzyme mutation studies (27), and most recently, single-molecule studies (28, 29). Identifying optimal cellulose degradation conditions and engineering new approaches to hydrolysis remain of high interest and high priority in the research community.

This work extends the knowledge gained from all previous studies by employing new techniques to characterize cellulose biosynthesis, degradation, and structural properties. Our methods unearth new findings related to the commitment and productivity of cellobiohydrolases, operating conditions and kinetic parameters of bacterial cellulose synthesis, and unexpected behaviors and properties of single-stranded cellulose. Additionally, we introduce high-resolution methods for the future analysis of cellulose molecular machinery. This work aims to be built upon, empowering the scientific community to tap into a greater understanding of some of the most prolific mechanisms enabling life.

1.1 Context and Motivation

Cellulose is the most abundant polymer on Earth and provides several kingdoms of life with structure, energy, and protection (30). Life biomanufactures and degrades cellulose on the order of a hundred billion tons annually (13, 18). Cellulose synthesis and degradation are two of the most prolific processes performed by life. In sole relation to humans, cellulose production directly or indirectly provides food, shelter, clothing, and energy, or poses issues such as disease or pipe fouling (31). Because of this, cellulose and its synthesis are of enormous interest in biotechnology with the possibilities to vastly improve agricultural yield, biofuel production, anti-microbial treatments and process engineering (1, 31).

Cellulose has been considered a viable feedstock for biofuels for some time now, but even with recent advances, biofuels are still not economically viable compared to fossil fuels. Overcoming the recalcitrance of plant material for bioconversion to ethanol is the main issue facing the biofuel industry (5, 24). The three key steps in biofuel conversion are 1) size reduction, 2) pretreatment, and 3) hydrolysis (32). The studies presented here focus on the most cost-inefficient step: hydrolysis, particularly enzymatic hydrolysis. Currently, about 25 kg of enzyme is needed to mostly convert one ton of cellulose (32). The enzymes are also not easily recycled, making the process extra costly. In order to make biofuels a competitor in the current energy market, reducing the cost associated with enzymatic hydrolysis is imperative.

Physical, chemical and thermal pretreatment processes have emerged in recent years to better prepare cellulose for degradation (33). Physical treatment is relatively self-explanatory, as it mostly consists of mashing, grinding and pulping creating more “pores” and surface area for enzymes (33). Chemical treatments generally involve ammonia pretreatment or a dilute acid treatment (24). Dilute acids, such as sulfuric acid or peroxides, often hydrolyze small amounts of cellulose and produce relatively pure cellulose slurries, while ammonia restructures the cellulose microfibril’s hydrogen bond network making it more susceptible to degradation (12, 33). Thermal treatment refers to elevating the temperature of the slurry so that the energetic barrier to treatment and hydrolysis is easier to hurdle. Often and effectively, all three techniques are used at once (33).

The main goal of the lignocellulose pre-treatment is to change the physical parameters of cellulose fibers to be more conducive to enzymatic hydrolysis. One such parameter that has been identified as a key indicator of enzymatic hydrolysis rate is cellulose crystallinity (23). Higher degrees of crystallinity have shown to increase the strength of interchain interactions, reducing opportunities to initiate degradation and the ability for individual strands to separate from the microfibril (23). Interestingly, exoglucanases prefer binding to more hydrophobic surfaces, such as highly crystalline regions (28). However, such binding has actually been shown to be detrimental as enzyme crowding and “traffic jams” significantly lower efficiency (20, 34). Efforts to reduce crystallinity, creating cellulose III from ammonia pre-treatment of cellulose I, have shown an increase in enzymatic productivity (12, 35).

More recently, the field has approached increasing enzymatic hydrolysis by augmenting the enzymes themselves. To date, there have been few studies that have demonstrated significant success in increasing activity for industrially relevant settings (36-38). The lack of success is largely attributed to the lack of information on the structure and function of individual cellulase domains, as well as the enzyme’s interactions with cellulose. This gap in information is limiting our ability to

engineer more efficient and robust hydrolysis mechanisms, which would greatly reduce the cost of biofuel production.

One large confusion is the impact of the exocellulase's binding mechanism to cellulose on degradation. Studies at low concentrations show that higher binding affinities leads to higher productivity (27), while others have shown that high binding affinities reduce the efficiency of hydrolysis, both collectively (20) and for individual exocellulases (29). Here, we employ single molecule techniques to study the specific interactions of the CBM of cellobiohydrolase to cellulose. Our results reveal nuances of substrate preference and multiple binding regimes. The work highlights the importance of multifaceted approaches to studying exocellulases and furthers the understanding of cellulase-cellulose interactions desperately required for the manufacturing of market-competitive biofuels.

Investigating alternative cellulose production, in addition to feedstock-derived sources, could lead to more efficient and cost-effective bioconversion processes. It has been suggested that genetic modification of plants to reduce lignin and increase the relative cellulose composition of secondary cell walls holds great potential in producing biofuels more efficiently, as a 5% reduction relative lignin results in twice the sugar production (5, 39). Additionally, during microbial conversion from sugars to biofuels, high solids loading can yield high concentrations of toxic compounds after hydrolysis (5, 32). To minimize complications during bioconversion, a pure, high-concentration sugar solution is ideal. Eliminating extraneous compounds by bioengineering plant feedstock sources is a priority for current research (5). One such solution would be to increase the relative cellulose content in feedstocks, reducing the complications involved with cell-wall digestion and producing less toxins (39, 40). Current solutions involve selective breeding and other genetic modification techniques (5). In fact, recent advances in CRISPR/Cas9 therapeutics have been very successful for producing biofuels more efficiently because of its ability to make genetic changes at specific, individual DNA base pairs (41). With these advances, great emphasis has been placed on understanding the molecular basis behind cell-wall formation. This dissertation provides a molecular understanding of how cellulose is biosynthesized.

A molecular understanding of cellulose synthesis in bacterial systems has also been sought, as cellulose is a main component to bacterial biofilms (1, 42). The kingdom of bacteria utilizes cellulose's structural and recalcitrant properties most commonly in biofilms surrounding microbial communities (43). The biofilm is a 3D, extracellular matrix of proteins, polysaccharides such as cellulose, nucleic acids and lipids that houses bacterial communities (44). Life's adaptation of biofilms for protection has been traced back ~3.25 billion years, making this ancient evolutionary development one of the most impactful occurrences for the formation of life today (45). Today, the

composition and structure of biofilms can vary greatly depending on the microorganisms, nutrients available, local shear stress and the environment (44, 46). Biofilms are able to adhere to almost all biological and non-biological surfaces and thrive when surfaces are wet and warm (45). Cellulose and other extracellular polymeric substances shape the biofilm providing structural integrity while maintaining a non-rigid, responsive physical barrier to mechanical stress (46). The biofilm structure must uphold adhesive properties and physical protection while encouraging nutrient transport and the communication of stimuli (47).

Despite the fascinating capabilities that bacterial biofilms hold, the sessile bacterial communities and their biofilms present a great risk to both industrial systems and human health. Adherent bacteria besiege industrial aquatic systems by corroding and fouling pipes, plugging filters and injection faces and creating harmful products (43). Bacteria colonies prefer to adhere to the water-cooled side of heat exchangers, reducing their efficiency by up to 10% (43). The most economically damaging effect in industrial systems comes from aquatic biofouling costing an estimated 0.25% of the gross domestic product of industrialized countries (43, 48, 49). The most common mitigation technique is using chemical agents, despite the resulting toxic substances introduced into the environment (48). More sustainable and effective techniques are needed to prevent bacterial biofilms from destroying aquatic systems.

In addition to non-biological surfaces, bacterial communities utilize biofilms to survive in animal hosts in what we call an infection (45). Bacterial communities are particularly common in healthcare settings and hospitals, as 65% of nosocomial infections result from biofilm-producing bacteria (50). Bacterial communities latch onto surgical instruments and implantable medical devices to infect their host, and such colonies most notably cause cases of endocarditis and cystic fibrosis (45). Unfortunately, the crusade to prevent and kill sessile bacteria has been challenging. The same reason biofilms have been used for billions of years for protection is exactly the problem when trying to prevent infection: biofilms prevent anti-microbial treatments from killing the bacteria (44-46, 51, 52).

The biological process of biofilm formation has proven to be very robust, as no gene knock-out or environmental stress has been able to dismantle biofilms (45). The redundancy of the pathways involved in biofilm production and differentiation prevents a simple solution to bacterial elimination (45). With the recent discoveries on how extracellular polymeric substances are essential to form and function of the biofilm, the field has moved towards focusing on better understanding how the polymers are made in hopes of bioengineering methods of sabotage (44). Cellulose synthases have emerged as subjects of interest in the pursuit of sabotage (1, 53). Great work has been done to understand the nuances of bacterial cellulose synthesis, including identifying substrates (53),

allosteric activators (16, 17), and interactions with other synthases (54). X-ray crystallography has mapped the bacterial cellulose synthase structure and identified likely mechanisms for cellulose elongation (55, 56). However, there are still gaps in our knowledge of the basic mechanisms of how this enzyme functions. A cohesive understanding of how cellulose synthase operates at the single-molecule level is paramount to developing sustainable and effective anti-microbial techniques. In this dissertation, we characterize both the chemical and physical operating conditions of single Bacterial cellulose synthase A-B complexes (BcsAB) unraveling valuable information about its activation, its kinetic parameters, and the fundamental drivers of cellulose biosynthesis.

1.2 Biological Systems

1.2.1 Cellulose biopolymer

Cellulose is a carbohydrate polymer comprising β -(1,4)-linked D-glucose monomers rotated 180° such that the repeating unit in the polymer is cellobiose, a disaccharide (Fig. 1.1a) (1). Due to extensive inter- and intra-strand hydrogen bonding and van der Waals stacking forces, the polymer lies flat against other strands to make microfibrils with a hexagonal crystal structure (Fig. 1.1b) (11, 12, 23). Cellulose polymers are typically very long with degrees of polymerization exceeding 10,000 (33). In plant systems, cellulose synthesis machinery multimerizes to form rosettes, causing cellulose microfibrils to conjoin immediately after synthesis (31, 33). Interestingly, bacterial systems typically do not multimerize making cellulose crystallization a less rigid process (1). Because of the variety in microfibril means of formation and the degree in polymerization, there exists a wide range in crystallinity between and within allomorphs (12, 33). The physical properties of microfibrils have been of great interest to the biofuels industry as cellulose sequesters energy extremely well, despite being quite resistant to degradation techniques (57). Previous studies have explored the mechanical properties of microfibrils, but due to cellulose's stability in crystalline form, no work has examined a single strand (11, 58-60). However, both cellulose synthesis and degradation occurs a single strand at a time (1, 29). The experiments in this dissertation provide a unique opportunity to study the physical properties and natural predispositions of single-stranded cellulose. The results provide unexpected polymeric qualities and insight into how microfibrils are formed.

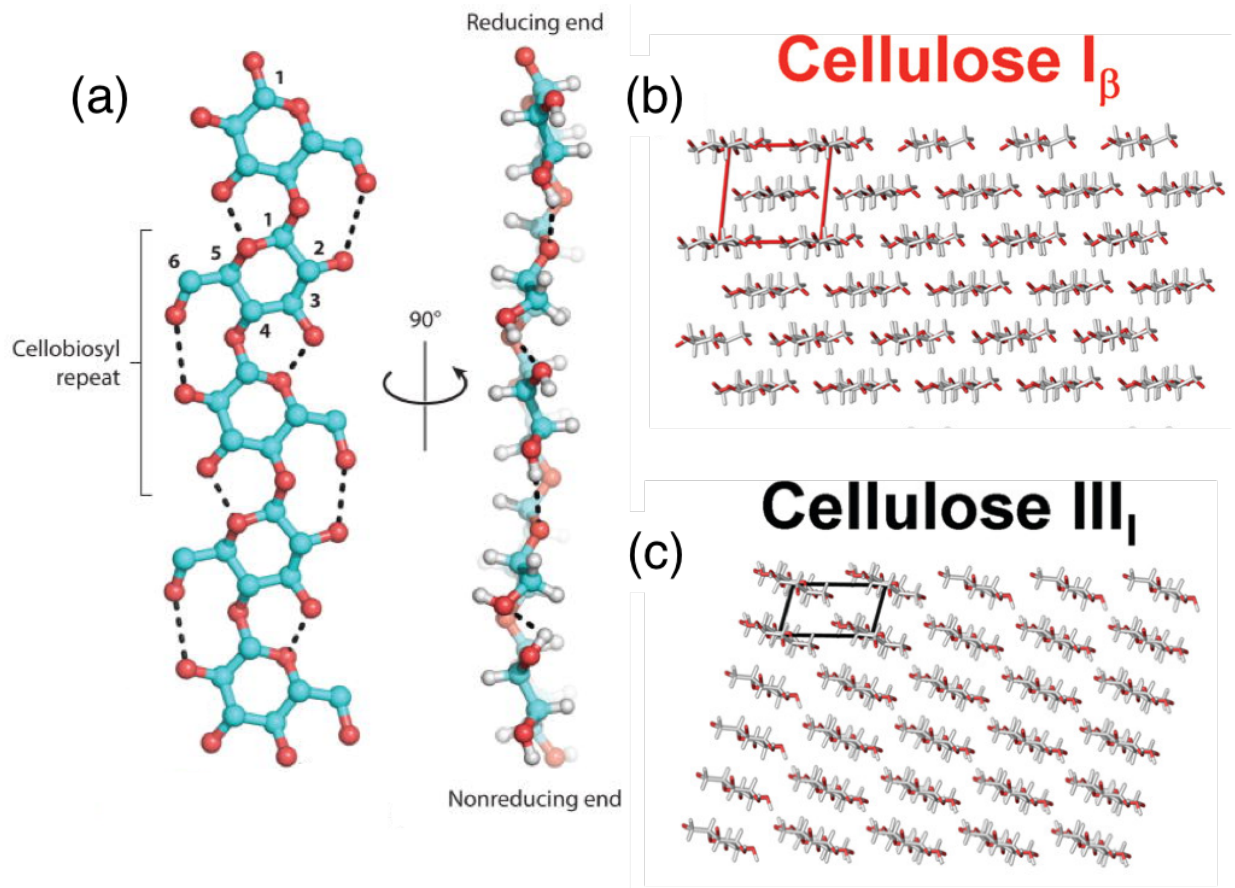


Figure 1.1. Cellulose molecular and lattice structure. (a) Cellulose is linear, flat polymer comprising glucose rings rotated 180° from the previous making the repeating base unit cellobiose. Extensive intra-strand hydrogen bonding (dashed black lines) leads to high stability (1). (b) Cellulose I contains tightly-packed, hexagonally organized cellulose strands. (b) and (c) are cross-sections the cellulose allomorphs. The hexagonal crystal structure encourages inter-strand hydrogen bonding that further strengthens cellulose’s physical properties and prevents chemical disassembly. The red box shows a lattice unit. (c) Ammonia pre-treatment of cellulose I reorganizes the crystal structure into cellulose III. The crystal organization becomes tetrahedral instead of hexagonal, which reduces the inter-strand hydrogen bonding, but increases the inter-sheet hydrogen bonding (12). Images are adapted from McNamara et al. (2015) (1) and Chundawat et al. (2011) (12).

1.2.2 Cellulose degradation machinery

Because cellulose is a great source of energy and carbon for organisms, several kingdoms of life have developed methods for catabolizing cellulose, including bacteria and fungi (18, 30). Despite many families of cellulases, cellulose degradation machinery is most simply broken down into two categories: endoglucanases and exoglucanases or cellobiohydrolases. Endoglucanases snip cellulose fibers through hydrolysis creating free ends, and cellobiohydrolases bind to free ends and

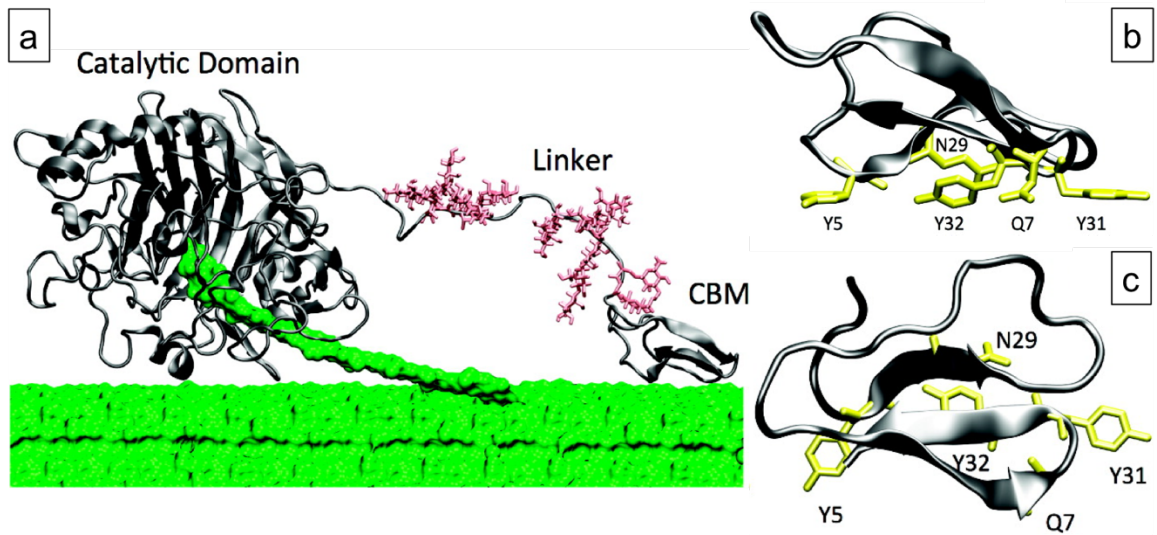


Figure 1.2. Cellobiohydrolase and its CBM. (a) The crystal structure of cellobiohydrolase reveals a large catalytic domain (CD) that threads cellulose through a pore and cleaves cellobiose units from the end of the strand. The carbohydrate binding module (CBM) binds to cellulose increasing the local concentration of free ends to enter the catalytic pore. A glycosylated linker connects the CD and CBM. A side view (b) and top-down view (c) of the CBM shows the five residues involved in binding to cellulose: three aromatic peptides, Y5, Y31A, and Y32a, and two residues engaged in hydrogen bonding, N29 and Q7. The images here are adapted from Beckham et al. 2010 (61).

process down the cellulose chain cleaving cellobiose units as it goes (18, 26).

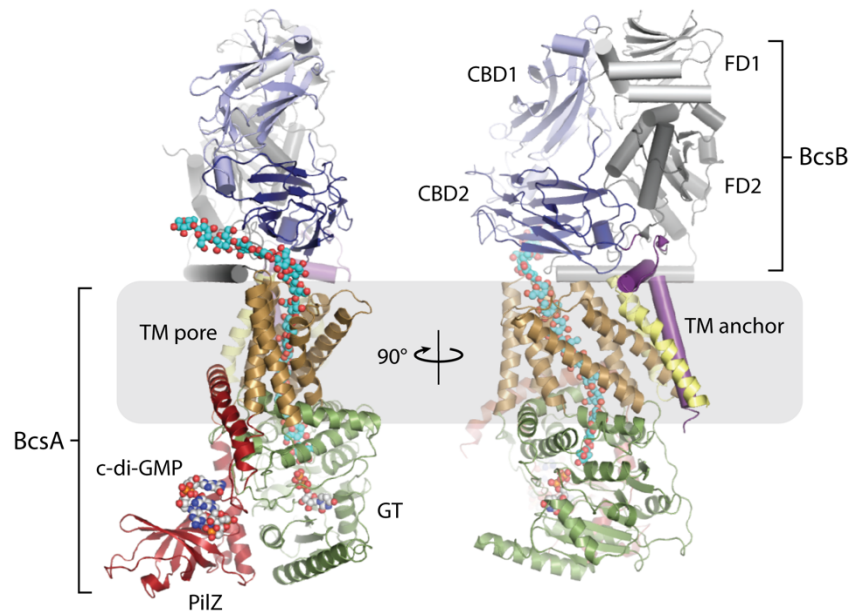
Together, cellulase cocktails are quite efficient at cutting, breaking down and processing cellulose. Molecularly, cellulases typically comprise a carbohydrate binding module (CBM), a neck linker, and a catalytic domain (CD) (Fig. 1.2a) (29, 61). However, only the CD is required for function and sometimes exists on its own (18, 29). The domains are readily interchangeable between families where a CBM frequently associated with one family may appear on a different cellulose family in different organisms (18). In fact, non-fungal cellulases have shown distinct evolutionary branches from fungi prompting studies comparing efficiencies (30). One such report exchanges CBM, linker and CD of a fungal cellobiohydrolase with a bacterial cellulase and found that combining the bacterial CBM and linker with the fungal CD produced a more efficient enzyme than the fungal cellulase by itself (62). It is thought that the CBM's purpose is to introduce the cellulase to cellulose through strand attachment, promoting the cellulase motor's commitment to motility (18, 63).

Family 7 cellulases (Cel7s) are classified as cellobiohydrolases and are responsible for the majority of hydrolytic turnover (30). Because of this and their ease to cultivate and isolate, fungal Cel7s are the most widely studied and most promising for biofuel production (30). Previous Cel7 studies from *Trichoderma reesei* have suggested that the CBM, although necessary to introduce cellulose ends to the CD, may be preventing the maximum efficiency of cellobiohydrolases (29, 35).

Because of the complex implications that CBM-cellulose interactions have on degradation, great effort has gone into identifying Cel7 CBM's binding mechanism and kinetics (27, 28, 61, 64). There are five peptide residues on the base of *TrCel7A* that are associated with binding: two hydrogen bonding residues, N29 and Q7, and three aromatic residues one cellobiose unit apart that engage in ring stacking interactions along a cellulose chain, Y5, Y31 and Y32 (Fig. 1.2b,c) (61, 65). The aromatic residues are expected to have the most contribution to binding (61). CBM-cellulose interactions are known to be reversible and temperature dependent (64), but, with the advancement of cellulose pre-treatment techniques, a detailed comparison of CBM-cellulose interactions between different allomorphs is needed. Additionally, bioengineering more productive cellobiohydrolases will require a detailed understanding of the CBM binding mechanism. This dissertation compares single CBM-cellulose bond lifetime data for filter paper cellulose, cellulose I, and cellulose III. Furthermore, the work presents the complex binding modalities of CBM and discusses possible mechanisms informed by mutant CBM bond rupture experiments.

1.2.3 Cellulose synthesis machinery

In order to address the problems outlined by the biofuel industry, healthcare systems, and industrial settings, we look towards one of the most common biological processes in nature: cellulose synthesis. The membrane-embedded enzyme complex, Cellulose Synthase, is relatively conserved across several kingdoms of life and is responsible for cellulose production for cell walls (plants) and biofilms (bacteria) (1, 31). Because several kingdoms can trace cellulose synthesis back to common ancestors, the cellulose synthase enzyme is a relatively ancient biological system (45). We chose to examine a Bacterial Cellulose Synthase (Bcs) from *Rhodobacter sphaeroides* because of its ease to express and purify (56). The two proteins BcsA and BcsB compose the BcsAB complex (Fig. 1.3) and are responsible for polymer elongation and translocation (53). The intracellular and catalytic BcsA includes an activation domain at the C-terminus referred to as the PilZ domain, eight transmembrane (TM) helices, and a highly conserved family-2 glycosyltransferase (GT) domain between TM helices 4 and 5, while the periplasmic BcsB contains a TM anchor, and two carbohydrate binding domains (CBDs) connected to two domains resembling a flavodoxin fold (FD) and thought to lack functionality (1). Other bacterial and plant systems have slight variations in structure, such as suspected placement of the GT domain between TM helices 2 and 3 in plants (31). Additionally, plant synthases are able to multimerize into triradial symmetric





 McNamara JT, et al. 2015.
 Annu. Rev. Biochem. 84:895–921

Figure 1.3. BcsAB complex crystal structure. The PilZ domain (red) binds c-di-GMP to open the gating loop and initiate biosynthesis. The glycosyltransferase domain (GT, green) accepts UDP-glucose-Mg²⁺ complexes for elongation, closing the gating loop after substrate entrance. Cellulose is then extruded out of the transmembrane (TM) pore (brown) and guided into the periplasmic membrane by the carbohydrate binding domains (CBD, blue) on BcsB before interacting with our Bcs enzymes for chaperoning (BcsC/D), modification (BcsG), or cutting (BcsZ). BcsB contains a TM anchor (purple) to maintain complex integrity. The flavodexin-like domains (FD) are in grey. The crystal structure was solved by the Zimmer group and this image was adapted from McNamara et al. (2015) (1). PDB: 5EJ1.

multi-motor complexes (31) It is imperative to have a comprehensive understanding of the processive mechanism of BcsAB to be able to engineer biofuel solutions or dismantle biofilms. Much work has been done by the Zimmer group to establish a crystal structure, identify important motifs and external components related to synthesis, and assemble snapshots of translocation (17, 55, 56). Synthesis begins with the activation of the BcsA complex by cyclic-di-GMP (c-di-GMP) binding to the PilZ domain and causing a gating loop covering the active site in the GT to swing open (55). Whether c-di-GMP binds once to induce an active state or continual binds and unbinds is unknown. Uridine diphosphate activated glucose (UDP-glc) enters the catalytic domain closing the gating loop behind it due to cation π -interactions and hydrogen bonding. In this substrate-bound state (Fig. 1.4a), the UDP group forms a complex with a Mg²⁺ ion placing the donor glucose

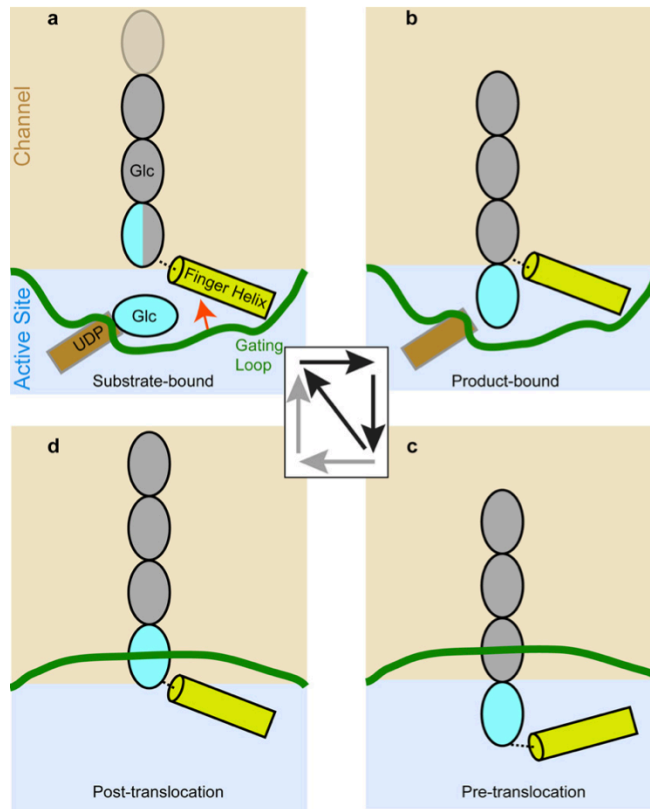


Figure 1.4. Cellulose biosynthesis cycle. Cartoon snapshots of the catalytic cycle in the GT show three expected states/steps. The substrate-bound state (a) includes insertion of UDP-glc and gating loop (green) into the catalytic site. After the addition of the glucose unit facilitated by the TED motif at the N terminus of the finger helix, the complex is in the product bound state (b). In the pre-translocation state (c), the gating loop exits expelling UDP. As the complex returns to (a), the finger helix pushes the polymer up and through the TM pore. (d) An unlikely mechanism suggests the finger helix thrusts independently of the gating loop. Images are adapted from Morgan et al. (2016) (56).

proximal to the polymer end. It is of note that cellulose synthases across kingdoms utilize several different divalent metal cations, such as Mn^{2+} for UDP complex formation (1) and Zn^{2+} for controlling multimerization states in plant systems (66). In a nucleophilic $Sn2$ -like reaction aided by the finger helix, the donor glucose attacks the hydroxyl group of the polysaccharide chain and inverts 180° to create a product-bound state (Fig. 1.4b). The gating loop reopens expelling the nucleotide and creating a hydrophobic pocket below the finger helix. The finger helix drops from the penultimate to the new ultimate saccharide unit in a pre-translocation state (Fig. 1.4c). The re-insertion of the gating loop and new substrate is thought to induce upward movement of the finger helix, translocating the polymer. Although a post-translocation state (Fig. 1.4d) without re-insertion is thermodynamically stable, it is unlikely that the finger helix alone possesses enough energy to exert

the force necessary for extrusion, suggesting substrate binding energizes procession (56). Although these crystallographic portraits reveal important structural details about BcsAB, the single-molecule characterization of the molecular motor presented in this dissertation will unearth output potentials, such as speed of production; limiting factors, such as fuel scarcity; and operating conditions, such as temperature dependence, among other specifics.

1.3 Single-molecule Methods

Biological systems are complex, even at the protein scale. Specific cell functions are dictated by a threshold constraint, such as the concentration of biochemical cues, for instance c-d-GMP concentrations determining cell division (67, 68) or the magnitude of mechanical stimuli (69, 70). Whether the ensemble of cues is above or below the particular threshold determines the degree of execution of the function. Experiments examining the effect of the ensemble on the function are useful in providing information into the tendencies of cell processes. Such studies can identify key players and patterns, but ultimately, they are measuring the average signal of all individual molecular dynamics. Because each molecule behaves incongruent to other similar molecules, there is a vast spectrum of performance within even a specific classification of proteins (71). A lion and a tabby are both felines but are vastly different in capabilities and behaviors. Therefore, the ability to independently observe single molecules can reveal important caveats and is an advantageous technique to study biological processes.

The realm of single-molecule studies has grown quickly as advances in physics breed new techniques. Single-molecule methods are particularly advantageous for achieving ultra-high resolution (≤ 1 nm) and probing mechanical dynamics of the system of interest. Specific techniques worth mentioning are atomic force microscopy (AFM), single-molecule fluorescence, optical and magnetic tweezers, and molecular dynamics/computational methods. Fluorescence techniques, such as Förster Resonance Energy Transfer (FRET) microscopy, total internal reflection fluorescence (TIRF) microscopy, and super-resolution microscopy, have emerged as champions of visualizing specific molecular dynamics (72-76). Additionally, atomic force microscopy (AFM) and optical and magnetic tweezers are able to observe molecular motion and interactions in real time to tease out significant features or events otherwise hidden by bulk averaging (77-83). On occasion, these hidden phenomena can drastically change our understanding of the biological processes, allowing for more

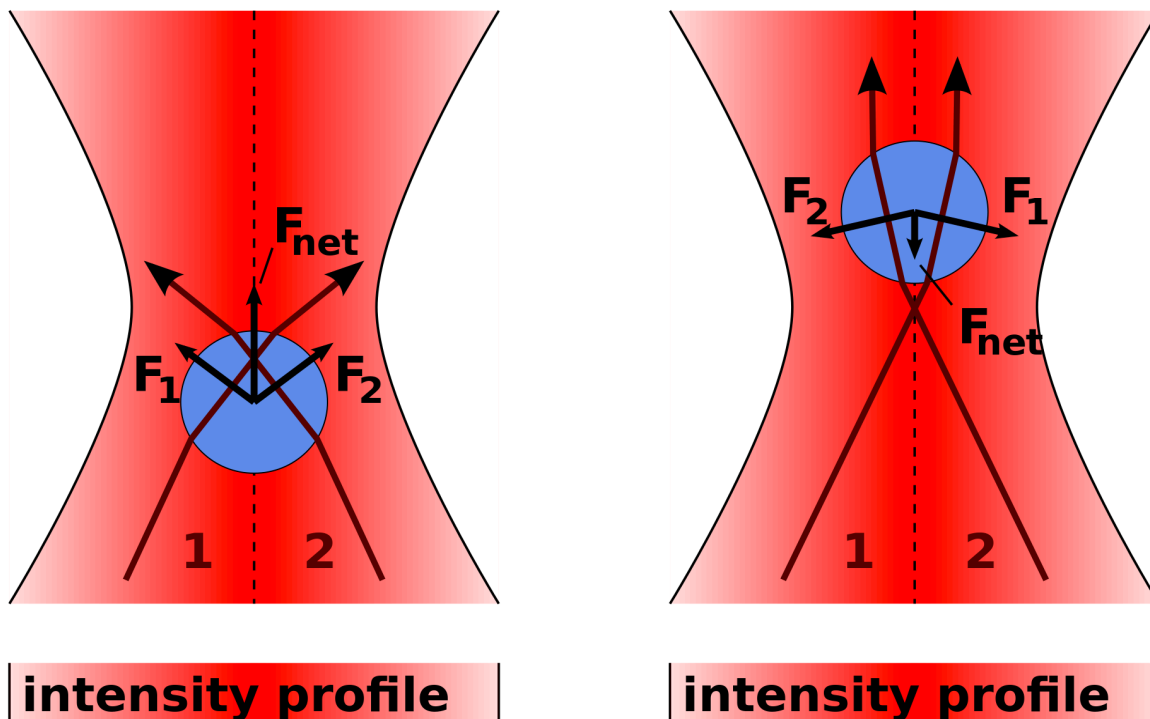


Figure 1.5. Optical tweezers diagram. At the tight focus of a laser, the gradient forces on a spherical dielectric particle, originating from interactions between the laser's electric field and the particles dipoles, exert equal and opposite forces trapping the particle at a fixed position in space near where the laser light is most intense. The force restoring the particle to the trap center is proportional to the distance the particle is from the trap center. Images here are adapted from those by Roland Koebler, Creative Commons Attribution 3.0 Unreported.

efficient and precise engineering, drug design, and industrial processes (71). While not a single-molecule technique, X-ray crystallography provides atomic-resolution pictures from purified ensemble proteins and aids in our understanding of molecular form and function (55, 56). Quantitatively evaluating the molecular dynamics is essential to properly characterize and utilize biological systems for biotechnology and engineering.

1.3.1 Optical tweezers

Optical tweezers have developed to be a versatile tool to study single-molecule dynamics and forces. This technique offers insights into the macromolecular physiology underlying some of the most important functions of life. The study of motor proteins, proteins that convert chemical energy into physical force or displacement, has particularly benefited from the use of optical tweezers, as tweezers provide nanometer and piconewton resolution (84-88).

Optical trapping occurs when a tightly focused laser beam imparts a gradient force on a dielectric

particle. The gradient force originates from the electric field gradient in the laser interacting with the electric polarization, or dipole, in the dielectric material. Hence, a tighter laser focus yields a steeper electric field gradient and imparts a large enough gradient force, transversely and axially, to overcome the axial scattering force from the bombardment of photons. The particle is then “trapped” in space at the focus of the laser. When the particle is displaced from the trap center by small distances (<200 nm), a restoring force, dictated by the gradient force, pulls the particle back towards the trap center. The restoring force is linearly proportional to displacement and can be modelled after a Hookeian spring. With this, we functionalize biology to our trapped particle (~1 μm), or trap biology itself (89), and impart forces on single molecule interaction while tracking translational displacement in real time (29, 90-92). A cartoon diagram of optical forces is shown in Fig. 1.5, and assay diagrams is shown in Figures 2.2 and 3.1. Optical tweezers have most commonly been used to study molecular motors, such as kinesins (85, 91, 93), myosins (86), ATPases (92), RNA and DNA polymerases (88, 94, 95), ribosomes (96) and recently cellobiohydrolase (29), uncovering physical step sizes, stall forces and conformational dynamics underlying a motor protein’s enzymatic cycle. Additionally, force-generation at the single-molecule scale allows for mechanical characterization of polymers, such as DNA (97, 98), RNA (99, 100), polynorbornene (101), peptide strands (102, 103), and tropocollogen (104) among others. Polymer stretching experiments reveal the persistence length (the distance the polymer remains straight before a natural bend / how resistant the polymer is to bending), the axial elasticity stiffness (how resistant the polymer is to axial stretching), the contour length (how long the polymer is), and any conformational structure changes with applied force. Optical tweezers also provide means to investigate single protein-substrate interactions using force spectroscopy, yielding bond lifetimes and chemical kinetic and thermodynamic data (29, 70, 90, 105). The work in this dissertation utilizes optical tweezers in all three mentioned facets: unraveling BcsAB motor protein dynamics, quantifying single-strand cellulose physical properties, and studying CBM-cellulose interactions by using force spectroscopy. BcsAB is the fourth polymerizing enzyme to be characterized at the single-molecule level, behind RNA polymerase (94), DNA polymerase (95), and ribosomes (96), but the only one to work without a DNA or RNA track template (1). Additionally, chapter 4 provides an in-depth description on optical tweezer construction and methods to enhance current practices enabling ultra-high resolution for slower cellulose molecular machinery.

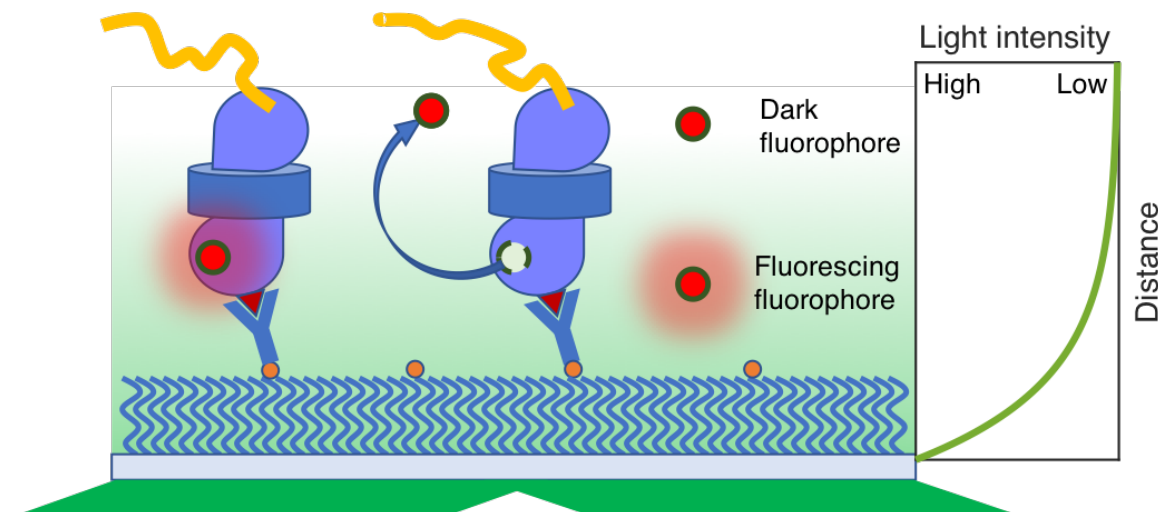


Figure 1.6. TIRF diagram. An example schematic of a TIRF assay shows that when light is reflected at an oblique enough angle off the bottom of the coverslip to internally reflect, an evanescent wave enters the specimen plane. Fluorophores near the surface will fluoresce while fluorophores further away from the surface will not. The curve to the right depicts the light intensity decreasing exponentially with the distance from the coverslip. Single-molecule resolution is possible at dilute enough ligands and substrates.

1.3.2 Total internal reflection fluorescence (TIRF) microscopy

Total internal reflection fluorescence (TIRF) is a powerful single-molecule technique that has been used previously to understand binding kinetics (106), protein conformational dynamics (106, 107), mechanotransduction (108), and enzyme processivity (28, 73, 76). TIRF requires a fluorescent laser beam to be directed at the interface boundary between the objective oil and the microscope slide at an oblique angle, such that the laser is reflected back to the oil, the “internal” medium. This can be accomplished using a high numerical aperture objective (~1.5 NA) and aligning the optical path at the edge of the objective entrance instead of the middle. When the incident light reaches the critical angle necessary for reflection, an evanescent wave travels through the microscope slide, the “external” medium and dissipates exponentially until about 200 nm into the specimen plane. Because of the incredibly short region of illumination, only fluorescent molecules at the surface will fluoresce. When limiting a fluorophore’s concentration, TIRF can be optimized for single-molecule resolution allowing one to build a population of individual molecular events instead of relying on ensemble measurements. A diagram can be viewed in Fig. 1.6 and Fig. 3.4. The work in this dissertation employs TIRF to uncover the binding and dissociation kinetics of c-d-GMP to BcsAB.

1.4 Summary

Cellulose, as the most abundant biopolymer, is an incredibly important material to sustain life. Because of its structural and chemical properties, it has emerged as a biofuel precursor candidate as well as a target for antibiotics. To fully tap into the potential of human use and treatment of cellulose, we must have a comprehensive understanding of how the material is biodegraded and biomanufactured. A greater understanding in these processes will lead to more efficient and cost-effective biofuel production, a theoretical net-zero carbon-emitting fuel source, and more robust and potent antibiotic treatments to prevent nosocomial infections, a leading cause of death in the United States, and prevent industrial biofouling, which costs industrialized nations ~0.25% of their GDP each year. This dissertation employs single-molecule techniques, such as optical tweezers force spectroscopy and total internal reflection fluorescence, to better understand 1) cellulase binding behavior to different cellulose allomorphs and its potential effect on degradation productivity, 2) the biochemical and physical operating conditions of the bacterial cellulose synthase molecular motor and 3) single-strand cellulose's mechanical properties and how they may relate to bacterial biofilm structural integrity. The knowledge gained from these studies will aid bioengineering efforts in biofuel production and spur directed and purposeful antibiotic discovery. Additionally, this dissertation outlines a novel optical tweezers microscope that uses a dual-laser detection system to eliminate drift when studying particularly slow molecular motors, such as carbohydrate synthases and cellulases. Advances herein aim to empower the scientific community with insight and tools to further expand our understanding and capabilities.

1.5 References

1. J. T. McNamara, J. L. W. Morgan, J. Zimmer, A molecular description of cellulose biosynthesis. *Annual Review of Biochemistry* **84**, 895-921 (2015).
2. D. Klemm, B. Heublein, H. P. Fink, A. Bohn, Cellulose: Fascinating biopolymer and sustainable raw material. *Angewandte Chemie - International Edition* **44**, 3358-3393 (2005).
3. W. H. Organization, Evaluation of certain food additives. *World Health Organ Tech Rep Ser*, 1-162 (2017).
4. Z. Peršin *et al.*, Novel cellulose based materials for safe and efficient wound treatment. *Carbohydr Polym* **100**, 55-64 (2014).
5. A. Carroll, C. Somerville, Cellulosic biofuels. *Annual Review of Plant Biology* **60**, 165-182 (2009).

6. A. Payen, Memoire sur la composition du tissu propre des plantes et du ligneux. *C. R. Hebd. Seances Acad. Sci.* **7**, 1052-1056 (1838).
7. Z. Gallot-Grubisic, P. Rempp, H. Benoit, Universal calibration for gel permeation chromatography. *J Polym Sci Polym Lett* **5**, 753-759 (1967).
8. K. Kamide, K. Okajima, K. Kowsaka, T. Matsui, CP/MASS [cross-polarization/magic angle sample spinning] carbon-13 NMR spectra of cellulose solids: an explanation by the intramolecular hydrogen bond concept. *Polym J* **17**, 701-706 (1985).
9. C. Liang, R. Marchessault, Infrared spectra of crystalline polysaccharides. I. Hydrogen bonds in native celluloses. *J Polym Sci* **37**, 385-395 (1959).
10. A. J. Michell, Second derivative F.t.i.r. spectra of celluloses I and II and related mono- and olig-saccharides. *AGRIS* **173**, 185-195 (1988).
11. A. Thygesen, J. Oddershede, H. Lilholt, A. B. Thomsen, K. Ståhl, On the determination of crystallinity and cellulose content in plant fibres. *Cellulose* **12**, 563-576 (2005).
12. S. P. S. Chundawat *et al.*, Restructuring the crystalline cellulose hydrogen bond network enhances its depolymerization rate. *Journal of the American Chemical Society* **133**, 11163-11174 (2011).
13. J. Engelhardt, Sources, industrial derivatives, and commercial applications of cellulose. *Carbohydr. Eur.* **12**, 5-14 (1995).
14. D. P. Delmer, CELLULOSE BIOSYNTHESIS: Exciting Times for A Difficult Field of Study. *Annu Rev Plant Physiol Plant Mol Biol* **50**, 245-276 (1999).
15. L. F. Leloir, Two decades of research on the biosynthesis of saccharides. *Science* **172**, 1299-1303 (1971).
16. U. Römling, M. Y. Galperin, M. Gomelsky, Cyclic di-GMP: the first 25 years of a universal bacterial second messenger. *Microbiol Mol Biol Rev* **77**, 1-52 (2013).
17. J. L. W. Morgan, J. T. McNamara, J. Zimmer, Mechanism of activation of bacterial cellulose synthase by cyclic di-GMP. *Nature Structural and Molecular Biology* **21**, 489-496 (2014).
18. B. Henrissat, Cellulases and their interaction with cellulose. *Cellulose* **1**, 169-196 (1994).
19. R. a. L. X. a. Y. G. Wolfenden, Spontaneous Hydrolysis of Glycosides. *Journal of the American Chemical Society* **120**, 6814-6815 (1998).
20. M. Kurasin, P. Väljamäe, Processivity of cellobiohydrolases is limited by the substrate. *J Biol Chem* **286**, 169-177 (2011).
21. C. M. Payne *et al.*, Glycoside Hydrolase Processivity Is Directly Related to Oligosaccharide Binding Free Energy. *Journal of the American Chemical Society* **135**,

- 18831-18839 (2013).
22. R. H. Bischof, J. Ramoni, B. Seiboth, Cellulases and beyond: the first 70 years of the enzyme producer *Trichoderma reesei*. *Microbial Cell Factories* **15**, 106 (2016).
 23. M. Hall, P. Bansal, J. H. Lee, M. J. Realff, A. S. Bommarius, Cellulose crystallinity—a key predictor of the enzymatic hydrolysis rate. *The FEBS journal* **277**, 1571-1582 (2010).
 24. S. P. S. Chundawat *et al.*, Multi-scale visualization and characterization of lignocellulosic plant cell wall deconstruction during thermochemical pretreatment. *Energy and Environmental Science* **4**, 973-984 (2011).
 25. B. C. Knott *et al.*, The mechanism of cellulose hydrolysis by a two-step, retaining cellobiohydrolase elucidated by structural and transition path sampling studies. *Journal of the American Chemical Society* **136**, 321-329 (2014).
 26. C. Divne, J. Ståhlberg, T. T. Teeri, T. A. Jones, High-resolution crystal structures reveal how a cellulose chain is bound in the 50 Å long tunnel of cellobiohydrolase I from *Trichoderma reesei*. *Journal of Molecular Biology* **275**, 309-325 (1998).
 27. S. Takashima *et al.*, Correlation between cellulose binding and activity of cellulose-binding domain mutants of *Humicola grisea* cellobiohydrolase 1. *FEBS Letters* **581**, 5891-5896 (2007).
 28. Y. Shibafuji *et al.*, Single-molecule imaging analysis of elementary reaction steps of *trichoderma reesei* cellobiohydrolase i (Cel7A) hydrolyzing crystalline cellulose Ia and III. *Journal of Biological Chemistry* **289**, 14056-14065 (2014).
 29. S. K. Brady, S. Sreelatha, Y. Feng, S. P. S. Chundawat, M. J. Lang, Cellobiohydrolase 1 from *Trichoderma reesei* degrades cellulose in single cellobiose steps. *Nature Communications* **6**, 1-9 (2015).
 30. C. M. Payne *et al.*, Fungal cellulases. *Chemical Reviews* **115**, 1308-1448 (2015).
 31. H. E. McFarlane, A. Döring, S. Persson, The cell biology of cellulose synthesis. *Annual Review of Plant Biology* **65**, 69-94 (2014).
 32. J. Houghton, S. Weatherwax, J. Ferrell (2006) Breaking the Biological Barriers to Cellulosic Ethanol: A Joint Research Agenda. (USDOE Office of Energy Efficiency and Renewable Energy (EERE), Transportation Office. Bioenergy Technologies Office., EERE Publication and Product Library, Washington, D.C. (United States)).
 33. D. B. Jordan *et al.*, Plant cell walls to ethanol. *Biochemical Journal* **442**, 241-252 (2012).
 34. K. Igarashi, M. Wada, R. Hori, M. Samejima, Surface density of cellobiohydrolase on crystalline celluloses. *The FEBS Journal* **273**, 2869-2878 (2006).
 35. K. Igarashi, M. Wada, M. Samejima, Activation of crystalline cellulose to cellulose III(I)

- results in efficient hydrolysis by cellobiohydrolase. *Febs j* **274**, 1785-1792 (2007).
36. D. L. Trudeau, T. M. Lee, F. H. Arnold, Engineered thermostable fungal cellulases exhibit efficient synergistic cellulose hydrolysis at elevated temperatures. *Biotechnol Bioeng* **111**, 2390-2397 (2014).
 37. S. P. Voutilainen, P. G. Murray, M. G. Tuohy, A. Koivula, Expression of *Talaromyces emersonii* cellobiohydrolase Cel7A in *Saccharomyces cerevisiae* and rational mutagenesis to improve its thermostability and activity. *Protein Eng Des Sel* **23**, 69-79 (2010).
 38. S. E. Lantz *et al.*, *Hypocrea jecorina* CEL6A protein engineering. *Biotechnol Biofuels* **3**, 20 (2010).
 39. F. Chen, R. A. Dixon, Lignin modification improves fermentable sugar yields for biofuel production. *Nature Biotechnology* **25**, 759-761 (2007).
 40. J. Ralph, S. Guillaumie, J. H. Grabber, C. Lapierre, Y. Barrière, Genetic and molecular basis of grass cell-wall biosynthesis and degradability. III. Towards a forage grass ideotype. *C R Biol* **327**, 467-479 (2004).
 41. M. R. Javed *et al.*, Current situation of biofuel production and its enhancement by CRISPR/Cas9-mediated genome engineering of microbial cells. *Microbiol Res* **219**, 1-11 (2019).
 42. C. E. Jahn, D. A. Selimi, J. D. Barak, A. O. Charkowski, The *Dickeya dadantii* biofilm matrix consists of cellulose nanofibres, and is an emergent property dependent upon the type iii secretion system and the cellulose synthesis operon. *Microbiology* **157**, 2733-2744 (2011).
 43. J. W. Costerton *et al.*, BACTERIAL BIOFILMS IN NATURE AND DISEASE. *Ann. Rev. Microbiol.* **41**, 435-464 (1987).
 44. L. Karygianni, Z. Ren, H. Koo, T. Thurnheer, Biofilm Matrixome: Extracellular Components in Structured Microbial Communities. *Trends in Microbiology* **28**, 668-681 (2020).
 45. L. Hall-Stoodley, J. W. Costerton, P. Stoodley, Bacterial biofilms: from the natural environment to infectious diseases. *Nat Rev Microbiol* **2**, 95-108 (2004).
 46. H. C. Flemming *et al.*, Biofilms: an emergent form of bacterial life. *Nat Rev Microbiol* **14**, 563-575 (2016).
 47. A. Persat, F. Inclan Yuki, N. Engel Joanne, A. Stone Howard, Z. Gitai, Type IV pili mechanochemically regulate virulence factors in *Pseudomonas aeruginosa*. *Proceedings of the National Academy of Sciences* **112**, 7563-7568 (2015).

48. N. T. Mathew, J. Kronholm, K. Bertilsson, M. Despeisse, B. Johansson, "Environmental and Economic Impacts of Biofouling on Marine and Coastal Heat Exchangers" in *EcoDesign and Sustainability II: Social Perspectives and Sustainability Assessment*, Y. Kishita, M. Matsumoto, M. Inoue, S. Fukushige, Eds. (Springer Singapore, Singapore, 2021), pp. 385-398.
49. N. Bloecher, O. Floerl, Towards cost-effective biofouling management in salmon aquaculture: a strategic outlook. *Reviews in Aquaculture* **13**, 783-795 (2021).
50. J. A. Otter *et al.*, Surface-attached cells, biofilms and biocide susceptibility: Implications for hospital cleaning and disinfection. *Journal of Hospital Infection* **89**, 16-27 (2015).
51. P. S. Stewart, J. W. Costerton, Antibiotic resistance of bacteria in biofilms. *Lancet* **358**, 135-138 (2001).
52. J. W. Costerton, P. S. Stewart, E. P. Greenberg, Bacterial biofilms: a common cause of persistent infections. *Science* **284**, 1318-1322 (1999).
53. O. Omadjela *et al.*, BcsA and BcsB form the catalytically active core of bacterial cellulose synthase sufficient for in vitro cellulose synthesis. *Proceedings of the National Academy of Sciences of the United States of America* **110**, 17856-17861 (2013).
54. S. Basu *et al.*, Cellulose Microfibril Formation by Surface-Tethered Cellulose Synthase Enzymes. (2016).
55. J. L. W. Morgan, J. Strumillo, J. Zimmer, Crystallographic snapshot of cellulose synthesis and membrane translocation. *Nature* **493**, 181-186 (2013).
56. J. L. W. Morgan *et al.*, Observing cellulose biosynthesis and membrane translocation in crystallo. *Nature* **531**, 329-334 (2016).
57. A. Mihranyan, Cellulose from cladophorales green algae: From environmental problem to high-tech composite materials. *Journal of Applied Polymer Science* **119**, 2449-2460 (2011).
58. S. Iwamoto, W. Kai, A. Isogai, T. Iwata, Elastic modulus of single cellulose microfibrils from tunicate measured by atomic force microscopy. *Biomacromolecules* **10**, 2571-2576 (2009).
59. Q. Cheng, S. Wang, A method for testing the elastic modulus of single cellulose fibrils via atomic force microscopy. *Composites Part A: Applied Science and Manufacturing* **39**, 1838-1843 (2008).
60. L. M. J. Kroon-Batenburg, P. H. Kruiskamp, J. F. G. Vliegthart, J. Kroon, Estimation of the Persistence Length of Polymers by MD Simulations on Small Fragments in Solution. Application to Cellulose. *The Journal of Physical Chemistry B* **101**, 8454-8459 (1997).

61. G. T. Beckham *et al.*, Identification of amino acids responsible for processivity in a family 1 carbohydrate-binding module from a fungal cellulase. *Journal of Physical Chemistry B* **114**, 1447-1453 (2010).
62. L. E. Taylor *et al.*, Engineering enhanced cellobiohydrolase activity. *Nature Communications* **9**, 1-10 (2018).
63. S. P. S. Chundawat *et al.*, Molecular origins of reduced activity and binding commitment of processive cellulases and associated carbohydrate-binding proteins to cellulose III. *The Journal of biological chemistry*, 100431-100431 (2021).
64. M. Linder, T. T. Teeri, The cellulose-binding domain of the major cellobiohydrolase of *Trichoderma reesei* exhibits true reversibility and a high exchange rate on crystalline cellulose. *Proc Natl Acad Sci U S A* **93**, 12251-12255 (1996).
65. J. Kraulis *et al.*, Determination of the three-dimensional solution structure of the C-terminal domain of cellobiohydrolase I from *Trichoderma reesei*. A study using nuclear magnetic resonance and hybrid distance geometry-dynamical simulated annealing. *Biochemistry* **28**, 7241-7257 (1989).
66. I. Kurek, Y. Kawagoe, D. Jacob-Wilk, M. Doblin, D. Delmer, Dimerization of cotton fiber cellulose synthase catalytic subunits occurs via oxidation of the zinc-binding domains. *Proceedings of the National Academy of Sciences* **99**, 11109-11114 (2002).
67. I. S. Pultz *et al.*, The response threshold of Salmonella PilZ domain proteins is determined by their binding affinities for c-di-GMP. *Mol Microbiol* **86**, 1424-1440 (2012).
68. U. Römling, M. Y. Galperin, Bacterial cellulose biosynthesis: diversity of operons, subunits, products, and functions. *Trends Microbiol* **23**, 545-557 (2015).
69. F. Martino, A. R. Perestrelo, V. Vinarský, S. Pagliari, G. Forte, Cellular mechanotransduction: from tension to function. *Frontiers in physiology* **9**, 824 (2018).
70. K. N. Brazin *et al.*, Structural features of the $\alpha\beta$ TCR mechanotransduction apparatus that promote pMHC discrimination. *Frontiers in Immunology* **6** (2015).
71. D. Rivelino, 'Single molecule': theory and experiments, an introduction. *Journal of nanobiotechnology* **11 Suppl 1**, S1-S1 (2013).
72. C. Grashoff *et al.*, Measuring mechanical tension across vinculin reveals regulation of focal adhesion dynamics. *Nature* **466**, 263-266 (2010).
73. R. D. Vale *et al.*, Direct observation of single kinesin molecules moving along microtubules. *Nature* **380**, 451-453 (1996).
74. L. Turnbull *et al.*, Explosive cell lysis as a mechanism for the biogenesis of bacterial membrane vesicles and biofilms. *Nat Commun* **7**, 11220 (2016).

75. L. Bacic, A. Sabantsev, S. Deindl, Recent advances in single-molecule fluorescence microscopy render structural biology dynamic. *Current Opinion in Structural Biology* **65**, 61-68 (2020).
76. Z. K. Haviland *et al.*, Nanoscale dynamics of cellulose digestion by the cellobiohydrolase TrCel7A. *Journal of Biological Chemistry* **297** (2021).
77. S. B. Smith, L. Finzi, C. Bustamante, Direct mechanical measurements of the elasticity of single DNA molecules by using magnetic beads. *Science* **258**, 1122-1126 (1992).
78. C. Bustamante, J. Marko, E. Siggia, S. Smith, Entropic elasticity of lambda-phage DNA. *Science* **265**, 1599-1600 (1994).
79. M. Rief, M. Gautel, F. Oesterhelt, J. M. Fernandez, H. E. Gaub, Reversible unfolding of individual titin immunoglobulin domains by AFM. *Science* **276**, 1109-1112 (1997).
80. Y. C. Lin *et al.*, Force-induced conformational changes in PIEZO1. *Nature* **573**, 230-234 (2019).
81. Y. Seol, K. C. Neuman, Magnetic tweezers for single-molecule manipulation. *Methods Mol Biol* **783**, 265-293 (2011).
82. J. Sung, S. Sivaramakrishnan, A. R. Dunn, J. A. Spudich, *Single-Molecule Dual-Beam Optical Trap Analysis of Protein Structure and Function* (Elsevier Inc., ed. 1, 2010), vol. 475, pp. 321-375.
83. J. A. Spudich, S. E. Rice, R. S. Rock, T. J. Purcell, H. M. Warrick, Optical traps to study properties of molecular motors. *Cold Spring Harb Protoc* **2011**, 1305-1318 (2011).
84. K. Visscher, S. P. Gross, S. M. Block, Construction of multiple-beam optical traps with nanometer-resolution position sensing. *IEEE Journal on Selected Topics in Quantum Electronics* **2**, 1066-1076 (1996).
85. M. J. Schnitzer, S. M. Block, Kinesin hydrolyses one ATP per 8-nm step. *Nature* **388**, 386-390 (1997).
86. J. T. Finer, R. M. Simmons, J. A. Spudich, Single myosin molecule mechanics: piconewton forces and nanometre steps. *Nature* **368**, 113-119 (1994).
87. M. J. Lang, C. L. Asbury, J. W. Shaevitz, S. M. Block, An automated two-dimensional optical force clamp for single molecule studies. *Biophys J* **83**, 491-501 (2002).
88. M. D. Wang *et al.*, Force and velocity measured for single molecules of RNA polymerase. *Science* **282**, 902-907 (1998).
89. A. Ashkin, J. M. Dziedzic, T. Yamane, Optical trapping and manipulation of single cells using infrared laser beams. *Nature* **330**, 769-771 (1987).
90. D. K. Das *et al.*, Pre-T cell receptors (Pre-TCRs) leverage V β complementarity

- determining regions (CDRs) and hydrophobic patch in mechanosensing thymic self-ligands. *Journal of Biological Chemistry* **291**, 25292-25305 (2016).
91. D. N. Reinemann, S. R. Norris, R. Ohi, M. J. Lang, Processive Kinesin-14 HSET Exhibits Directional Flexibility Depending on Motor Traffic. *Current Biology* **28**, 2356-2362.e2355 (2018).
 92. J. C. Cordova *et al.*, Stochastic but highly coordinated protein unfolding and translocation by the ClpXP proteolytic machine. *Cell* **158**, 647-658 (2014).
 93. K. Svoboda, C. F. Schmidt, B. J. Schnapp, B. S. M. Block, Direct observation of kinesin stepping by OT interferometry. *Nature* **365**, 721-727 (1993).
 94. H. Yin *et al.*, Transcription against an applied force. *Science* **270**, 1653-1657 (1995).
 95. G. J. L. Wuite, S. B. Smith, M. Young, D. Keller, C. Bustamante, Single-molecule studies of the effect of template tension on T7 DNA polymerase activity. *Nature* **404**, 103-106 (2000).
 96. S. Uemura *et al.*, Peptide bond formation destabilizes Shine–Dalgarno interaction on the ribosome. *Nature* **446**, 454-457 (2007).
 97. M. D. Wang, H. Yin, R. Landick, J. Gelles, S. M. Block, Stretching DNA with optical tweezers. *Biophysical Journal* **72**, 1335-1346 (1997).
 98. A. Bosco, J. Camunas-Soler, F. Ritort, Elastic properties and secondary structure formation of single-stranded DNA at monovalent and divalent salt conditions. *Nucleic Acids Research* **42**, 2064-2074 (2014).
 99. M. H. Larson, W. J. Greenleaf, R. Landick, S. M. Block, Applied Force Reveals Mechanistic and Energetic Details of Transcription Termination. *Cell* **132**, 971-982 (2008).
 100. K. Hayashi *et al.*, Influence of RNA Strand Rigidity on Polyion Complex Formation with Block Cationomers. *Macromol. Rapid Commun* **37**, 493-493 (2016).
 101. C. Liu *et al.*, Single polymer growth dynamics. *Science* **358**, 352-355 (2017).
 102. G. Stirnemann, D. Giganti, J. M. Fernandez, B. J. Berne, Elasticity, structure, and relaxation of extended proteins under force. *Proceedings of the National Academy of Sciences* **110**, 3847 (2013).
 103. M. E. Aubin-Tam, A. O. Olivares, R. T. Sauer, T. A. Baker, M. J. Lang, Single-molecule protein unfolding and translocation by an ATP-fueled proteolytic machine. *Cell* **145**, 257-267 (2011).
 104. M. Hillgärtner, K. Linka, M. Itskov, Worm-like chain model extensions for highly stretched tropocollagen molecules. *Journal of Biomechanics* **80**, 129-135 (2018).

105. Y. Feng *et al.*, Mechanosensing drives acuity of $\alpha\beta$ T-cell recognition. *Proc Natl Acad Sci U S A* **114**, E8204-e8213 (2017).
106. Y. Shin *et al.*, Single-molecule denaturation and degradation of proteins by the AAA+ ClpXP protease. *Proceedings of the National Academy of Sciences of the United States of America* **106**, 19340-19345 (2009).
107. D. Banik *et al.*, Single Molecule Force Spectroscopy Reveals Distinctions in Key Biophysical Parameters of $\alpha\beta$ T-Cell Receptors Compared with Chimeric Antigen Receptors Directed at the Same Ligand. *J. Phys. Chem. Lett.* 2021 **12**, 7573-7573 (2021).
108. S. A. Rashid *et al.*, DNA Tension Probes Show that Cardiomyocyte Maturation Is Sensitive to the Piconewton Traction Forces Transmitted by Integrins. *ACS Nano* **16**, 5335-5348 (2022).

CHAPTER 2

Cellobiohydrolase Carbohydrate Binding Module 1 from *Trichoderma Reesei* exhibits reduced binding to cellulose III and multiple binding schemes to various cellulose substrates.

This chapter is adapted from Chundawat et al, "Molecular origins of reduced activity and binding commitment of processive cellulases and associated carbohydrate-binding proteins to cellulose III" *J. Biol. Chem.* 2021 Jan-Jun; 296:100431. by permission granted under the CC-BY license and by corresponding authors.

2.1 Summary

Efficient enzymatic degradation of cellulosic biomass into fermentable sugars can enable the production of biofuels like ethanol. Enzymatic hydrolysis of native crystalline cellulose, or cellulose I, is relatively inefficient, but cellulose I can be converted into the structurally distinct cellulose III allomorph. Cellulase cocktails derived from *Trichoderma reesei* convert cellulose III up to 20-fold faster than cellulose I. However, individual cellulases from *T. reesei*, like the processive exocellulase Cel7A, show reduced binding and activity at low enzyme loadings toward cellulose III. Studies using single-molecule optical tweezers force spectroscopy to analyze the initial binding commitment and subsequent processivity of TrCel7A enzymes cellulose revealed a 48% lower initial binding commitment and 32% slower processive motility of Cel7A on cellulose III. We hypothesize that this discrepancy derives from a reduced binding affinity of the Cel7A binding domain CBM1. Force spectroscopy measurements of CBM1–cellulose interactions corroborate the reduced binding affinity and indicate that the binding behavior cannot be explained by just one or two unique and independent binding sites. Interestingly, CBM1 binding affinity to filter paper cellulose was greater than to either cellulose I or III, while exhibiting the same multimodal behavior. Additionally, the force vs lifetime measurements of CBM1 mutants (Y5A and Y31A) to cellulose I indicate a potential loss of a binding regime for each and reveal a surprisingly higher affinity of Y31A to cellulose under 10-15 pN of applied force. These findings suggest the various binding orientations of CBM1, dictated by the crystal structure of the substrate and position of aromatic rings along the base of CBM1, contribute to the binding affinity, productivity and therefore efficiency of TrCel7A.

2.2 Introduction

Plant biomass, composed of polysaccharides like cellulose, is an ideal feedstock for bioconversion

into various bioproducts like ethanol (1, 2). Cellulose is a β -(1 \rightarrow 4)-glucose polymer that self-assembles to form crystalline fibrils that are recalcitrant to enzymatic depolymerization (3). Cellulolytic microbes (like *Trichoderma reesei* and *Clostridium thermocellum*) have therefore evolved with enzymes called cellulases that can deconstruct cellulose into fermentable sugars (4-6). Cellulases comprise two or more polypeptide domains called catalytic domains (CDs) and CBMs (4). CBMs are characterized by a planar binding motif that is complementary to crystalline cellulose fibril structure to facilitate CD activity toward insoluble and structurally heterogeneous cellulosic substrates (7). Although CBMs facilitate CD activity by proximity-based targeting effects, cellulolytic enzymes are inefficient for industrial applications often due to nonproductive interactions with the substrate that necessitate high protein loading requirements (4, 8).

Thermochemical pretreatment using acids, bases, or ionic liquids is therefore employed to increase polysaccharide accessibility to enzymes and reduce nonproductive cellulase binding (9-11). Pretreatment with anhydrous liquid ammonia results in conversion of native cellulose I to cellulose III allomorph (12), thereby improving hydrolytic activity of several fungal (13) and bacterial cellulase mixtures (14). However, processive exocellulases such as *TrCel7A* (or *Cel7A* from *T. reesei*) and *TfCel6B* (or *Cel6B* from *Thermobifida fusca*), which are workhorse cellulolytic enzymes, often show reduced activity on pretreated cellulose III for reasons poorly understood (14, 15). Although the processive mechanism of *Cel7A* on native cellulose I has been studied extensively using classical biochemical assays (16-19) and molecular simulations (20, 21), there is limited consensus on how to monitor the initial enzyme association with the cellulose chain (18) or dissociation of nonproductively bound enzymes (16, 17) to identify rate-limiting steps impacting cellulose hydrolysis. Hence, there is a need for better experimental methods that can track cellulase binding and processive motility in real time with atomic-scale resolution for distinct substrates. Single-molecule fluorescence imaging allows estimation of exocellulase binding kinetics parameters (e.g., adsorption and desorption rates) (8, 22, 23), whereas high-speed atomic force microscopy allows tracking of motility of single cellulase molecules (24, 25). However, these methods cannot resolve the slower subnanometer translational rates of processive cellulases relevant to cellulose decrystallization and hydrolysis into cellobiose. We recently reported an optical tweezers force spectroscopy-based cellulase assay technique to track the single-molecule motility of *Cel7A* on native cellulose with subnanometer and millisecond resolution (26). Of interest, *Cel7A* CD in the absence of CBM1 showed lower dwell times between catalytic turnover steps suggesting that CBMs could impede full-length cellulase motility on native cellulose I owing to nonproductive binding. However, we lack a detailed understanding of the mechanistic role of CBMs in full-length

processive cellulase binding and motility on cellulose I and other industrially relevant cellulosic substrates like cellulose III. Single-molecule cellulase motility assays were previously performed on both cellulose allomorphs and found that Cel7A was much more less committal to binding and motility on cellulose III than on cellulose I (27). From these studies, we hypothesize that the CBM likely plays a prominent role in this phenomenon, as its primary function is to increase the proximity of CD near cellulose surface (to within a few nanometers).

Here, we have developed a new optical tweezers–based CBM–cellulose bond “rupture” assay to characterize the binding behavior of single CBM1 proteins alone to distinct cellulose allomorph surfaces under applied force to investigate the role of CBMs in single-molecule binding instability of Cel7A toward cellulose III. In addition to studying CBM binding to cellulose I, III and filter paper allomorphs, we removed signature cellulose binding motifs in CBM mutants (CBMY5A and CBMY31A) to explore any changes cellulose association behavior. In summary, our work highlights how changes in CBM binding to distinct cellulose allomorphs can critically impact processive cellulase motility. Furthermore, our work highlights the necessity of using a multifaceted approach for characterizing the binding heterogeneity and multimodal nature of cellulase–cellulose interactions.

2.3 Results

Cladophora sp. (Cladophora glomerata)–derived highly crystalline cellulose I fibers were isolated, as described previously (26), followed by anhydrous liquid ammonia pretreatment to prepare cellulose III (28). Details about cellulose isolation, ammonia pretreatment, and spectroscopic characterization are in the Material and Methods section. Spectroscopic characterization using X-ray diffraction (XRD) and Fourier transform Raman spectroscopy were conducted to confirm the conversion of cellulose I to cellulose III allomorph following ammonia pretreatment and also measure substrate characteristics like cellulose crystallinity index and crystallite size. XRD equatorial reflections for the (100), (010), and (110) crystallographic planes for native *Cladophora* cellulose I were at approximately 14.9°, 17.1°, and 23.0° Bragg angles (2Θ), respectively, while equatorial reflections for (010), (002), and (100) crystallographic planes for *Cladophora* cellulose III were at approximately 11.8°, 17.4°, and 20.9° Bragg angles (2Θ), respectively (Fig. 2.1A). The results are consistent with previous work (28-32). Based on the Segal method, cellulose crystallinity

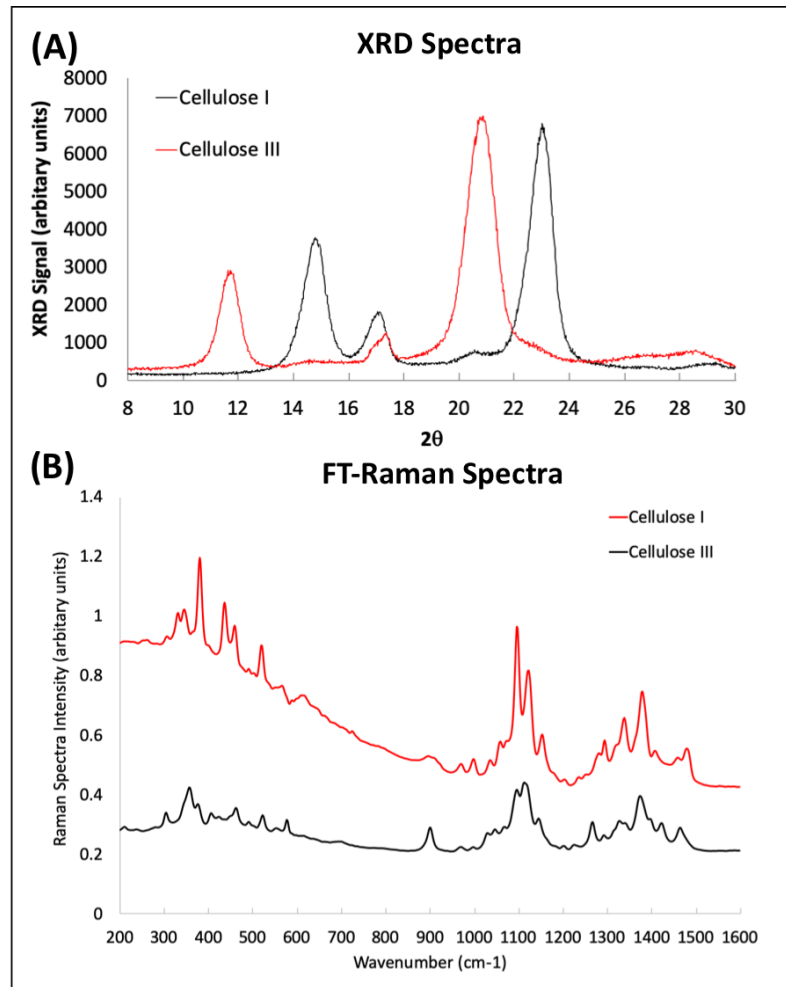


Figure 2.1. Cladophora-derived highly crystalline cellulose III allomorph is more readily hydrolyzed by synergistic combinations of cellulases. XRD (A) and Fourier transform Raman spectra (B) for cellulose I and cellulose III derived from Cladophora confirms respective allomorphic states. XRD and Raman spectra were collected by the Chundawat group.

index was estimated to be about 90% to 95% for both allomorphs. Similar to previous reports (15, 33, 34), Raman spectroscopy also independently confirmed that native Cladophora cellulose I was completely converted into cellulose III following ammonia treatment (Fig. 2.1B).

2.3.1 Substrate-dependent binding

Here, we designed an optical tweezers–based CBM–cellulose bond rupture assay under applied force to systematically characterize the binding behavior of CBM1 (from Cel7A) toward Cladophora cellulose I and cellulose III. Our tweezers CBM–cellulose assay design is similar to the Cel7A enzyme motility assay as reported in Brady et al. 2015 (26). Here, instead of Cel7A, GFP-CBM1 was tethered via a 1010-bp DNA tether and attached to a 1.09- μm streptavidin-coated polystyrene

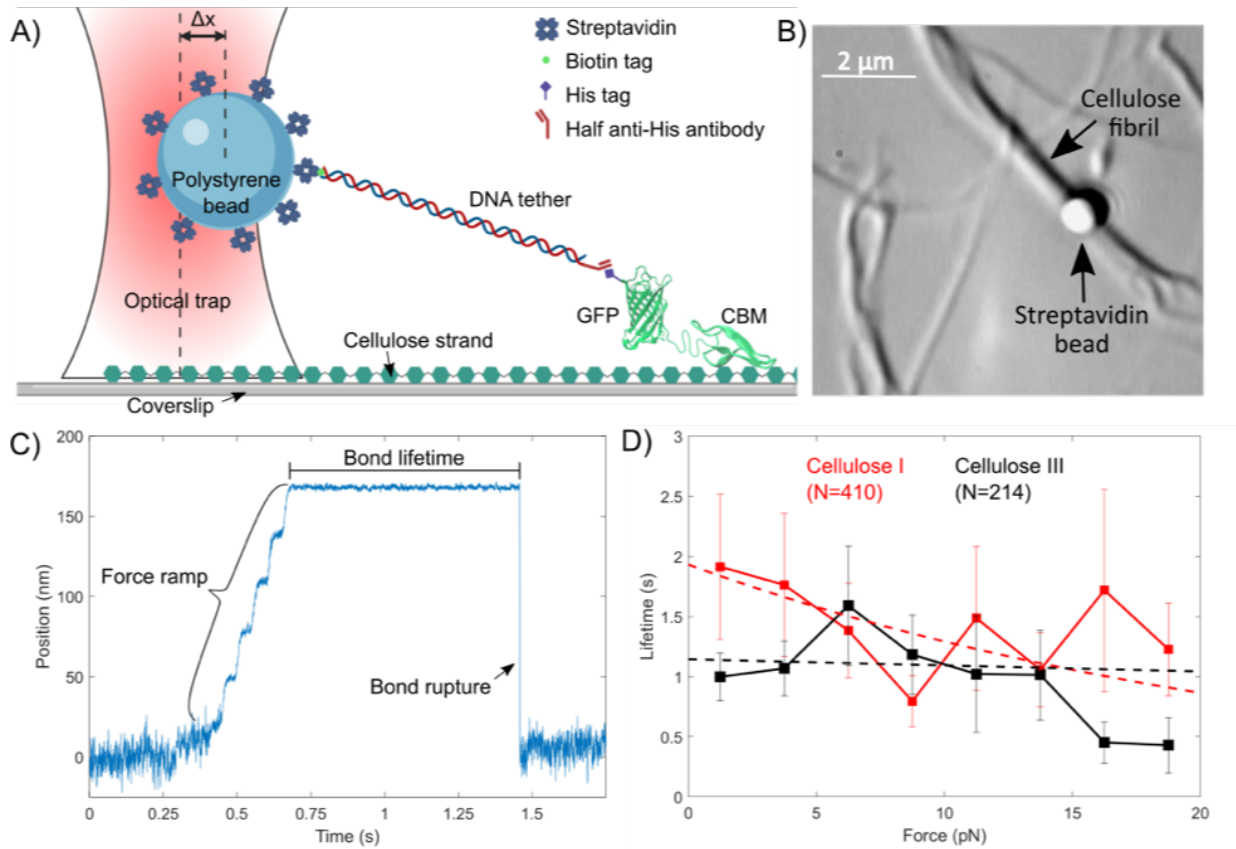


Figure 2.2. Optical tweezers–based single-molecule bond “rupture” assay reveals the multimodal nature of CBM1–cellulose binding interactions. Schematic of rupture assay setup (not to scale) is shown in (A) where a streptavidin-coated bead is tethered to a single His-GFP–labeled CBM1 via a DNA linker containing an anti-His antibody Fab and a biotin tag on opposite ends. The biotin end specifically binds to streptavidin, whereas the anti-His antibody Fab specifically binds to the histidine tag of the GFP-labeled CBM1. Here, Δx represents that the distance bead is displaced from the trap center. The figure was created with BioRender.com. Published structures of CBM1 (Protein Data Bank code: 1CBH) and GFP (Protein Data Bank code: 2B3P) were used in this rendering. (B) Bright-field image of rupture assay showing *Cladophora*-based cellulose microfibrils localized on the glass cover slip. CBM–cellulose binding is facilitated by moving the optically trapped bead close to the fiber. Bead position is tracked by a detection laser as force is loaded across the bond. (C) representative position trace for a single CBM–cellulose rupture event showing bond lifetime, and a single rupture is shown here. (D) Force versus Lifetime relationship for the CBM1–cellulose interaction on *Cladophora* cellulose I (black) and cellulose III (red) is shown. Lifetimes were binned at 2.5-pN intervals. Weighted single exponential fits are shown as dashed lines. Error bars depict standard error from the reported mean for each bin. N represents the total number of CBM–cellulose bond rupture events measured for each substrate. Additional supporting raw data scatterplots can be found in Figures 2.3, 2.5, and 2.8.

bead (Fig. 2.2A). Cellulose fibers were affixed to a glass coverslip. For each single CBM–cellulose rupture assay run, individual beads were optically trapped and placed in the immediate vicinity of individual cellulose microfibrils to facilitate a noncovalent CBM–cellulose bond formation (Fig. 2.2B). Upon stable noncovalent bond formation, the piezo stage was moved to a fixed position pulling the DNA tether taut and exerting a force on the CBM–cellulose bond. After the bond rupture,

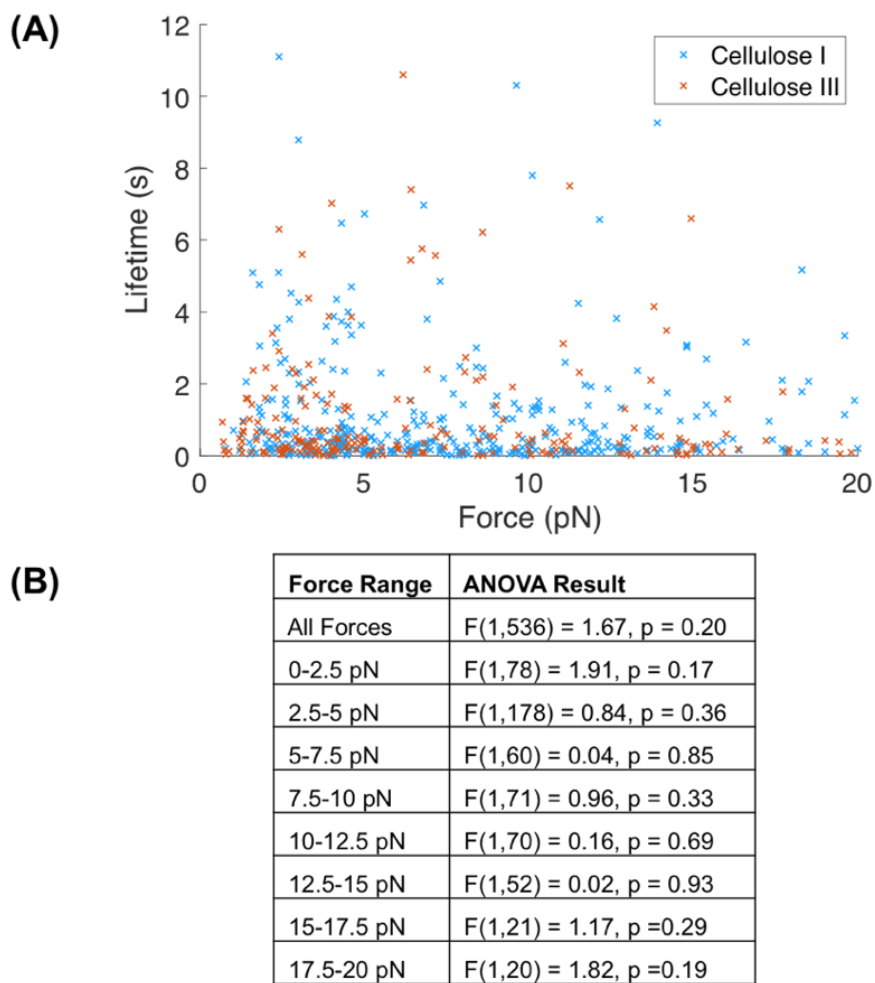


Figure 2.3. (A) Force vs lifetime raw data scatterplot for the CBM1 non-covalent bond on *Cladophora* cellulose I using the wild-type CBM1 protein (blue) and using the Y31A CBM1 mutant (brown). Total number of events measured (N) using CBM1 is 410 and using the mutant is 93. For visual clarity, we omitted data points above 20 pN or 12 s from the scatterplot (31 for CBM1; 11 for Y31A-CBM1). We did not exclude any data from our report or analysis. Our one-way ANOVA test (B) concluded that there was no significant difference between the two entire datasets or at the 0-5 pN, 5-10 pN, and 15-20 pN ranges. However, there was a significant difference observed at the 10-15 pN range indicating that structural changes on CBM does indeed affect the CBM1-cellulose interactions measured using our single-molecule rupture assay method. Future single molecule studies could explore the effects of other protein structural changes on binding to cellulose.

total bond lifetime and rupture force were then calculated for each individual CBM–cellulose interaction (Fig. 2.2C). Hundreds of rupture events from individual assay runs were pooled and binned at 2.5-pN intervals for cellulose I and cellulose III to generate force-lifetime distribution plots (Fig. 2.2D). Raw force-lifetime scatterplots are provided in Figure 2.3A. Averaging all rupture events, we find that the mean lifetime of CBM1 binding to cellulose I was 1.41 ± 0.20 s (SEM; N = 410) and to cellulose III was 1.11 ± 0.12 s (SEM; N = 214). Since the bond rupture lifetime under

applied force is related to the equilibrium binding off-rate, our rupture assay results are corroborated by the weaker binding affinity of CBM1 estimated by both the pull-down assay dataset as well as the PMF calculations in previous work (27). Of more importance, our bond rupture CBM1–cellulose I and CBM1–cellulose III bonds were 4.12 and 1.82 s, respectively. Although marginal differences can be seen at the lowest (0–2.5 pN) and highest (17.5–20 pN) rupture force ranges, one-way ANOVA test suggests that the lifetime dataset over the entire rupture force range is not statistically different (Fig. 2.3B). Mean lifetime results suggest that simple one-site Langmuir adsorption models are more appropriate than complex multisite adsorption models to estimate the marginal differences in CBM1 binding affinity for distinct cellulosic allomorphs. Note that the standard deviation of lifetimes of the

2.3.2 Multiple binding regimes

Although the average lifetimes show different profiles, there was also a broad spread in the distribution of observed bond lifetimes with a great deal of overlap between cellulose I and cellulose III indicating that multiple binding states with distinct characteristic bond lifetimes are possible for CBM1 binding to both cellulose I and III (Fig. 2.2D). As seen previously for protein–ligand interactions in other single-molecule studies (35), CBM–cellulose binding was expected to show classic slip-bond behavior; i.e., as the rupture force increases, the total bond lifetime decreases. However, fits to the force-lifetime distribution failed to converge to a single exponential decay suggesting that multiple binding modes are likely present for CBM to cellulose (Fig. 2.2D). A classical unimodal slip bond would exhibit a single exponential decay (36). Therefore, the data suggests that CBM1 does not follow this simple model when interacting with either cellulose allomorph. Binding of CBM1 on cellulose instead revealed a spread with a more complex multimodal and heterogeneous binding behavior. This multimodal distribution was independent of the source of cellulose, and similar results were also seen with filter paper–derived cellulose fibrils (Fig. 2.4). We also performed controls to test for artifacts associated with conjugating CBM1 to full anti-His antibody versus to the Fab fragment in our assay design, but there was no significant difference seen in the multimodal distribution of the force-lifetime results (Fig. 2.5).

We speculated that the observed multimodal distribution seen for the force-lifetime dataset indicates multiple classes of overlapping binding modes with contributions from different cellulose substructures (37), namely, crystalline regions with varying degrees of disorder, different crystal binding faces (39), and varied binding orientation/modes of CBM binding on the hydrophobic face

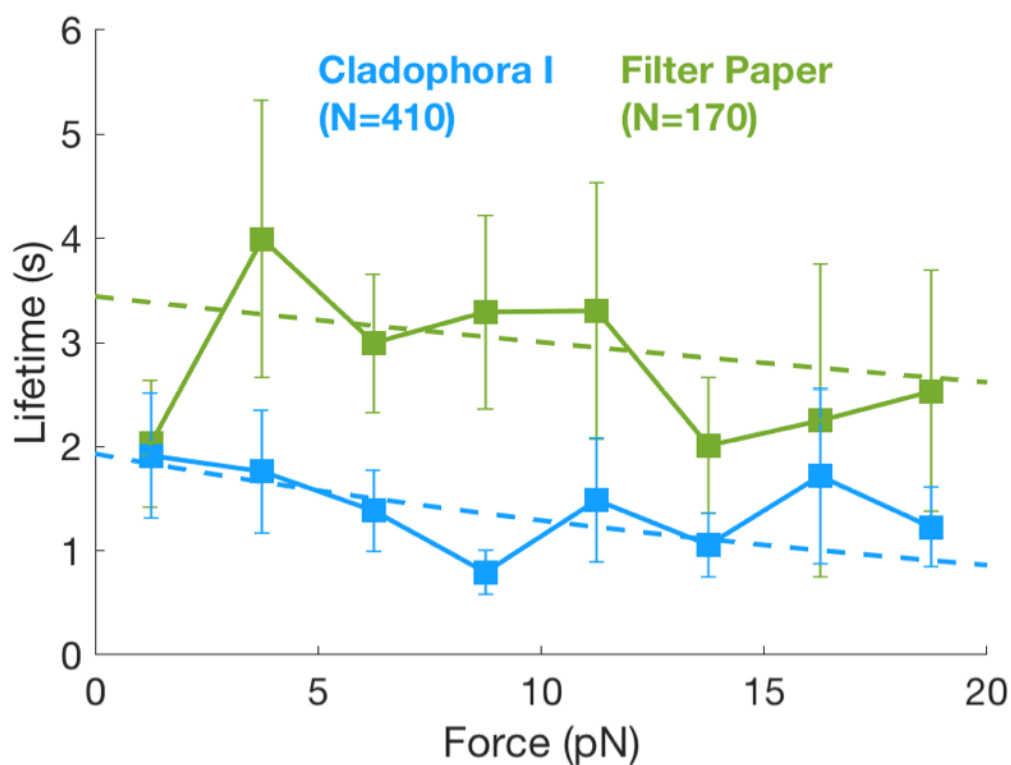
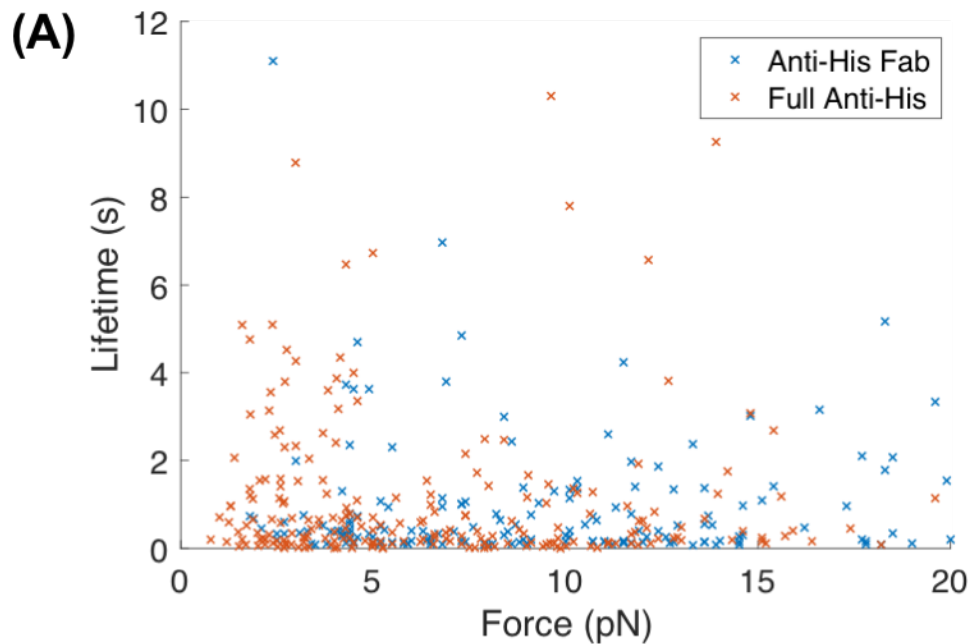


Figure 2.4. Force vs lifetime relationships for the CBM1 non-covalent bonds to Cladophora derived cellulose I (blue) and filter paper (green) derived cellulose microfibrils. Both force-lifetime distributions failed to converge to the classical slip bond model and revealed that the CBM1-cellulose interaction is multimodal across different native cellulosic substrates. Interestingly, the reported mean lifetime of the CBM1-filter paper cellulose bond (3.03 ± 0.37 SEM) is higher than that of the CBM1-cladophora cellulose bond (1.41 ± 0.20 SEM).

of crystalline cellulose (as summarized in Fig. 2.6). However, owing to the

highly crystalline nature of our Cladophora-derived cellulosic substrates (with 90%–95% crystallinity index) and the previous observations that CBM1 likely binds predominantly to one preferred cellulose crystalline face (39), we hypothesize that the multimodal distribution in the force-lifetime dataset could also arise from multiple binding equilibria of CBM1 for each axial face (Fig 2.6). It is also likely that some of these CBM orientations are productive for catalysis, whereas some orientations are nonproductive. For Cel7A to perform a successful processive step, the CBM needs to step in tandem with the CD along a cellulose chain (40). However, if the CBM orients itself in nonproductive orientations (across adjacent cellulose chains, for instance), we speculate that this could lead to increased dwell times for full-length Cel7A as seen on cellulose III. Additional mutant full-length Cel7A assays are necessary to unravel molecular origins of such multimodal binding behavior during cellulase catalytic turn-over cycles.



(B)

Force Range	ANOVA Result
All Forces	$F(1,370) = 2.74, p = 0.10$
0-5 pN	$F(1,149) = 0.13, p = 0.72$
5-10 pN	$F(1,104) = 1.10, p = 0.30$
10-15 pN	$F(1,86) = 3.00, p = 0.09$
15-20 pN	$F(1,25) = 0.13, p = 0.72$

Figure 2.5. CBM1-cellulose bond lifetimes using Fab vs full antibody linker. (A) Force vs lifetime raw data scatterplot for the CBM1 non-covalent bond on *Cladophora* cellulose I using an anti-His Fab in the assay construct (blue) and using full anti-His antibody (brown). Total number of events measured (N) using the full antibody is 233 and using the Fab is 187. For visual clarity, we omitted data points above 20 pN or 12 s from the scatterplot (8 for full antibody; 23 for Fab). We did not exclude any data from our report or analysis. Our one-way ANOVA test (B) concluded that there was no significant difference between the two entire datasets or at 5 pN intervals. Because of the statistical similarity, we combined both datasets to represent our CBM1-cellulose I data.

2.3.3 CBM1 mutants and binding orientations

We hypothesized that the multimodal unbinding distribution of CBM1 to all probed cellulose allomorphs may originate from statistical geometric orientation of which CBM1 binds to cellulose. We modeled the binding orientation after the Buffon needle problem (41), which describes the probability of a needle, when dropped over parallel lines, landing along or across lines based on the width between lines and the length of the needle. In our case, CBM1 is our needle, with three

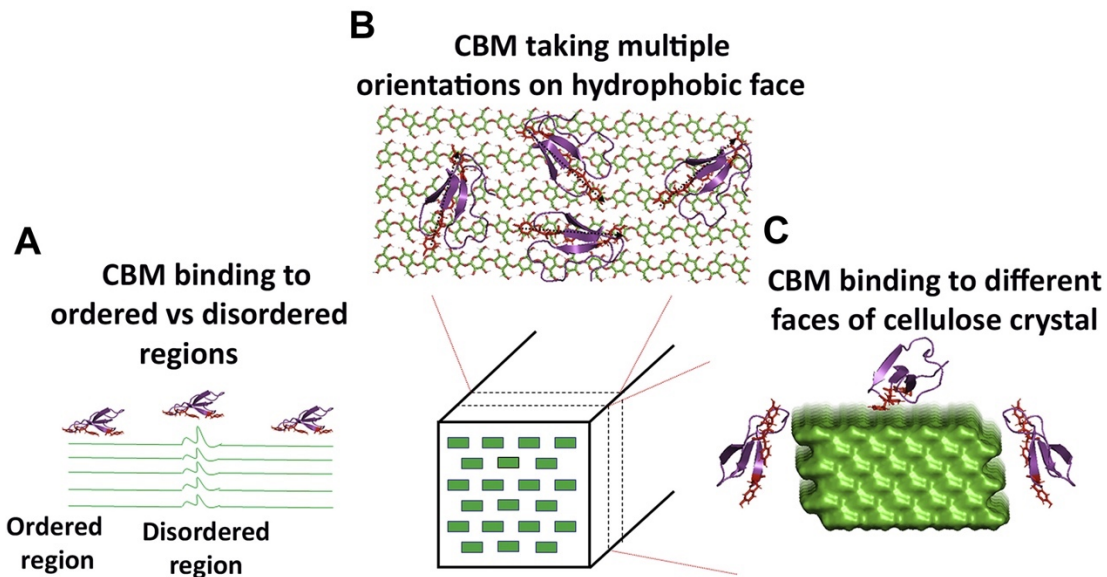


Figure 2.6. CBM possible binding modes. The schematic outlines three possible classes of binding modes theoretically accessible by CBM1 on native cellulose I fibers. (A) One class of binding modes originates from the likely difference in binding free energies when CBM1 binds to local regions of disorder (amorphous regions) compared to more crystalline regions. (B) Previous molecular simulation studies show that the hydrophobic face of cellulose crystal is the preferred binding face for type A CBMs such as CBM1 (38). However, it is likely that the CBM possesses multiple binding orientations with respect to a cellulose chain. (C) Although molecular simulations predict that the hydrophobic face is the “preferred” binding site for CBM, transmission electron microscopy studies have shown CBM binding to various other faces of the cellulose crystal (39), giving rise to yet another class of binding modes. Overall, it is likely that the combination of all these potential binding sites, depending on cellulose source and overall ultrastructure, leads to the heterogeneity observed in CBM bond lifetimes to distinct cellulose allomorphs. Here, CBM1 (PDB: 1CBH) from Cel7A was used to generate the figure.

hydrophobic binding residues 2.08 nm in length, and the cellulose lattice represents our parallel lines 0.8 nm across. A diagram is shown in Fig. 2.7. We performed Monte Carlo simulations to predict that the geometric probability of a CBM1 wild type ‘needle’ to bind along a single cellulose chain is ~42%, while the remaining ~58% of events would include binding across multiple cellulose chains (ignoring any energetic barriers to binding orientation) (see Table 2.1). Interestingly, if a mutation on CBM1 (Y31A for instance) is considered as having reduced needle length, that would increase the percentage of events along the chain to 90%. Hence, performing these planar aromatic residue mutations and testing the impact of these mutations on the heterogeneity of CBM binding to cellulose using bond rupture assays could give us some insight into the source of the binding modalities.

Of interest, the multimodal distribution of the force-lifetime was sensitive to the CBM structure as illustrated by the differences in rupture force-lifetime distribution seen for wildtype CBM1 and its Y31A mutant, which has a modification to the planar aromatic binding residue (Figs 1.2 and 2.8).

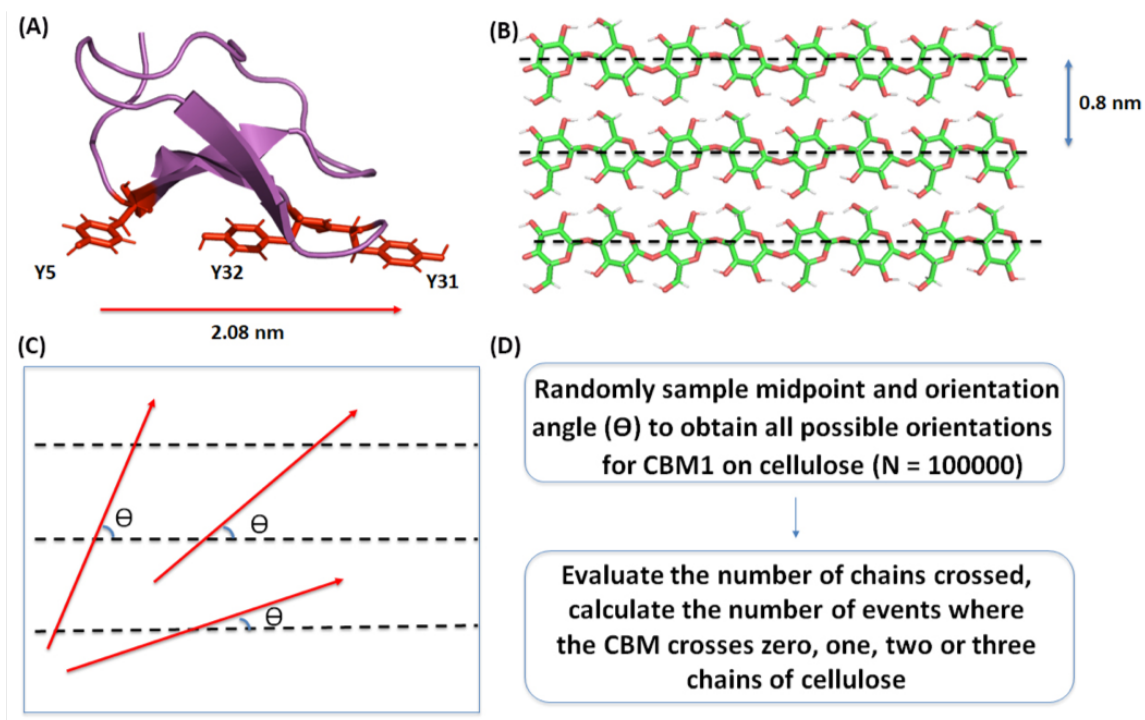
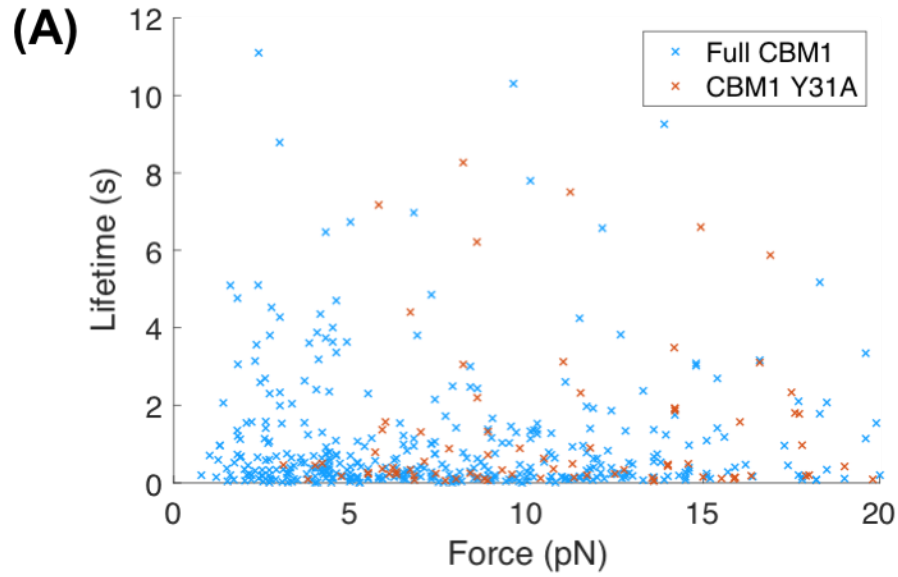


Figure 2.7. Buffon needle approximation for CBM1 binding orientations. Buffon needle problem inspired a geometric probability model to determine likely orientations of CBM1 on a flat cellulose surface. (A) The crystal structure of CBM1, (PDB code: 1CBH) represented as a needle (solid red line) of length 2.08 nm, and (B) the hydrophobic face of cellulose I, represented as an array of parallel lines (dotted black line) with a spacing of 0.8 nm, were used to generate a (C) Buffon needle inspired CBM-cellulose model schematic to determine geometric probability of all possible orientations of CBM1 on cellulose surface. The original Buffon model formulation is discussed in his classical 1777 paper (41). A brief description of our Monte Carlo simulation methodology is shown in (D).

Protein Type	Along the chain events	Across the chain events
CBM1 WT	58%	42%
CBM1 Y31A	90%	10%

Table 2.1. Buffon needle orientation results. CBM-cellulose Buffon needle model simulation predicts that wild-type (WT) CBM1, with a needle length of 2.08 nm is equally likely to bind with its aromatic residues aligned both along a single (58% probability) or across multiple (42% probability) cellulose chains. However, the mutant CBM1 (Y31A), with a 'shortened' needle 1.12 nm, is more likely to align and bind along a single cellulose chain (90% probability).



(B)

Force Range	ANOVA Result
All Forces	$F(1,455) = 2.36, p = 0.13$
0-5 pN	$F(1,154) = 0.34, p=0.56$
5-10 pN	$F(1,139) = 2.44, p = 0.12$
10-15 pN	$F(1,115) = 5.66, p = 0.02$
15-20 pN	$F(1,41) = 0.13, p = 0.71$

Figure 2.8. Bond lifetimes comparison between wtCBM1 and Y31A CBM1. (A) Force vs lifetime raw data scatterplot for the CBM1 non-covalent bond on *Cladophora* cellulose I using the wild-type CBM1 (blue) and using the Y31A CBM1 mutant (brown). Total number of events measured (N) using CBM1 is 410 and using the mutant is 93. For visual clarity, we omitted data points above 20 pN or 12 s from the scatterplot (31 for CBM1; 11 for Y31A-CBM1). We did not exclude any data from our report or analysis. Our one-way ANOVA test (B) concluded that there was no significant difference between the two entire datasets or at the 0-5 pN, 5-10 pN, and 15-20 pN ranges. However, there was a significant difference observed at the 10-15 pN range (red) indicating that structural changes on CBM does indeed affect the CBM1-cellulose interactions measured using our single-molecule rupture assay method. Future single molecule studies could explore the effects of other protein structural changes on binding to cellulose.

Although the overall lifetime dataset over all rupture forces tested shows no significant difference based on the one-way ANOVA result. However, there seems to be significant difference in the bond lifetimes of CBM1 wildtype and Y31A mutant on cellulose I over certain rupture force ranges (0-2.5 pN and 10-15 pN ranges in Fig. 2.8). The Y31A mutation is known to significantly lower CBM1 bulk-ensemble binding affinity toward native cellulose I (42), but it is unknown how this single mutation impacts the processive motility of the full-length Cel7A enzyme. Alternatively, preliminary bond-

rupture experiments with CBMY5A mutants revealed a weaker interaction with cellulose with a mean bond lifetime of 0.43 ± 0.14 s (SEM, N=9), suggesting that different mutations will affect binding heterogeneity in separate ways. Although the slight differences in CBM bond lifetimes might contribute to the reduced single-molecule velocity or initial binding commitment of Cel7A, the significant changes in lifetime distributions indicates CBM1 orientation relative to cellulose may play a role in the productivity of cellulose degradation.

2.4 Discussion

Pretreatments can increase cellulose accessibility to facilitate efficient enzymatic saccharification (43). Extractive ammonia (EA) pretreatment converts cellulose I to cellulose III to reduce biomass recalcitrance toward enzymatic hydrolysis. EA pre-treatment achieves cellulosic biomass hydrolysis yields equivalent to its precursor ammonia fiber expansion pretreatment but with 60% lower enzyme loading requirements (e.g., 18.75 mg enzyme/g cellulose for ammonia fiber expansion versus 7.5 mg/g for EA-treated biomass hydrolyzed using commercial enzyme mixture consisting of 50% C.Tec2, 25% H.Tec2, and 25% Multifect Pectinase on a total protein basis) (12). However, there is a need to further reduce total enzyme loading equivalent to the range employed in a commercially viable corn starch liquefaction process using amylases (e.g., less than 1 mg amylase/g starch). One approach to reduce enzyme loading is to identify the potential rate-limiting enzymes in a complex cocktail critical for cellulose III hydrolysis. Endocellulases have been identified to show improved activity toward cellulose III, at various enzyme loadings tested, but they concomitantly also show lower binding to the substrate unlike cellulose I. But it is surprising that exo- cellulases like Cel7A (*T. reesei*) and Cel6B (*T. fusca*) have mostly shown lower or comparable activity on cellulose III versus native cellulose I, particularly at ultra-low enzyme loadings as reported in this study. Although this is not detrimental to the action of cellulase enzyme mixtures, as both fungal and bacterial derived endo- and exocellulase mixtures have shown overall improved activity (up to 10-fold as reported here) toward cellulose III versus cellulose I largely owing to increased endo–exo cellulase synergy (14, 15), there is clearly room for making improvements in enhancing processive cellulase activity toward cellulose III. Both endo- and exocellulases were previously reported to exhibit lowered binding toward cellulose III during saccharification. Although these results can be explained based on the Sabatier principle recently applied to modeling cellulase action on cellulose (19), since tighter cellulase binding to cellulose need not always correspond to improved activity (13), we still lack a first-principles mechanistic basis for the reduced binding of most full-length cellulases observed to date toward nonnative cellulose III allomorph using advanced optical tweezers–based single-molecule assays (22).

Understanding CBM–polysaccharide binding interactions is critical to gaining mechanistic insights into biomass conversion (44–46) and developing more efficient industrial-grade enzymes (47, 48). Although molecular simulations have been employed to study specific steps of the Cel7A cellulase processive cycle such as chain decrystallization (49), glycosylation (21), deglycosylation (20), and dissociation (50), the role of CBMs in initial motility commitment of CDs has not yet been studied in detail (9, 12). From an evolutionary standpoint, type A CBMs and cellulase CDs have naturally evolved to breakdown native cellulose I (51) but not cellulose III. Therefore, here we used classical CBM–cellulose pull-down binding assays, molecular dynamics simulations, and optical tweezer–based bond rupture assays to obtain a comprehensive understanding of the binding interactions of a model CBM1 (isolated from Cel7A) toward cellulose I and cellulose III.

Although classical pull-down binding assays and MD simulations explain how the impaired cellulase motility commitment on cellulose III could arise from CBM1, the CBM1–cellulose binding/unbinding forces relevant to the processive motility cycles of Cel7A were unclear (27). Hence, we developed and applied a single-molecule noncovalent bond rupture assay to characterize CBM–cellulose binding interactions under applied force. Single-molecule force spectroscopy has been employed previously to distinguish the nature of protein–ligand bonds (35) and infer multimodality or conformational transitions involved in protein–ligand binding interactions (52). However, the application of AFM-based force spectroscopy to study CBM–cellulose binding has revealed challenges in distinguishing specific versus nonspecific interactions (53). Our single-molecule optical tweezer–based bond rupture assay, with piconewton (pN) force resolution and millisecond (ms) time resolution (52), uncovered heterogeneity of CBM–cellulose unbinding behavior under the application of force. The ultimate goal of the bond rupture assay was to understand the role of CBM1 binding in the anomalous processive motility of Cel7A on cellulose III (27). CBM1 showed multimodal force-lifetime behavior toward both cellulose I and cellulose III with no statistically significant differences in mean bond lifetimes except, even under force ranges where the differences were slightly more pronounced (Fig. 2.2D & 2.3). Of interest, the rupture assay mean bond lifetime of CBM1 with filter paper–derived cellulose I fibrils was significantly higher (by ~2-fold) than that of *Cladophora* cellulose I (Fig. 2.4). Overall, these results highlight how subtle differences in cellulose fibril ultrastructure can play an important role in impacting CBM binding dynamics at the single-molecule level. Rupture assay bond lifetimes estimated from dynamic force spectroscopy assays can be used to predict protein–ligand unbinding off-rates that relate directly to the classical binding affinity constant (54). Considering the mean bond lifetime for CBM1 was only marginally higher for cellulose I versus cellulose III, these results further suggest that a simple

one-site Langmuir adsorption model used to fit the pull-down binding assay data would be more appropriate than other multisite models that predict much larger differences in binding affinity (27).

Our single-molecule CBM–cellulose bond rupture assay suggests that the binding behavior cannot be explained by the presence of just one or even two classes of unique and independent binding sites. However, fitting a high-quality binding assay dataset to a simple Langmuir one-site model can still yield a global average affinity constant that arises from a combination of binding sites or modes, rather than data overfitting via a two-site or more complex binding models. Our analysis also suggests the future use of complementary approaches to cross-validate the molecular-level origins in binding behaviors observed for distinct ligands and/or protein mutants. Recent reports on even simpler protein–ligand systems like streptavidin–biotin suggests that ligand unbinding undergoes transition across multiple intermediate states as a function of the loading rate (i.e., applied force), unlike the classical two-state models, to explain the long lifetime of the complexes (55). Therefore, further studies are necessary for the CBM–cellulose system at multiple loading rates. We speculate that the nonproductive binding of CBMs with high bond lifetimes could increase CD dwell time, and mutant CBMs/cellulases should be analyzed to test this hypothesis further.

Finally, we were interested to see if it would be theoretically possible to explain the multimodality observed for CBM–cellulose force-lifetime distributions using a simple geometrical probability-based model whereby the CBM is hypothesized to survey multiple binding orientations on the hydrophobic face of cellulose, assuming that different orientations would give a distinct bond lifetime at a given applied force. We were inspired by the classical Buffon needle problem and therefore developed a simple model based on this original problem to predict the probabilistic distribution of the orientation of CBM proteins on the surface of cellulose (41). Here the size of our needle is interpreted as the physical length of the planar binding motif surface (e.g., Y5-Y31-Y32) known to participate in cellulose binding, whereas the distance between the adjacent cellulose chains on the hydrophobic binding surface is equated to the distance between the parallel lines over which the needle can (Fig. 2.7). Our Buffon needle model for the wildtype CBM1 predicted that the distribution of CBM1 binding states should mostly align along the cellulose chain axis versus across the chain axis under the assumption that these states are energetically equivalent. Alignment of the CBM needle along the cellulose chain axis is also supported by previous MD simulations (40), lending some credence to this overly simplistic geometrical interpretation of the CBM–cellulose binding problem. Of interest, “shortening” of the effective CBM needle length (i.e., by mutation of Y31A for CBM1) increased the likelihood of along the cellulose chain/axis binding

events as predicted by the Buffon model. It was interesting to note that our single molecule tweezer-based CBM–cellulose rupture assay also indicated 2.6-fold higher rupture bond lifetimes in 10–15 pN rupture force range for the Y31A mutant compared with the wildtype CBM1 on cellulose I, suggesting the intriguing possibility that a subset of the force-lifetime data observed could be representative of specific CBM1 orientations on the cellulose surface. Again, we note this is an over-simplistic model and an understanding of the energetic constraints could better simulate the complex reality of CBM-cellulose interactions. Moreover, we currently lack the ability to theoretically relate this simple model's predictions back directly to the bond rupture assay results. Most previous CBM binding focused studies (38, 40, 56) have not emphasized the possible orientations of CBM1 on the surface of cellulose I. Beckham *et al.* (40) previously showed that although CBM1 prefers to bind along the cellulose chain as well, slightly rotated (by $\sim 10\text{-}15^\circ$) CBM1 orientations across multiple cellulose chains are energetically feasible as well on individual fiber surfaces. A similar flanking aromatic residue mutation on other type A CBMs planar binding sites was recently shown to also enhance engineered endocellulase catalytic toward native cellulose, possibly owing to reduced nonproductive mutant enzyme binding driven by particular binding orientations (57). Future work combining site-directed mutagenesis of CBMs, force spectroscopy rupture assays, and MD simulations is necessary to test the impact of specific CBM-binding motif mutations on altering certain binding modalities, as analogously illustrated by Jobst *et al.* (58) for the cohesin–dockerin binding system.

Binding modules like CBM1 play an oft-neglected synergistic role in the association of Cel7A CD to cellulose that likely fine-tunes the subtle balance between productive versus nonproductive binding (59). Future work will address the role of CBMs in both the association and dissociation mechanism of full-length cellulases to obtain a better understanding of the relationship between binding affinity and overall catalytic efficiency for processive cellulases (19). Our work has also shown that, although the exact stalling force for halting processive cellulases like Cel7A likely exceeds 30 pN to prevent cellulase motility entirely (26), it is possible that particular CBM binding orientations on the cellulose surface could hinder cellulase motility or processive activity. However, the connection between data collected from single-enzyme motility/rupture assays, enzyme binding/activity, and enzyme–substrate structure dynamics still needs to be more clearly established. In addition, future work should address the interplay of CBM-driven binding affinity and hydrolytic activity of multimodular cellulases using biochemical assays similar to those reported in a recent study that applied the Sabatier principle to characterize interfacial cellulose hydrolysis by bound cellulases (19). It is likely that the lower binding and improved activity of endocellulases and

exocellulases toward cellulose III at certain enzyme loadings is in accordance with the Sabatier principle.

2.5 Materials and Methods

2.5.1 CBM1 expression

CBM1 expression and purification was executed by the Chundawat group before GFP-CBM1 samples, including CBMY5A and CBMY31A, were sent to us for single-molecule studies. *E. coli* BL21-CodonPlus-RIPL [IDE3] (Stratagene, Santa Clara, CA) or RosettaGami 2 [DE3] (Novagen, Santa Clara, CA) competent strains were transformed with the relevant pEC-GFP- CBM plasmid based on the small-scale expression results. Suitable transformants were inoculated into 50 mL of chemically defined non-inducing medium (60), in the presence of 50 µg/mL kanamycin and 25 µg/mL chloramphenicol selection antibiotics. The non-inducing medium contained 2 mM MgSO₄, a 1:1000 dilution of trace metal salts mixture (equivalent to 50 mM Fe³⁺, 20 mM Ca²⁺, 10 mM Mn²⁺, 10 mM Zn²⁺, 2 mM Co²⁺, 2 mM Cu²⁺, 2 mM Ni²⁺, 2 mM Mo⁶⁺, 2 mM Se⁴⁺, 2 mM H₃BO₃) into the medium, 0.5% glucose, 0.25% aspartate, 50 mM NH₄Cl, 25 mM KH₂PO₄, 25 mM Na₂HPO₄, 5 mM Na₂SO₄, 0.01% methionine, 1% of 17 amino acids (except cysteine, tyrosine, and methionine) each, and a vitamin cocktail (200 nM of vitamin B₁₂, nicotinic acid, pyridoxine, thiamine, p-aminobenzoic acid, and pantothenate; 5 nM folic acid, and riboflavin). The culture was incubated overnight at 25 °C and then used to inoculate 2 liters of auto-induction medium (60). The auto-induction medium contained 1.2% tryptone, 2.4% yeast extract, 2.3% KH₂PO₄, 12.5% K₂HPO₄, 0.375% aspartate, 2 mM MgSO₄, 0.8% glycerol, 0.015% glucose, and 0.5% α-lactose. The cultures were grown at 25 °C for ~27 h. The cells were harvested by centrifugation at 8000xg for 10 minutes at 4 °C and the cell pellet was stored at -80 °C until further use. All chemicals were purchased from Sigma-Aldrich (St. Louis, MO).

2.5.2 CBM1 purification

Again, CBM purification was performed by the Chundawat group. The recovered cell pellet was thawed and re-suspended in 150 mL of ice cold 20 mM phosphate, pH 7.4, containing 500 mM NaCl, 20% v/v glycerol, 10 µg/ml lysozyme, and a protease inhibitor cocktail (containing benzamidine, EDTA and E-64 protease inhibitor from Sigma-Aldrich). The cells were sonicated with an ultrasound sonicator (550 Sonic Dismembrator, Fisher Scientific, Pittsburgh, PA) fitted with a

microprobe (1-inch probe diameter) at 4 °C for 5 min with 10-s on-bursts and 30-s off periods. The cell debris containing the inclusion bodies was pelleted at 21,000 rpm at 4 °C (30 min) and the supernatant was collected in all cases except for GFP-CBM2a (ActE). Details regarding GFP-CBM2a (ActE) expression and purification are provided elsewhere (61). Briefly, due to the insolubility of the expressed GFP-CBM2a (ActE) under all conditions tested, this protein construct was first isolated from inclusion bodies, refolded, and then purified using IMAC as described previously (61). For all other GFP-CBMs, IMAC using Ni²⁺-NTA based columns/media (GE Healthcare) was first used to isolate and purify His₈-tagged proteins from the *E. coli* cell lysate. All column-based protein purifications were carried out on a ÄKTA-FPLC system (GE Healthcare, Pittsburgh, PA). The cell lysate supernatant was first loaded onto the IMAC column at a medium flow rate of 1 – 2 ml/min. The column was then washed with buffer A (100 mM MOPS, pH 7.4, containing 10 mM imidazole and 100 mM NaCl), followed by additional washing using 95% IMAC buffer A spiked with 5% IMAC buffer B (100 mM MOPS, pH 7.4, containing 500 mM imidazole and 100 mM NaCl), and last followed by elution in 100% IMAC buffer B at a flow rate of 5 ml/min. Protein purity and molecular weight at each stage of the protein purification process was examined by SDS- PAGE (Criterion XT Bis-Tris Precast Gels, Bio-Rad). The presence of partially cleaved GFP-CBMs was identified in the IMAC-B eluents for some protein constructs (namely CBM1, CBM2a, CBM5, CBM10), which necessitated further purification using an amorphous cellulose or hydrophobic interaction affinity-based purification method, as already outlined elsewhere (61, 62), to isolate the intact protein fractions. Briefly, for cellulose affinity-based purification method, IMAC-B protein eluents were directly applied to a phosphoric acid swollen amorphous cellulose (PASC) media at the recommended loading (~200 mg crude protein added per gram dry weight cellulose) for preparative-scale purification (62). The amorphous cellulose slurry was prepared ahead of time and preequilibrated in a 50 mM pH 6.5 MES buffer (equilibration buffer or buffer A) at the desired solids concentration (10 g/L), prior to addition of the IMAC-B protein eluent. The crude protein-cellulose slurry was then intermittently and gently mixed at room temperature for a total incubation time of 0.5 h. The protein bound to PASC was then separated from the unbound protein in the supernatant by gentle centrifugation at 3500xg for 10 min at 25 °C. The recovered PASC pellet was then resuspended in a wash buffer (i.e., equilibration buffer+1M NaCl), using a 4:1 buffer to PASC pellet ratio (v/v), and gently mixed at room temperature for 10 mins to remove non-specifically bound proteins. The recovered PASC pellet containing the adsorbed GFP-CBMs was then finally suspended in 100% ethylene glycol elution solution, using a 4:1 glycol to PASC pellet ratio (v/v). The final ethylene glycol concentration of ~80% (v/v) was sufficient to elute a significant fraction of reversibly bound GFP-CBMs into the supernatant. The eluted protein rich supernatant was

separated from PASC pellet and stored in 80% glycol solution at -20°C for short term storage or immediately concentrated using IMAC columns prior to buffer exchange into 10 mM pH 6.5 MES (or pH 5.5) buffer and storage at -80°C for long term storage in 0.5-1 ml aliquots. The molecular weight of the intact purified GFP-CBM monomers was confirmed by SDS-PAGE to match with the predicted translation products. Protein concentrations were estimated spectrophotometrically at 280 nm using the extinction coefficients calculated from the amino acid sequences for each construct. The histidine tags were not removed and have been reported to not influence CBM binding to cellulose (61, 63).

2.5.3 Bead Functionalization

For the rupture assays, CBM1 was tethered to polystyrene beads via the His8-tag on the N-terminus of our purified GFP-CBM1 construct, with minor modifications from our previously published work (26). Using PCR, 1,010-bp DNA linkers were created from the M13mp18 plasmid template with a biotin tag on one end and an amine group on the other. The anti-His antibody was crosslinked to the amine group using a sulfo-SMCC (sulfosuccinimidyl 4-(N-maleimidomethyl)cyclohexane-1-carboxylate) intermediate. In the cases of using the anti-His Fab, the anti-His antibody was cleaved using 3-MEA (2-Mercaptoethylamine) before crosslinking. To functionalize the beads with GFP-CBM1, 1.09 μm streptavidin beads (Spherotech), biotin/anti-His functionalized DNA linkers, and His8-tagged GFP-CBM1 constructs were incubated together in PBS at 4°C for 45 minutes on a rotator. After incubation, the beads were washed by spinning down at 7,500 g for 3.5 minutes, removing the unreacted components in the supernatant, resuspending in 50 mM acetate buffer (pH 5.0), and sonicating for 2 minutes at 20% amplitude. This process was repeated thrice total. Beads were functionalized such that, statistically, zero or one GFP-CBM1 molecule is bound to each bead. This was determined through serial dilution until a maximum of half the beads bound to cellulose fibers during the experiment.

2.5.4 *Cladophora* cellulose isolation and liquid ammonia pretreatment

Highly crystalline cellulose I and cellulose III preparations were performed by Shishir Chundawat and are explained in detail in Brady et al. 2015 (26). Briefly, cellulose I α from *Cladophora* sp. (*Cladophora glomerata*, green algae) was harvested from freshwater Lake Mendota (Madison, WI, USA), the Yahara river and adjoining bodies of water (30, 38). The harvested algae were first washed with deionized water before being bleached with 10% acetic acid and 20% w/v sodium chlorite. The bleached algae solution was incubated with 4% sodium hydroxide twice overnight to remove non-cellulosic polysaccharides. Then, to hydrolyze and remove amorphous cellulose,

the fibers were incubated in 5% hydrochloric acid. The resulting crystalline cellulose fibrils were washed with copious amounts of deionized water resulting in a cellulose slurry. The slurry was either stored at 4°C with sodium azide added as an anti-microbial or lyophilized for long-term storage and x-ray diffraction characterization, Fourier transform Raman Spectroscopy and composition analysis.

2.5.5 Cellulose characterization using XRD & FT-Raman Spectroscopy

X-ray diffraction (XRD) and FT-Raman spectroscopy characterization was performed by the Chundawat group. Details regarding the XRD method and data analysis methods/results are provided elsewhere (15, 28). Briefly, XRD was performed on an X-ray diffractometer with beam parallelized by a Gobel mirror (D8 Advance with Lynxeye detector; Bruker, Bruker AXS Inc., Madison, WI, USA). CuK α radiation (wavelength = 1.5418 Å) was generated at 40 kV with 40 mA current and the detector slit was set to 2.000 mm. Samples were analyzed using a coupled $2\theta/\theta$ scan type with a continuous PSD fast scan mode. The 2θ started at 8.000° and ended at 30.0277° with increments of 0.02151°, while θ started at 4.0000° and ended at 15.0138° with increments of 0.01075°. Step time was 1.000 s (i.e., 1025 total steps, effective total time 1157 s per run). Dry cellulose samples (approximately 0.5 g) were placed in a specimen holder ring made of PMMA with 25 mm diameter and 8.5 mm height, rotating at 5 degrees per minute during analysis. Cellulose crystallinity was estimated based on the Segal peak height (for Cladophora derived samples) and amorphous peak deconvolution-based methods (64, 65). Please note that Miller indices used here for each contributing predominant diffraction peak/s conform to the convention with 'c' as the fiber axis, a right-handed relationship among the axes and the length of $a < b$, as recommended recently by Alfred French (66), to avoid confusion with other naming conventions. Briefly, for the XRD Segal peak height method, cellulose crystallinity index was calculated from the ratio of the height of the (110) or (200) plane equatorial reflection peak and the height of the minimum between the (110) or (200) and (010) or (110) plane equatorial reflection peaks for Cladophora or Avicel PH-101 cellulose I, respectively. For cellulose III, cellulose crystallinity index was calculated from the ratio of the height of the (100) plane equatorial reflection peak and the height of the minimum between the (100) and (002) plane equatorial reflection peaks. Note that, the three main peaks for native Cladophora cellulose I one-chain triclinic unit cell have Miller indices of (100), (010) and (110), which are the counterparts to the (110), (110) and (200) peaks of Avicel PH101 cellulose I pattern. Peak deconvolution methods have been used extensively to calculate cellulose crystallinity index (32, 65, 67, 68). Avicel derived cellulose I and III samples were recently analyzed using the amorphous peak deconvolution method (69). XRD peak deconvolutions were carried out using

PeakFIT (Version 4.12, Systat Software Inc, San Jose, CA) as described elsewhere (15, 65). For all peak deconvolutions F values are always > 30,000 while R-squares > 0.999.

Regarding the FT (Fourier Transform) Raman based spectroscopic characterization, a MultiRam FT-Raman spectrometer (Bruker) was used to collect Raman spectra for cellulose samples. The FT-Raman spectrometer was equipped with a 1064-nm 1000-mW Nd:YAG laser. For Raman analysis, cellulose pellets were first prepared from either air-dried or lyophilized samples prior to analysis. In most cases, spectra with high signal-to-noise (S/N) ratios were obtained upon using a 660-mW laser power setting and collecting over 512 scans per sample. The spectra were converted to ASCII format and exported to Microsoft Excel for direct plotting/analysis. The interconversion of cellulose I to III was confirmed based on previously published reports using Cladophora or cotton linters derived cellulose allomorphs (28, 34, 70-72). Peak assignments of the vibrational spectrum of cellulose I and III have been described elsewhere (28, 33, 70). Briefly, 250-550 cm^{-1} region for cellulose has predominant group motions attributed to skeletal-bending modes involving C-C-C, C-O-C, O-C-C, and O-C-O internal bond coordinates. The 550-750 cm^{-1} region corresponds to mostly out-of-plane bending modes involving C-C-C, C-O-C, O-C-O, C-C-O, and O-H internal bond coordinates. The peaks around 900 cm^{-1} are shown to involve bending of H-C-C and H-C-O bonds localized at C-6 atoms of the hydroxymethyl group. The 950-1200 cm^{-1} region corresponds to mostly stretching motions involving C-C and C-O internal bond coordinates. The 1200-1500 cm^{-1} region corresponds to mostly bending motions involving H-C-C, H-C-O, H-C-H, and C-O-H internal bond coordinates. The region of 1400-1500 cm^{-1} for cellulose has been shown to be particularly sensitive to the CH₂ scissor bending modes that are sensitive to the *Trans-Gauche* or TG (1480 cm^{-1}) and *Gauche-Trans* or GT (1460 cm^{-1}) conformations of the C6-hydroxymethyl group (70).

2.5.6 Filter paper preparation

The cellulose derived from filter paper originated from Whatman Grade 1 Filter Paper (Sigma – WHA1001110) and contains 99% cellulose. Small pieces (~20 mg) were cut from the larger sheets and placed into a tissue homogenizer with a few drops of DI water. The sample was homogenized thoroughly (~15 minutes) and diluted to 10 mL with 50 mM acetate buffer (pH 5.0) resulting in a 2 mg/mL mixture. The cellulose solution was then vortexed, sonicated, and sheared with a syringe to further break down the fibers further to the desired diameter (100 nm – 2 μm). The sample was stored at 4°C.

2.5.7 Slide preparation

Purified and dried cellulose samples (*Cladophora* based cellulose I or III) were used to create a heterogeneous cellulose mixture by first mixing the desired cellulose sample to deionized water in a 1 mg/mL ratio. The mixture was then sonicated for 2 minutes at 50% in a cup sonicator and vortexed for 15 s on high setting. The cellulose, still clumped at this point, was pulled up and down in solution with a 16-gauge syringe for 1-2 minutes before going back on the vortex for 15 s. These steps were repeated three times. The resulting mixture was then diluted in a 1:20 ratio by mixing 500 μ L of the prepared solution with 500 μ L deionized water. This slurry suspension was then stored at 4 °C. Whatman Grade 1 Filter Paper based cellulose stock suspension slurry was prepared as described previously (26), to be used for some control GFP-CBM1 binding-rupture assays. When preparing to load a slide, a small sample (~100 μ L) of the stored cellulose mixture is removed from the stock and the cellulose pulled apart by sonicating for 2 minutes at 50% in a cup sonicator. This solution was directly loaded onto the glass slide. Slides are prepared by creating a 10-15 μ L volume flow cell using a KOH etched coverslip and double-sided sticky tape. The stock cellulose solution (*Cladophora* based cellulose I or III) was then added to the flow cell and allowed to dry out in an oven at ~95 °C for an hour, allowing cellulose fibrils to non-specifically bind to the slide surface. The surface was then blocked with 10 mg/mL BSA in acetate buffer (pH 5.0) for 15 minutes to prevent non-specific sticking of the beads to the glass surface. Finally, the GFP-CBM1 functionalized beads solution was loaded onto the slide and the slide sealed shut. For the Cel7A motility assays, 0.75 μ m non-functionalized polystyrene beads (Spherotech—PP-08-10) were allowed to nonspecifically adhere to the coverslip surface, in an incubation step before BSA blocking, to serve as fiducial markers allowing for instrumental drift tracking during data acquisition.

2.5.8 Single-molecule data collection and analysis

CBM1 functionalized beads were trapped using a 1064-nm laser setup as described before (Brady et al.) and placed alongside a surface-bound, stationary fiber (26). Experiments were conducted at a fixed room temperature (21 °C). After position calibration and trap stiffness measurements, the bead was actively placed on a cellulose fiber and roughly run along the fiber in the axis of the microscope stage. Upon binding, the bead was centered, acquisition started, and a force was applied to the tethered bead by stepping the piezo stage along the axis of the fiber. With force applied, the position of the bead was held until rupture. Once a tether ruptured, it is sometimes possible to tether the bead to the fiber again, in which case, the same method of force application is used while data acquisition continues. Data were collected at a 3-kHz sampling frequency and then filtered with a 10-point exponential moving average before analysis. Custom Matlab codes were then used to determine the rupture forces and the bond lifetimes of full ruptures. A rupture is

defined as a position change back to baseline within 0.03 seconds. The force-lifetime data was binned every 2.5 pN and then fit to a single or a double exponential decay characteristic of a slip bond, despite the poor fit.

2.6 Acknowledgements

I would like to thank collaborators and other contributing authors from the publication in which the work here resides for their support, feedback, and help: Shishir P. S. Chundawat, Bhargava Nemmaru, Markus Hackl, Sonia K. Brady, Madeline M. Johnson, Sungrok Chang, Matthew J. Lang, Hyun Huh, Sang-Hyuk Lee, John M. Yarbrough, Cesar A. López, and Sandrasegaram Gnanakaran. We would like to particularly thank Professor Brian Fox (UW Madison) and Professor Bruce Dale (MSU) for kindly providing access to their laboratory's resources at the onset of this project for generation of relevant plasmid DNA and cellulose substrates, respectively. Special thanks to Izak Smith for collection of *Cladophora* algae from the Yahara River- Lake Watershed, Sungsoo and Amy Lim for help with generation of GFP-CBM constructs, Leonardo Sousa for conducting ammonia pretreatment, Shashwat Gupta for XRD data analysis, and Umesh Agarwal for access to the FT-Raman spectrometer. Figure 2A was created with BioRender.com.

Funding and additional information—The authors acknowledge support from the NSF CBET awards (1604421 and 1846797), ORAU Ralph E. Powe Award, NSF MCB award (1330792), NIH Grant (R01GM101001), Rutgers Global Grant, Rutgers Division of Continuing Studies, Rutgers School of Engineering, DOE Bio- imaging Award (Office of Science DE-SC0019313), and the Great Lakes Bioenergy Research Center (DOE BER Office of Science DE- FC02-07ER64494). C. A. L. and S. G. acknowledge support from LANL LDRD ER (XWX2) and LANL institutional program for computational resources. J. M. Y. acknowledges support from the Department of Energy, Office of Energy Efficiency and Renewable Energy (EERE) under agreement no. 28598. The content is solely the responsibility of the authors and does not necessarily represent the official views of the National Institutes of Health.

2.7 References

1. N. Santoro *et al.*, A High-Throughput Platform for Screening Milligram Quantities of Plant Biomass for Lignocellulose Digestibility. *BioEnergy Research* **3**, 93-102 (2010).

2. B. Bals, C. Rogers, M. Jin, V. Balan, B. Dale, Evaluation of ammonia fibre expansion (AFEX) pretreatment for enzymatic hydrolysis of switchgrass harvested in different seasons and locations. *Biotechnol Biofuels* **3**, 1 (2010).
3. M. E. Himmel *et al.*, Biomass recalcitrance: engineering plants and enzymes for biofuels production. *Science* **315**, 804-807 (2007).
4. C. M. Payne *et al.*, Fungal cellulases. *Chemical Reviews* **115**, 1308-1448 (2015).
5. L. R. Lynd, P. J. Weimer, W. H. van Zyl, I. S. Pretorius, Microbial cellulose utilization: fundamentals and biotechnology. *Microbiol Mol Biol Rev* **66**, 506-577 (2002).
6. J. Lombard, Once upon a time the cell membranes: 175 years of cell boundary research. *Biology Direct* **9**, 32 (2014).
7. P. Tomme, A. L. Creagh, D. G. Kilburn, C. A. Haynes, Interaction of polysaccharides with the N-terminal cellulose-binding domain of *Cellulomonas fimi* CenC. 1. Binding specificity and calorimetric analysis. *Biochemistry* **35**, 13885-13894 (1996).
8. A. R. Mudinoor *et al.*, Interfacial molecular interactions of cellobiohydrolase Cel7A and its variants on cellulose. *Biotechnology for Biofuels* **13**, 10 (2020).
9. S. P. Chundawat, G. T. Beckham, M. E. Himmel, B. E. Dale, Deconstruction of lignocellulosic biomass to fuels and chemicals. *Annu Rev Chem Biomol Eng* **2**, 121-145 (2011).
10. D. Gao, S. P. S. Chundawat, N. Uppugundla, V. Balan, B. E. Dale, Binding characteristics of *Trichoderma reesei* cellulases on untreated, ammonia fiber expansion (AFEX), and dilute-acid pretreated lignocellulosic biomass. *Biotechnology and Bioengineering* **108**, 1788-1800 (2011).
11. V. Novy *et al.*, Quantifying cellulose accessibility during enzyme-mediated deconstruction using 2 fluorescence-tagged carbohydrate-binding modules. *Proc Natl Acad Sci U S A* **116**, 22545-22551 (2019).
12. L. da Costa Sousa *et al.*, Next-generation ammonia pretreatment enhances cellulosic biofuel production. *Energy & Environmental Science* **9**, 1215-1223 (2016).
13. D. Gao *et al.*, Increased enzyme binding to substrate is not necessary for more efficient cellulose hydrolysis. *Proceedings of the National Academy of Sciences of the United States of America* **110**, 10922-10927 (2013).
14. Y. Liu, B. Nemmaru, S. P. S. Chundawat, *Thermobifida fusca* Cellulases Exhibit Increased Endo–Exo Synergistic Activity, but Lower Exocellulase Activity, on Cellulose-III. *ACS Sustainable Chemistry & Engineering* **8**, 5028-5039 (2020).
15. S. P. S. Chundawat *et al.*, Restructuring the crystalline cellulose hydrogen bond network

15. S. P. S. Chundawat *et al.*, Restructuring the crystalline cellulose hydrogen bond network enhances its depolymerization rate. *Journal of the American Chemical Society* **133**, 11163-11174 (2011).
16. N. Cruys-Bagger, J. Elmerdahl, E. Praestgaard, K. Borch, P. Westh, A steady-state theory for processive cellulases. *The FEBS Journal* **280**, 3952-3961 (2013).
17. M. Kurasin, P. Våljamäe, Processivity of cellobiohydrolases is limited by the substrate. *J Biol Chem* **286**, 169-177 (2011).
18. J. M. Fox, S. E. Levine, H. W. Blanch, D. S. Clark, An evaluation of cellulose saccharification and fermentation with an engineered *Saccharomyces cerevisiae* capable of cellobiose and xylose utilization. *Biotechnology Journal* **7**, 361-373 (2012).
19. J. Kari *et al.*, Sabatier Principle for Interfacial (Heterogeneous) Enzyme Catalysis. *ACS Catalysis* **8**, 11966-11972 (2018).
20. B. C. Knott *et al.*, The mechanism of cellulose hydrolysis by a two-step, retaining cellobiohydrolase elucidated by structural and transition path sampling studies. *Journal of the American Chemical Society* **136**, 321-329 (2014).
21. B. C. Knott, M. F. Crowley, M. E. Himmel, J. Ståhlberg, G. T. Beckham, Carbohydrate-protein interactions that drive processive polysaccharide translocation in enzymes revealed from a computational study of cellobiohydrolase processivity. *J Am Chem Soc* **136**, 8810-8819 (2014).
22. Y. Shibafuji *et al.*, Single-molecule imaging analysis of elementary reaction steps of trichoderma reesei cellobiohydrolase i (Cel7A) hydrolyzing crystalline cellulose I α and III. *Journal of Biological Chemistry* **289**, 14056-14065 (2014).
23. A. Nakamura *et al.*, Single-molecule Imaging Analysis of Binding, Processive Movement, and Dissociation of Cellobiohydrolase Trichoderma reesei Cel6A and Its Domains on Crystalline Cellulose. *J Biol Chem* **291**, 22404-22413 (2016).
24. K. Igarashi *et al.*, Visualization of cellobiohydrolase I from Trichoderma reesei moving on crystalline cellulose using high-speed atomic force microscopy. *Methods Enzymol* **510**, 169-182 (2012).
25. K. Igarashi *et al.*, Traffic jams reduce hydrolytic efficiency of cellulase on cellulose surface. *Science* **333**, 1279-1282 (2011).
26. S. K. Brady, S. Sreelatha, Y. Feng, S. P. S. Chundawat, M. J. Lang, Cellobiohydrolase 1 from Trichoderma reesei degrades cellulose in single cellobiose steps. *Nature Communications* **6**, 1-9 (2015).
27. S. P. S. Chundawat *et al.*, Molecular origins of reduced activity and binding commitment

- of processive cellulases and associated carbohydrate-binding proteins to cellulose III. *Journal of Biological Chemistry* **296**, 100431-100431 (2021).
28. L. d. C. Sousa, J. Humpala, V. Balan, B. E. Dale, S. P. S. Chundawat, Impact of Ammonia Pretreatment Conditions on the Cellulose III Allomorph Ultrastructure and Its Enzymatic Digestibility. *ACS Sustainable Chemistry & Engineering* **7**, 14411-14424 (2019).
 29. M. Wada, H. Chanzy, Y. Nishiyama, P. Langan, Cellulose III Crystal Structure and Hydrogen Bonding by Synchrotron X-ray and Neutron Fiber Diffraction. *Macromolecules* **37**, 8548-8555 (2004).
 30. Y. Nishiyama, J. Sugiyama, H. Chanzy, P. Langan, Crystal Structure and Hydrogen Bonding System in Cellulose Ia from Synchrotron X-ray and Neutron Fiber Diffraction. *Journal of the American Chemical Society* **125**, 14300-14306 (2003).
 31. Y. Nishiyama, P. Langan, H. Chanzy, Crystal Structure and Hydrogen-Bonding System in Cellulose I from Synchrotron X-ray and Neutron Fiber Diffraction. *J. Am. Chem. Soc.* **124**, 9074-9082 (2002).
 32. C. J. Garvey, I. H. Parker, G. P. Simon, On the Interpretation of X-Ray Diffraction Powder Patterns in Terms of the Nanostructure of Cellulose I Fibres. *Macromolecular Chemistry and Physics* **206**, 1568-1575 (2005).
 33. J. H. Wiley, R. H. Atalia, Band assignments in the Raman spectra of celluloses. *Carbohydrate Research* **160**, 113-129 (1987).
 34. R. H. Atalia, D. L. Vanderhart (1987) Studies on the structure of cellulose using Raman spectroscopy and solid state ¹³C NMR. in *IPC technical paper series ; no.217* (Georgia Institute of Technology, Appleton, Wisconsin: the institute,).
 35. S. Rakshit, Y. Zhang, K. Manibog, O. Shafraz, S. Sivasankar, Ideal, catch, and slip bonds in cadherin adhesion. *Proc Natl Acad Sci U S A* **109**, 18815-18820 (2012).
 36. G. I. Bell, Models for the specific adhesion of cells to cells. *Science* **200**, 618-627 (1978).
 37. J. M. Fox *et al.*, A single-molecule analysis reveals morphological targets for cellulase synergy. *Nat Chem Biol* **9**, 356-361 (2013).
 38. M. R. Nimlos *et al.*, Binding preferences, surface attachment, diffusivity, and orientation of a family 1 carbohydrate-binding module on cellulose. *J Biol Chem* **287**, 20603-20612 (2012).
 39. J. Lehtiö *et al.*, The binding specificity and affinity determinants of family 1 and family 3 cellulose binding modules. *Proc Natl Acad Sci U S A* **100**, 484-489 (2003).
 40. G. T. Beckham *et al.*, Identification of amino acids responsible for processivity in a family

- 1 carbohydrate-binding module from a fungal cellulase. *Journal of Physical Chemistry B* **114**, 1447-1453 (2010).
41. G. Buffon, "Essai d'arithmétique morale" in *Histoire naturelle, générale et particulière*, Supplément 4. (1777), pp. 46-123.
 42. M. Linder *et al.*, Identification of functionally important amino acids in the cellulose-binding domain of *Trichoderma reesei* cellobiohydrolase I. *Protein Sci* **4**, 1056-1064 (1995).
 43. A. T. Hendriks, G. Zeeman, Pretreatments to enhance the digestibility of lignocellulosic biomass. *Bioresour Technol* **100**, 10-18 (2009).
 44. C. Hervé *et al.*, Carbohydrate-binding modules promote the enzymatic deconstruction of intact plant cell walls by targeting and proximity effects. *Proc Natl Acad Sci U S A* **107**, 15293-15298 (2010).
 45. F. Cuskin *et al.*, How nature can exploit nonspecific catalytic and carbohydrate binding modules to create enzymatic specificity. *Proceedings of the National Academy of Sciences* **109**, 20889-20894 (2012).
 46. H. J. Gilbert, J. P. Knox, A. B. Boraston, Advances in understanding the molecular basis of plant cell wall polysaccharide recognition by carbohydrate-binding modules. *Curr Opin Struct Biol* **23**, 669-677 (2013).
 47. R. Brunecky *et al.*, Synthetic fungal multifunctional cellulases for enhanced biomass conversion. *Green Chemistry* **22**, 478-489 (2020).
 48. A. Várnai *et al.*, Carbohydrate-binding modules of fungal cellulases: occurrence in nature, function, and relevance in industrial biomass conversion. *Adv Appl Microbiol* **88**, 103-165 (2014).
 49. G. T. Beckham *et al.*, Molecular-level origins of biomass recalcitrance: decrystallization free energies for four common cellulose polymorphs. *J Phys Chem B* **115**, 4118-4127 (2011).
 50. J. V. Vermaas *et al.*, The dissociation mechanism of processive cellulases. *Proc Natl Acad Sci U S A* **116**, 23061-23067 (2019).
 51. A. W. Blake *et al.*, Understanding the biological rationale for the diversity of cellulose-directed carbohydrate-binding modules in prokaryotic enzymes. *J Biol Chem* **281**, 29321-29329 (2006).
 52. D. K. Das *et al.*, Pre-T cell receptors (Pre-TCRs) leverage V β complementarity determining regions (CDRs) and hydrophobic patch in mechanosensing thymic self-ligands. *Journal of Biological Chemistry* **291**, 25292-25305 (2016).

53. J. R. King, C. M. Bowers, E. J. Toone, Specific binding at the cellulose binding module-cellulose interface observed by force spectroscopy. *Langmuir* **31**, 3431-3440 (2015).
54. K. Dudko Olga, G. Hummer, A. Szabo, Theory, analysis, and interpretation of single-molecule force spectroscopy experiments. *Proceedings of the National Academy of Sciences* **105**, 15755-15760 (2008).
55. F. Rico, A. Russek, L. González, H. Grubmüller, S. Scheuring, Heterogeneous and rate-dependent streptavidin-biotin unbinding revealed by high-speed force spectroscopy and atomistic simulations. *Proc Natl Acad Sci U S A* **116**, 6594-6601 (2019).
56. E. M. Alekozai, P. K. GhattyVenkataKrishna, E. C. Uberbacher, M. F. Crowley, Simulation analysis of the cellulase Cel7A carbohydrate binding module on the surface of the cellulose I β . *Cellulose* **21**, 951-971 (2014).
57. B. Nemmaru *et al.*, Reduced type-A carbohydrate-binding module interactions to cellulose I leads to improved endocellulase activity. *Biotechnology and Bioengineering* **118**, 1141-1151 (2021).
58. M. A. Jobst *et al.*, Resolving dual binding conformations of cellulosome cohesin-dockerin complexes using single-molecule force spectroscopy. *eLife* **4**, e10319 (2015).
59. R. Kont, J. Kari, K. Borch, P. Westh, P. Våljamäe, Inter-domain Synergism Is Required for Efficient Feeding of Cellulose Chain into Active Site of Cellobiohydrolase Cel7A. *J Biol Chem* **291**, 26013-26023 (2016).
60. F. W. Studier, Protein production by auto-induction in high density shaking cultures. *Protein Expr Purif* **41**, 207-234 (2005).
61. S. Lim, S. P. Chundawat, B. G. Fox, Expression, purification and characterization of a functional carbohydrate-binding module from *Streptomyces* sp. SirexAA-E. *Protein Expr Purif* **98**, 1-9 (2014).
62. J. Hong, X. Ye, Y. Wang, Y. H. Zhang, Bioseparation of recombinant cellulose-binding module-proteins by affinity adsorption on an ultra-high-capacity cellulosic adsorbent. *Anal Chim Acta* **621**, 193-199 (2008).
63. B. W. McLean *et al.*, Analysis of binding of the family 2a carbohydrate-binding module from *Cellulomonas fimi* xylanase 10A to cellulose: specificity and identification of functionally important amino acid residues. *Protein Eng* **13**, 801-809 (2000).
64. W. Ruland, X-ray determination of crystallinity and diffuse disorder scattering. *Acta Crystallographica* **14**, 1180-1185 (1961).
65. S. Park, J. O. Baker, M. E. Himmel, P. A. Parilla, D. K. Johnson, Cellulose crystallinity index: measurement techniques and their impact on interpreting cellulase performance.

Biotechnol Biofuels **3**, 10 (2010).

66. A. D. French, Idealized powder diffraction patterns for cellulose polymorphs. *Cellulose* **21**, 885-896 (2014).
67. E.-L. Hult, T. Iversen, J. Sugiyama, Characterization of the supermolecular structure of cellulose in wood pulp fibres. *Cellulose* **10**, 103-110 (2003).
68. J. He, S. Cui, S.-y. Wang, Preparation and crystalline analysis of high-grade bamboo dissolving pulp for cellulose acetate. *Journal of Applied Polymer Science* **107**, 1029-1038 (2008).
69. S. P. S. Chundawat *et al.*, Ammonia-salt solvent promotes cellulosic biomass deconstruction under ambient pretreatment conditions to enable rapid soluble sugar production at ultra-low enzyme loadings. *Green Chemistry* **22**, 204-218 (2020).
70. U. P. Agarwal, 1064 nm FT-Raman spectroscopy for investigations of plant cell walls and other biomass materials. *Front Plant Sci* **5**, 490 (2014).
71. U. P. Agarwal, R. S. Reiner, S. A. Ralph, Cellulose I crystallinity determination using FT-Raman spectroscopy: univariate and multivariate methods. *Cellulose* **17**, 721-733 (2010).
72. R. H. Atalla, D. L. Vanderhart, Native cellulose: a composite of two distinct crystalline forms. *Science* **223**, 283-285 (1984).

CHAPTER 3

Single-molecule mechanical and biochemical characterization of cellulose biosynthesis in the Bacterial Cellulose Synthase A-B complex from *Rhodobacter sphaeroides*

This chapter is adapted from Hilton et al, "Single-molecule investigations of single-chain cellulose biosynthesis" *PNAS*. 2022 by permission granted under the Proceedings of the National Academy of Sciences (PNAS) license terms and by corresponding authors.

3.1 Summary

The most abundant biopolymer, cellulose, is utilized as cellular structural scaffolding capable of harboring life from plants to bacteria. Bacteria produce cellulose in biofilms as a means of physical and chemical protection. Cellulose biosynthesis in sessile bacterial colonies originates in the membrane-integrated BcsAB complex. We utilize optical tweezers to measure single-strand cellulose biosynthesis by BcsAB from *R. sphaeroides*. Synthesis is highly processive and depends on UDP-glucose, Mg^{2+} and cyclic-di-GMP, with the latter displaying a retention time of ~80 minutes. Below a stall force of 12.7 pN, biosynthesis is relatively insensitive to force and proceeds at a rate of one glucose addition every 2.5 seconds at room temperature, increasing to two additions per second at 37 degrees. At low forces conformational hopping is observed. Single-strand cellulose stretching unveiled a persistence length of 6.2 nm, an axial stiffness of 40.7 pN and an ability for complexes to maintain a tight grip with forces nearing 100 pN. Stretching experiments exhibited hysteresis suggesting that cellulose microstructure underpinning robust biofilms begins to form during synthesis. Cellohexaose spontaneously binds to nascent single cellulose strands impacting polymer mechanical properties and increasing BcsAB activity. BcsAB is the fourth polymerizing enzyme to be studied at the single-molecule level and the only one that does not use an established

track template (DNA or RNA).

3.2 Introduction

Cellulose is an integral structural component utilized by several kingdoms of life for its high mechanical strength and chemical stability (2, 3). Lately, cellulose's contribution to cell walls and microbial mats has garnered great interest as cellulosic biofuels become increasingly competitive (4) and as cellulose-stabilized bacterial biofilms are shown to play significant roles in pathogenesis (5-7). Cellulose is a polysaccharide composed of repeating glucosyl units linked by $\beta(1-4)$ glycosidic bonds. Investigations of its crystalline fibrillar form show that strands are linearly arranged and flat (8). In gram-negative bacteria, cellulose is manufactured through a multi-subunit trans-envelope bacterial cellulose synthase (Bcs) complex containing the evolutionarily conserved (9) catalytic BcsA subunit and an inner membrane anchored domain known as BcsB (10). The membrane-embedded BcsAB complex likely interacts with BcsC in the outer membrane to form a continuous transmembrane conduit for cellulose secretion. *In vitro* functional and structural studies on the purified *Rhodobacter sphaeroides* BcsAB complex revealed that it, alone, is sufficient for cellulose synthesis and secretion across the inner bacterial membrane (10). BcsA is allosterically activated by cyclic-di-GMP (c-d-GMP), enabling its glycosyltransferase domain to bind the Mg^{2+} -coordinated UDP-glucose (UDP-glc) substrate (11, 12). UDP-glc reacts with and elongates the non-reducing terminal end of the cellulose chain one glucose unit at a time, releasing UDP byproduct afterward (13). Subsequently, the polymer translocates through a transmembrane channel formed by BcsA and is likely guided into the periplasmic space by BcsB (14). Surprisingly, the degree of processive polymerization from cellulose synthases of different origins ranges from hundreds to thousands of glucose units (15, 16).

The cellulose polymer produced by BcsAB is a main component of biofilm matrices that encase sessile bacterial colonies, particularly among enterobacteria (7). Adherent bacterial populations besiege industrial systems by plugging filters, corroding metal surfaces, and fouling pipes (17). In healthcare settings, robust biofilms are responsible for ~65% of nosocomial infections and are considerably resistant to antimicrobial treatments (6, 18). Inhibiting the production of extracellular polymeric substances, such as polysaccharides, is a strong potential antibiofilm strategy (19). Thus, a molecular understanding of bacterial cellulose synthesis is paramount for the development of powerful antibacterial agents.

BcsAB has been well described by crystallographic snapshots and *in vivo* analyses, however,

these methods lack details of biosynthesis at the molecular level (14, 20). Extensive work has been done to characterize cellulose synthesis and the properties of cellulose (2, 3, 10, 11, 14, 20-22). Cellulose, as an abundant wall polymer of vascular plants, has been described substantially in its amorphous and crystalline forms using X-ray diffraction(23), molecular dynamics simulations (23, 24), and atomic force microscopy(25) among other methods (21, 26, 27). In all cases, studies included cellulose aggregates or atomistic models. While it is known that BcsAB produces high-molecular weight amorphous cellulose (9), the physical and dynamic properties of single cellulose chain synthesis leading to this structure have not been characterized.

A real-time, molecular-scale analysis of cellulose synthesis and single-chain cellulose offers essential insight into the formation and structural qualities of this abundant biopolymer. Biosynthesis requires multiple elements including activated glucose, c-d-GMP and Mg^{2+} . Furthermore, product transport and product microstructure may also impact biosynthesis. Cellulose production may be impacted by mechanical force, as seen in other molecular machines (28-30). Here, we use optical tweezers to directly probe mechanical and catalytic activity of single BcsAB molecules and their single-strand cellulose polymer products.

3.3 Results

The cellulose synthase BcsAB complex from *Rhodobacter sphaeroides* has been successfully expressed and purified in prior studies (13, 14). The complex is catalytically active in detergent-solubilized as well as lipid nanodisc-reconstituted states (9), providing an ideal model system for single-molecule measurements. Accordingly, the BcsAB complex was reconstituted into MSP1D1 lipid nanodiscs formed from *E. coli* total lipid extract using a His-tagged membrane scaffold protein (see Methods).

3.3.1 Single molecule activity of BcsAB

Cellulose synthesis was directly monitored with a tethered bead assay configuration (Fig. 3.1a). Our motility assay utilized a flow cell fabricated from a microscope slide and a KOH etched coverslip with a gasket of double-sided sticky tape. Streptavidin, blocking protein, biotinylated anti-His antibodies and aforementioned nanodiscs containing BcsAB were deposited sequentially through a series of buffer exchanges and incubations. Beads decorated with cellulose-binding DNA aptamers (31) were introduced, initiating tether formation to free cellulose strands emanating from surface-bound synthases. After an incubation period to permit bead binding, a wash step

removed free beads. A motility buffer containing UDP-glc, c-d-GMP, and Mg^{2+} was introduced. Tethered beads showing significant mobility after 15 minutes indicate actively synthesizing complexes. These beads were located by eye, centered in the measurement zone and trapped. The sample stage was translated until the desired tension was applied to the strand. Motility traces monitoring the bead position relative to the center of the trap were recorded as described below.

Motility records were generally captured for ~5 minutes yielding synthesis trajectories ~10-40 nm in length, depending on the collection window size, with some trajectories reaching as long as 100 nm. Linear fits to motility traces reveal BcsAB synthesizes cellulose at an average velocity of $0.22 \pm 0.01 \text{ nm s}^{-1}$ (SEM, N=176) at 21°C with velocities ranging from 0.05 nm s^{-1} to 0.7 nm s^{-1} .

Example traces are shown in Fig. 3.1b. Force is proportional to the bead's distance from the trap center and decreases as cellulose is synthesized. Tether lengths varied in size (400 nm to 3 μm). Motility trajectories were typically straight, maintained a constant velocity, and lacked long pauses. In some cases, abrupt extensions and retractions were observed as described below.

3.3.2 Temperature dependence of BcsAB

The observed rate of synthesis in our isolated minimal system is lower than reported rates gathered through other methods including elevated temperatures: 1.5 nm s^{-1} (32), 2 nm s^{-1} (33), and $2.5\text{-}9 \text{ nm s}^{-1}$ (34) (Table 3.1). Motility studies at elevated temperatures revealed on possible source of

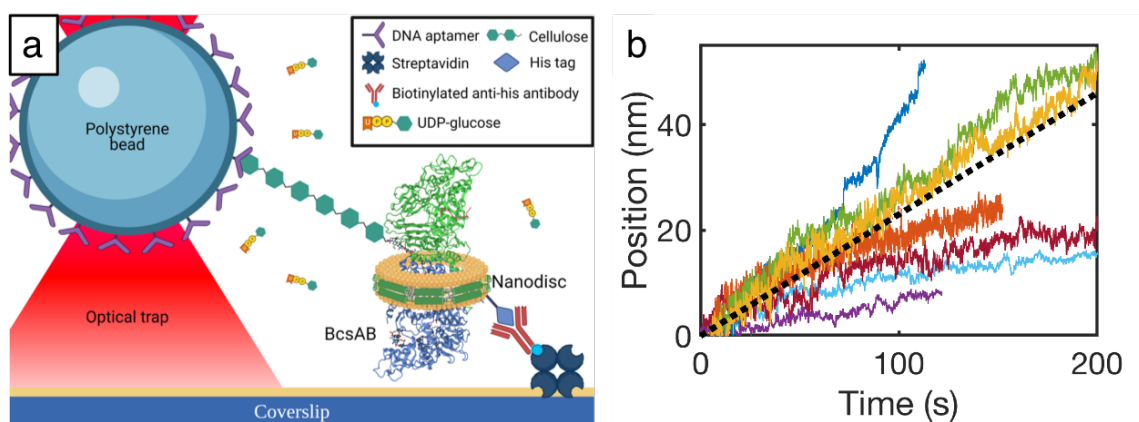


Figure 3.1. BcsAB cellulose synthesis. (a) Schematic of the BcsAB synthesis assay in which a single BcsAB complex (PDB: 4P00) is enveloped in a surface-bound nanodisc. A cellulose-binding DNA aptamer-coated bead binds the cellulose product strand, and the position and applied force are measured with nanometer and piconewton resolution using optical tweezers. (b) Cellulose synthesis traces. The black dotted line indicates the average velocity of $0.22 \pm 0.01 \text{ nm s}^{-1}$ (SEM, N=176).

Reference	Velocity	Temperature	Preparation	Species
This work	0.22 nm/s	21°C	Isolated single synthase in Nanodisc	<i>Rhodobacter Sphaeroides</i> (Bacteria)
This work	0.26 nm/s	21°C	Isolated single synthase in Nanodisc with cellohexaose	<i>Rhodobacter Sphaeroides</i> (Bacteria)
This work	1.2 nm/s	37°C	Isolated single synthase in Nanodisc	<i>Rhodobacter Sphaeroides</i> (Bacteria)
Du et al.	1.5 nm/s	30°C	Purified synthase in detergent	<i>Gluconacetobacter hansenii</i> (Bacteria)
Omadjela et al.	45 nm/s	37°C	Synthase expressed in inverted membrane vesicles	<i>Rhodobacter Sphaeroides</i> (Bacteria)
Cifuentes et al.	2 nm/s	25°C	Synthase rosettes in detergent	<i>Nicotiana tabacum</i> cv. BY-2 (Plants)
Paredes et al.	2.5-8.3 nm/s	Not reported	Synthase rosettes <i>in vivo</i>	<i>Arabidopsis</i> plants (Plants)

Table 3.1. Comparison of biosynthesis velocities across studies (4-7).

*This study measures synthesis by monitoring the release of UDP, which includes hydrolysis by transfer to water. Therefore, this method is not an accurate assessment of cellulose elongation.

discrepancy between our studies and the literature. The velocity of synthesis increases substantially with temperature to a mean velocity of $1.2 \pm 0.1 \text{ nm s}^{-1}$ (SEM, N=50) at the upper limit of our instrument's capabilities of 37°C, consistent with the literature (Fig. 3.2a). In between, the velocity of synthesis at 27°C is $0.49 \pm 0.05 \text{ nm s}^{-1}$ (SEM, N=25) and at 32°C is $0.87 \pm 0.10 \text{ nm s}^{-1}$ (SEM, N=20). An Arrhenius fit of BcsAB motility from 21°C to 37°C yields an activation energy of 32.5 k_BT (80.5 kJ mol⁻¹) (Fig. 3.2b). Additionally, components absent from our single-molecule studies, such as BcsC, could further enhance the cellulose synthesis rates (32).

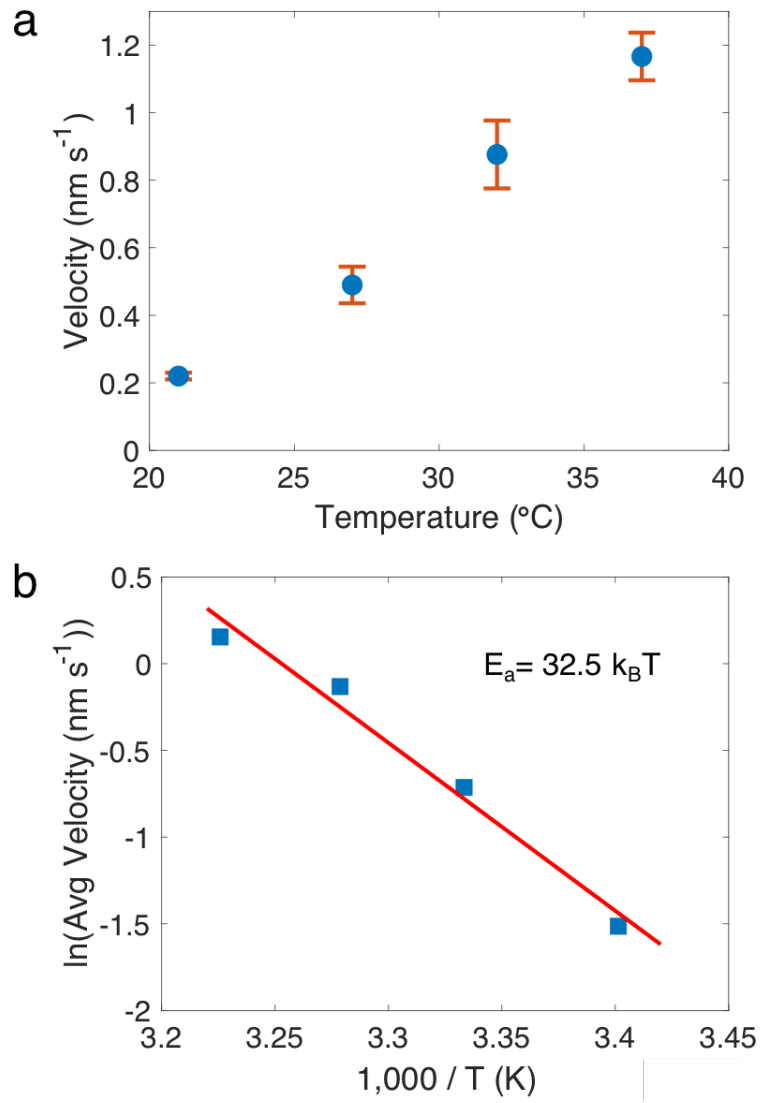


Figure 3.2. Cellulose biosynthesis at varying temperatures. (a) There is a significant increase in activity with increasing temperatures. The velocity of synthesis at 27°C is $0.49 \pm 0.05 \text{ nm s}^{-1}$ (SEM, N=25), at 32°C is $0.87 \pm 0.10 \text{ nm s}^{-1}$ (SEM, N=20) and at 37°C is $1.2 \pm 0.1 \text{ nm s}^{-1}$ (SEM, N=50). Error bars are SEM. (b) An Arrhenius fit of BcsAB motility from 21°C to 37°C yields an activation energy of $32.5 \text{ k}_B\text{T}$ (80.5 kJ mol^{-1}).

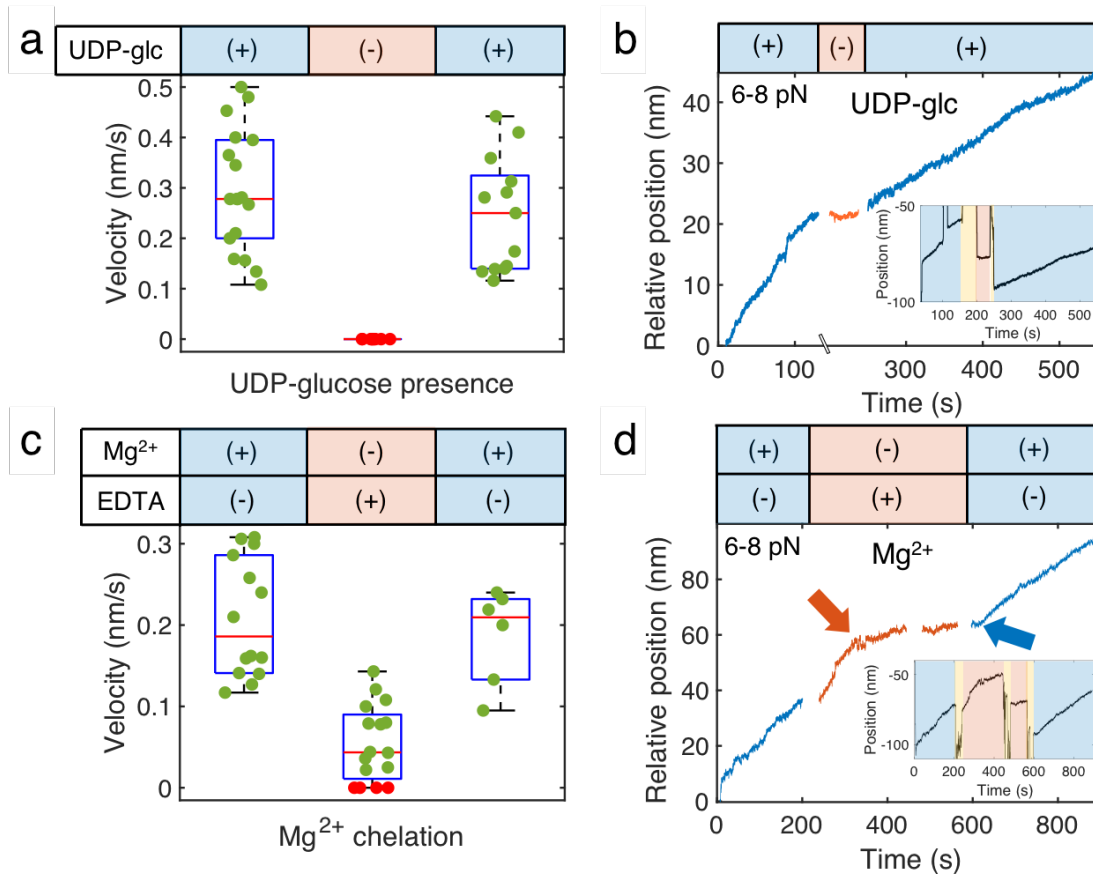


Figure 3.3. Biochemical controls. (a) All BcsAB complexes sampled in the absence of UDP-glc (N=10) showed no activity, while synthases sampled before removal (N=18) and after replenishment (N=13) displayed clear motility. Green and red points indicate synthesis and no synthesis of individual BcsAB, respectively. (b) An example trace of UDP-control buffer exchanges while monitoring the same tether shows that synthesis halts without available monomer. (c) Sampled synthases before introduction (N=14), in the presence (N=16), and after removal (N=6) of an EDTA control buffer reveal that velocity slows to $0.05 \pm 0.01 \text{ nm s}^{-1}$ (SEM). (d) Mg²⁺/EDTA control buffer exchange on a single tether indicates synthesis is severely hindered after Mg²⁺ chelation. Red and blue arrows point to the moments Mg²⁺ was chelated and replenished, respectively. All activity was recovered when both control buffers were washed out. The insets in (b) and (d) are the raw traces including large perturbations where buffers were exchanged mid-experiment. Blue indicates a complete synthesis solution, yellow indicates flow, and red indicates control buffer. We note the force range for each example trace, with the typical range spanning 2-3 pN. The break between control regions in (d) at ~450 s is from preparing the next flow step, but no buffer exchange occurred.

3.3.3 Biochemical dependence of BcsAB

To confirm that these records depend on synthase activity, we investigated the effects of critical assay components such as UDP-glc and Mg²⁺ on catalysis by probing for activity under varying control conditions. In general, we randomly sampled multiple synthases before and after washing out the synthesis buffer and replacing it with three flow channel volumes (3x15 μL) of control buffer.

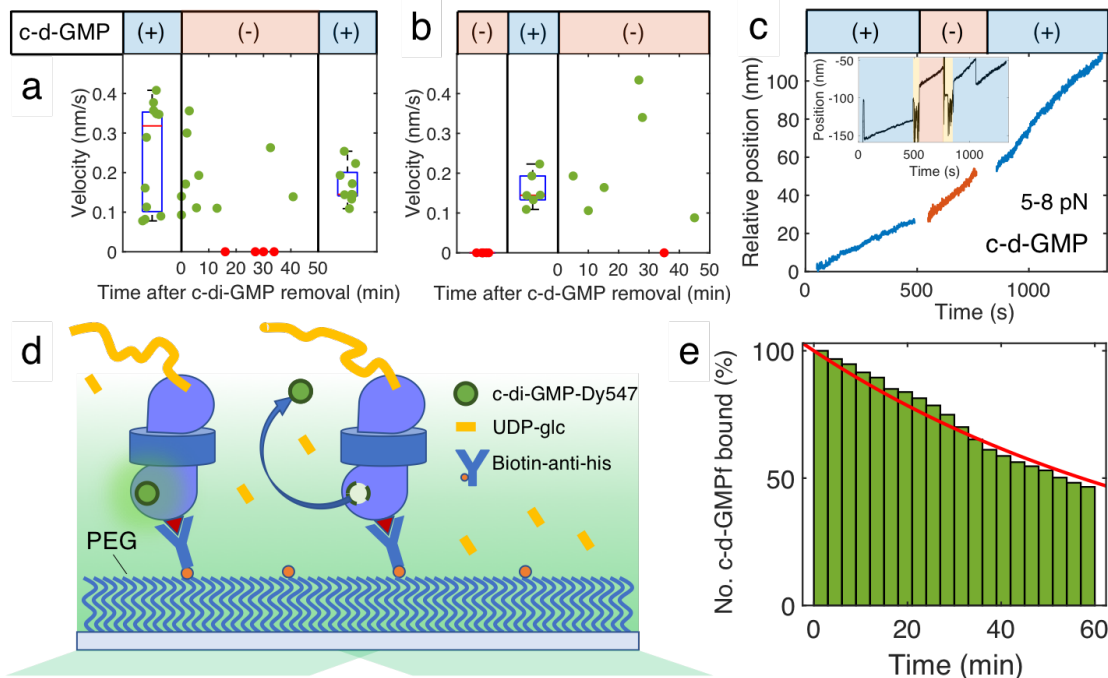


Figure 3.4. C-d-GMP controls and fluorescence. (a) Different complexes were sampled for synthesis before removal, at varying time points after removal, and after replenishment of c-d-GMP. Motility persists in most cases. (b) We performed a null experiment starting without c-d-GMP, introducing it to the system, and removing again. C-d-GMP is necessary for synthesis but remains bound for long periods of time. (c) Single-tether c-d-GMP controls show synthesis is relatively unaffected when the activator is removed from solution. The applied force range is 5-8 pN for this example. (d) Schematic of fluorescence assay in which BcsAB is bound to the surface in the same design as the synthesis experiments, except the coverslip includes a non-stick PEG brush layer between the coverslip and the complex. If c-d-GMP-DY-547 (c-d-GMPf) is bound to BcsAB, we detect fluorescence. The signal disappears in a single step when the molecule dissociates or photobleaches. (e) The number of bound and fluorescing c-d-GMPf decreases over time (N=247). We record incredibly long bond lifetimes of c-d-GMPf, as 70% of molecules remain associated past 30 minutes with 46% persisting until the 60 min acquisition time limit. An exponential fit (red) reveals a time constant of 82.5 min corresponding to an off-rate of $2.0 \times 10^{-4} \text{ s}^{-1}$. Due to potential photobleaching, our results show the lower bound of the time constant.

We sampled again after replenishing the system with the synthesis buffer. In some experiments, we were able to monitor continued activity of the same tether. All controls were sampled between 3-8 pN of applied force with a mean of 6 pN. Force nominally changes within a finite range of 2-3 pN along a given trajectory, but rates were unaffected by force within this range. As expected, the removal of the substrate UDP-glc suspended cellulose production in all cases until the fuel was reintroduced, at which point BcsAB resumed normal catalysis (Fig. 3.3a, Fig. 3.3b). To confirm Mg^{2+} dependence, 50 mM EDTA was included in the control buffer, in addition to excluding Mg^{2+} , to chelate any residual ions. Sampled complexes in EDTA showed a 75% decrease in synthesis velocity ($0.05 \pm 0.01 \text{ nm s}^{-1}$, SEM) from those sampled before chelation (Fig. 3.3c, Fig. 3.3d), and,

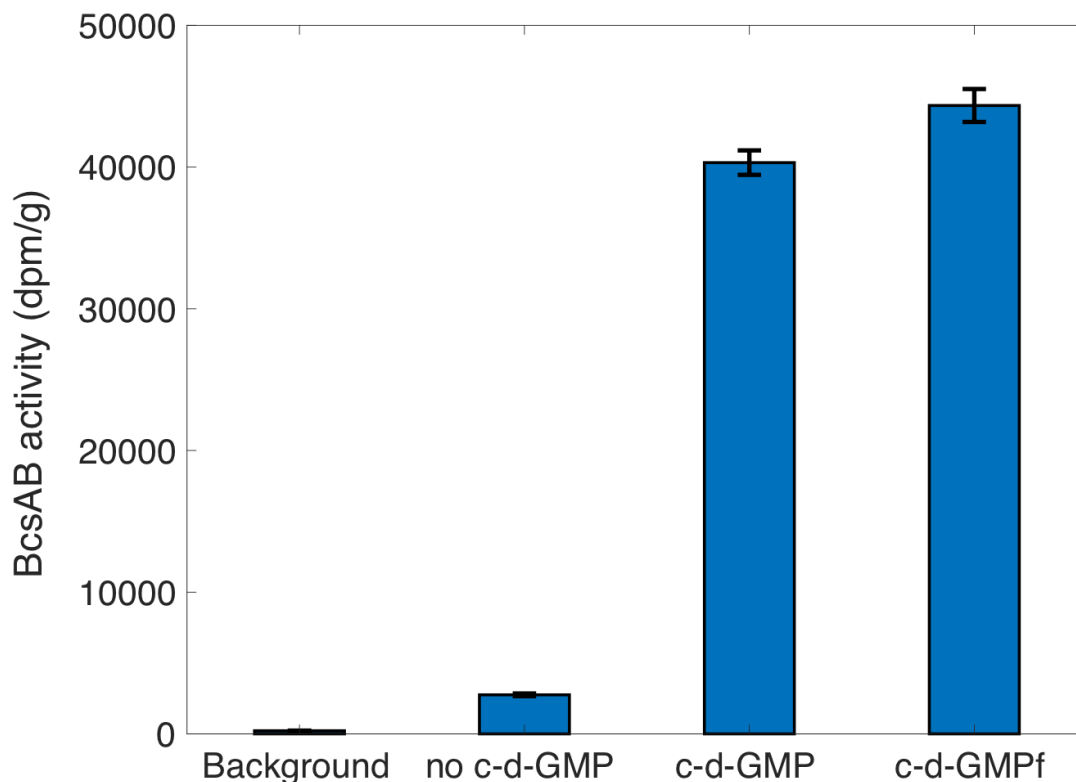


Figure 3.5. C-d-GMP vs c-d-GMPf bulk synthesis rates. UDP-glc uptake rates in disintegration per minute of BcsAB (dpm). The background contained no BcsAB. The control without c-d-GMP shows a significant reduction in activity, while there is no significant difference between synthesis rates in the presence of c-d-GMP versus c-d-GMPf. Error bars denote SEM.

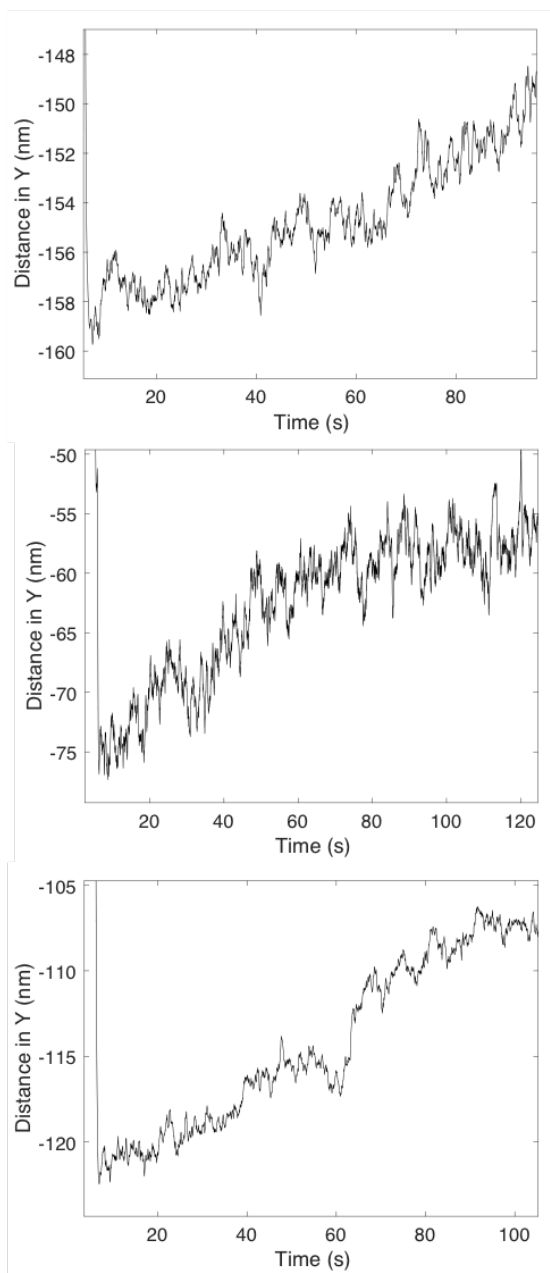
again, velocity was rescued with reintroduction. Thus, as expected, Mg^{2+} facilitates catalysis (11).

3.3.4 Cyclic-di-GMP refuses dissociation

C-d-GMP is an allosteric activator of BcsA and binds to its C-terminal PilZ domain. Binding of c-d-GMP mobilizes a ‘gating loop’ necessary for substrate binding to BcsA’s catalytic pocket (11). It was previously unclear whether the activator remains bound to BcsA during cellulose biosynthesis or is released from the enzyme after the initiation reaction.

We performed buffer exchange sampling experiments with c-d-GMP identical to those described above to identify the effects on synthesis (Fig. 3.4a). Prior to removal, all BcsAB were shown to be active (N=12). After removal, 71% of the synthases sampled (10 of 14) were active with some active synthases still present at 45 minutes, indicating c-d-GMP binds very strongly to BcsA during synthesis and is likely required to remain bound. Stalled complexes were first detected ~20 minutes after the buffer exchange. To demonstrate that c-d-GMP is necessary for motility, the buffer order

c-d-GMP



Fluorescent c-d-GMP

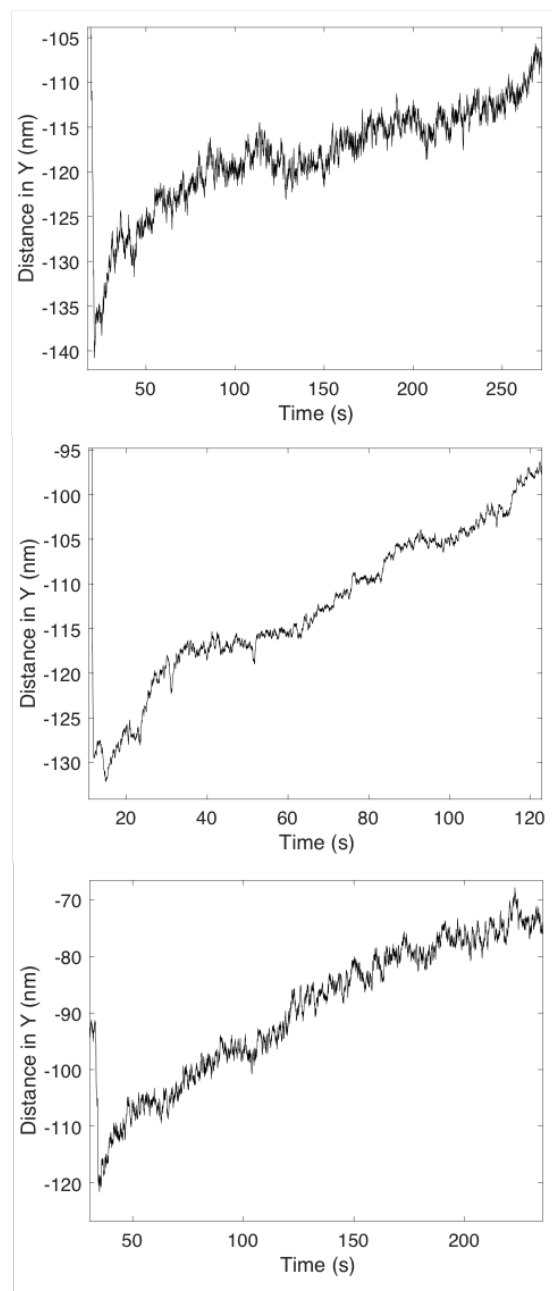


Figure 3.6. C-d-GMP vs c-d-GMPf single-molecule synthesis rates. Example traces of single-molecule cellulose synthesis under normal synthesis buffer conditions (left column) and with c-d-GMPf replacing c-d-GMP (right column). For this experiment, all measurements were between 4-8 pN of force. The mean velocity was $0.25 \pm 0.02 \text{ nm s}^{-1}$ (N=39, SEM) under normal conditions and was $0.25 \pm 0.3 \text{ nm s}^{-1}$ (N=8, SEM) in the presence of c-d-GMPf. The fluorescent dye had no apparent effect on single-molecule cellulose synthesis.

was reversed, starting with a motility buffer lacking c-d-GMP (Fig. 3.4b). As expected, BcsAB initially displayed no synthesis in the buffer lacking c-d-GMP (N=6). Immediately after addition of c-d-GMP, 100% of complexes sampled (N=6) demonstrated production. C-d-GMP was removed again after 45 minutes, and the sampled synthases behaved as observed before, exhibiting catalysis with only 1 of 7 stalling. Individual tether tests showed no immediate effect on polymerization rates (N=2) after c-d-GMP depletion (Fig. 3.4c).

With apparent c-d-GMP retention times of ~20 minutes or more, we developed a single-molecule TIRF assay to directly monitor the presence of dye-labeled c-d-GMP over extended periods (Fig. 3.4d). In these studies, we used a c-d-GMP molecule with a DY-547 dye labeled to one ribose group (c-d-GMPf). Both bulk synthesis and single-molecule synthesis tests showed no change in activity in the presence of 30 μM of c-d-GMPf versus unlabeled dinucleotide (Fig. 3.5, Fig. 3.6). BcsA binds an intercalated c-di-GMP dimer (11). In our assays, the BcsAB complexes were incubated, along with other synthesis components, with c-d-GMPf at 300 nM and unlabeled c-d-GMP at 29.7 μM to ensure the formation of mixed c-d-GMP dimers containing only a single c-d-GMPf. Just before data acquisition, c-d-GMPf was washed out with ten times the flow cell volume (10x20 μL) of normal synthesis buffer so that the only remaining fluorophores were bound to BcsAB. We recorded signal for 60 min, sampling at 0.33 s^{-1} . To minimize photobleaching, images were acquired by triggering excitation for only 100 ms during each acquisition with 120 s of total illumination. Example measurements are shown in Fig. 3.7.

Consistent with single-tether measurements, 70% (172 of 246) of the c-d-GMPf remained bound for 30 minutes with a considerable 46% of events (114 of 246) showing bond lifetimes longer than the 60-minute acquisition limit (Fig. 3.4e). An exponential fit to the percentage of remaining c-d-GMPf over time (Fig. 3.4e) reveals a bound time constant of 82.5 min and a dissociation rate of $2.0 \times 10^{-4} \text{ s}^{-1}$. Our results represent the lower bound because of potential photobleaching. Control flow cells lacking BcsAB showed no decoration, indicating signal from c-d-GMPf only occurs when bound to BcsAB (Fig. 3.8). Once bound, most c-d-GMP refused to dissociate or exchange with others in solution.

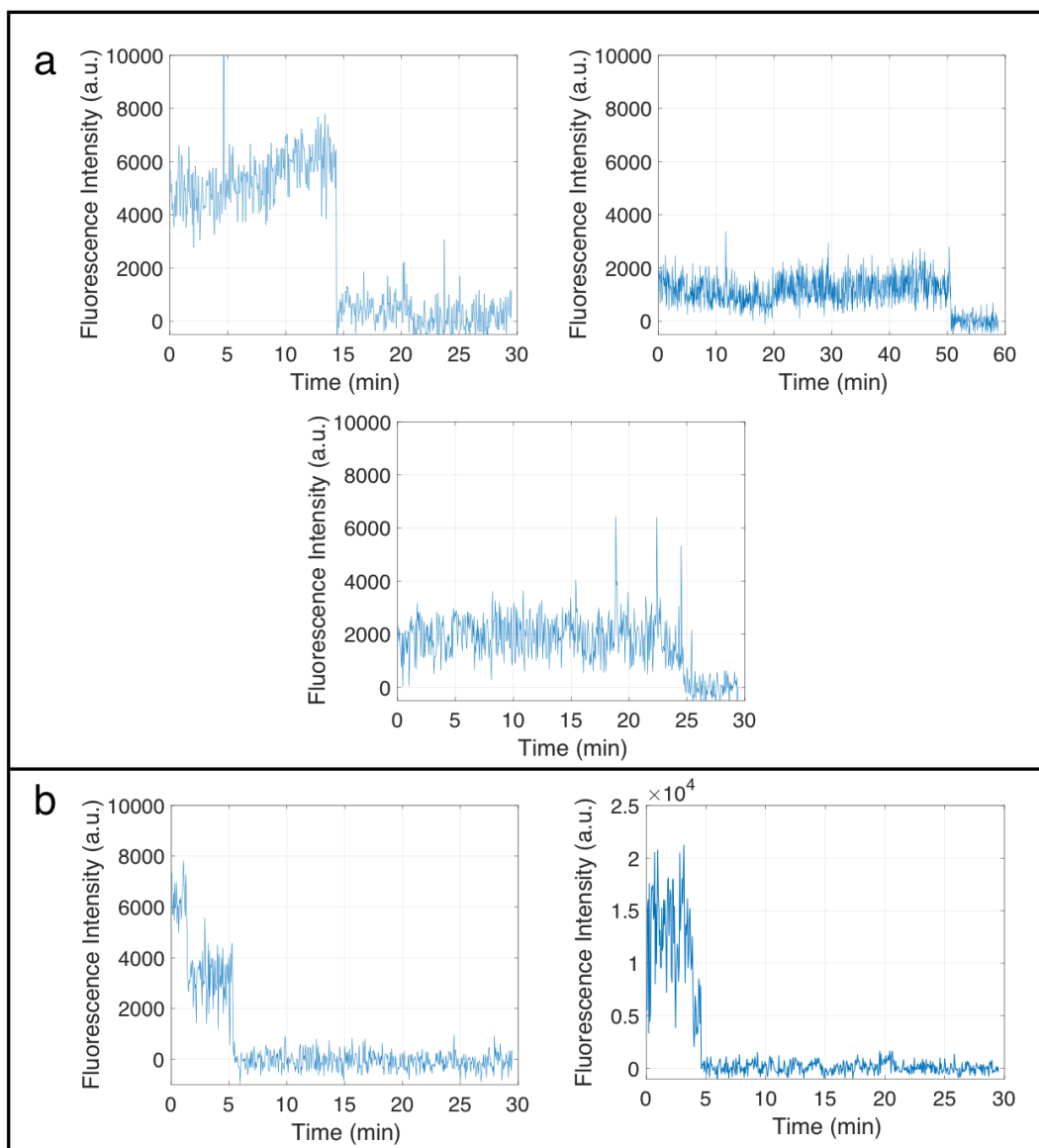
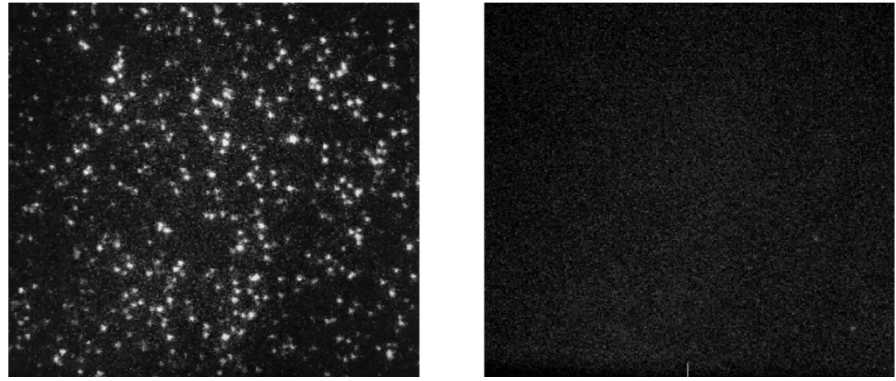


Figure 3.7. Example fluorescence traces. (a) Example fluorescence traces show high signal to noise ratio and single photobleaching/dissociation steps indicating single-molecule events. Only signals that remained constant at a brightness consistent with single-molecule fluorescence were considered. Note in these experiments the intensity of the excitation laser is not uniform over the whole field of view, resulting in a range of spot brightness levels. Single-molecule fluorescence brightness criteria were appraised from the brightness of single photobleaching events as well as from previous experiments (2). (b) Few traces contained two photobleaching/dissociation steps representative of two c-d-GMPf binding to the activation site.



BcsAB	+	-
1 nM DY547 c-di-GMP	+	+
30 μM Unlabeled c-di-GMP	+	+

Figure 3.8. TIRF control. To test the non-specific blocking capabilities of our PEG coverslip and ensure no fluorescently labelled c-d-GMP in solution triggered a response, we ran our assay with and without BcsAB, to which c-d-GMP binds. With BcsAB, we see many spots indicating c-d-GMPf is binding near the surface. Spots vary in intensity as two c-d-GMP bind to the PilZ domain and as the laser intensity varies across the specimen plane. Without BcsAB, we see no signal nor non-specifically bound c-di-GMPf near the surface. We can conclude that a fluorescent signal originates from c-d-GMPf bound to BcsA.

3.3.5 Stall force, microstructure and kinetic analysis

To determine the impact of force on synthesis rates, we constructed a force-velocity plot ranging from 2-20 pN (Fig. 3.9a). A fit to the general Boltzmann distribution, revealed that velocity remained constant as applied force increased, until a stall force of 12.7 pN, after which a decrease in activity is observed (Fig. 3.9a) (29). The fit parameters of the relationship reveal that most of the enzymatic cycle does not involve load dependent steps. Thus, cellulose synthesis is a biochemically limited process, and force (for example translocation) has negligible impact on synthesis rates until the ~13 pN level is reached, after which synthesis halts. The fits also reveal a characteristic distance of 4 nm for the load dependent mechanical transition, which is comparable to the length of BcsAB complex's transmembrane channel (14). The characteristic distance represents the distance along the reaction coordinate to the transition state, the apex of the energy landscape, of a mechanical step within one full catalytic cycle.

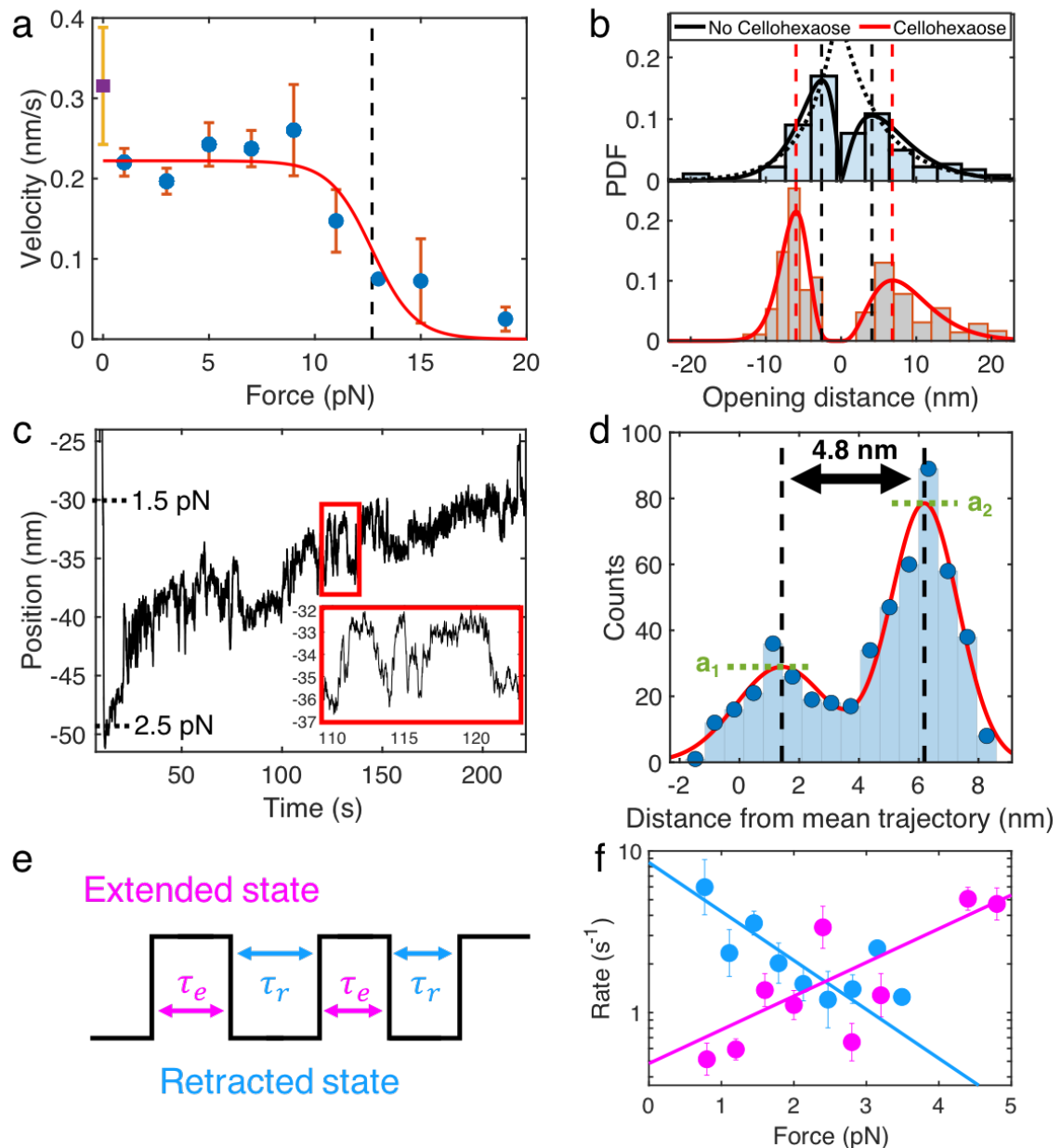


Figure 3.9. Kinetics analysis. (a) Recorded polymerization velocities from motility traces are binned and averaged every 2 pN (blue circles) and fit to a general Boltzmann relationship (N=176) revealing a distance to the mechanical transition state of 4.0 nm. The correlation indicates synthesis is biochemically limited, and synthesis begins to stall with an assisting load of 12.7 pN (black dashed line). Unloaded velocity (purple square) was recorded from a change in contour length over time (*SI Appendix Fig. S9*). Error bars denote SEM. (b, top) We detected a large range in extensions (2-100 nm, positive distance change) and retractions (2-20 nm, negative distance change). The average extension during motility was 10.6 ± 1.9 nm (SEM, N=73) and the average retraction was -4.6 ± 0.7 nm (SEM, N=26). Exponential fits (dotted black) generated length scales of 5.6 and -4.0 nm, respectively, while gamma distribution fits reveal peaks at 4.1 nm and -2.6 nm (dashed, vertical, black lines). (b, bottom) In the presence of cellohexaose, the extension and retraction profiles were best fit to gamma distributions, with peak locations appearing larger than for single cellulose at 6.8 nm and -6.0 nm (dashed, vertical, red lines). Transition magnitudes below 3 nm were not observed with cellohexaose present. Outlier extensions greater than 40 nm were excluded from diagrams but included in mean calculations. (c) Rapid extensions and retractions of 3-10 nm during cellulose synthesis at ~ 2 pN. Force reference markers note the slight decrease in

applied force as cellulose is synthesized. (d) A histogram of distances from the mean trajectory for the inset in (c) is fit to the sum of two gaussian distributions separated by a displacement of 4.8 nm. The mean distance between states is 5.0 ± 0.1 nm (SEM, N=201 from 51 molecules). The ratio of amplitudes (a_2/a_1) is equal to the ratio of the equilibrium force (1.8 ± 0.2 pN, SEM, N=201 segments from 51 molecules) to the acquisition force. Very few segments (<1%) displayed multimodal behavior and were excluded from this analysis. (e) Schematic of a reversible hopping between extended and retracted states. (f) Extension/retraction rates vs force for all non-gaussian, bimodal segments (N=322 events over 14 traces) fit to a logarithmic equation of the Bell model: $k=k_1 \exp(\Delta x F/k_b T)$. Only segments with a hopping distance within the range of 4-6 nm were considered, as the rates will change with transition distance. The intersection of fits reveals an equilibrium force of 2.4 pN, but both transitions share similar rates over the 2-3 pN range.

Abrupt extension and retraction transitions ranging 2-100 nm in size were frequently observed (seen in 49% of traces, Fig. 3.9b, Fig. 3.10). Such features are larger than expected from incorporation of individual glucose molecules (0.56 nm) (35), and several are larger than the size of the complex (15 nm) (14). Results also revealed larger position fluctuations than those typically observed in similar tethered bead experiments (36-38). Larger extensions generally appeared earlier in traces with few events occurring after initial extensions. To investigate the fluctuations, we analyzed 51 traces by first subtracting the average velocity and then plotting the distribution of the bead position from the mean trajectory over successive 5-second time windows. While some segments exhibited fluctuations consistent with Brownian motion, many showed structure deviating from a single distribution, suggesting there are underlying hops in length (Fig. 3.9c, Fig. 3.9d). Tests using a DNA strand of similar length and tension revealed distributions (N=16) that fit well to a single Gaussian distribution (Fig. 3.11). The discrete fluctuations in the cellulose strand likely originate from non-uniform motions in the synthesis machinery and/or rearrangements of the cellulose strand configuration during strand growth. Analysis of abrupt extensions and retractions during synthesis revealed exponential distributions in distance for both extension and retraction. The mean extension and retraction were 10.6 ± 1.9 nm, (SEM, N=73, Fig. 3.9b) and 4.6 ± 0.7 nm (SEM, N=26, Fig. 3.9b) respectively. Exponential fits to the distributions of extension and retraction distances (Fig. 3.9b) yielded exponential fit lengths of 5.6 nm and 4.0 nm, respectively.

In some cases, when tension was held at approximately 2 pN, the extensions and retractions alternated rapidly indicating an equilibrium point and giving rise to the previously observed non-gaussian position fluctuations (Fig. 3.9c). Interestingly, the rapid extensions and retractions were the same or very close in size for each individual molecule but varied in size between cellulose strands. Additional example traces can be seen in Fig. 3.12. The mean magnitude of the fluctuations was 5.0 ± 0.1 nm (SEM, N=201 over 51 traces) with >95% of events between 2.3 nm and 9 nm (Fig. 3.9d, Fig. 3.13).

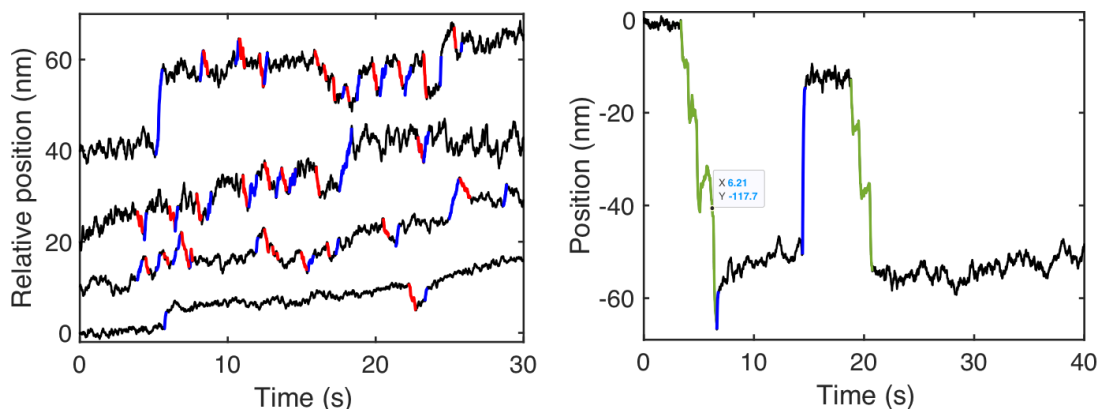


Figure 3.10. Extensions and retractions. During motility traces, abrupt extensions (blue) and retractions (red) are seen. Some examples are shown. Extensions and retractions vary in size (2-100 nm) with smaller events shown on the left (2-16 nm) and larger on the right (10 and 40 nm). Position changes due to stage translation are in green.

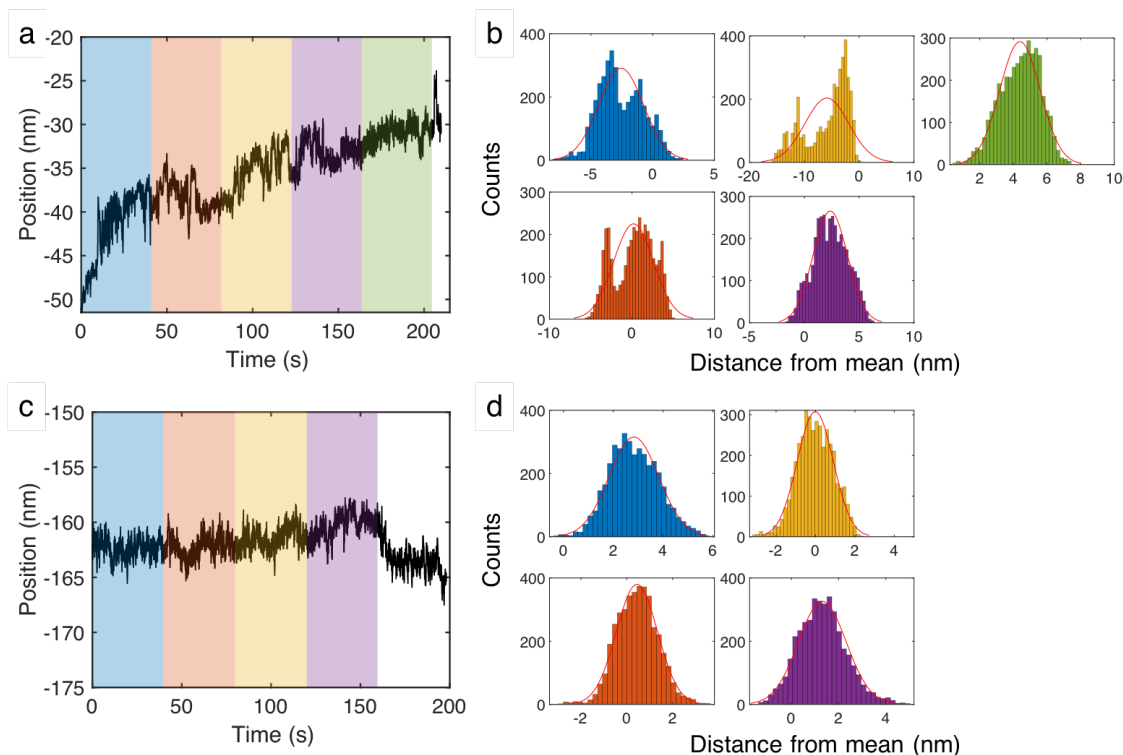


Figure 3.11. Cellulose vs DNA position distributions. (a) An example trace of cellulose synthesis under approximately 2 pN of tension segmented into 40-second intervals for analysis. (b) The position distributions from the mean over each time interval. Some segments display gaussian behavior, while 75% show evidence of repeated jumps ($N=25$). Distributions are color coded to match the respective segment on the trace. A gaussian fit is shown for comparison purposes. (c) An example trace of a DNA tether under approximately 5 pN of tension also segmented into 40-second intervals. (d) The corresponding position distributions for each segment. All distributions for DNA traces ($N=16$) show gaussian behavior. Segments maintained a predetermined size for accurate comparisons, which excludes the remainder of each trace when not divisible by the time window.

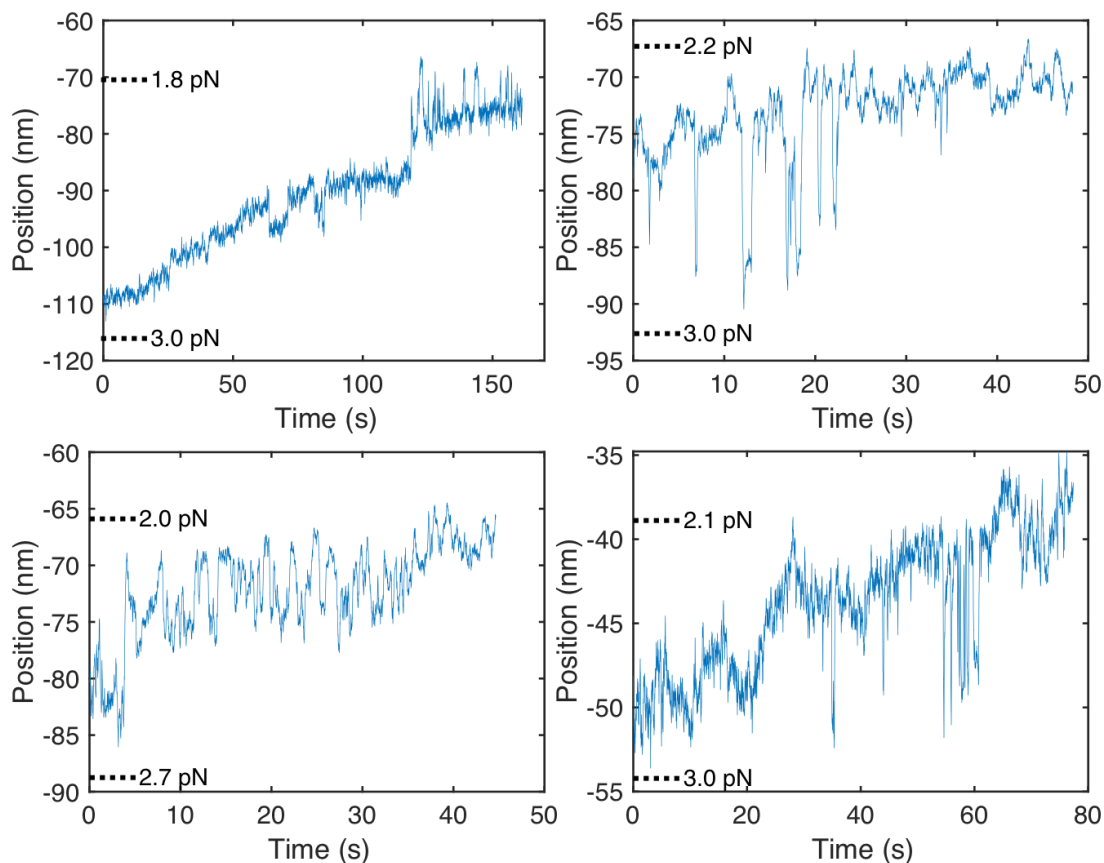


Figure 3.12. Example traces with rapid reversible transitions. Above are example traces in which reversible and rapid structural transitions are apparent. We observed a total of 51 out of 201 traces that exhibit this transition behavior. The transitions range from 3-10 nm in size and are typically only seen at a force range of 1-4 pN. The mean frequency of elongation transitions is 4.0 s^{-1} , while the mean retraction frequency is 4.1 s^{-1} . We note reference forces for the given distance from the center of the trap to show the applied force conditions during synthesis.

Force applied to the system alters the probability that the system exists in an extended or retracted state. Higher force favors an extended state, while lower force favors a retracted one. An analysis of the ratios between gaussian amplitudes from multiple two-state segments revealed an equilibrium force, force applied at which both states are equally likely, of $1.8 \pm 0.2 \text{ pN}$ (SEM, $N=201$ over 51 traces).

Additionally, the rates of extension and retraction derived from the dwell times within each state change exponentially with force. Fig. 3.9e shows a schematic of such hopping between states and Fig. 3.14 contains example analyses. Calculating the kinetics as a function of force from the time domain, assuming a linear relationship between the log rate and force, yielded an equilibrium force of 2.4 pN where the transition rate was 4 s^{-1} (Fig. 3.9f, $N=322$ over 14 traces). For this analysis, only molecules exhibiting a consistent hopping distance in the range of 4-6 nm,

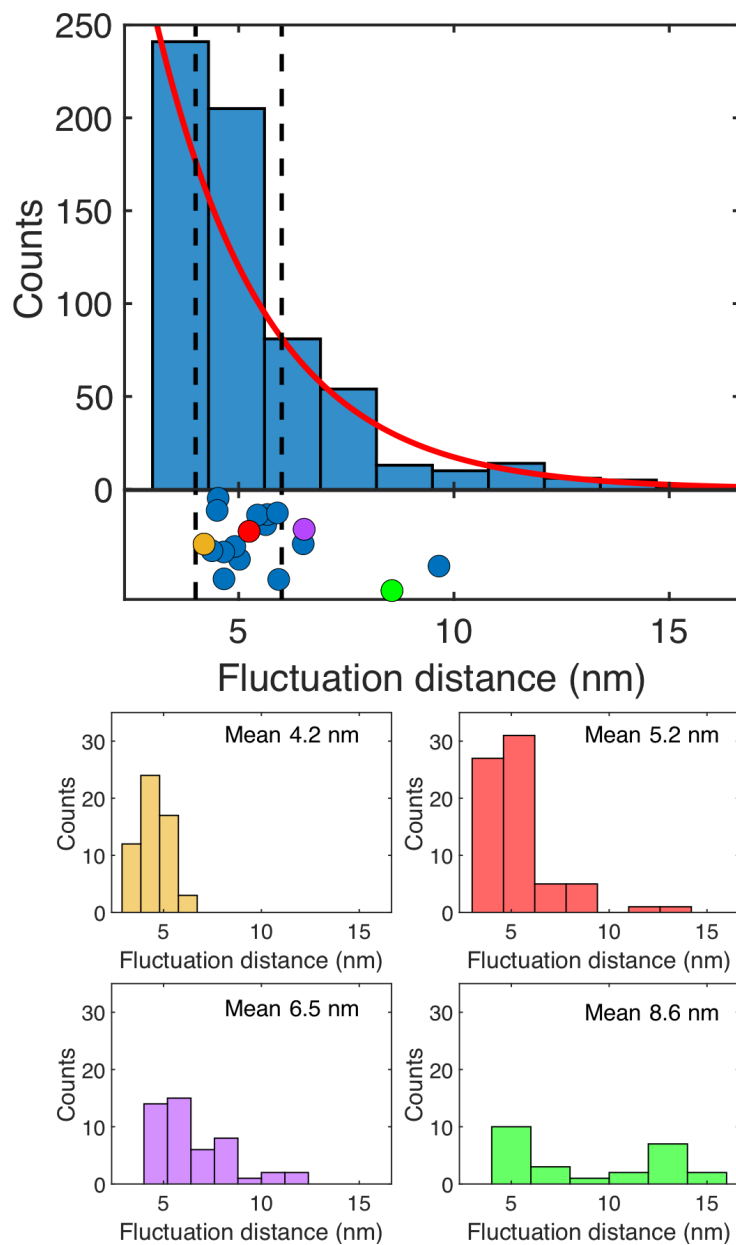


Figure 3.13. Histogram of observed fluctuation distances. distances between gaussian peaks from bimodal, 5-second segments represented by Fig. 4d. We see a range of 2.3 nm to 15 nm in repeated jump sizes with >95% occurring between 2.3 nm and 9 nm. We assume that there are upper and lower limits to the size of folds while under tension. The lower limit, determined by hydrogen bonding along the polymer chain, steric clashes and bending restrictions prevents small folds, while the upper limit is defined by the work required to close a fold under tension, the probability of which will grow exponentially with the size of the fold. *In vivo*, larger folds are certainly possible, as seen from initial pulls on cellulose tethers grown without tension (Fig. 3.10). The scatter plot below shows the mean fluctuation distance of each molecule represented by a single point. Representative distributions for a few points are shown in their corresponding color. A majority (14 of 18) of the molecules have mean fluctuations between 4 and 6 nm, with the range denoted by black dotted lines. The yellow and red molecules are considered for the Bell analysis while still limiting all events to 4-6 nm. The purple and green molecules were excluded. Despite an expected lower limit of fluctuation distances, the distribution appears to be exponential.

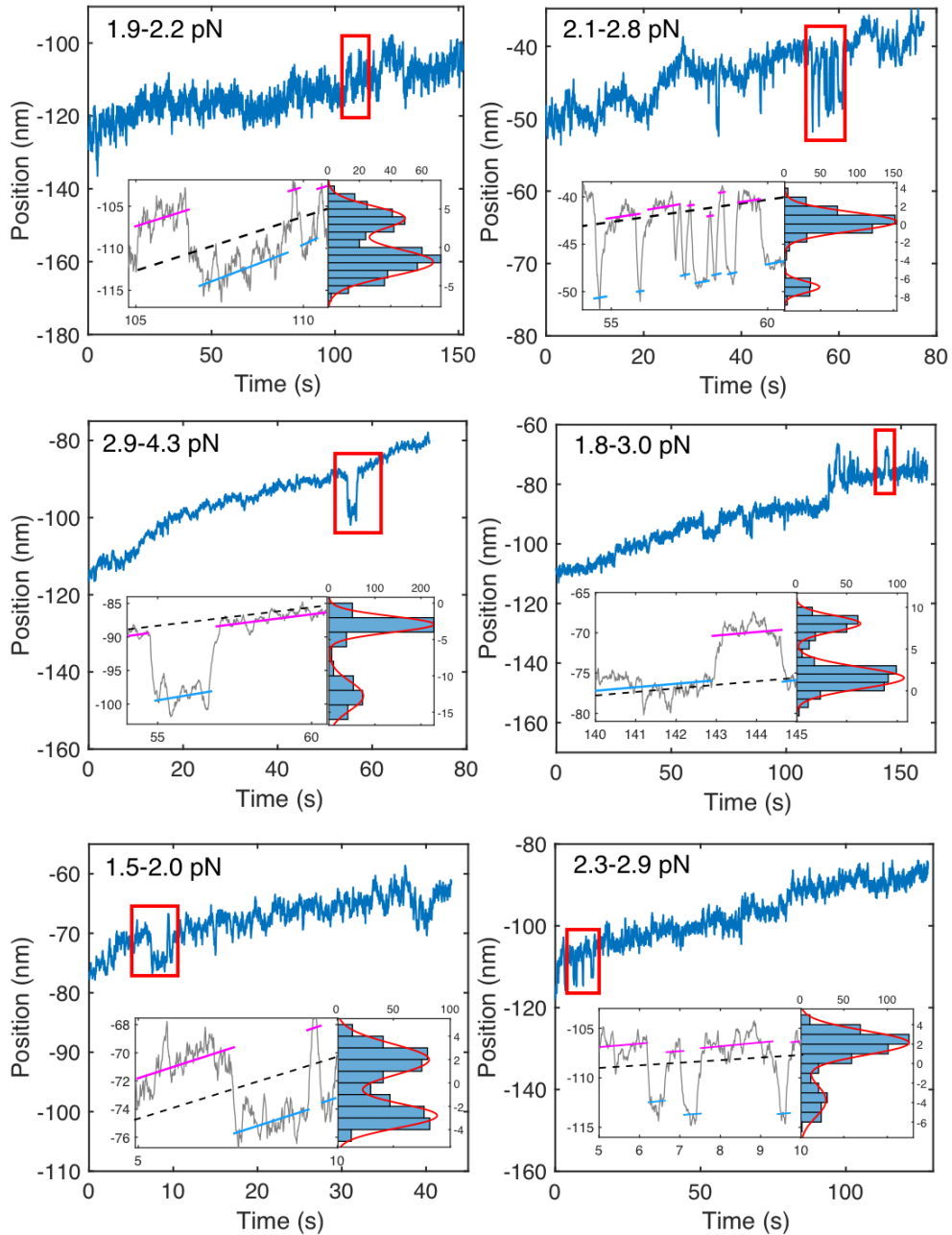


Figure 3.14. Reversible transition analysis example. Example traces with segments containing reversible transitions that were used to measure the lifetimes in both extended and retracted states. The insets show the red boxed portions of the full trace. The black dotted line denotes the mean trajectory while the histogram shows the distance from the mean trajectory, similar to Fig. 3.9d. The histograms show bimodal behavior between an extended state and retracted state. The extended (pink) and retracted (blue) states are outlined in the inset. The lifetimes of each state were measured to find a transition rate between states. A total of 14 traces and 322 events with fluctuation distances between 4-6 nm were considered. We note force ranges for each trace. As cellulose is synthesized, the bead is drawn towards the trap center and the force applied weakens slightly during the trace. The black box around the first six examples denotes no cellohexaose, and the red box around the last two examples indicates the presence of cellohexaose. Rapid transitions also occurred in the presence of cellohexaose, here in the 4-6 pN range. The mean transition size for these particular events was 5.9 nm and the mean rate of transition was 0.8 s^{-1} ($N=110$ events over 2 molecules).

representing >85% of events, were included. The bimodal nature of the traces suggest that the structural changes occur at the same site along the polymer. Given the ~4-5 nm transitions occur at 2-3 pN of tension, the work done during these transitions is ~8-15 pN nm, which is similar to the energy of 1-3 hydrogen bonds (39). Because the size of extensions varied widely with applied force and are larger than glucose or the complex, the extensions and retractions most likely occur when the 'secondary structure' of single-stranded cellulose unfolds or assembles microstructures via "interstrand" hydrogen bonds. One explanation of the observed reversible transitions is that a hairpin-like structure of cellulose is continually opening and reforming. Alternatively, although less likely, the transitions may be a construct of the synthase's conformational changes during synthesis. Unlike the chemical structure of DNA and RNA hairpins with a defined distance between states that behave similarly (40), identical units along the cellulose strand permits varying folding sizes at a great number of folding sites along the strand. Given the distribution seen in cellulose-based, hairpin-like transition distances (Fig. 3.13), estimates from this type of analysis should only be interpreted locally.

The relative straightness or wandering of a trajectory is also an indicator of the underlying kinetics. Fewer rate limiting steps within the catalytic cycle will lead to a more random and less consistent path of synthesis, straying from the mean trajectory. In contrast, more complex schemes including multiple parallel steps, similar rate limiting steps and paths that deviate from the motility cycle can yield a straighter motility trajectory. The rate-limiting steps within the catalytic reaction cycle are the individual chemical reactions or physical motions that determine the amount of time required to initiate, execute, and restart the cyclic biosynthesis progression unique to the processive behavior of BcsAB. An analysis of the randomness, or variance of the bead position from the mean trajectory, reveals how many similar rate limiting steps underlie a motility cycle for a given characteristic step size (41-43). Two randomness parameters, dimensionless values of the fluctuations in polymerization cycle completion times, were calculated using two different, plausible physical step-sizes of biosynthesis (Fig. 3.15). We calculate randomness parameters for each individual molecule to isolate the stochasticity in the catalytic cycle from the heterogeneity in enzyme rates. When using the distance to the transition state along the reaction coordinate, given from the force-velocity fit (Fig. 3.9a), as the step size (4 nm), the mean randomness variable was 0.94 ± 0.12 (SEM, N=50), indicating only one rate limiting step. However, the complex is known to extrude cellulose one glucosyl unit at a time (13). Using the known spacing of one glucose molecule (0.56 nm) (35) yields a mean randomness parameter of 6.75 ± 0.84 (SEM, N=50), compelling a model that includes off-pathway or multiple kinetic schemes (44).

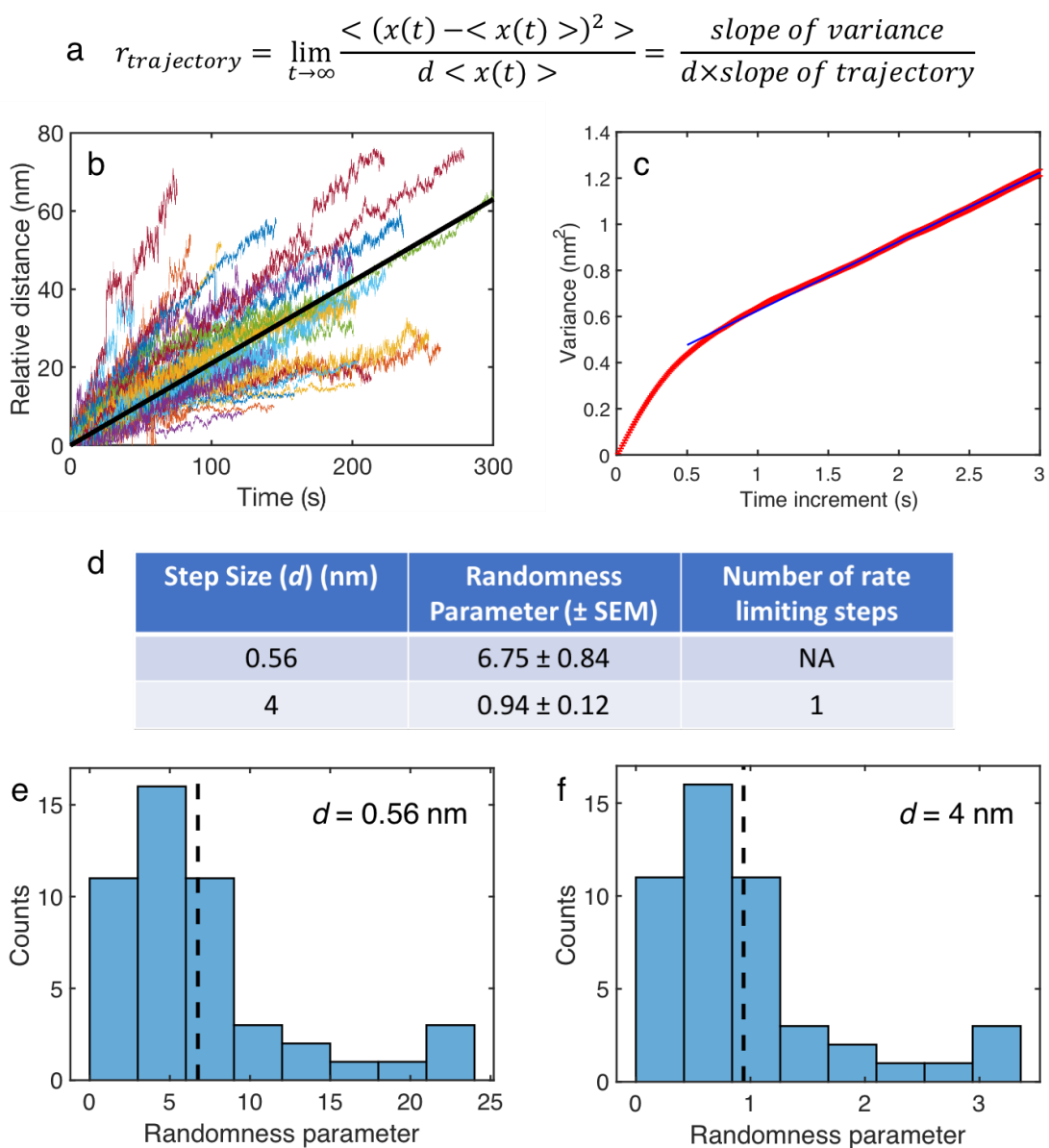


Figure 3.15. Variance analysis. From a collection of motility traces, we calculated the variance from each mean trajectory, and, using the equation in (a), revealed a randomness parameter for each motor sampled ($N=50$). (b) A selection of motility traces in various colors in which each trace's slope of trajectory was used to find its randomness parameter. The black line indicates mean velocity. (c) An example variance calculation of a motility trace over increasing time increments. The slope of variance is used in equation (a) as well as both the monomer size and the distance between transition states from the force-velocity fit as the step size d in equation (a). (d) A step size of one glucose unit (0.56 nm) yields a randomness parameter of 6.75 ± 0.84 (SEM) suggesting a complex off pathway kinetic may underpin motility, while the distance between transition states (4 nm) indicates a randomness parameter of 0.94 ± 0.12 (SEM) representative of one rate limiting step. Histograms of the randomness parameters for step sizes of 0.56 nm (e) and 4 nm (f) show the spread in the variance parameter exhibited by the collection of molecules compared to the mean randomness depicted by a dashed line. Multiple kinetic schemes create higher likelihood of dynamic disorder likely giving rise to the spread between molecules (3).

3.3.6 Cellulose stretching reveals microstructure and elasticity

To investigate the extensions and larger position fluctuations observed in motility measurements and to mechanically characterize the polymer, we created a cellulose stretching assay similar to previously developed stretching assays (45-50). Single-strand cellulose synthesis by BcsAB provides an opportunity to measure the core properties of an isolated polymer. Beads tethered via a single cellulose strand were centered directly over the coverslip attachment point and pulled parallel to the surface. As force is applied, the bead is pulled out of the trap center. Strands were stretched and relaxed repeatedly.

In one set of experiments designed to track strand growth, we applied the cellulose stretching technique at various time points throughout a ~4-minute window of active synthesis to monitor velocity. By analyzing the relative apparent contour length (the tether length mapping to the polymer backbone distance) for each of the stretching time points, we were able to obtain a velocity for direct comparison to the assay that directly monitors tether synthesis (Fig. 3.16). Such stretching measurements, which are nominally at zero load, revealed an average velocity of $0.32 \pm 0.07 \text{ nm s}^{-1}$ (SEM, N=6), consistent with the direct monitoring of contour length under tension. In all stretching experiments, the true extension is determined from the angle of incidence of the tether (51).

In another set of stretching experiments, we allowed a strand to grow and then performed repeated stretching measurements to measure the polymer properties. Our measurements include a range of tether lengths depending on time allowed for synthesis and the productivity of individual synthases. Hysteresis was observed, especially earlier in stretching measurements (Fig 3.17a). In every case, hysteresis vanished after multiple successive stretches, revealing the fundamental state of single-chain cellulose. During stretching measurements, we observed abrupt extensions similar to those from motility traces in 26% of stretched cellulose strands (Fig. 3.17b). Larger extensions appeared earlier in repeated stretching experiments before reaching a tempered state. The extensions were measured by noting the change in contour length in stretching experiments (mean: $18.1 \pm 4.9 \text{ nm}$, SEM, N=22). At forces below 5 pN, retraction/refolding events occurred implying that a folded state may be more favorable, even under light tension. We expect a larger spread in extensions and fewer retraction events from stretching experiments compared to polymer synthesis trajectories, because the applied tension is greater and can catastrophically open multiple extension elements in one event. Both stretching and polymer synthesis traces revealed a large range of transition distances (2-110 nm) suggesting the presence of

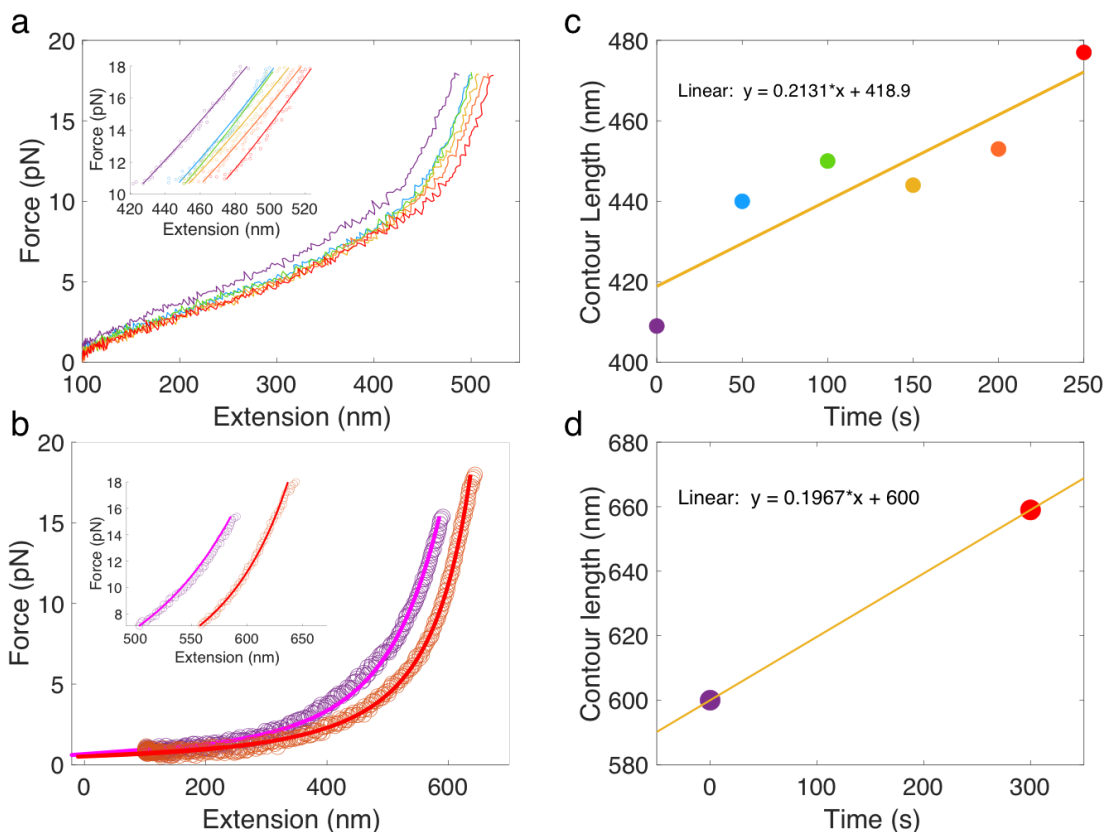


Figure 3.16. Unloaded velocity. We measured the velocity of synthesis using a second method in which we measured the contour length of a growing strand of cellulose over time. As time progresses, the color scheme changes from purple to red. The consecutive stretches seen in (a,b) were fit to the eWLC model, and contour lengths were plot against time (c,d). to extrapolate a velocity. We performed this experiment 6 times revealing an average unloaded velocity of $0.32 \pm 0.07 \text{ nm s}^{-1}$ (SEM), similar to that observed from motility data. For these experiments, measurements are typically performed slightly off the glass surface to prevent nonspecific sticking. This slight pulling up in the z direction will impact the slope of the entropic region of the curve as seen in (a) for the region spanning 100-400nm in contrast to the flatter region seen in (c). The relative flatness of the entropic region does not impact the ability to determine a change in apparent contour length which depends on the steeper rise location towards the end of each stretching curve.

inhomogeneous microstructure due to cellulose folding back on itself. Models of expected microstructures, such as overhang folds or hairpins, giving rise to extensions, retractions or hopping are shown in Fig. 3.17c.

After repeated stretching on a single chain, cellulose resembled classical tethered polymer profiles with a low force region typical of entropic configuration rearrangement and a higher force region typical of enthalpic polymer stretching. This shape is consistent with models where the persistence length (the distance the polymer points in the same direction) is smaller than the contour length (45, 48, 50, 52). The resulting force vs extension plots were fit to the extendible

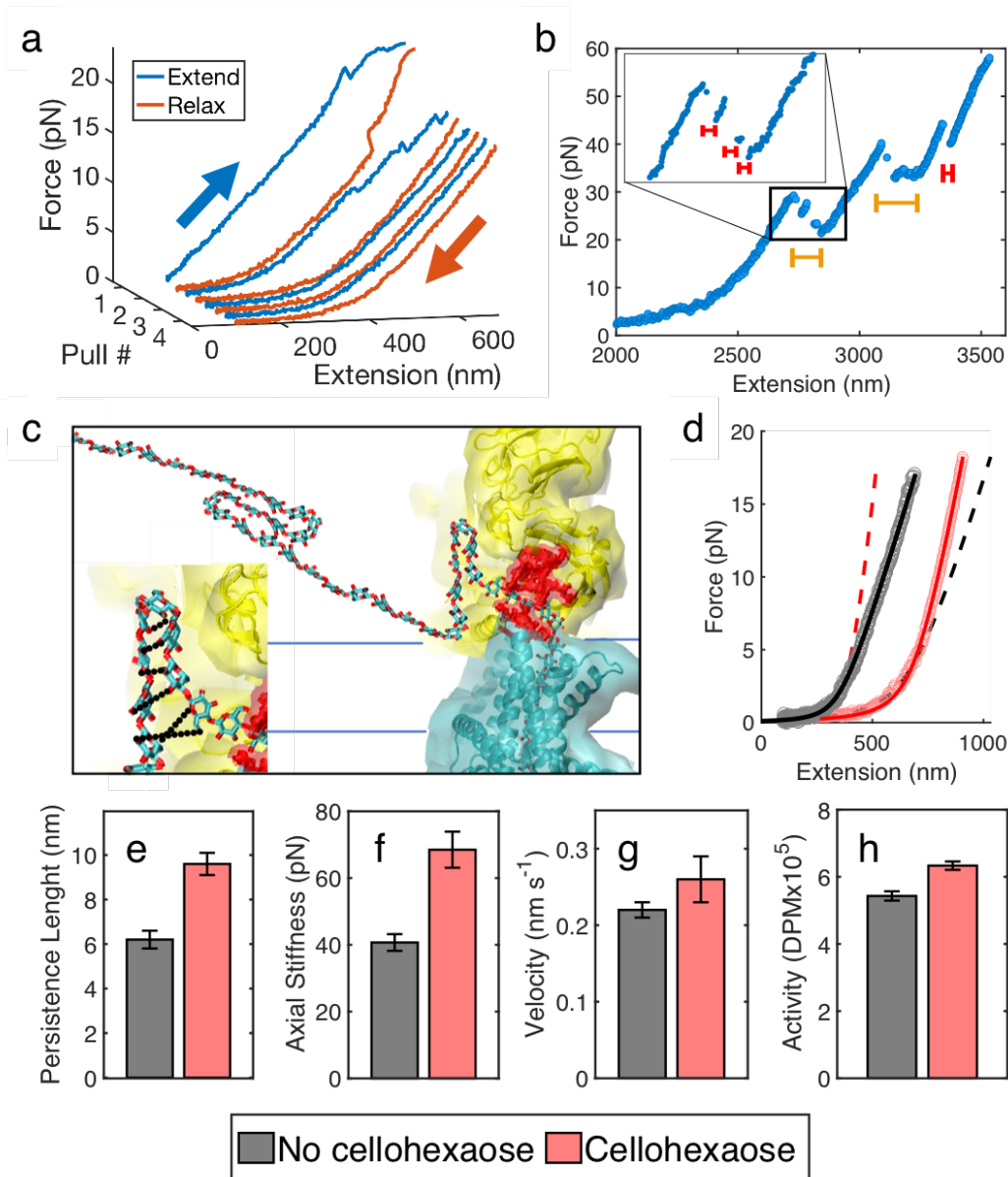


Figure 3.17. Single cellulose strand stretching and effects of cellohexaose hybridization. (a) At the beginning of consecutive stretches, 26% of cellulose strands exhibit hysteresis until microstructures are unfurled and cellulose reaches a fundamental state. (b) During stretching, cellulose undergoes sudden elongations of random distances between regions of stability. Within larger events (yellow bars) exist smaller jumps (red bars, inset). The change in extension is likely due to the unfolding of microstructures. (c) Cellulose product likely forms hairpins or other secondary microstructures upon or after extrusion from the complex. BcsA is shown in cyan, BcsB is shown in yellow and the residues comprising the complex's exit pore are shown in red. Formation of secondary structure through hydrogen bonding (inset, black dotted lines) between strand segments may also assist with translocating cellulose through the synthase. (d) Single cellulose chain follows the extendible WLC model after being fully extended (grey points and black fit). Experiments with cellohexaose (pink points and red fit) show a larger persistence length and axial stiffness. The dashed lines are theoretical fits using the same contour length of each respective data curve but the persistence length and axial stiffness of the opposite condition, with or without cellohexaose. The juxtaposition highlights the change in axial stiffness caused by cellohexaose hybridization. Bar graphs display the increase in (e) persistence length, (f) axial stiffness, (g) single-molecule synthesis velocity, and (h) bulk BcsAB overnight activity in the presence of cellohexaose.

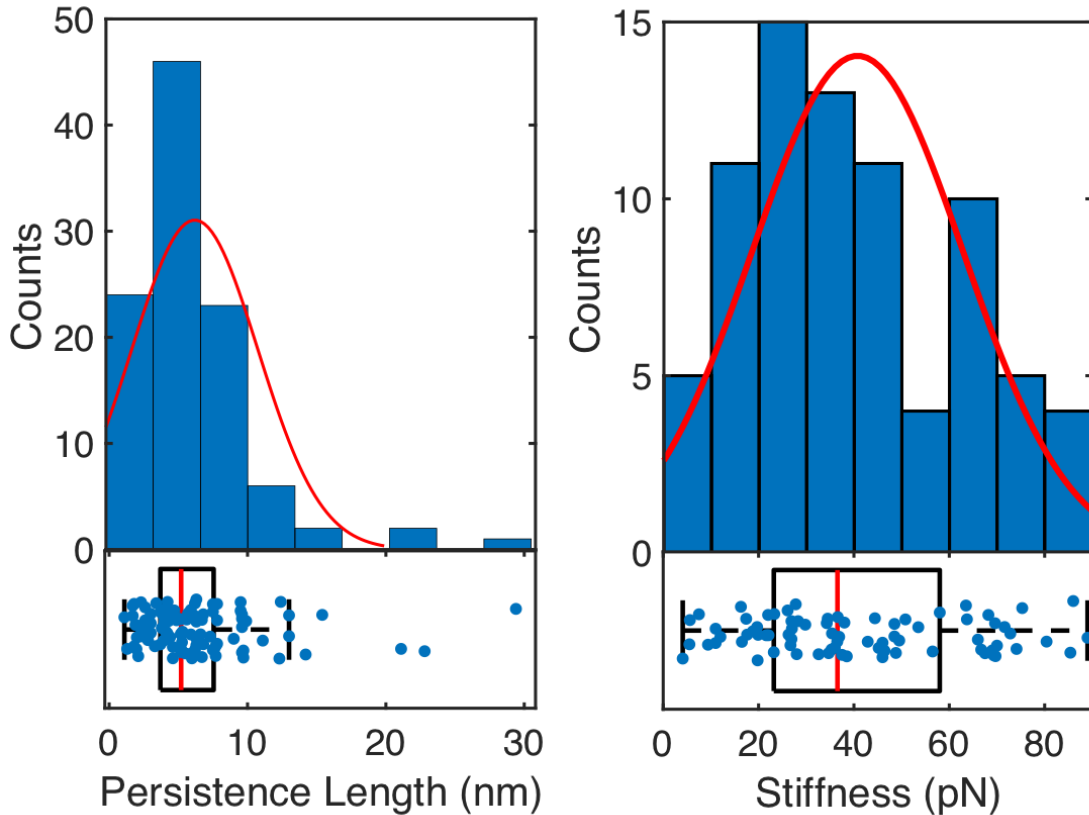


Figure 3.18. Persistence length and axial stiffness. Above are histograms of the persistence length and stiffness measured from cellulose stretching experiments, and below are boxplots showing distributions. Observed persistence lengths converge to gaussian behavior and reveal a mean persistence length of 6.2 ± 0.4 nm (SEM, N=104). Stiffnesses have a much wider distribution, but still exhibit gaussian behavior. The average stiffness was 40.7 ± 2.5 pN (SEM N=78). The contour length of the strand had no effect on the measured stiffness. The range is possibly due to irregularities in cellulose microstructure.

worm-like chain (eWLC) model first proposed by Odijk, 1995, which includes an elasticity stiffness term for the enthalpic region (Fig. 3.17d) (52). Single cellulose chains displayed a persistence length of 6.2 ± 0.4 nm (SEM, N=104) and an elasticity stiffness of 40.7 ± 2.5 pN (SEM N=78) (Fig. 3.18).

Metric	Motility buffer without additives	Cellotetraose (5mM)	Cellotetraose (50 mM)	Cellohexaose (0.45 mM)
Persistence Length (nm \pm SEM)	6.2 \pm 0.4 N = 104	5.6 \pm 0.4 N = 57	9.5 \pm 0.4 N = 113	9.6 \pm 0.5 N = 134
Axial Stiffness (pN \pm SEM)	40.7 \pm 2.5 N = 78	44.1 \pm 3.0 N = 53	60.9 \pm 3.8 N = 107	68.5 \pm 5.4 N = 134
% motility traces w/ microstructure	49%	40%	45%	84%
Mean number of structure events per trace	1.5	1.4	1.14	5.1
Mean extension (retraction) size (nm \pm SEM)	10.6 \pm 1.9 N = 73 (4.6 \pm 0.7) N = 26	-	-	13.5 \pm 1.0 N = 196 (6.6 \pm 0.3) N = 63
% stretches w/ microstructure	26%	40%	69%	94%
Mean number of structure events per stretch	0.45	0.36	0.38	1.1
Velocity (nm s ⁻¹ \pm SEM)	0.22 \pm 0.01 N = 176	0.19 \pm 0.3 N = 20	0.19 \pm 0.2 N = 24	0.26 \pm 0.3 N = 45

Table 3.2. Comparison of various properties of both BcsAB and cellulose in the presence and absence of cello-oligosaccharides of different lengths. Comparison of various properties of both BcsAB and cellulose in the presence and absence of cello-oligosaccharides of different lengths. The mean number of events per trace/stretch represents the total number of events divided by the total number of traces/stretches. Mechanical properties appear unchanged in the presence 5 mM of cellotetraose. The high solubility of cellotetraose may weaken its association to cellulose compared to more hydrophobic oligosaccharides or other cellulose strands. At high concentrations (50 mM) of cellotetraose, cellulose becomes straighter and stiffer with an increase in persistence length and axial stiffness, indicating spontaneous hybridization. The concentration dependence suggests an association/dissociation constant on the order of 10 mM. Cellohexaose, near saturating conditions, was able to hybridize at a much lower concentration. The increase in mechanical properties of cellulose in the presence of cellohexaose is comparable to those seen from introducing cellotetraose. Cellohexaose's greater hydrophobicity likely decreases the association/dissociation constant and encourages binding to cellulose. Hydrophobic cello-oligosaccharides hybridizing to cellulose surprisingly increase both the frequency and size of microstructure folding/unfolding events, with the greatest increase occurring in the presence of cellohexaose. The microstructure results suggest an intense propensity for cellulose to self-associate. Motility experiments revealed an increase in velocity in the presence of cellohexaose and no change or a small decrease in productivity in the presence of cellotetraose. Seeing as cellohexaose readily hybridizes to cellulose, while cellotetraose requires much larger concentrations to achieve similar results, hydrophobic interactions likely play a role in cellulose self-association and contribute to the cellulose synthesis process in BcsAB.

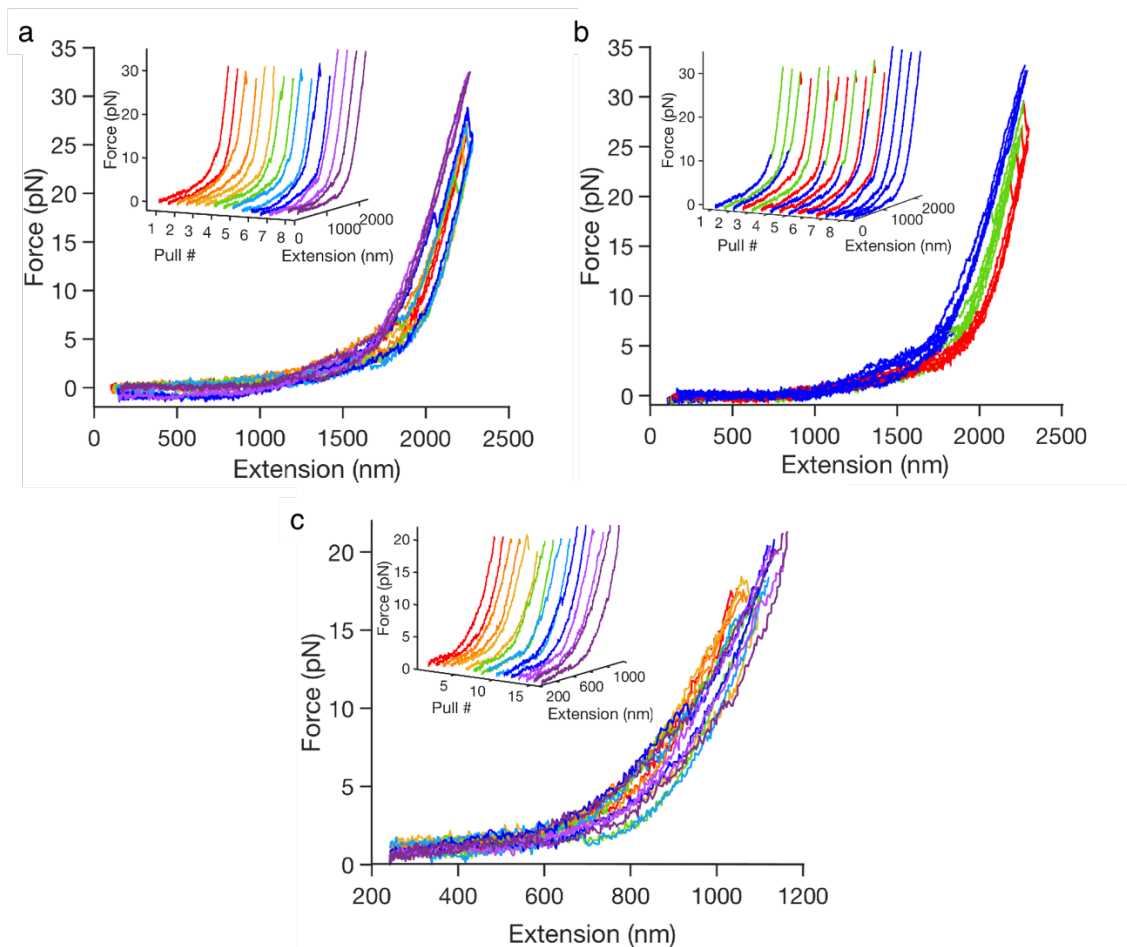


Figure 3.19. Cellulose stretching hysteresis with cellohexaose. Subsequent stretching of cellulose in the presence of 0.45 mM cellohexaose revealed multiple refolding events, preventing the generation of a stable tempered state, even under force. All figures show a side view overlapping sequential cellulose-cellohexaose hybrid stretching curves, while the insets display a diagonal view to better track the relative pull sequence of each individual curve. (a) Repeated cellulose stretching curves are shown to progress in time from red to purple. In this example, the final four curves displayed stable states with shorter contour lengths, indicating cellulose-cellohexaose hybrid microstructure is secure even under 30 pN of force. This behavior is absent in isolated single cellulose strands (Fig 5a). (b) State-based rendering of the same cellulose-cellohexaose hybrid as in (a) appears to follow three local minima, evident by the blue, green, and red force-extension pathways. Designation of specific states is unique to the specific hybrid strand and varies between strands. The hybrid strand in (c) shows a great number of possible states and frequent transitions between them. Each hybrid strand exhibited the ability to adopt smaller apparent contour lengths and more compact configurations under considerable force, further highlighting the predisposition for self-binding within the strand. Additionally, the probability at which microstructure reforms between stretches appears much greater with cellohexaose present than without, indicating a larger than expected propensity to form microstructure.

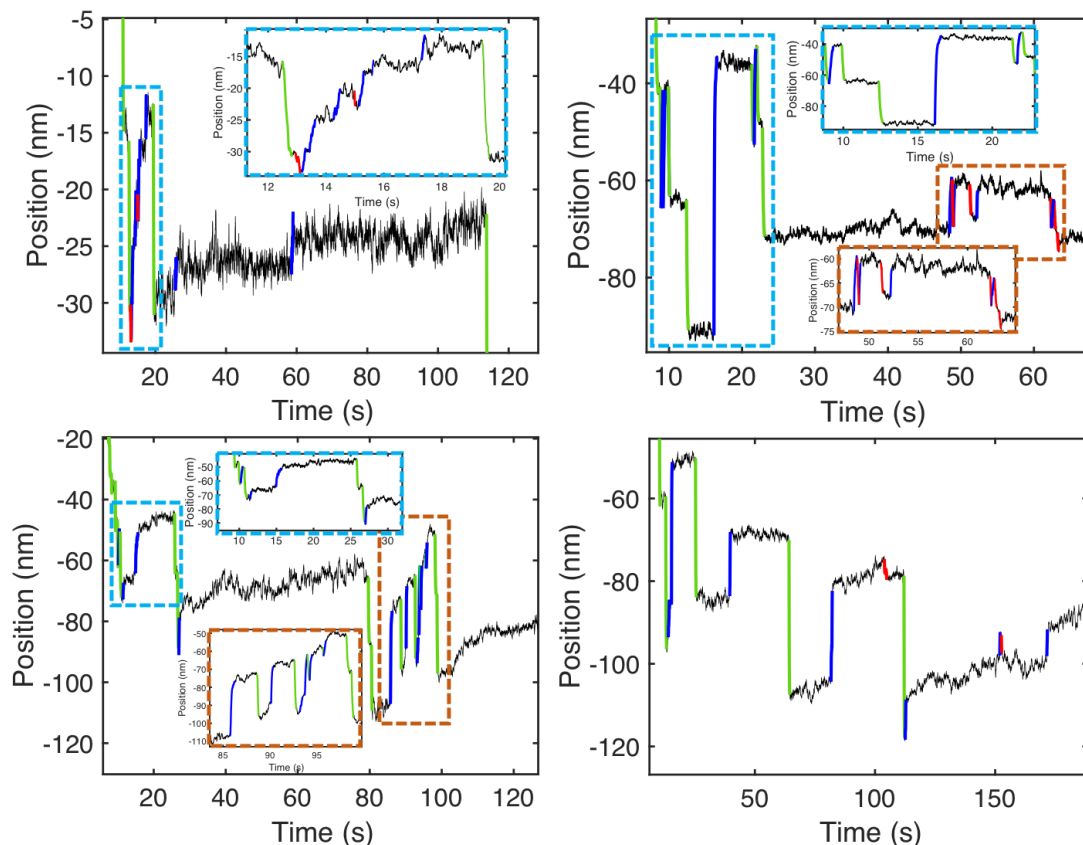


Figure 3.20. Cellohexaose and microstructure. Cellohexaose and microstructure. Example traces of cellulose biosynthesis in the presence of 0.45 mM cellohexaose show numerous microstructure unfolding or folding events. Stage translations are represented in green, extension events are blue, and retractions are shown in red. Cyan and orange insets display zoomed images of their respective boxed regions. In general, there were approximately three times as many microstructure events per trace in the presence of cellohexaose than in its absence (*SI Appendix* Fig. S6), further highlighting cellulose’s propensity to self-associate. All data presented were recorded in the 2-8 pN range.

3.3.6 Cello-oligosaccharides bind nascent cellulose strands and increase activity.

With the observation of microstructure formation through self-association, we added cello-oligosaccharides to solution to investigate their ability to bind cellulose and influence strand synthesis and mechanical properties. Here, we investigated two partially soluble cello-oligosaccharides, cellotetraose and cellohexaose. In the presence of 5mM cellotetraose, we observed no significant change in mechanical parameters (Table 3.2). However, at 50 mM cellotetraose, both cellulose’s persistence length and axial stiffness increased to 9.5 ± 0.4 nm (SEM, N=113, Table 3.2) and 60.9 ± 3.8 pN (SEM, 107, Table 3.2). Similar changes to strand

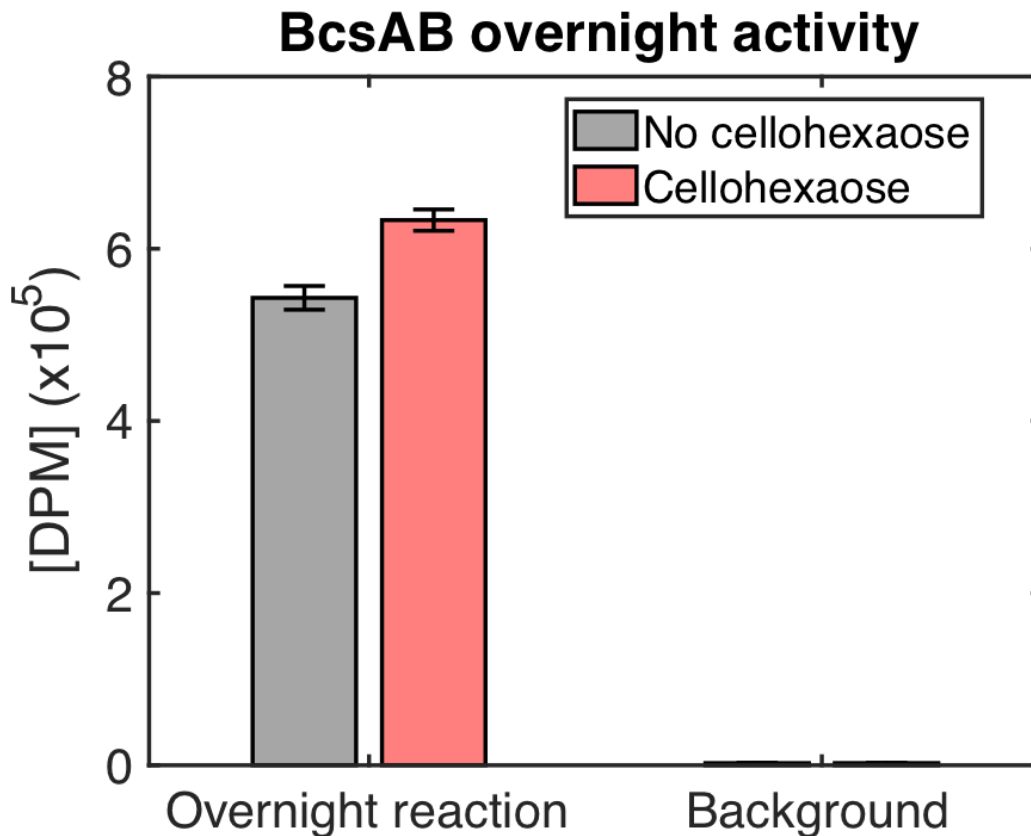


Figure 3.21. BcsAB bulk activity with cellohexaose. BcsAB bulk overnight activity with cellohexaose. Overnight activity experiments of detergent solubilized BcsAB in the presence and absence of 0.45 mM cellohexaose. There was a significant increase in the amount of cellulose biosynthesized by BcsAB with cellohexaose present as opposed to without, indicating that hybridization aids in the catalytic reaction of cellulose elongation. Free-floating cellohexaose and extended single-strand cellulose are likely at higher energy states than when hydrophobic faces can stabilize through cellulose self-association. The energy of hybridization would then contribute to overcoming the activation energy of glucose addition. The background measurements contained no BcsAB.

properties were observed in the presence of 0.45 mM cellohexaose yielding a persistence length of 9.6 ± 0.5 nm (SEM, N=134, Figs 3.17d-3.17e, Table 3.2) and an increase in axial stiffness to 68.5 ± 5.4 (SEM, N=134, Figs 3.17d-3.17f, Table 3.2). The increase in persistence length and mechanical resistance to tension indicates that the cello-oligosaccharides bind and alter the mechanical properties of the nascent cellulose strand.

Microstructure formation was also impacted through hybridization of cellotetraose and cellohexaose. In cellulose-cello-oligo stretching experiments with cellohexaose, microstructure appeared in 94% of traces compared to in 26% without cello-oligos (Table 3.2). In fact, cellohexaose appeared to cause frequent refolding between subsequent stretches, preventing ultimate formation of a final, homogeneous tempered state (Fig. 3.19). Note that single cellulose strands not in the presence of cello-oligos will persist in this final state for a period of time, even if

they are not under tension (Fig. 3.17a). Microstructure also appeared in 84% of motility experiment traces with cellohexaose compared to 49% without. Example traces are displayed in Fig. 3.20. The mean extension and retraction event sizes observed in motility traces increased from 10.6 ± 1.9 nm and 4.6 ± 0.7 nm, respectively, to 13.5 ± 1.0 nm (SEM, N=196) and 6.6 ± 0.3 (SEM, N=63), respectively, in the presence of cellohexaose (Fig. 3.9b, and Table 3.2). There is also a clear non-zero maximum in the distribution of microstructure size (Fig. 3.9b). We also observed rapid position fluctuations in the 4-6 pN range (Fig. 3.14). Cellohexaose increased the frequency and size of cellulose microstructure.

Notably, motility experiments in the presence of cellohexaose also revealed an increase in mean biosynthesis velocity to 0.26 ± 0.3 nm s⁻¹ (SEM, N=45) from 0.22 ± 0.2 nm s⁻¹ (Fig. 3.17g, Table 3.2). Consistent with our single molecule experiments, bulk activity assays of BcsAB in the presence of cellohexaose showed slightly increased cellulose synthesis as well (Fig. 3.17h, Fig. 3.21). In bulk assays, cellulose polymers produced by different BcsAB complexes may already interact, thereby mimicking the effect observed for cellohexaose in single molecule assays. Thus, binding of hydrophobic cello-oligos to the cellulose product not only impacts mechanical properties but increases BcsAB's productivity.

3.4 Discussion

Optical tweezer records provide insight into force dependence of synthesis and the ability to directly track the progress in real time. Below an assisting load of ~13 pN, BcsAB was relatively immune to force (Fig. 4a). However, above ~13 pN of tension, slowing or stalling occurred. Curiously, cellulose stretching measurements show that BcsAB maintains a tight grip to cellulose, as up to 100 pN of pulling force failed to dislodge the strand from the synthase's grip. This suggests that cellulose is unlikely to diffuse spontaneously from the synthase. Currently, the glucan channel of BcsA is thought to bind weakly, if at all, to the growing strand, facilitating translocation (9). Only the acceptor-binding site at the transmembrane pore's entrance has been suggested to contribute any grip and prevent backsliding (11). The observed strong binding and stall force may be a result of protein or product deformation disrupting the lubricating CH- π interactions and hydrogen bonding between the protein and cellulose (9). In a physiological setting, shearing forces or tension from increased cellulose interactions in the extracellular space can be greater than 13 pN and may stall biosynthesis, allowing for cleavage through hydrolysis and preventing unproductive cellulose production.

Fits to a Boltzmann energy barrier model (Fig. 3.9a) yielded a characteristic distance to the transition state associated with a mechanical transition of 4 nm, roughly corresponding to the length of BcsA's transmembrane channel (~4 nm), a length scale of ~7 glucose molecules, or ~27% of the length of the BcsAB complex (15 nm) (14). Another length scale of 5.0 nm was extracted from positional hopping seen in some motility traces under an apparent critical force of ~2-3 pN (Fig. 3.9d). Such motion may originate from conformational changes in the machinery itself. A more likely possibility, however, is that hopping arises from changes to the product strand length during growth, such as a segment repeatedly folding back on itself and unfolding. While we use the Bell relationship to characterize the apparent two-state fluctuations (Fig. 3.9f), we note that, unlike defined transitions in nucleotide-based hairpins, cellulose folding inherently accommodates a distribution of states and structures and analysis of such should be interpreted locally. Additionally, abrupt extensions and retractions appear to be exponentially distributed in length (Fig. 3.9b, top) with fit parameters of 5.6 nm and 4 nm, respectively, suggesting a similar length scale is associated with a probability of forming such structures. In the presence of cellohexaose, the probability of forming structures increases as well as the length scale of such structures.

The relative straightness of motility records was striking. Variance analysis is a method that relates the relative wandering of a record to constraints on kinetic models consistent with this motility profile. Here, one needs to assume a length scale associated with forward progress of a motility cycle. Assuming a length scale associated with the glucose repeat unit, 0.56 nm (35), variance analysis predicts the off-path (exiting the motility cycle and then returning) or multiple kinetic schemes for the biosynthesis cycle (44). However, if one assumes a length scale consistent with the Boltzmann fit and conformational change, ~4-5 nm, a single rate limiting step within the motility cycle is sufficient. Congruence between models is possible with a base unit of biosynthesis and single cellulose structure to be a 7-glucose segment, given that 7 glucose bond additions per cycle results in a 4-nm increase of cellulose synthesis.

With a one-step kinetic cycle size of 4 nm, a distance to the transition state of 4 nm (Fig. 3.9a), an exponential fit length of 5.6 nm from the distribution of extensions (Fig. 3.9b), a hopping distance of 5.0 nm (Fig. 3.9d), and a persistence length of 6.2 nm (Fig. 3.17d), BcsAB appears to operate based on a unit length standard of 4-6 nm. The energetics of the polymerization cycle or the resulting cellulose structure upon extrusion may dictate this length scale.

One requirement of processive synthesis is transport. Other polymerases that have been measured at the single-molecule level, which include RNAP (53), DNAP (54), and the ribosome (55), utilize templates in their motility cycle and have the ability to interpret instructions for initiation, termination etc. The temperature study revealed an activation energy of 32.5 k_bT (80.5 kJ mol^{-1} ,

Fig. 3.2), of which glycosidic bond formation comprises 5 $k_B T$ (12.5 kJ mol^{-1}) (37). Interestingly, the energy available from UDP-glucose (17.4 $k_B T$ or 43.0 kJ mol^{-1}) only supplies about half of the needed energy (56), which implies that two glucose additions may underly a cycle. Substrate-induced conformational changes at the enzyme's catalytic pocket have been shown to be essential for polymer translocation (13). In addition, strand folding or cellulose-cellulose association likely helps drive transport of the newly synthesized strand, as evident by the increase in both bulk activity and single-molecule velocity of BcsAB in the presence of celohexaose (Fig. 3.17g-3.17h). These interactions may also facilitate cellulose alignment and microfibril formation in plants and other bacterial species (57). Energetically each hydrogen bond represents $\sim 1.6 k_B T$ (4 kJ mol^{-1} or 6.6 pN nm) (39). Conformational hopping observed in our experiments represent an exchange of work of ~ 10 pN nm which represents approximately 1-2 hydrogen bonds. While energetically one must consider contributions from all bonds forming and breaking during a strand extension cycle, including contributions from solvation, the addition of 2-4 hydrogen bonds appears to be available to help drive transport of the nascent strand, especially through organization of cellulose microstructure. Because of this, bacterial cellulose synthesis may be encouraged in proximity to existing extracellular cellulose bundles.

Cellulose biosynthesis is dictated by the biochemical components available to BcsAB. Our studies directly test such biochemical elements' impact on synthesis. Synthesis proceeds by addition of one glucose unit (13). Without the substrate, synthesis was halted as expected (Fig. 3.3a). Many glycosyltransferases are dependent on metal ion complexes to coordinate with UDP-glc and catalyze the reaction (13, 58). In our Mg^{2+} chelating experiments, motility slowed dramatically yet some minimal synthesis appears to proceed (Fig. 3.3c). One explanation is that that coordination is not absolutely necessary, and some minimal synthesis is possible without Mg^{2+} . However, it is also possible that our chelation experiments may have not completely removed Mg^{2+} from UDP-glc coordination.

It is well known that c-d-GMP is necessary for activating synthesis (9-11, 59, 60). BcsA recognizes an intercalated c-d-GMP dimer with most of the interactions mediated by one nucleotide (11). Our studies suggest at least one c-d-GMP molecule maintains an incredible affinity towards BcsA. The population of the remaining fluorescent c-d-GMPf are consistent with a bond lifetime of 82.5 min and dissociation rate of $2.0 \times 10^{-4} \text{ s}^{-1}$ (Fig 3.4e). Note, this is a lower bound due to potential photobleaching. Our studies were performed at dilute c-d-GMPf, 300 nM, where a shorter lifetime state might have been missed. In some cases, we did record traces where two molecules were bound to the same BcsA (Fig. 3.7). Other groups have predicted much lower binding affinity, including c-d-GMP to BcsAB ($K_A = 1.8 \mu\text{M}$) (10), to the bacterial ATPase MshE ($K_A = 0.5 \mu\text{M}$) (61) and

to a mixture of bacterial c-d-GMP binding proteins ($K_A=7 \mu\text{M}$) (62), but all were calculated from enzyme kinetics of bulk cellulose production, isothermal titration calorimetry, or pull-down assays, respectively. To calculate a K_A for comparison, we can assume the k_{on} is dictated by diffusion (estimated to be $10^6\text{-}10^8 \text{ M}^{-1}\text{s}^{-1}$) yielding a K_A in the range of 2 pM to 200 pM (63). If we assume the binding rate is similar to that of ATP to kinesin ($2 \times 10^7 \text{ M}^{-1}\text{s}^{-1}$) or myosin ($10^4 \text{ M}^{-1}\text{s}^{-1}$), we calculate K_{AS} of 10 pM and 20 nM respectively (64). However, ligand-receptor interactions that require conformational rearrangement have on-rates closer to $10^2\text{-}10^4 \text{ M}^{-1}\text{s}^{-1}$ (63), yielding K_A in the range of 20 nM to 2 μM , well within the range of reported K_{AS} . BcsAB undergoes large conformational changes with the aid of c-d-GMP, so it is within reason to suspect that a certain conformation is required for binding (11). Maintaining a specific K_A relative to other PilZ proteins is important for cell function (65). Additionally, temperature may also affect the binding kinetics of c-d-GMP to various proteins. *In vivo*, enzymatic degradation of c-di-GMP may contribute to release of c-d-GMP from BcsA and thus termination of cellulose biosynthesis (66).

Cellulose stretching experiments provide physical properties of the polysaccharide. The persistence length determined here was ~ 6 nm (on the same length scale as the Boltzmann distance, transition distance, and extensions). This value is larger compared to other single-strand folding or clumping polymers, such as a polypeptide strand (0.4-0.6 nm) (67, 68), ssRNA (0.91 nm) (69), ssDNA (0.7-1.2 nm) (70) or polynorbornene (0.71 nm) (49). However, these values are much smaller than those seen in other ordered thicker polymers such as dsDNA (47 nm) (46), dsRNA (62 nm) (71) and amyloid fibers (1.5 μm) (47). Hydrogen bonding between adjacent glucose elements of the cellulose polymer is likely preventing swivel resulting in a larger persistence length than similar polymers. Hysteresis was seen early on in stretching experiments with large opening distances (Fig. 3.17). Abrupt changes in position during motility traces suggest microstructures are present along the nascent polymer chain (Fig 3.9b). We suspect single-strand cellulose is engaging in intrastrand hydrogen bonding and hydrophobic interactions creating switchbacks and tangles, similar to microstructures observed in polynorbornene and tropocollagen (23, 49, 72). One may expect cellulose to readily form crystal-like structures if produced near other microfibrils, as seen in AFM studies (73). The non-uniformity in size of extensions and retractions is attributed to the homogeneity in celluloses chemical composition. The extensions and retractions are not confined to a single length, location or pairing registration. Cellulose retains some memory for how the chain was originally associated, as refolds are commonly the same size as the previous unfolding events. Eventually, repeat stretching physically tempers the strand resulting in smooth, consistent physical properties (Fig 3.17). At this point, cellulose maintains a very low axial stiffness (~ 40 pN) compared to other biomolecules (ssRNA: 1600 pN (69); ssDNA: ~ 700 pN (70); dsDNA: ~ 1100 pN (46)). When

cellohexaose binds, the resulting structure may include loops or other parallel structured regions that simply act as springs in parallel compared to the native chain. Assuming the whole contour contains parallel springs, this model suggests a limit to the equivalent spring constant $K_{eq} = K_1 + K_2$ of ~80 pN (40 pN +40 pN) for the hybrid strand. While this is greater than our measured stiffness of 68.5 pN, the measured strands likely contains segments where only one strand is present to sustains the load.

Cellulose produced by cellulose synthase complexes in plants (and some bacterial species) forms crystalline microfibrils containing multiple aligned cellulose polymers (74, 75). These microfibrils are unlikely to fold or exist in an entangled state. In contrast, our studies show that single-chain cellulose produced from individual BcsAB complexes appears compliant and amorphous and can actually fold on itself during strand synthesis. Previous TEM images of isolated cellulose synthases from *G. hansenii* show no microfibril formation (32) despite successfully imaging microfibrils from isolated plant cellulose synthase rosettes (33), suggesting isolated bacterial cellulose synthases are unable to form microfibrils alone. Only high concentrations of surface-immobilized BcsAB synthases produce non-physiological cellulose-2 fibers (73). Such elasticity and tendency to clump may play a crucial role in maintaining the biofilm's gel-like structure and could also be critical for the coalescence of individual cellulose polymers into microfibrils. In biofilms of uropathogenic *Escherichia coli*, amorphous and chemically-modified cellulose acts as a mortar-like scaffold that maintains amyloid curli association and greatly increases bacterial adhesion strength to bladder cell surfaces (76). Higher-order cellulose production could jeopardize the biofilm's structural, cohesive-adhesive, and protective qualities (19).

Our reported cellulose biosynthesis rates are slower than expected from bulk measurements in the literature, which includes a large range of reported rates (1.5-9 nm s⁻¹) (32-34). While these measurements often do not determine the concentration of catalytically active enzyme for accurate rate measurements, our room temperature conditions (21°C) were lower than those of other investigations of cellulose production (25°C, 30°C and 37°C). The single-molecule experiments eliminate the availability of nearby cellulose microfibrils from assisting synthases, to which the extruded cellulose strand can hydrogen bond. The lack of available hydrogen bonds to assist with transport may also hinder synthesis rates. Additionally, other cellulose synthase subunits, such as BcsC and BcsD, are excluded from single-molecule experiments and are thought to play a crucial role in transport (9, 32). With the ability of cellulose to fold upon extrusion, shortening the apparent tether length during elongation, our apparent velocities represent the lower bound of possible biosynthesis rates. These, together with enzyme tethering, could explain the apparent slower synthesis rates observed (10, 33).

One key differentiation between BcsAB and cellulose synthases found in land plants is that the plant enzymes multimerize in a six-fold symmetry supramolecular cellulose synthase complex (CSC) that is thought to produce an 18-strand microfibril immediately after synthesis (3, 59). Multimers likely exploit cellulose's propensity to self-associate into microfibrils to form the load-bearing component of plant cell walls, while *E. coli*, for example, modifies cellulose polymers with lipid-derived phosphoethanolamine (77). The different cellulose biosynthetic machineries indicate evolutionary adaptations between the kingdoms to suit each one's needs. Our studies provide the first insights into the physico-chemical properties of individual cellulose polymers underlying a plethora of biological functions. The presented assay offers a foundation for future single-molecule studies on polysaccharide synthases, including trimer bacterial cellulose synthases and plant CSCs, for which their products and functions are extraordinarily different (3, 74).

3.5 Materials and Methods

3.5.1 Materials

Bovine Serum Albumin (EMD Millipore – 12657), Casein (Sigma – C7078), biotinylated anti-his antibody (Qiagen - 34440), streptavidin (EMD Millipore – 189730), cyclic-di-GMP (BioLog – C057-01), UDP-glucose (Sigma – U4625), ³H-labelled UDP-glc (PerkinElmer NET1163250UC), MgCl₂ (Mallinckrodt – 5958), cellobiose (Acros Organics – 108460250), glycerol (Sigma – G7893), 1.09 mm streptavidin-coated polystyrene beads (Spherotech – SVP-10-5), 0.75 mm polystyrene beads (Spherotech – PP-08-10), biotinylated cellulose-binding DNA aptamer (IDT 5'-biotin/GCG GGG TTG GGC GGG TGG GTT CGC TTG GCA GGG GGC GAG TG-3'), Amine terminated cellulose-binding DNA aptamer (IDT 5'-Am/ GCG GGG TTG GGC GGG TGG GTT CGC TTG GCA GGG GGC GAG TG-3'), PBS (1x pH 7.4), Tris-HCl buffer (RPI – 1185-53-1, 20 mM pH 7.0), purified bacterial cellulose synthase BcsAB complexes reconstituted into nanodiscs, NaH₂PO₄ (Mallinckrodt – 7892), NaCl (Sigma – S7653), deionized water, EDTA (Sigma E6758), biotin-3500 bp DNA-digoxigenin (78), protein G-coated 1.09 mm polystyrene beads (Spherotech – PGP-08-5), anti-digoxigenin, KH₂PO₄ (Mallinckrodt – 7100), Na₂HPO₄ (Mallinckrodt – 7917), DY 547-cyclic-di-GMP (BioLog – D116), mPEG-silane MW 5,000 (Laysan Bio), biotin-PEG silane MW 5,000 (Laysan Bio), KOH (Fisher Chemical), β-D-glucose (Calbiochem – 34635), glucose oxidase from *Aspergillus niger* (Sigma – G2133), catalase from bovine liver (Sigma – C100), Trolox (6-hydroxy-2,5,7,8-tetramethylchroman-2-carboxylic acid) (Sigma – 238813), cellohexaose

(Megazyme – O-CHE), cellotetraose (Megazyme – O-CTE-50MG).

3.5.2 BcsAB expression and purification

The *Rhodobacter sphaeroides* 2.4.1 BcsAB complex was expressed and purified as described. (14) The purified complex was reconstituted into *E. coli* total lipid nanodiscs using the MSP1D1 scaffold protein, as recently described for related enzymes (79). In short, dried *E. coli* total lipid film was solubilized at a final concentration of 25 mM in buffer containing 20 mM Tris pH 7.5, 100 mM NaCl, and 100 mM sodium cholate. The nanodisc reconstitution mixture was prepared according to a 1:4:160 molar ratio of BcsAB, MSP1D1 membrane scaffold protein, and lipid, respectively. Removal of detergents was initiated by the addition ~ 200 mg mL⁻¹ Bio-Beads SM2 (Bio-Rad) followed by incubation at 4°C for 1 hour. The same mass of Bio-Beads SM2 was added a second time and the mixture was incubated at 4°C overnight. The next day, the same mass of Bio-Beads SM2 was added followed by incubation at 4°C for 1 hour. After removal of Bio-Beads SM2, the nanodisc-reconstituted BcsAB complex was incubated at room temperature for 15 minutes with 5 mM UDP-glc, 20 mM MgCl₂ and 30 μ M c-d-GMP to synthesize cellulose tether. After that, the complex was purified on a Superdex 200 column equilibrated in nanodisc gel filtration buffer (20 mM Tris pH 7.5, 100 mM NaCl). Peak fractions containing the BcsAB complex were snap frozen in liquid nitrogen until further use.

3.5.3 Motility and stretching assay preparation

We use one primary assay construction for both synthesis and stretching measurements. Flow cells are made with double-sided tape between a glass slide and a KOH etched glass coverslip. A single BcsAB complex bound in a His-tagged nanodisc is fixed to the glass coverslip using a non-specifically bound streptavidin (0.1 mg mL⁻¹) and a biotinylated anti-His antibody construct (0.01 mg mL⁻¹). A 5 mg mL⁻¹ solution of casein is incubated to block non-specific binding after streptavidin placement and before BcsAB attachment. To prevent mixing of reagents, a solution containing 5 mg mL⁻¹ BSA and 1 mg mL⁻¹ casein is washed between incubation steps. Surface-bound BcsAB complexes (600 pM) are incubated with 1.09 μ m polystyrene beads completely coated with cellulose binding DNA aptamers via biotin/streptavidin interactions, allowing for the beads to bind to the extruded cellulose chain. After, a complete synthesis buffer (pH 7.5) containing 25 mM NaH₂PO₄, 50 mM NaCl, 10 mM cellobiose, 10% glycerol, 5 mM UDP-glucose, 30 μ M cyclic-di-GMP, and 20 mM MgCl₂ is flowed into the flow cell directly before data acquisition. Control buffers comprise the same ingredients as the complete synthesis buffer, except excluding one component in each case. Mg²⁺ control buffer includes 50 mM EDTA. All experiments were conducted at 21 °C. During control experiments, the flow cell is left open, and mid experiment, 45 μ L of control buffer

exchanges with the complete synthesis buffer before being washed out again. For hybridization experiments, cellotetraose (5 mM and 50 mM) and cellohexaose (0.45 mM) were included separately in the motility buffer maintaining the final concentrations of the complete synthesis buffer. The concentrations of cellotetraose and cellohexaose were determined by the available supply and the solubility limit, respectively.

3.5.4 Motility data acquisition and analysis

Once the flow cell is loaded on the microscope, beads are trapped by a 1,064-nm laser and calibrated for trap stiffness and position within our detector zone. Tethered beads are centered over the complex and subsequently displaced by moving the piezo stage. In the instances where the tether shows evidence of folding and microstructure formation, we continue to move the stage as the tether undergoes extensions and mechanical relaxation before we record biosynthesis rates. As cellulose is synthesized, bead position is recorded at 5 kHz for as long as 10 min. Fiducial 0.75 μm polystyrene beads bound to the coverslip facilitate drift tracking and correction through a custom cross correlation video tracking algorithm similar to Brady et al. (37). Motility traces are corrected for drift and then decimated to 100 Hz. The actual tether length is calculated with a correction factor of $1/\sin(\theta)$ where θ is the incidence angle (angle from a line perpendicular to the coverslip surface) (51). Custom MATLAB scripts determine a velocity and average force for the entire trace. Velocities less than 0.01 nm s^{-1} were considered an absence of synthesis. For the force-velocity curve, velocities were binned by force and averaged every 2 pN. Each bin was weighted corresponding to the number of items in each bin for the fit. We fit the weighted averaged velocities to the general Boltzmann relationship (29). Abrupt extensions or retractions were located by a sliding step-finding MATLAB script that distinguished changes in mean position greater than two standard deviations from the previous segment's mean (80). The two sliding segments were 0.2 s in size. Typical force ranges for all control experiments were 3-8 pN, within the active range unaffected by force. The randomness parameter was calculated individually for each trace from the variance from the mean trajectory and averaged to find the mean randomness parameter for each given characteristic distance.

3.5.5 BcsAB bulk activity measurements

To assess the activity of the purified, nanodisc-reconstituted BcsAB complex in the presence of DY547-labelled c-d-GMP (c-d-GMPf), 0.01 mg mL^{-1} protein was incubated overnight at 37°C in the presence of 5mM UDP-Glc, 20mM MgCl_2 , 0.25 mCi of ^3H -labelled UDP-glc and 30 μM of either c-d-GMP, c-d-GMPf or no c-d-GMP present. After the synthesis, the reaction mixture as subjected to

paper chromatography and liquid scintillation measurements to quantify the amount of product, as previously described (10). Each reaction was carried out in triplicate (*SI Appendix Fig. S2*). To test the bulk activity of BcsAB in the presence of cellohexaose, a similar protocol was followed. The protein was incubated with all reaction components in the presence or absence of 0.45 mM cellohexaose.

3.5.6 Stretching data acquisition and analysis

During cellulose stretching experiments, tension is increased by moving the sample at a velocity of 64 nm s^{-1} and at loading rates between 2.25 pN s^{-1} and 8.5 pN s^{-1} , depending on trap stiffness, until the bead is pulled out of the trap center. The stage direction is then reversed to relax the polymer until the bead is centered over the complex again. To avoid tether beads from sticking to the coverslip, the bead is slightly lifted off the surface. The tether length is calculated using the same correction factor as in motility experiments. (51). Trap stiffness varied with laser intensity. The position of the bead relative to the trap is sampled 1000 times at 50,000 Hz and averaged every 4 nm. The extension of the polymer is calculated from stage position measurements, angle correction for assay geometry, and bead position data. We can assume the mechanical properties of BcsAB are negligible because the size of the complex ($\sim 15 \text{ nm}$) is much less than that of the strand ($\sim 1 \mu\text{m}$). Multiple sequential stretches are acquired in a single run to observe hysteresis and mechanical relaxation and to monitor the relative changes in apparent contour length over time. The elevation of the bead from the surface does not affect the change in apparent contour length. A custom MATLAB script was used to fit stretching curves to the extendible Worm-Like Chain model (52) taking into account assay geometry angle. Unfolding distances of cellulose were determined by calculating the difference in contour lengths before and after an elongation event.

DNA tether controls were performed by nonspecifically binding streptavidin to the glass coverslip and incubating with casein, as done in BcsAB assays. Next, a solution of 30.7 ng mL^{-1} biotin-3500 bp DNA-digoxygenin was incubated followed by anti-digoxygenin coated beads to form coverslip tethered beads. The DNA constructs and beads were made using a protocol outlined in Banik et al. (78). The rest of the experiment and analysis mimicked that of cellulose experiments exactly.

3.5.7 TIRF measurements

Synthase surface attachment methods were the same as the motility assay preparation described above. However, a 1% biotin-PEG coverslip replaced the KOH etch coverslip to prevent nonspecific binding of fluorophores, and polystyrene beads were excluded. Assay design and signal measurements are similar to those reported by Shin et al. (81). Synthases were incubated for 20

minutes in the complete synthesis buffer containing 300 nM of DY547 labeled c-d-GMP (Biolog) and 29.7 μ M unlabeled c-d-GMP. The synthesis buffer also included an oxygen scavenging mixture of 0.8% glucose, 165 units/mL glucose oxidase and 2,170 units/mL catalase in Trolox to minimize photobleaching.

Immediately before data acquisition, c-d-GMPf was washed out with ten times the flow cell volume (10x20 μ L) of normal synthesis buffer. The sample was illuminated by a 532-nm laser only during image sampling. A laser power of 40 μ W illuminated a field of 3000 μ m². Images of the specimen plane were collected at 0.33 Hz for one hour with Andor's iXon camera via a triggering mechanism to illuminate the sample for 100 ms only during each frame of image acquisition, culminating in 120 seconds of total exposure. Custom MATLAB scripts identified and measured the lifetime of bound fluorescent c-d-GMP. Spots with brightnesses that varied or drifted considerably were excluded. Single-molecule fluorescence was identified by a steep photobleaching or unbinding event in which the signal returned to baseline. For those that did not photobleach or unbind, the only spots with a brightness signal consistent with the single-molecule events were considered.

3.6 Acknowledgements

I thank collaborators and other authors who have contributed to this work: Harris W. Manning, Ireneusz Gorniak, Sonia K. Brady, Madeline M. Johnson, Jochen Zimmer and Matthew J. Lang. We thank Katarzyna J Zienkiewicz for her support with experiment preparation and members of the Olivares and Lang labs for their helpful comments. We also thank the anonymous reviewers for their helpful suggestions. This work is supported by the National Institutes of Health grant (5R01GM101001), the Department of Energy Bio-imaging award (Office of Science DE-SC0019313), the National Science Foundation CBET award (1604421), and the National Science Foundation MCB award (1330792). The illustration in Figure 1 was created with BioRender.com.

3.7 References

1. Y. Shibafuji *et al.*, Single-molecule imaging analysis of elementary reaction steps of trichoderma reesei cellobiohydrolase i (Cel7A) hydrolyzing crystalline cellulose Ia and III. *Journal of Biological Chemistry* **289**, 14056-14065 (2014).
2. A. C. O'Sullivan, Cellulose: the structure slowly unravels. *Cellulose* **4**, 173-207 (1997).

3. H. E. McFarlane, A. Döring, S. Persson, The Cell Biology of Cellulose Synthesis. *Annual Review of Plant Biology* **65**, 69-94 (2014).
4. A. Carroll, C. Somerville, Cellulosic biofuels. *Annual Review of Plant Biology* **60**, 165-182 (2009).
5. L. K. Vestby, T. Grønseth, R. Simm, L. L. Nesse, Bacterial biofilm and its role in the pathogenesis of disease. *Antibiotics* **9** (2020).
6. J. A. Otter *et al.*, Surface-attached cells, biofilms and biocide susceptibility: Implications for hospital cleaning and disinfection. *Journal of Hospital Infection* **89**, 16-27 (2015).
7. C. E. Jahn, D. A. Selimi, J. D. Barak, A. O. Charkowski, The *Dickeya dadantii* biofilm matrix consists of cellulose nanofibres, and is an emergent property dependent upon the type iii secretion system and the cellulose synthesis operon. *Microbiology* **157**, 2733-2744 (2011).
8. A. Thygesen, J. Oddershede, H. Lilholt, A. B. Thomsen, K. Ståhl, On the determination of crystallinity and cellulose content in plant fibres. *Cellulose* **12**, 563-576 (2005).
9. J. T. McNamara, J. L. W. Morgan, J. Zimmer, A molecular description of cellulose biosynthesis. *Annual Review of Biochemistry* **84**, 895-921 (2015).
10. O. Omadjela *et al.*, BcsA and BcsB form the catalytically active core of bacterial cellulose synthase sufficient for in vitro cellulose synthesis. *Proceedings of the National Academy of Sciences of the United States of America* **110**, 17856-17861 (2013).
11. J. L. W. Morgan, J. T. McNamara, J. Zimmer, Mechanism of activation of bacterial cellulose synthase by cyclic di-GMP. *Nature Structural and Molecular Biology* **21**, 489-496 (2014).
12. J. B. Thoden, H. M. Holden, Active site geometry of glucose-1-phosphate uridylyltransferase. *Protein Science* **16**, 1379-1388 (2007).
13. J. T. M. M. F. J. R. H.-M. C. S. G. W. Jacob L. W. Morgan, Z. Jochen, Observing cellulose biosynthesis and membrane translocation in crystallo. *Nature* **531**, 329-334 (2016).
14. J. L. W. Morgan, J. Strumillo, J. Zimmer, Crystallographic snapshot of cellulose synthesis and membrane translocation. *Nature* **493**, 181-186 (2013).
15. D. Klemm, B. Heublein, H. P. Fink, A. Bohn, Cellulose: Fascinating biopolymer and sustainable raw material. *Angewandte Chemie - International Edition* **44**, 3358-3393 (2005).
16. C. Somerville, Cellulose synthesis in higher plants. *Annual Review of Cell and Developmental Biology* **22**, 53-78 (2006).
17. K. J. C. G. G. T. I. L. J. C. N. M. D. T. J. M. J. William Costerton, BACTERIAL BIOFILMS IN NATURE AND DISEASE. *Ann. Rev. Microbiol.* **41**, 435-464 (1987).
18. P. S. Stewart, J. W. Costerton, Antibiotic resistance of bacteria in biofilms. *Lancet* **358**, 135-138 (2001).
19. L. Karygianni, Z. Ren, H. Koo, T. Thurnheer, Biofilm Matrixome: Extracellular Components in Structured Microbial Communities. *Trends in Microbiology* **28**, 668-681 (2020).
20. J. B. McManus, L. Wilson, H. Yang, J. D. Kubicki, M. Tien, Kinetic analysis of cellulose synthase of *Gluconacetobacter hansenii* in whole cells and in purified form. *Enzyme and Microbial Technology* **119**, 24-29 (2018).

21. K. O. Reddy *et al.*, Extraction and characterization of cellulose single fibers from native african napier grass. *Carbohydrate Polymers* **188**, 85-91 (2018).
22. D. Ciolacu, F. Ciolacu, V. I. Popa, AMORPHOUS CELLULOSE – STRUCTURE AND CHARACTERIZATION. *Cellulose Chemistry and Technology* **45**, 13-21 (2011).
23. S. P. S. Chundawat *et al.*, Restructuring the crystalline cellulose hydrogen bond network enhances its depolymerization rate. *Journal of the American Chemical Society* **133**, 11163-11174 (2011).
24. L. M. J. Kroon-Batenburg, P. H. Kruiskamp, J. F. G. Vliegthart, J. Kroon, Estimation of the persistence length of polymers by MD simulations on small fragments in solution. Application to cellulose. *Journal of Physical Chemistry B* **101**, 8454-8459 (1997).
25. Q. Cheng, S. Wang, A method for testing the elastic modulus of single cellulose fibrils via atomic force microscopy. *Composites Part A: Applied Science and Manufacturing* **39**, 1838-1843 (2008).
26. C. Zhu, C. Krumm, G. G. Facas, M. Neurock, P. J. Dauenhauer, Energetics of cellulose and cyclodextrin glycosidic bond cleavage. *Reaction Chemistry and Engineering* **2**, 201-214 (2017).
27. S. H. Cho *et al.*, Synthesis and self-assembly of cellulose microfibrils from reconstituted cellulose synthase. *Plant Physiology* **175**, 146-156 (2017).
28. D. Goldman *et al.*, Mechanical force releases nascentchain-mediated ribosome arrest in vitro and in vivo. *Science* **348**, 457-460 (2015).
29. M. D. Wang *et al.*, Force and velocity measured for single molecules of RNA polymerase. *Science* **282**, 902-907 (1998).
30. K. Svoboda, C. F. Schmidt, B. J. Schnapp, B. S. M. Block, Direct observation of kinesin stepping by OT interferometry. *Nature* **365**, 721-727 (1993).
31. B. J. Boese, R. R. Breaker, In vitro selection and characterization of cellulose-binding DNA aptamers. *Nucleic Acids Research* **35**, 6378-6388 (2007).
32. J. Du, V. Vepachedu, S. H. Cho, M. Kumar, B. T. Nixon, Structure of the cellulose synthase complex of *Gluconacetobacter hansenii* at 23.4 Å resolution. *PLoS ONE*, 1-24 (2016).
33. C. Cifuentes, V. Bulone, A. M. C. Emons, Biosynthesis of Callose and Cellulose by Detergent Extracts of Tobacco Cell Membranes and Quantification of the Polymers Synthesized in vitro. *Journal of Integrative Plant Biology* **52**, 221-233 (2010).
34. A. R. Paredez, C. R. Somerville, D. W. Ehrhardt (Visualization of Cellulose Synthase Demonstrates Functional Association with Microtubules.
35. Y. Nishiyama, P. Langan, H. Chanzy, Crystal Structure and Hydrogen-Bonding System in Cellulose I from Synchrotron X-ray and Neutron Fiber Diffraction. *J. Am. Chem. Soc.* **124**, 9074-9082 (2002).
36. D. K. Das *et al.*, Pre-T cell receptors (Pre-TCRs) leverage Vβ complementarity determining regions (CDRs) and hydrophobic patch in mechanosensing thymic self-ligands. *Journal of Biological Chemistry* **291**, 25292-25305 (2016).
37. S. K. Brady, S. Sreelatha, Y. Feng, S. P. S. Chundawat, M. J. Lang, Cellobiohydrolase 1 from

- Trichoderma reesei degrades cellulose in single cellobiose steps. *Nature Communications* **6**, 1-9 (2015).
38. D. N. Reinemann, S. R. Norris, R. Ohi, M. J. Lang, Processive Kinesin-14 HSET Exhibits Directional Flexibility Depending on Motor Traffic. *Current Biology* **28**, 2356-2362.e2355 (2018).
 39. J. M. Berg, J. L. Tymoczka, L. Stryer, *Biochemistry* (W H Freeman, ed. 5th, 2002).
 40. J. Liphardt, B. Onoa, S. B. Smith, I. Tinoco, C. Bustamante, Reversible unfolding of single RNA molecules by mechanical force. *Science* **292**, 733-737 (2001).
 41. S. C. Kou, B. J. Cherayil, W. Min, B. P. English, X. S. Xie, Single-molecule Michaelis - Menten equations. *Journal of Physical Chemistry B* **109**, 19068-19081 (2005).
 42. D. L. Floyd, S. C. Harrison, A. M. Van Oijen, Analysis of kinetic intermediates in single-particle dwell-Time distributions. *Biophysical Journal* **99**, 360-366 (2010).
 43. J. R. Moffitt, C. Bustamante, Extracting signal from noise: kinetic mechanisms from a Michaelis-Menten-like expression for enzymatic fluctuations. *FEBS Journal* **281**, 498-517 (2014).
 44. B. P. English *et al.*, Ever-fluctuating single enzyme molecules: Michaelis-Menten equation revisited. *Nat Chem Biol* **2**, 87-94 (2006).
 45. J. F. Marko, E. D. Siggia, Stretching DNA. *Macromolecules* **28**, 8759-8770 (1995).
 46. M. D. Wang, H. Yin, R. Landick, J. Gelles, S. M. Block, Stretching DNA with optical tweezers. *Biophysical Journal* **72**, 1335-1346 (1997).
 47. C. E. Castro, J. Dong, M. C. Boyce, S. Lindquist, M. J. Lang, Physical properties of polymorphic yeast prion amyloid fibers. *Biophysical Journal* **101**, 439-448 (2011).
 48. S. B. Smith, L. Finzi, C. Bustamante, Direct mechanical measurements of the elasticity of single DNA molecules by using magnetic beads. *Science* **258**, 1122-1126 (1992).
 49. C. Liu *et al.*, Single polymer growth dynamics. *Science* **358**, 352-355 (2017).
 50. C. Bustamante, J. Marko, E. Siggia, S. Smith, Entropic elasticity of lambda-phage DNA. *Science* **265**, 1599-1600 (1994).
 51. A. L. Stout, W. W. Webb, "Chapter 6 Optical Force Microscopy" in *Methods in Cell Biology*, M. P. Sheetz, Ed. (Academic Press, 1997), vol. 55, pp. 99-116.
 52. T. Odijk, Stiff Chains and Filaments under Tension. *Macromolecules* **28**, 7016-7018 (1995).
 53. H. Yin *et al.*, Transcription against an applied force. *Science* **270**, 1653-1657 (1995).
 54. G. J. L. Wuite, S. B. Smith, M. Young, D. Keller, C. Bustamante, Single-molecule studies of the effect of template tension on T7 DNA polymerase activity. *Nature* **404**, 103-106 (2000).
 55. S. Uemura *et al.*, Peptide bond formation destabilizes Shine-Dalgarno interaction on the ribosome. *Nature* **446**, 454-457 (2007).
 56. A. L. Lehninger, D. L. Nelson, M. M. Cox, *Lehninger principles of biochemistry* (Macmillan, 2005).
 57. M. Benziman, C. H. Haigler, R. M. Brown, A. R. White, K. M. Cooper, Cellulose biogenesis: Polymerization and crystallization are coupled processes in *Acetobacter xylinum*. *Proc Natl Acad Sci U S A* **77**, 6678-6682 (1980).
 58. J. R. Pear, Y. Kawagoet, W. E. Schreckengost, D. P. Delmert, D. M. Stalker (1996) Higher

- plants contain homologs of the bacterial *celA* genes encoding the catalytic subunit of cellulose synthase. pp 12637-12642.
59. P. Purushotham, R. Ho, J. Zimmer, Architecture of a catalytically active homotrimeric plant cellulose synthase complex. *Science* **369**, 1089-1094 (2020).
 60. K. E. Low, P. L. Howell (2018) Gram-negative synthase-dependent exopolysaccharide biosynthetic machines. (Elsevier Ltd), pp 32-44.
 61. Y. C. Wang *et al.*, Nucleotide binding by the widespread high-affinity cyclic di-GMP receptor MshEN domain. *Nature Communications* **7** (2016).
 62. J. R. Chambers, K. Sauer, "Detection of Cyclic di-GMP Binding Proteins Utilizing a Biotinylated Cyclic di-GMP Pull-Down Assay". (Springer Science+Business Media LLC, 2017), pp. 317-329.
 63. P. Peluso *et al.*, Role of 4.5S RNA in assembly of the bacterial signal recognition particle with its receptor. *Science* **288**, 1640-1643 (2000).
 64. K. A. Johnson, S. P. Gilbert, Pathway of the microtubule-kinesin ATPase. *Biophys J* **68**, 173S-176S; discussion 176S-179S (1995).
 65. I. Swanson Pultz *et al.*, The response threshold of Salmonella PilZ domain proteins is determined by their binding affinities for c-di-GMP. (2012).
 66. U. Römling, M. Y. Galperin, M. Gomelsky, Cyclic di-GMP: the First 25 Years of a Universal Bacterial Second Messenger. (2013).
 67. G. Stirnemann, D. Giganti, J. M. Fernandez, B. J. Berne, Elasticity, structure, and relaxation of extended proteins under force. *BIOPHYSICS AND COMPUTATIONAL BIOLOGY CHEMISTRY* **110**, 3847-3852 (2013).
 68. M. E. Aubin-Tam, A. O. Olivares, R. T. Sauer, T. A. Baker, M. J. Lang, Single-molecule protein unfolding and translocation by an ATP-fueled proteolytic machine. *Cell* **145**, 257-267 (2011).
 69. M. H. Larson, W. J. Greenleaf, R. Landick, S. M. Block, Applied Force Reveals Mechanistic and Energetic Details of Transcription Termination. *Cell* **132**, 971-982 (2008).
 70. A. Bosco, J. Camunas-Soler, F. Ritort, Elastic properties and secondary structure formation of single-stranded DNA at monovalent and divalent salt conditions. *Nucleic Acids Research* **42**, 2064-2074 (2014).
 71. K. Hayashi *et al.*, Influence of RNA Strand Rigidity on Polyion Complex Formation with Block Cationomers. *Macromol. Rapid Commun* **37**, 493-493 (2016).
 72. M. Hillgärtner, K. Linka, M. Itskov, Worm-like chain model extensions for highly stretched tropocollagen molecules. *Journal of Biomechanics* **80**, 129-135 (2018).
 73. S. Basu *et al.*, Cellulose Microfibril Formation by Surface-Tethered Cellulose Synthase Enzymes. *ACS Nano* **10**, 1896-1907 (2016).
 74. P. Ross, R. Mayer, A. N. D. M. Benziman, Cellulose biosynthesis and function in bacteria positive control. *Microbiological Reviews* **55**, 35-58 (1991).
 75. W. J. Nicolas, D. Ghosal, E. I. Tocheva, E. M. Meyerowitz, G. J. Jensen, Structure of the Bacterial Cellulose Ribbon and Its Assembly-Guiding Cytoskeleton by Electron Cryotomography. *Journal of Bacteriology* **203**, 1-24 (2021).

76. E. C. Hollenbeck *et al.*, Phosphoethanolamine cellulose enhances curli-mediated adhesion of uropathogenic *Escherichia coli* to bladder epithelial cells. *Proceedings of the National Academy of Sciences of the United States of America* **115**, 10106-10111 (2018).
77. W. Thongsomboon *et al.*, Phosphoethanolamine cellulose: A naturally produced chemically modified cellulose. *Science* **359**, 334-338 (2018).
78. D. Banik *et al.*, Single Molecule Force Spectroscopy Reveals Distinctions in Key Biophysical Parameters of $\alpha\beta$ T-Cell Receptors Compared with Chimeric Antigen Receptors Directed at the Same Ligand. *J. Phys. Chem. Lett.* 2021 **12**, 7573-7573 (2021).
79. C. A. Caffalette, J. Zimmer, Cryo-EM structure of the full-length WzmWzt ABC transporter required for lipid-linked O antigen transport. *Proceedings of the National Academy of Sciences of the United States of America* **118**, 1-10 (2021).
80. B. C. Carter, M. Vershinin, S. P. Gross, A Comparison of Step-Detection Methods: How Well Can You Do? *Biophysical Journal* **94**, 306-319 (2008).
81. Y. Shin *et al.*, Single-molecule denaturation and degradation of proteins by the AAA+ ClpXP protease. *Proceedings of the National Academy of Sciences of the United States of America* **106**, 19340-19345 (2009).

CHAPTER 4

Construction of high-resolution optical tweezers with advanced drift correction

4.1 Summary

Optical tweezers have emerged as one of the most productive instruments for studying single-molecule dynamics. As a testament, Arthur Ashkin won the Nobel Prize for Physics in 2018 for the invention of optical tweezers (1). Since its inception in 1970, many biological systems have been studied at the single-molecule level using force-spectroscopy (1). The field of molecular motors has especially benefitted from the use of optical tweezers because of its ability to track position changes with nanometer resolution and the capability of applying force or observe force being applied. With the urgency of climate change, enzymatic saccharification for biofuel production recently prompted the need to understand cellulose machinery at the single-molecule level (2). Unfortunately, cellulose machinery operates relatively slowly (~ 0.2 nm/s vs 8-100 nm/s) and takes small steps (0.5 nm and 1 nm) making data collection susceptible to drift (2-5). To prevent false observed behavior in cellulose machinery, single-molecule force spectroscopy techniques need to develop drift tracking/elimination techniques. This dissertation details the construction of a high-resolution optical tweezers instrument with advanced drift correction and environmental temperature control.

4.2 Introduction

Single molecule techniques have emerged as powerful tools to describe biological subjects of interest, specifically molecular machines or protein conformational changes (6-11). Force spectroscopy is particularly unique in that it reimagines the biological micro-environment from a conglomerate of biochemicals into an active, dynamic system in which the molecules push and pull on each other. Amazingly, biology has evolved to utilize the forces to accomplish important functions. Directed cellular transport occurs from proteins breaking chemical bonds and using the energy to propel itself forward carrying its cargo behind (12, 13). Cells prevent self-poisoning by

tagging hazardous, misfolded, or overpopulated proteins and then enzymes attach to the tags, pull on and chew up the proteins (4, 14). Cells identify their surroundings and change behaviors based on whether or not their probes recognize specific stimuli (15, 16). The development of force applying/measuring tools, such as atomic force microscopes, magnetic tweezers and optical tweezers, has allowed researchers to study and understand the dynamics of molecular biological forces (10, 17-19). In this dissertation, we specifically use optical tweezers to study cellulose molecular machinery and the interactions with cellulose. As such, we will focus on optical tweezers, their development, recent advances, and novel advancements for the duration of this chapter.

The first glimpse of optical tweezers force spectroscopy was demonstrated when Arthur Ashkin displaced and levitated micrometer-sized particles by using the radiation pressure from the focus of a laser beam (1). The unprecedented means of object manipulation continued to develop with the discovery that 1064-nm lasers (typically from Nd:YAG) is better for biological samples because of its relatively non-damaging wavelength (20, 21). Early force calculations for three-dimensional particle trapping were computed from laser power, particle size and light ray geometry (22). Particle position tracking with quadrant photodiodes and optical tweezers interferometry created opportunities for new force calibration methods, such as the equipartition method, the drag force method and the power spectrum method (23-25). These force calibration methods are still standard today, although position detection methods have adapted the source from which forces are calibrated.

Instrumentation is constantly pushing the boundaries of resolution in order to gain more information on the system being studied. The addition of a second, lower-powered detection laser reduces the sensitivity to mechanical vibrations, and therefore lowers noise (25-27). A dual-trap configuration isolates the biological system between two beads, instead of one bead and the coverslip, eliminating most mechanical vibrations but making assay construction significantly more difficult (28-31). Additionally, dual-trap assays are very difficult for molecular motors that utilize certain biopolymers, such as actin, microtubules or cellulose, as tracks (2, 27, 32).

Recent advances in increasing optical tweezers' spatial resolution have addressed both the short time-scale noise sources (acoustic noise, electrical noise, laser pointing instability, optical aberrations, intensity, mode and polarization fluctuations) and long time-scale noise sources (thermal expansion, laser drift, air currents). For surface-coupled optical-trapping assays, such as those with microtubules or cellulose machinery, mechanical perturbations and thermal expansion are larger issues (33, 34). To combat mechanical acoustics, most optical tweezers microscopes are built on a very heavy (~700 lbs.) floating optical table in the basement and behind soundproof doors (2, 15, 25). Additionally, all optical components are typically encased in a box, sealed from

the rest of the noise in the room protecting from acoustics, air flow and dust alike (4, 6). Rooms that are highly temperature controlled reduce thermal expansion, despite some studies requiring higher local temperatures (2, 15). One technique to reduce pointing instability is to place all optics in a helium-filled or vacuum enclosure (35). Adaptive optics have been successful in preventing optical aberrations, which can increase trap stiffness, increase detection laser resolution and lower pointing instability (36). Similar photodiode feedback systems have been used to modulate laser power with measured intensity fluctuations to drastically reduce intensity noise (33).

Unfortunately, surface-bound assays also succumb to instrumental drift, commonly caused by thermal expansion. Techniques of tracking fiducial markers to eliminate drift have been successful in the past but have limitations (2, 33, 37). Video tracking of fiducial markers has emerged as a common practice in which a video records the specimen plane for the duration of the experiment and video analysis software (often custom-made) tracks the position of a fiducial marker (2, 37). This method relies on high spatial and temporal resolution cameras and massive data files (>5 MB) for each trace. Still, high spatial resolution cameras and novel video tracking software usually can only resolve several nanometers. A method of using a second detection laser to track fiducial drift was introduced in 2007 (34). However, it did not gain much traction because the rigid fiducial components required specific biological placement on the specimen plane. The method also depends on fabricating of coverslips with either glass posts or silicon disks, which require cleaning with dangerous Piranha solutions to be re-used (33). However, with the emergence of the study of cellulose machinery, which operate at much slower velocities than other molecular motors (2, 6, 12), the use of a second detection laser to track drift becomes more advantageous. As high resolution was necessary to understand RNA polymerase base-pair stepping or ClpXP's stochastic stepping (4, 35), the same high resolution is required to understand single-cellobiose steps (2), single-glucose steps, or similar stochastic behavior. In this dissertation, we revisit the laser-based fiducial tracking methods with the construction of a new optical tweezers microscope. Our detection system improves on previous (33) by adding automated detection laser positioning, so that simple, non-specifically bound polystyrene particles can act as fiducial markers making assays cheaper and easier to construct. Instead of using fiducial detection to provide positioning feedback directly to the piezo stage (33), we will simply subtract the drift trace from the data trace. The end-result data is corrected for both drift and some mechanical noise. Additionally, this optical tweezers instrument was equipped with a small volume heating chamber for elevated temperature studies. However, the main purpose of this Chapter is to detail the work done to create this optical tweezers design so that the reader may reconstruct and build upon a similar model.

4.3 Results

4.3.1 Optical path and components

The actual optical tweezers comprised a 1064-nm continuous-wave laser, while the dual-detection system utilized a fiber-coupled 785-nm laser and a fiber-coupled 830-nm laser. A schematic of the optical path can be found Fig. 4.1, and acronym and color references in the text relate to the schematic. The trapping laser was initially sent through a $\lambda/2$ waveplate to vertically, linearly polarize the beam. The beam then passed through a polarizing beam splitter cube (PBS) which reflected vertically polarized light into a beam block (BB), assuring that only horizontally polarized light passed through. On the breadboard, horizontally polarized light reflected off the optics. The beam then reflected off a piezo tip-tilt mirror (light grey, PI E-616), in which the mirror changes angles depending on the magnitude of a continuous, analog voltage signal sent to the device. The tilt mirror was our beam-steering device replacing commonly used acousto-optical deflectors (25, 26) while still benefiting from computerized steering. Intensity, and therefore stiffness, modulation was performed at the power supply with stable intensities at a various range of input currents (11.50 A to 13.50 A) and corresponding display power (0.05 W to 0.60 W). A trap-steering device is essential for position calibration, as explained further in section 4.3.5. The trapping laser then passed through a pair of lenses to collimate the beam (L1-2). The first lens (L1) was placed on a 3-axis stage (grey) to assist with walking the beam to a symmetrical beam profile at the desired height in the specimen plane. After the trap positioning was established, the lens did not move.

Both detection lasers passed through a similar pair of lenses (L3-4 and L5-6) with the first of each on a 3-axis stage. Each 3-axis stage employed two piezo actuators (PZA12 of the PZC200 system – Newport) in the X and Y directions (light blue). Control of these actuators could be alternated between a hand-knob for manual detection laser placement and the computer for automated positioning. The 785-nm laser reflected off a mirror, was vertically polarized with another $\lambda/2$ waveplate and passed through a short-pass dichroic mirror (DSP1) with a cut-off wavelength of 805 nm. The 830-nm laser reflected off the same dichroic (DSP1) combining paths with the 785-nm laser. A waveplate was omitted from vertically polarizing the 830-nm laser because more power was lost going into the objective than without a waveplate. The two detection beams reflected off a long-pass dichroic mirror (DLP1, 1,000 nm cutoff) joining the trapping laser as it passed through. The beams were then collimated again (L7-8) before reflecting into the objective (NA 1.4, oil) by another short-pass dichroic (DSP2, 650 nm cutoff). All laser beam profiles were made symmetrical

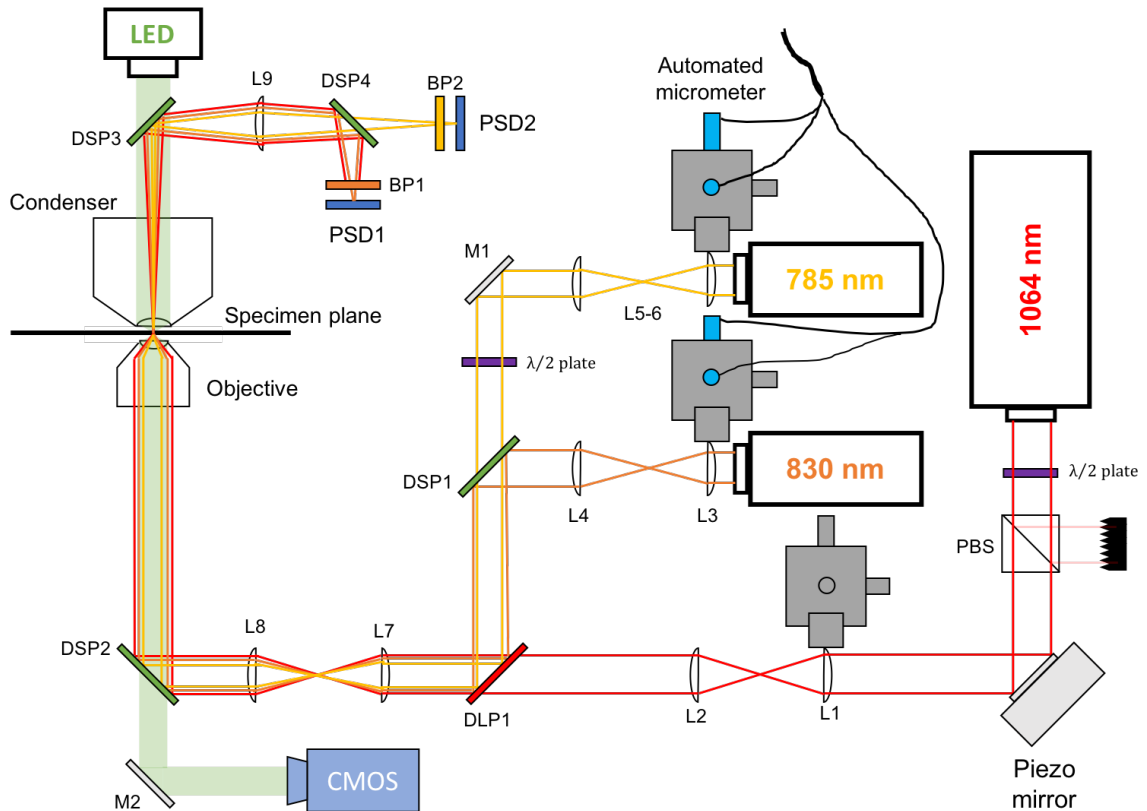


Figure 4.1. Optical tweezers optics diagram. The optical tweezers instrument consisted of one trapping laser at 1064 nm (red) and two detection lasers at 830 nm (orange) and 785 nm (yellow). The diagram is not drawn to scale. The actual optical set-up included several mirrors three mirrors between the polarizing beam splitter (PBS) for the beam to diverge naturally before collimation. The third of the mirrors was used in beam-walking to optimize the beam profile in the specimen plane. The acronyms are as follows: L is lens, BB is beam block, PBS is polarizing beam splitter cube, M is mirror, DSP is short-pass dichroic mirror, LSP is long-pass dichroic mirror, BP is bandpass filter, PSD is position sensing device, LED is light-emitting diode, CMOS is the complementary metal-oxide semiconductor camera. The 3-axis stages are shown in gray with gray micrometers at each axis. The micrometers that are automated through a piezo actuator are in light blue. Everything before DSP2 is contained inside a machine cut, compressed wood container with a plexiglass removable top. The CMOS camera uses the front port of the microscope. There is an additional DAGE camera (not shown) for viewing the specimen plane between data collection.

in the specimen plane.

The beams passed through the specimen plane and the condenser (NA 1.4, oil) before being reflected again by a second 650-nm cutoff short-pass dichroic (DSP3). The beams passed through one final lens (L9) before being separated by another short-pass dichroic (DSP4, cutoff 805 nm) and projected on position sensing devices (PSD1-2) located at a plane optically conjugate to the back focal plane of the condenser (38, 39). Each position sensing device holds a bandpass filter (BP1-2) optimized for the respective, specific detection wavelengths preventing undesirable signal from other lasers or light sources.

4.3.2 Video recording

A green (532 nm) LED illuminated the specimen plane for visuals and video recording. The specimen plane was projected onto a Teledyne FLIR Blackfly S USB3 CMOS camera (4 megapixel). The camera feed was analyzed by both SpinView, a GUI with Teledyne FLIR's camera library Spinnaker SDK, and Labview (2019, 32-bit), depending on the use. SpinView was an optimal program for video tracking and image capture and saving, ideal for fiducial tracking or initial trap position calibrations (Section 4.3.3). Labview was used in conjunction with the NanoPZ piezo actuator system to identify and assign coordinates to locations in the specimen plane to which the actuators sent the fiducial tracking laser (Section 4.3.5).

4.3.3 Piezo tilt mirror position calibrations

One of the most important aspects of optical tweezers is the high position resolution. However, without a highly accurate position reference, the values acquired from the PSDs are only an electrical signal. In order to calibrate the detection lasers, one must first calibrate the trap-steering device. A piezo stage (PI E-710) was a highly accurate positioning device with 1 nm resolution and was used effectively with video tracking/image acquisition to calibrate the magnitude of the continuous analog voltage input signal for the tilt mirror to a specific position displacement. To do this, 1 μm beads were affixed with a high-salt solution to the surface of a coverslip and moved in a 30 μm x 60 μm grid in both 5 μm and 10 μm increments while images were taken by camera at each increment. A custom image analysis software was able to localize the same bead to a single pixel for each grid position. The distances between each pixel were calculated in pixel space and juxtaposed to known nanometer space to get a nanometer to pixel ratio. From there, the tilt mirror steered the trap in a grid to uncover a pixel to input voltage ratio. Complications with the tilt mirror arose from hysteresis and asymmetry. Hysteresis was overcome by always inputting a lower voltage, at least 0.1 V lower than the desired voltage, before the desired voltage as to always approach a position from the same direction. The input voltage range of 0-4 V displayed the least asymmetry and the highest position displacement per volt, indicating the highest positioning sensitivity. Therefore, the tilt mirror was zeroed at 2 V in the X-direction and 2 V in the Y-direction. With these adaptations, the tilt mirror behaved reliably and reproducibly. From these calibrations, the tilt mirror revealed to move 573.27 nm/V in the X-direction and 799.74 nm/V in the Y-direction.

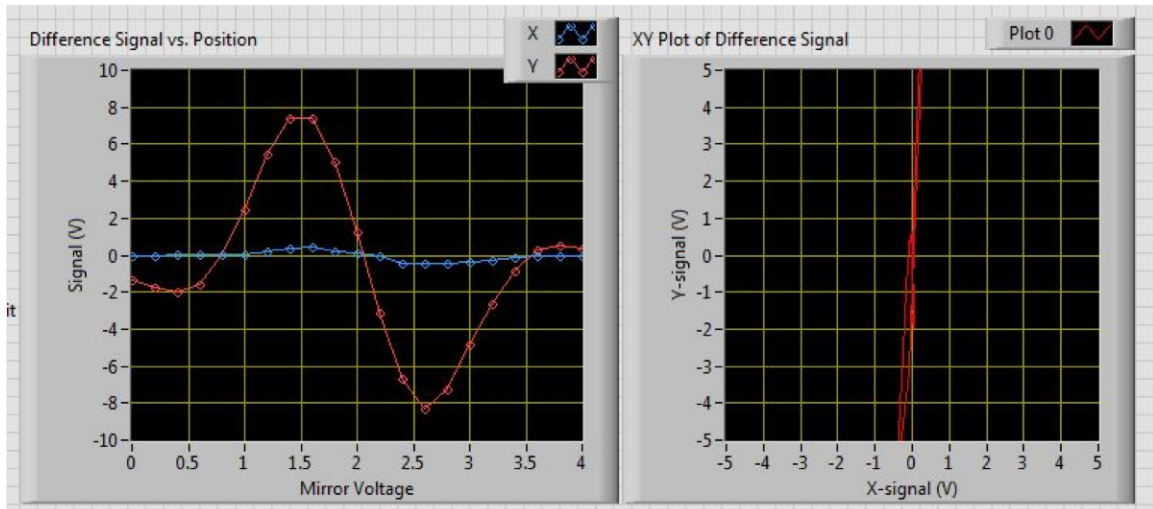


Figure 4.2. Tilt mirror steered the trap through the detection zone. In this image, a trapped particle was steered by the tilt mirror in both the positive and negative Y-direction following the path of a triangle wave. The PSD positions were adjusted so that the detection deflections were centered on the PSD, indicated by the signal (y-axis) approaching 0 V as the mirror voltage (x-axis) approaches 0 V and 4 V. The detection beam is then positioned by the piezo actuators such that the signal in the x-direction is minimized, indicating that the movement of the bead in the Y-axis only yields a signal in the Y-axis. This process is repeated for the X-axis and often requires a few iterations.

4.3.4 Detection position calibrations

The position calibrations for the tilt mirror are essential for calibrating the position detection system. As mentioned in section 4.3.1, the position detection system comprised two detection lasers and two position sensing devices. The goal of this section was to correlate the signal received at the PSD from deflections of the detection beam off of the trapped particle to a coordinate position in the specimen plane. The methods used here have been described previously (26). First, the detection lasers were centered in the XY-plane over the trapping laser. For this, a trapped particle was steered in the positive and negative directions at specific points along a line in both the X- and Y-axis while sampling the PSD signal at each point. The piezo actuator system was used to move each detection beam until the respective axis shows a curve representing the derivative of a gaussian and the off-axis essentially flat-lines (Fig. 4.2). After both axes are centered, the positioning system was ready for calibration.

For this, a trapped particle was raster-scanned through a grid of known positions by the tilt mirror through the detection zone of the detection laser. Because of the tilt mirror hysteresis, each grid point was approached from a lower input voltage. The X- and Y-signal from the PSD at each grid point was plotted as a surface (Fig. 4.3), and a 2D, fifth-order polynomial fit mapped the PSD output

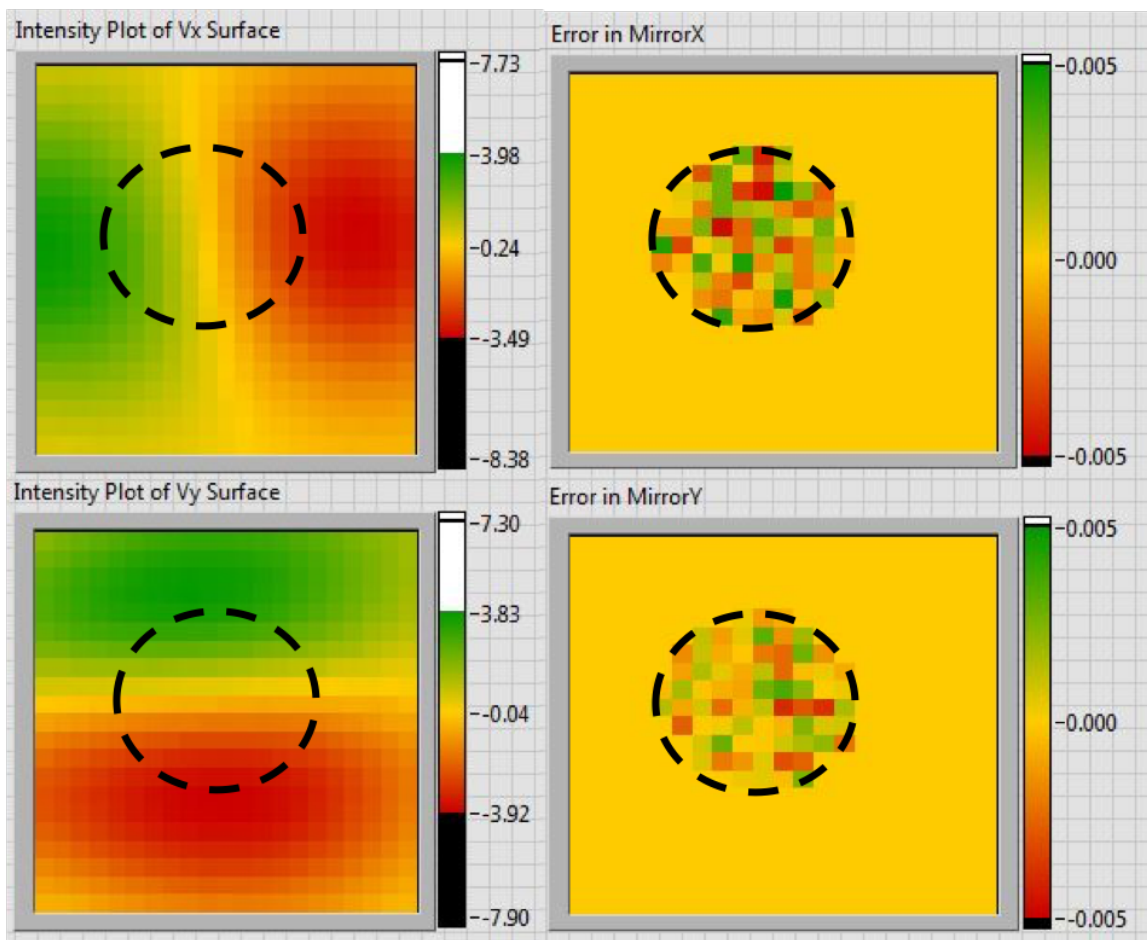


Figure 4.3. 5th order position calibrations. The left two plots show the intensity profiles of the X-signal (top) and Y-signal (bottom) as a bead is raster-scanned through the detection zone. The dotted black circles represent the zones in which PSD signal to nanometers is single valued and highly accurate. Each profile is fit to a 5th order polynomial equation so that voltage data collected from the PSD can be run through the polynomial equation giving accurate positions. The right two plots show the root mean square error voltage for each position of the particle scan within the detection range of interest.

voltages into nanometer space using the nm/V ratios calculated in the previous section. The PSD signal can only reliably be used in the region where voltage is most accurately related to position (~400-nm diameter). The residual error of the fit within this region was <0.005 V rms (Fig. 4.3). The fifth-order polynomial fits, and therefore position calibrations, were comparable for particles of similar sizes. For each bead used in experiments, the position detection system was calibrated, and the fit coefficients were saved to a file for signal to position conversions during data analysis.

The ideal detection system is one that has the highest sensitivity. One method of increasing sensitivity was to optimize the z-position of the focus of the detection beams to align perfectly with the center of a trapped particle. This position was just above the trapping laser focus due to

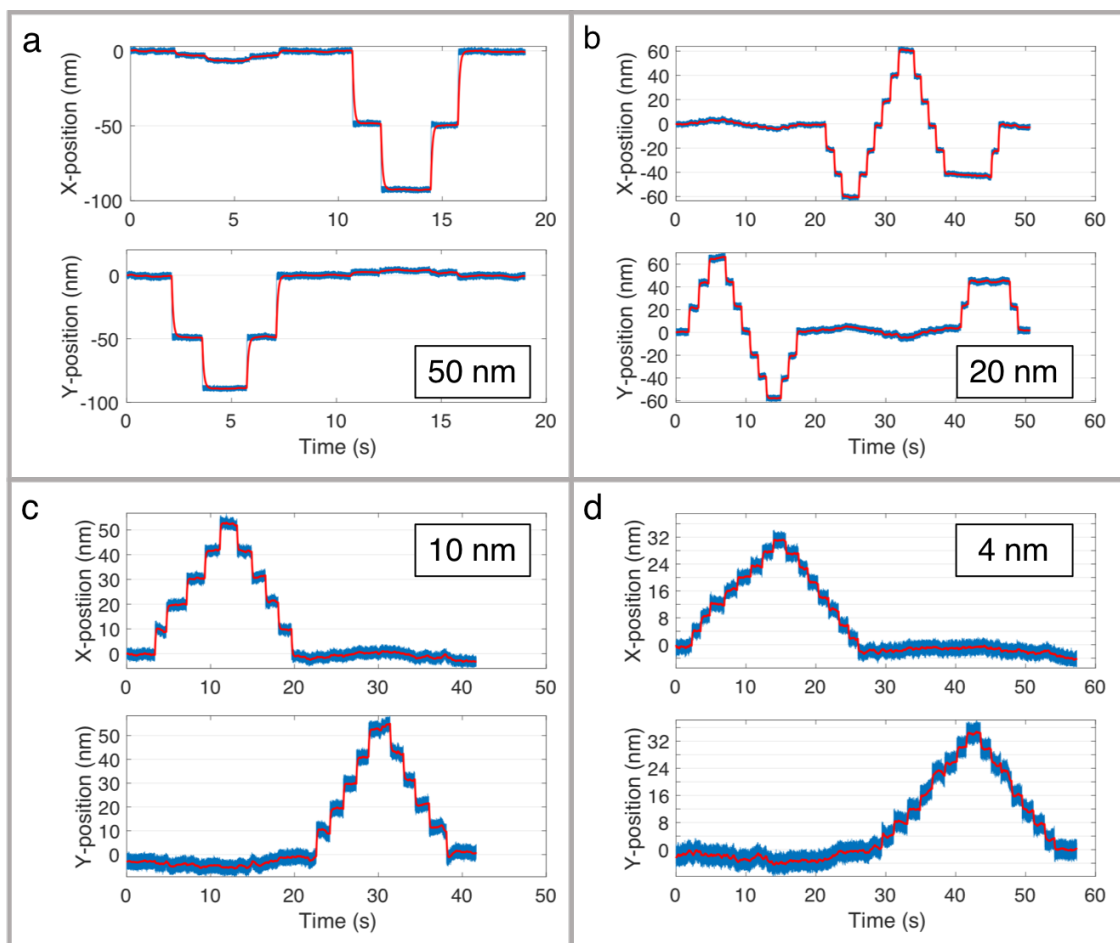


Figure 4.4. Step detection of a fixed bead. A 1- μm bead was stepped through the detection zone at 50 nm, 20 nm, 10 nm, and 4 nm steps. The blue line is the raw data, and the red line is a decimated moving average. Each measured step size corresponds well with the actual distance, as the horizontal pauses of the red moving average between vertical steps aligns well with the Y-grid. The traces demonstrate that the calibration methods successfully and accurately translate voltage signal from the PSD into nanometer space, as well as showing that 4-nm steps are easily resolved.

scattering forces. In order to optimize z-position, the z-micrometer (labelled gray and not light blue in Fig. 4.1) was adjusted slightly, the detection laser was centered, and PSD signals were calibrated again. This process repeated until the size of the usable calibrated range was minimized and the sensitivity (slope of the linear region) was maximized. To demonstrate the sensitivity and accuracy, a 1- μm bead stuck to the coverslip surface was centered in the detection region and translated with the piezo stage by 50 nm, 20 nm, 10 nm, and 4 nm step intervals. The resulting position measurements from 5th order calibration convolution are shown in Figure 4.4 and reveal that 4 nm steps are easily resolved. The position detection system was capable of accurate, sensitive and reliable signal to position calibrations.

4.3.5 Trap stiffness calibrations

For force spectroscopy, one needs to know how much force is being applied. As mentioned in Chapter 1, the force applied scales linearly with the distance from the trap center within ~200 nm from the trap center and can be modelled as a Hookean Spring. In general, the trap stiffness is measured for each bead as stiffness will change with each particle's shape, size and topography. This optical tweezers system was calibrated for stiffness using four separate methods with <10% agreement between all except for one, which is discussed. There are more than four methods for stiffness calibrations, and a majority have been detailed in Visscher et al., 1996 (25). The methods used here were the Drag Force Method, the Power Spectrum Method, the Equipartition Method, and a biological control of stretching DNA. For most experiments, the Equipartition Method was more than adequate at measuring trap stiffness. All calibrations were performed on a 1 μm polystyrene carboxy bead.

For using the Drag Force Method, the polystyrene bead used was a spherical object in a very low Reynolds number regime, so Stokes law for drag force ($F_d = 6\pi\eta Rv$) was applicable to equate to calculate trap stiffness ($\alpha = F/\Delta x$). A trapped bead translated through solution at a known velocity using the piezo stage, and drag forces displaced the bead from the trap center. The stiffness could then be calculated from a force balance: $\alpha = 6\pi\eta Rv/\Delta x$, where α is trap stiffness, η is the dynamic viscosity of water, R is the bead radius, v is the translation velocity and Δx is the displacement from the trap center. However, translating the stage with the bead ~500 nm from the coverslip introduces additional viscosity considerations. Faxén's law provided a correction factor determined by the bead radius and distance from the surface that accounted for this phenomenon. Calibrations are shown in Table 4.1.

The Power Spectrum Method relies on obtaining the power spectrum of the position fluctuations of a trap object. The trapped particle in low Reynolds regime can be modelled as bound in a harmonic potential, in which the power spectrum of positions is Lorentzian. The roll-off frequency $f_c = \alpha/2\pi\beta$, where α is the trap stiffness and β is the first order coefficient in the Langevin differential equation of $\beta x'(t) + \alpha x(t) = F(t)$ relating position to force (F). Lorentzian fits to the power spectra of positions then yields a stiffness. A full description of this method can be found in Visscher et al., 1996 (25). High sampling rate (~100,000 s^{-1}) is required for this method. The power spectrum was sensitive to noise which both aided in identifying and eliminating noise

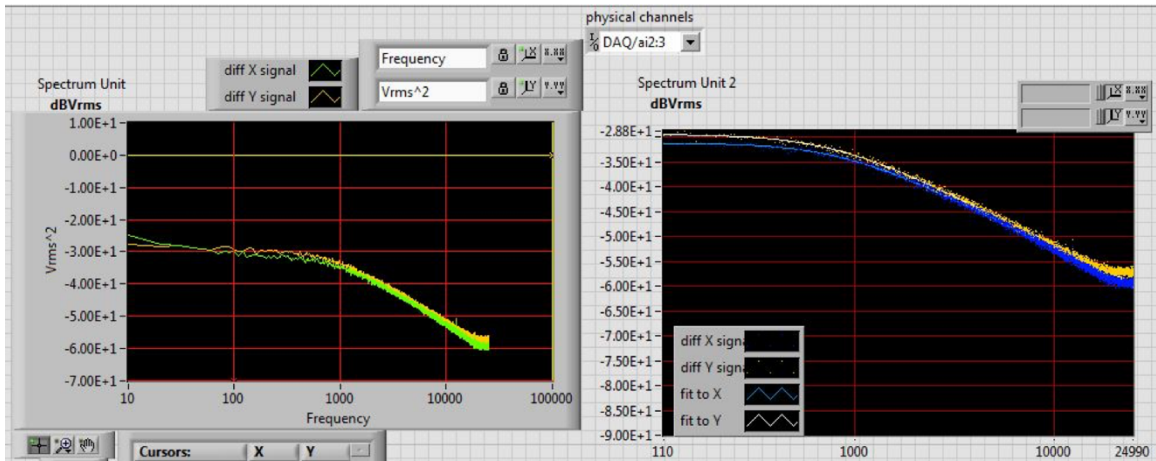


Figure 4.5. Power spectrum calibration. (left) An example power spectrum of the position of a 1- μm polystyrene bead in the trap with a stiffness of 0.04 pN/nm. A total of 200 power spectrums are collected and averaged to yield the example on the left. (right) The power spectrum is fit to a Lorentzian in which the roll-off frequency is directly proportional to the trap stiffness. Fits are shown as blue and yellow lines. Note that the spectrum at lower frequencies (<200 Hz) ideally does not change. Here, we see slight increases in the spectrum towards 10 Hz, which causes the fits to underestimate the stiffness values, resulting in the discrepancies in Table 4.1.

Current (A)	Power on power supply (W)	Laser power into obj. (mW)	Power Spectrum (pN/nm)	Drag Force (pN/nm)	Equipartition (pN/nm)
11.5	0.05	80	X – 0.025 Y – 0.023	X – 0.046 Y – 0.041	X – 0.040 Y – 0.036
12	0.14	157	X – 0.042 Y – 0.046	X – 0.078 Y – 0.067	X – 0.072 Y – 0.077
12.5	0.24	260	X – 0.055 Y – 0.082	X – 0.141 Y – 0.146	X – 0.136 Y – 0.132
13	0.41	397	X – 0.064 Y – 0.118	X – 0.211 Y – 0.208	X – 0.199 Y – 0.199
13.5	0.59	562	X – 0.080 Y – 0.175	X – 0.293 Y – 0.302	X – 0.283 Y – 0.288

Table 4.1. Calibration chart for different input currents on the power supply. The cw trapping laser is stable in mode, intensity, and pointing from 11.5 A (80 mW) to 13.5 A (562 mW), allowing a wide versatility of stiffness ranges for experiments. Stiffness values for both the X- and Y-directions are in the right three columns. As mentioned, power spectrum calibrations for this instrument are underestimated, but drag force and equipartition calibrations agree within 10%. The stiffness values used for biological checks and all experiments are from the Equipartition method (right-most column).

sources and also distorted some Lorentzian fits to underestimate the roll-off frequency. A sample power spectrum and fit are shown in Fig. 4.5, and results are available in Table 4.1. This was the least accurate calibration method due to lower frequency (<100 Hz) noise distorting spectra.

The most commonly used calibration method uses the Equipartition theorem to relate

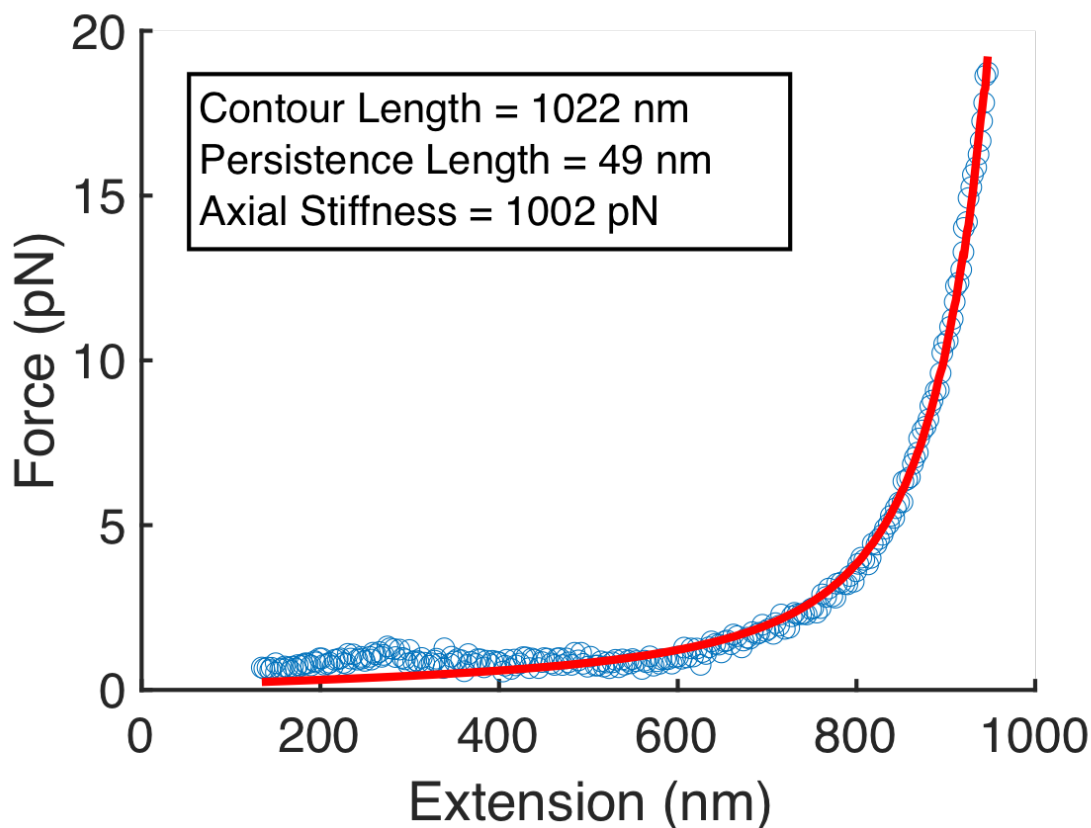


Figure 4.6. DNA stretching control. A DNA stretching assay, similar to those in Chapter 3, was constructed to validate the position and force calibrations. The tethered bead was centered, the stage was translated using a custom tether stretching Labview program. The polymer extension was calculated from the known stage positions, the distance the bead was from the center of the trap and using a geometry correction factor, detailed in Stout et al., 1997 (17), assuming the bead was 100 nm from the coverslip surface. The force vs extension curve was fit to the modified Marko-Siggia WLC model. Fit parameters revealed a contour length of 1022 nm, a persistence length of 49 nm, and an axial stiffness of 1002 nm. The contour length agrees with the length expected from a 3500 bp DNA strand, 1020 nm. The persistence length and axial stiffness agree with the literature ranges of 38-47 nm and 1000-1200 pN respectively (40). This indicates that the instrument is calibrated well for both position and force when using the equipartition method.

thermal fluctuation of Brownian motion to position fluctuations. For this method, we again assume that the trapped particle is bound in a harmonic potential in which the stiffness can be calculated from the magnitude of position fluctuations: $\frac{1}{2} kT = \frac{1}{2} \alpha \langle x^2 \rangle$, where kT is Boltzmann's constant multiplied by the temperature in Kelvin and $\langle x^2 \rangle$ is the mean of the squared positions sampled. This method is sensitive to systemic noise from electronics and mechanical vibrations from fans or air currents but is quite accurate and reliable. The position of the trapped bead was sampled at 100 kHz and filtered at 30 kHz for 100,000 data points to calculate the mean of the squared positions. Results are in Table 4.1.

Finally, to check the validity of our force calibrations, a DNA stretching assay was created to test the instruments ability to report the correct mechanical properties of the polymer. The assay consisted of binding DNA, functionalized with digoxigenin on one end and biotin on the other, to streptavidin non-specifically attached on the surface of a KOH coverslip. Anti-digoxigenin functionalized beads were introduced to create a DNA tether between the beads and the coverslip. Beads were centered over the attachment point and pulled laterally until force was applied and the DNA was stretched taught. The stiffness calibrations used to evaluate fits were gather from the Equipartition method. The resulting force vs extension curve was fit to the modified Marko-Siggia worm-like chain equation (40) and fit values for contour length (L_c), persistence length (L_P), and axial stiffness (K) agree with what is expected both from the DNA length (3500 bp $\sim L_c = 1020$ nm) and from the literature ($L_P = 38-47$ nm, $K = 1000-1200$ pN, depending on solution salinity (40)) (Fig. 4.6). Additionally, DNA overstretching occurs at 65 pN and is also a robust force calibration test. However, the tether attachment in our assay always ruptured before 65 pN of tension could be applied. A different assay design could be used in the future to further validate calibrations.

4.3.6 Drift correction

Drift correction using a second detection laser to monitor a fiducial marker, such as a stuck, 0.75 μm polystyrene beam requires beam positioning and separate position calibrations. We used our piezo actuator NanoPZ system to move a lens and direct the detection laser to the fiducial marker. The NanoPZ system connected to Labview through a USB serial port. The FLIR camera, also connected to Labview, serves as our positioning reference. The positioning logic was as follows: (1) Labview brought up an image of the specimen plane with multiple fiducial markers in view, (2) the user clicked on the image over the fiducial marker of choice, (3) Labview would record the pixel chosen and send serial commands to the piezo actuators to move the detection laser into position.

However, the piezo actuators first needed to be calibrated into pixel space as the image of the specimen plane provides a 3,000 x 4,000 pixel grid of known relative positions. The calibration was accomplished by telling the piezo actuator to move specific distances followed by capturing an image and recording the pixel location of the detection laser focus. Through this, we generated a global piezo actuator map with corresponding pixel locations. The pixel to nm ratio of the FLIR camera was already known from tilt-mirror position calibrations. Because the pixel resolution was high (19.0 nm/pixel in the x-direction and 18.9 nm/pixel in the y-direction), movement of the detection focus to a desired pixel was adequate in positioning the detection over the fiducial marker without further alignment.

After the detection laser was properly positioned, position calibrations were necessary. Instead

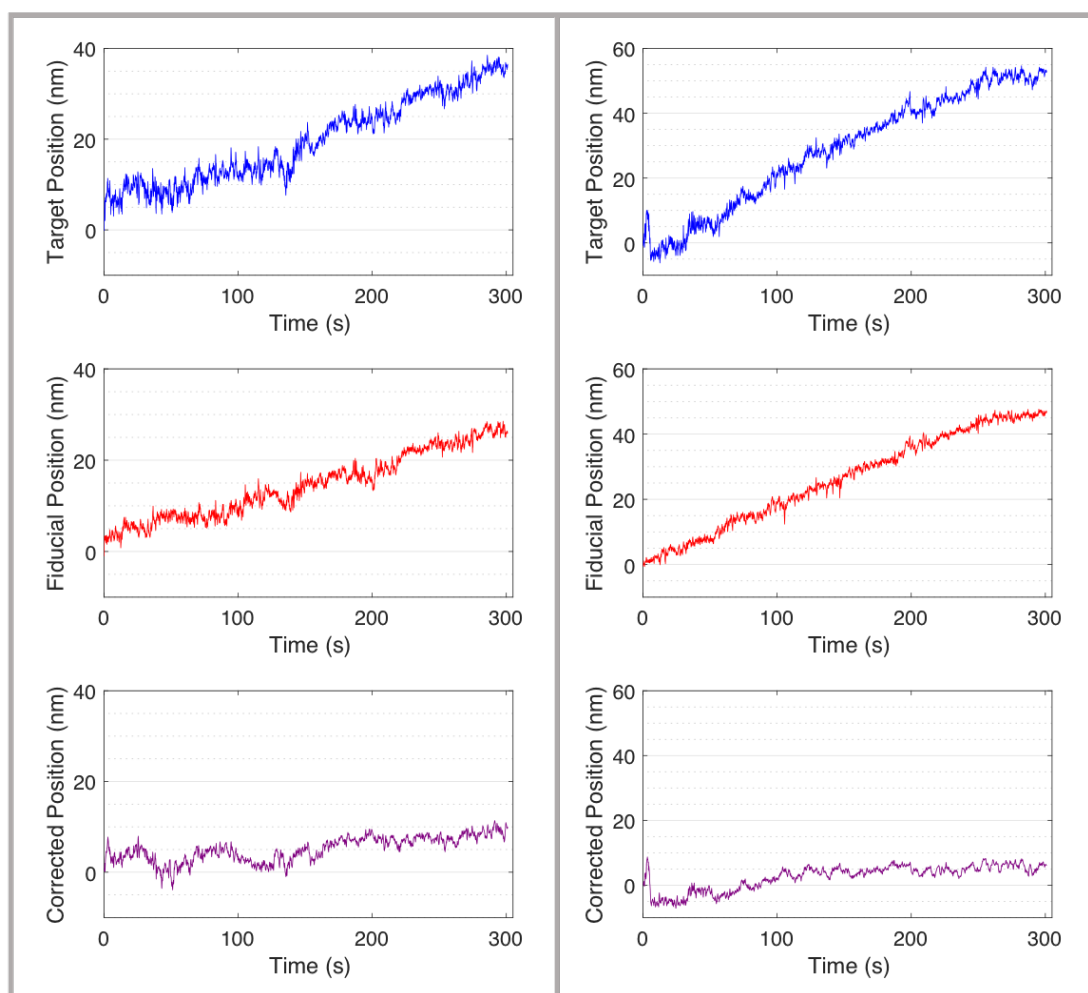


Figure 4.7. Example drift correction traces. The position of a stationary target bead (blue) was tracked while the position of a fiducial bead (red) was simultaneously recorded over a five-minute window. The fiducial trace was subtracted from the target trace to yield the resulting corrected position trace (purple). The corrected position trace showed ≤ 10 nm over the five-minute window, comparable or better than video drift correction (2). The local spatial resolution of the corrected trace is ~ 1 nm while acquiring data at 3 kHz. The stationary bead was calibrated using the tilt mirror 5th order calibrations while the fiducial bead was calibrated using the piezo stage 5th order calibrations. The magnitudes of drift in the two pre-corrected Target examples shown are larger than those in most traces with $\sim 70\%$ of traces containing < 10 nm of drift.

of using the tilt mirror to raster-scan through the detection zone, we used the piezo stage to step the marker through the fiducial detection zone in a known grid. Again, the intensity profile was fit to a 5th order polynomial equation that converted PSD signal voltages into nanometer positions. During data analysis, the fiducial nanometer positions could be subtracted from the trapped particle positions to eliminate drift. Additionally, some mechanical vibrations in the stage may also be subtracted from the data, reducing noise. However, not all noise was eliminated as some mechanical vibrations may be absorbed by the tether, causing an overcompensation in noise

subtraction. Example drift elimination traces in Figure 4.7 show the stationary target bead position (blue), the fiducial bead position representing drift (red), and the corrected drift position (purple) demonstrating that this method reduces drift to ≤ 10 nm over five minutes. The examples in Figure 4.7 are some of the larger magnitudes of drift observed, as many traces ($\sim 70\%$) contain less than 10 nm of drift. Overall, this method of drift correction has high spatial resolution (~ 1 nm) and high temporal resolution (3-10 kHz), allowing for discrete conformation changes or steps to be resolved.

4.3.7 Temperature control chamber

For several biological systems, elevated temperature studies reveal information about the kinetics of reaction pathways and, in some cases, are necessary to sustain biological function for observation (2, 41). Previous experiments have utilized a large environmental chamber surrounding the microscope stage and arm with a heater and fan to raise the air temperature inside (2, 41). Chapter 3 improved on these techniques with the addition of local resistive heating pads placed on aluminum blocks in direct contact with the specimen microscope slide. Temperature could be regulated within $\pm 1^\circ\text{C}$ with a controller and variable transformer. However, there is still significant heat loss through the bottom of the chamber making high temperature studies ($>32^\circ\text{C}$) prone to larger temperature fluctuations ($>\pm 2^\circ\text{C}$) and the mechanical drift that accompanies them.

The environmental chamber constructed here utilizes a smaller environmental chamber that fits around the microscope stage and condenser such that only a small volume within and just above the specimen plane is heated (Fig. 4.8). The elimination of local heating prevented large temperature/mechanical fluctuations, while the smaller volume than before allowed for rapid, highly tunable heating. The box was constructed using compressed wood and coated with 1" of foam insulation. The bottom of the box was open with 1"-thick polyurethane memory foam (McMaster-Carr) lining the edges so that the piezo stage could be moved freely while the heated volume remained closed. The memory foam also dampened any mechanical vibrations that could possibly be transferred from the box-table attachment point to the optical trap. Memory foam also surrounded the objective inside to prevent heat/air loss down the microscope. Inside the box, five resistive heaters totaling 70 W were affixed to heat sinks, one of which had a small, quiet 12-V computer fan attached to circulate air within the box and equilibrate box temperature quickly (Fig. 4.9). The fan was controllable on its own and was turned off during data collection to reduce noise. The resistive heaters were connected to a controller and a variable transformer with a K-type thermocouple thermometer, with the tip sheathed in wiring insulation, suspended near the specimen. The box is able to achieve desired temperature within 15 minutes and maintain temperatures within $\pm 1^\circ\text{C}$.

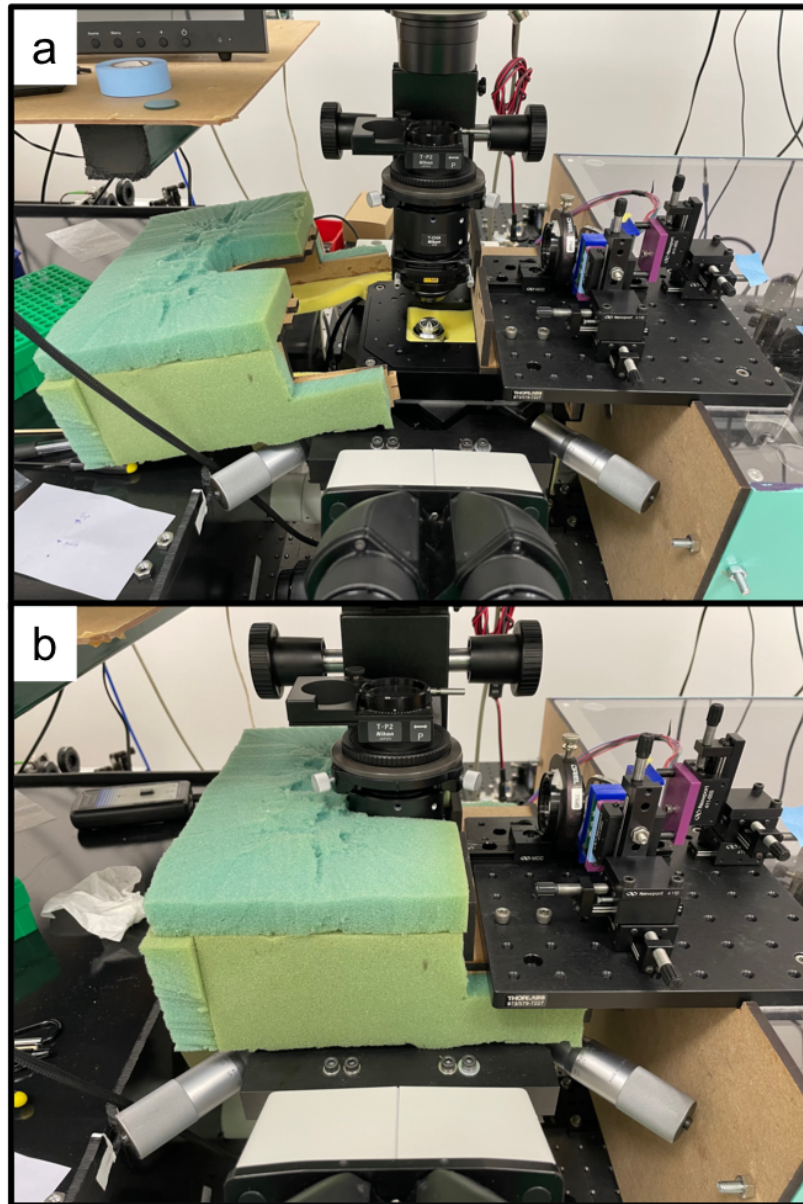


Figure 4.8. Temperature control box on the microscope. The temperature control box slides onto the side of the microscope and docks into fittings bolted to the detection platform. The memory yellow foam around the objective and base of the box is shown in (a) while the box is detached. (b) When attached, the box fits snug against its fittings without contact with the condenser and memory foam completely lining the perimeter of the piezo stage. The insulation provides additional sound dampening, and the apparatus is mechanically isolated from the room by being fully coupled to the floating optical table.

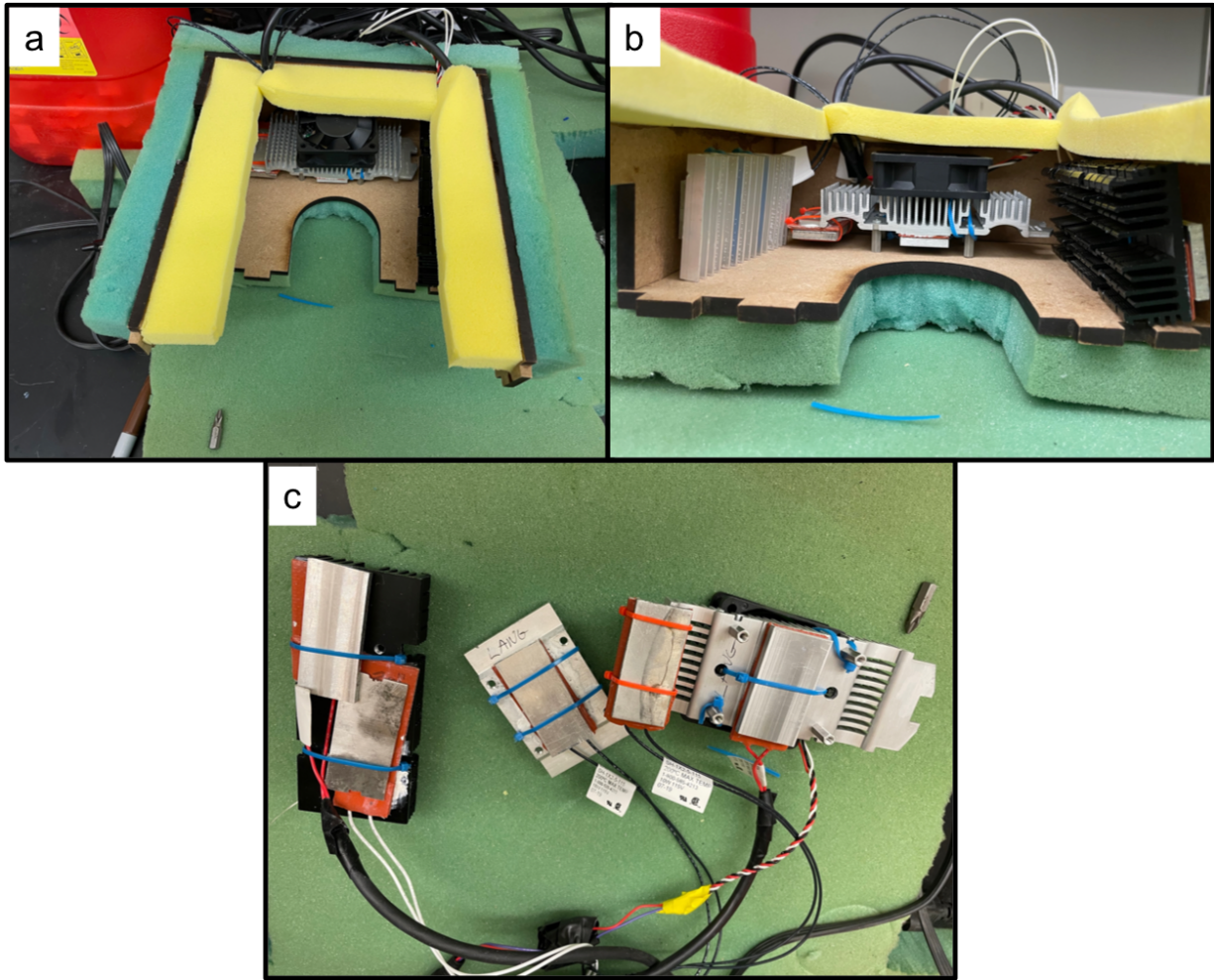


Figure 4.9. Inside the temperature control box. The temperature control box contained five resistance heaters, totaling 70 W, affixed to three heat sinks (left 2" W x 4 3/4" L x 7/8" H, center 1 7/8" W x 3" L x 1/2" H, right 1 1/2" W x 5 1/4" L x 7/8" H). A fan is attached to one of the heat sinks to circulate air. The heat sinks and fan did not come into contact with either the stage or condenser to mechanically isolate the specimen. A bottom-up view (a) and side view (b) of the temperature control box are shown. (c) The resistance heaters were attached to the heat sinks via zip ties around thin aluminum blocks, sandwiching the heaters to maximize the surface contact with the sinks. Thermal paste was applied between the heaters and sinks to facilitate heat transfer. The left-most and right-most heaters are 20 W (red wires), while the three middle heaters are each 10 W (black wires 1", white wires 1.5").

4.4 Discussion

This chapter details the construction of an optical tweezers instrument for the study of cellulose machinery, which are particularly slow when compared to other molecular motors (2, 6, 8, 29, 42). The advanced drift detection proposed certifies that the movement observed from the trapped particle is indeed caused by the biology being studied. The instrument is inherently very quiet by itself because of the soundproof room, large optical table (4' x 8', ~1,000 lbs.), stable optics and stable lasers. But the additional detection system offers the capability of subtracting some mechanical noise from data. The improved resolution will be imperative to observe single glucose or cellobiose steps (0.5 nm and 1 nm, respectively (2, 3)) from slower motors (~0.2 nm/s (2,3)), or detect protein conformational changes underlying the catalytic cycles.

There are many modifications made here that can be interchanged with other systems to achieve similar results. As mentioned, the tilt mirror here replaces the commonly used acousto-optical deflectors (AODs) (2, 26). AODs come with an additional ability to modulate laser intensity so that the power supply can be set to a stable, consistent amperage reducing intensity and mode fluctuations (26). However, power modulation comes at a cost in laser intensity, as AODs disperse 50-70% of the laser's power. Additionally, AODs have proved to be finicky and hard to replace, requiring significant work to fix the optical tweezers instrument if not working properly. However, the tilt mirror as a method of beam steering also contains drawbacks in its hysteresis. Although it can be overcome, the hysteresis can make calibrations and data collection less intuitive requiring more practice with the instrument than if AODs were used. Tilt mirrors and AODs both have similar ranges of steering (on the order of microns) with the optimal range of the tilt mirror used on this instrument being ~2 μm in the X-direction and ~3 μm in the Y-direction. The full range of steering of this tilt mirror is ~4 μm x ~6 μm . One can increase the steering range by placing the tilt mirror further from the specimen plane along the optical path in which the same degree tilt would result in larger displacement. Other options for beam steering include attaching a mirror or lens to a mounted 3-axis piezo stage. This will allow for very fine and accurate steering, but the stage will require significant mechanical stabilization when mounting and is susceptible to thermal fluctuations. The mass of the lens may hinder piezo stage movement speed. Currently, there is no best beam steering method, as each have pitfalls. Fortunately, as long as the trapping laser beam has little pointing instability, the 5th order polynomial fit position calibrations can overcome most asymmetries.

Additionally, there are numerous methods to control temperature, ranging from commercially fabricated to custom builds. The temperature box described here leaves very little physical space

for error in design or attachment. Avoiding contact with the microscope is challenging with this design, and many iterations are required to optimize a similar temperature control box. However, the localized and robust heating without thermal drift is very advantageous. Larger boxes require more heat to bring to temperature, potentially hold temperature better, and also lose heat rapidly upon opening. Larger apparatuses also require more insulation to prevent heat loss.

Even with the high resolution of this optical tweezers microscope, the lasers can be further stabilized. The power spectrums here show low frequency noise. Identifying this source and isolating the optical trap will also increase stability as well as improve the Lorentzian fits. Of note, laser powers of over 300 mW entering the objective will also cause temporary thermal expansion, especially at intensities over 500 mW. However, the expansion usually equilibrates after 5 minutes, and after, as long as the trap is not blocked from entering for too long, there is very little drift.

It is also important to note arguably the largest impact on the development of optical trapping: biofunctionalization of dielectric particles. Some of the first biofunctionalizations involved simple incubations of beads with proteins (24). The introduction of using DNA tethers to probe biological forces quickly disseminated through the field (4, 7, 11, 43). DNA tethers brought a number of bead or biology attachment methods, including biotin-streptavidin (15, 37), anti-bodies with respective tags (digoxigenin, histidine, biotin, Halo) (4, 37, 41), and direct covalent protein functionalization through EDC chemistry (41, 44). Novel DNA structures has expanded the capacity for how scientists can attach to and probe their biological system of interest (45, 46). Additionally, optical tweezers have been used in conjunction with single-molecule fluorescence microscopy and microfluidics to expand the capabilities of studying molecular motion (7, 30, 47-50). This dissertation explores the use of cellulose tethers to study molecular motors, which comes with its own challenges such as elasticity and microstructure. The scientific community will undoubtedly invent more creative methods in the future for high position resolution biophysical studies.

4.5 Materials and Methods

4.5.1 Materials

Coherent Vector power supply 10W Laser, Innovative Photonic Solutions 830 nm laser I0830SU0050PA-USB, Integrated optics Matchbox 785 nm laser, TMC optical table 4' x 8', Nikon 100x 1.40 NA objective, Cargille immersion oil Type DF $n_d=1.5150$, Nikon Immersion oil Type A $n_d= 1.515$, Nikon eclipse TE2000-U microscope, Nikon T-BDCA front port camera attachment,

DAGE-MTI camera with BNC video, Orion video display, Newport NanoPZ series actuators (PZC200, PZ12, PZC-SB), FLIR Blackfly USB3 BFS-U3-120S4M-CS monochrome camera, Labview 2019 32-bit, Physik Intrumente E-616 Controller for Piezo tip/tilt mirror, Physik Instrumente, E-710 Piezo stage controller, Benchmark Thermal silicone rubber heater 10 W and 20 W, SL25.4BM Newport mirror mounts, National Instruments DAQ BNC-2090, Krohn-Hite 3384 filter 8 Pole LP/HP butterworth/Bessel. K-Type Thermocouple Thermometer (Digi-Key TMD-50), Ultra-comfortable polyurethane foam 1" thick (Mcmaster-Carr 86195K13), aluminum heat sinks (DigiKey, 2" W x 4 3/4" L x 7/8" H; 1 7/8" W x 3" L x 1/2" H; 1 1/2" W x 5 1/4" L x 7/8" H).

4.5.1 DNA stretching assay

DNA tether stretching experiments were performed by nonspecifically binding streptavidin to the glass coverslip and incubating with casein, as done in Chapter 3. Next, a solution of 30.7 ng mL⁻¹ biotin-3500 bp DNA-digoxigenin was incubated followed by anti-digoxigenin coated beads to form coverslip tethered beads. The DNA constructs and beads were made using a protocol outlined in Banik et al. (41). The rest of the experiment and analysis mimicked that of cellulose experiments exactly. A custom MATLAB script was used to fit stretching curves to the modified Marko-Siggia Worm-Like Chain model (40) taking into account assay geometry angle (17).

4.6 Acknowledgements

I thank Matthew J Lang for the guidance, instruction, mentorship and suggestions involved with the construction of the optical tweezers instrument. I thank Dibyendu (Dev) Das for starting me on the project and laying groundwork, Madeline M Johnson for her help with setting up video recording equipment and work with the detection system, and Allyson Karmazyn and Elizabeth Holliday for their assistance with force calibrations and the fiducial detection system. This work was supported by the National Institutes of Health grants (5R01GM101001, R01AI136301 and P01AI143565) the Department of Energy Bio-imaging award (Office of Science DE-SC0019313), the National Science Foundation CBET award (1604421), and the National Science Foundation MCB award (1330792).

4.7 References

1. A. Ashkin, Acceleration and Trapping of Particles by Radiation Pressure. *Physical Review Letters* **24**, 156-159 (1970).
2. S. K. Brady, S. Sreelatha, Y. Feng, S. P. S. Chundawat, M. J. Lang, Cellobiohydrolase 1 from *Trichoderma reesei* degrades cellulose in single cellobiose steps. *Nature*

- Communications* **6**, 1-9 (2015).
3. Y. Nishiyama, J. Sugiyama, H. Chanzy, P. Langan, Crystal Structure and Hydrogen Bonding System in Cellulose Ia from Synchrotron X-ray and Neutron Fiber Diffraction. *Journal of the American Chemical Society* **125**, 14300-14306 (2003).
 4. J. C. Cordova *et al.*, Stochastic but highly coordinated protein unfolding and translocation by the ClpXP proteolytic machine. *Cell* **158**, 647-658 (2014).
 5. S. K. Guo, W. C. Wang, P. Y. Wang, P. Xie, Force Dependence of Velocity and Run Length of Kinesin-1, Kinesin-2 and Kinesin-5 Family Molecular Motors. *Molecules* **24** (2019).
 6. M. E. Aubin-Tam, A. O. Olivares, R. T. Sauer, T. A. Baker, M. J. Lang, Single-molecule protein unfolding and translocation by an ATP-fueled proteolytic machine. *Cell* **145**, 257-267 (2011).
 7. Z. Ganim, M. Rief, Mechanically switching single-molecule fluorescence of GFP by unfolding and refolding. *Proceedings of the National Academy of Sciences of the United States of America* **114**, 11052-11056 (2017).
 8. M. J. Schnitzer, S. M. Block, Kinesin hydrolyses one ATP per 8-nm step. *Nature* **388**, 386-390 (1997).
 9. S. Sudhakar *et al.*, Germanium nanospheres for ultraresolution picotensiometry of kinesin motors. *Science* **371**, eabd9944-eabd9944 (2021).
 10. Y. C. Lin *et al.*, Force-induced conformational changes in PIEZO1. *Nature* **573**, 230-234 (2019).
 11. M. D. Wang *et al.*, Force and velocity measured for single molecules of RNA polymerase. *Science* **282**, 902-907 (1998).
 12. K. Visscher, M. J. Schnltzer, S. M. Block, Single kinesin molecules studied with a molecular force clamp. *Nature* **400**, 184-189 (1999).
 13. W. Hwang, M. J. Lang, M. Karplus, Kinesin motility is driven by subdomain dynamics. *eLife* **6**, e28948 (2017).
 14. J. C. Cordova, A. O. Olivares, M. J. Lang, Mechanically Watching the ClpXP Proteolytic Machinery. *Methods Mol Biol* **1486**, 317-341 (2017).
 15. D. K. Das *et al.*, Pre-T cell receptors (Pre-TCRs) leverage V β complementarity determining regions (CDRs) and hydrophobic patch in mechanosensing thymic self-ligands. *Journal of Biological Chemistry* **291**, 25292-25305 (2016).
 16. Y. Feng *et al.*, Mechanosensing drives acuity of $\alpha\beta$ T-cell recognition. *Proc Natl Acad Sci U S A* **114**, E8204-e8213 (2017).

17. A. L. Stout, W. W. Webb, "Chapter 6 Optical Force Microscopy" in *Methods in Cell Biology*, M. P. Sheetz, Ed. (Academic Press, 1997), vol. 55, pp. 99-116.
18. K. Svoboda, S. M. Block, Biological applications of optical forces. *Annual Review of Biophysics and Biomolecular Structure* **23**, 247-285 (1994).
19. I. Vilfan, J. Lipfert, D. Koster, S. Lemay, N. Dekker, "Magnetic Tweezers for Single-Molecule Experiments". (1970), pp. 371-395.
20. A. Ashkin, J. M. Dziedzic, T. Yamane, Optical trapping and manipulation of single cells using infrared laser beams. *Nature* **330**, 769-771 (1987).
21. K. C. Neuman, E. H. Chadd, G. F. Liou, K. Bergman, S. M. Block, Characterization of Photodamage to *Escherichia coli* in Optical Traps. *Biophysical Journal* **77**, 2856-2863 (1999).
22. A. Ashkin, Forces of a single-beam gradient laser trap on a dielectric sphere in the ray optics regime. *Biophysical Journal* **61**, 569-582 (1992).
23. W. Denk, W. W. Webb, Optical measurement of picometer displacements of transparent microscopic objects. *Appl Opt* **29**, 2382-2391 (1990).
24. K. Svoboda, C. F. Schmidt, B. J. Schnapp, B. S. M. Block, Direct observation of kinesin stepping by OT interferometry. *Nature* **365**, 721-727 (1993).
25. K. Visscher, S. P. Gross, S. M. Block, Construction of multiple-beam optical traps with nanometer-resolution position sensing. *IEEE Journal on Selected Topics in Quantum Electronics* **2**, 1066-1076 (1996).
26. M. J. Lang, C. L. Asbury, J. W. Shaevitz, S. M. Block, An automated two-dimensional optical force clamp for single molecule studies. *Biophys J* **83**, 491-501 (2002).
27. J. Sung, S. Sivaramakrishnan, A. R. Dunn, J. A. Spudich, *Single-Molecule Dual-Beam Optical Trap Analysis of Protein Structure and Function* (Elsevier Inc., ed. 1, 2010), vol. 475, pp. 321-375.
28. J. van Mameren, G. J. L. Wuite, I. Heller, "Introduction to Optical Tweezers: Background, System Designs, and Commercial Solutions" in *Single Molecule Analysis: Methods and Protocols*, E. J. G. Peterman, Ed. (Springer New York, New York, NY, 2018), pp. 3-23.
29. Y. Shin *et al.*, Single-molecule denaturation and degradation of proteins by the AAA+ ClpXP protease. *Proceedings of the National Academy of Sciences of the United States of America* **106**, 19340-19345 (2009).
30. P. Gross *et al.*, Quantifying how DNA stretches, melts and changes twist under tension. *Nature Physics* **7**, 731-736 (2011).
31. J. R. Moffitt, Y. R. Chemla, D. Izhaky, C. Bustamante, Differential detection of dual traps

- improves the spatial resolution of optical tweezers. *Proceedings of the National Academy of Sciences of the United States of America* **103**, 9006-9011 (2006).
32. D. N. Reinemann *et al.*, Collective Force Regulation in Anti-parallel Microtubule Gliding by Dimeric Kif15 Kinesin Motors. *Curr Biol* **27**, 2810-2820.e2816 (2017).
 33. A. R. Carter, Y. Seol, T. T. Perkins, Precision surface-coupled optical-trapping assay with one-basepair resolution. *Biophys J* **96**, 2926-2934 (2009).
 34. A. R. Carter *et al.*, Stabilization of an optical microscope to 0.1 nm in three dimensions. *Appl Opt* **46**, 421-427 (2007).
 35. E. A. Abbondanzieri, W. J. Greenleaf, J. W. Shaevitz, R. Landick, S. M. Block, Direct observation of base-pair stepping by RNA polymerase. *Nature* **438**, 460-465 (2005).
 36. M. C. Müllenbroich, N. McAlinden, A. J. Wright, Adaptive optics in an optical trapping system for enhanced lateral trap stiffness at depth. *Journal of Optics (United Kingdom)* **15** (2013).
 37. S. P. S. Chundawat *et al.*, Molecular origins of reduced activity and binding commitment of processive cellulases and associated carbohydrate-binding proteins to cellulose III. *Journal of Biological Chemistry* **296**, 100431-100431 (2021).
 38. F. Gittes, C. F. Schmidt, Interference model for back-focal-plane displacement detection in optical tweezers. *Optics Letters* **23**, 7-9 (1998).
 39. L. Nugent-Glandorf, T. T. Perkins, Measuring 0.1-nm motion in 1 ms in an optical microscope with differential back-focal-plane detection. *Optics Letters* **29**, 2611-2613 (2004).
 40. M. D. Wang, H. Yin, R. Landick, J. Gelles, S. M. Block, Stretching DNA with optical tweezers. *Biophysical Journal* **72**, 1335-1346 (1997).
 41. D. Banik *et al.*, Single Molecule Force Spectroscopy Reveals Distinctions in Key Biophysical Parameters of $\alpha\beta$ T-Cell Receptors Compared with Chimeric Antigen Receptors Directed at the Same Ligand. *J. Phys. Chem. Lett.* **2021** **12**, 7573-7573 (2021).
 42. D. N. Reinemann, S. R. Norris, R. Ohi, M. J. Lang, Processive Kinesin-14 HSET Exhibits Directional Flexibility Depending on Motor Traffic. *Current Biology* **28**, 2356-2362.e2355 (2018).
 43. J. F. Marko, E. D. Siggia, Stretching DNA. *Macromolecules* **28**, 8759-8770 (1995).
 44. Y. Feng, E. L. Reinherz, M. J. Lang, $\alpha\beta$ T Cell Receptor Mechanosensing Forces out Serial Engagement. *Trends Immunol* **39**, 596-609 (2018).
 45. D. Kostrz *et al.*, A modular DNA scaffold to study protein–protein interactions at single-molecule resolution. *Nature Nanotechnology* **14**, 988-993 (2019).

46. M. E. Aubin-Tam *et al.*, Adhesion through single peptide aptamers. *Journal of Physical Chemistry A* **115**, 3657-3664 (2011).
47. P. Gross, G. Farge, E. J. G. Peterman, G. J. L. Wuite, "Chapter 17 - Combining Optical Tweezers, Single-Molecule Fluorescence Microscopy, and Microfluidics for Studies of DNA-Protein Interactions" in *Methods in Enzymology*, N. G. Walter, Ed. (Academic Press, 2010), vol. 475, pp. 427-453.
48. P. Honarmandi, H. Lee, M. J. Lang, R. D. Kamm, A microfluidic system with optical laser tweezers to study mechanotransduction and focal adhesion recruitment. *Lab on a Chip* **11**, 684-694 (2011).
49. P. B. Tarsa *et al.*, Detecting force-induced molecular transitions with fluorescence resonant energy transfer. *Angew Chem Int Ed Engl* **46**, 1999-2001 (2007).
50. L. Bacic, A. Sabantsev, S. Deindl, Recent advances in single-molecule fluorescence microscopy render structural biology dynamic. *Current Opinion in Structural Biology* **65**, 61-68 (2020).

Conclusions and Future Work

Gaining an understanding of biological processes at the single-molecule scale is imperative not only to our fundamental understanding of life, but also to our ability to create tools and solve problems. Humanity has designated climate change, nosocomial infections, and industrial inefficiencies as problems, all of which are associated with cellulose. To create solutions, we are first tasked with learning why the problem exists and what causes it. Understanding the fundamental reasons why cellulases lack the necessary efficiencies and why bacterial biofilms are exceptional shelter will lead to effective measures to curb our dependence on fossil fuels or overcome the shortcomings of current anti-microbial treatments. Additionally, development of new tools to approach issues from multiple perspectives strengthens our comprehension. Our labors here to better understand cellulose, its synthesis and its degradation are steppingstones for the collective human effort to transcend current limitations.

Economically viable biomass enzymatic conversion is highly dependent on the efficiency of the cellulases that degrade cellulose. The carbohydrate binding module on cellobiohydrolase I from *Trichoderma reesei*, one of the most prominent cellulases for biofuel production, displays varying binding modalities to a variety of substrate interfaces. The clear lack of a one, or even two, CBM-cellulose bond lifetime distributions indicates a non-specificity to particular cellulose binding sites, yet CBM still retains a preference to cellulose. The hydrophobic interactions between the CBM and cellulose aid in its preference, but the number and location of binding residues likely causes multiple possible orientations in which CBM can bind. This provides challenges to enzymatic hydrolysis because it increases the likelihood of non-productively bound cellulases decreasing overall efficiency.

The work here presents slight substrate allomorph preferences for CBM. This suggests that altering cellulose's hydrogen bond network may be a solution to reduce non-productively bound enzymes. However, there likely exists a goldilocks zone between lowering binding affinity enough so that dissociation discourages stagnancy but not so much that successful substrate introduction is significantly reduced. Even if the goldilocks zone of binding affinity were to be achieved, this is unlikely to attain the desired efficiency results. Fortunately, and unfortunately, the situation is much more complex than simple one-site binding models. Studies with CBM mutants revealed that changing the protein structure instead of the substrate structure not only affected binding affinity, but also the modalities in which it binds. Future studies with mutant CBMs on full Cel7A enzymes should be investigated in order to observe an overall efficiency shift or shift in ratio between

productive and unproductive machines. Additionally, cellulase optimization could also highly benefit from directed evolution studies, in which rapid, random point mutations are made, efficiencies are tested, and the best performing mutants continue through to the next round of mutations. This method would be successful in identifying a specific protein structure, but further advancements in bioengineering and large-scale bacterial enzyme manufacturing and harvest would be required for feasible production. There are several additional considerations in enzyme performance outside of efficiency, such as recyclability and stability in high temperatures or acidic mediums. The pursuit of biofuels consistently grows in importance as the pressure to become independent of fossil fuels reaches existential levels.

Cellulose biosynthesis has garnered great interest not just as a bioengineering technique to produce pure biofuel feedstocks, but also in the efforts to dismantle bacterial biofilms plaguing healthcare and industrial aquatic settings. Much work is being done studying amyloid fibers and cellulose within the biofilm as the two main structural components. The studies presented here focuses on the latter, which is linked to the chemical and physical protection of bacteria. BcsAB is highly dependent on its monomer, UDP-glucose, Mg^{2+} , and its activator, c-d-GMP. Methods to biochemically starve BcsAB may be successful in preventing biofilm regrowth in the event anti-microbial treatments successfully penetrate the biofilm and reach part of the colony. Even with the biofilm's gel-like composition, significant shear stress, like those applied when scrubbing, is still successful in disrupting protection methods. However, relying on shear stress for every surface that requires disinfection is impractical.

Cellulose also proves to readily fold on itself and seek out other strands for cellulose-cellulose interactions. This, along with the mechanical characterization of the polymer, aids in our understanding of the structural qualities of the biofilm itself. Amorphous globular cellulose provides protection against shear stress while crystalline cellulose provides resistance to compression. Previous studies have tracked BcsAB motility within the plasma membrane, but future studies should investigate the cooperation of BcsAB motility and biofilm structural integrity in response to stress. Any directed motility would suggest signaling pathways associated with purposeful biofilm structural alterations. Disrupting any directed motility signaling pathways would be detrimental to the biofilm's integrity. One of the largest challenges of overcoming biofilm protection is the diffusion-limiting regime preventing most anti-microbials from penetrating while still allowing nutrients to readily transport. This regime exists largely due to the presence of extracellular polymeric substances, such as cellulose. The degradation of such polymers could liquify the biofilm allowing for quicker anti-microbial transport. Alternatively, a coagulation technique would halt all nutrient transport, starving the bacteria. Additionally, BcsAB-BcsAB interactions should be explored

as cooperation may promote crystalline cellulose production, as seen in plant multimers. Information from these studies can direct artificial synthase super-cooperation as potential biofilm disruption as well. There is likely a reason why bacteria cellulose synthases do not multimerize while plant systems do.

Because of the highly conserved nature of cellulose synthases across kingdoms, findings presented here can be translated to plant systems as well. As mentioned, BcsAB is the fourth polymerizing enzyme to be studied at the single molecule level, after RNA polymerase, DNA polymerase and ribosome, and the first to produce a carbohydrate. This dissertation provides a starting point for future single-molecule studies on carbohydrate synthase machines, including, but not limited to, cellulose synthase trimers, plant cellulose synthase rosettes, callose synthases, starch synthases, chitin synthases, and hyalouronic acid synthases. A logical direct extension of this work would be to study BcsAB motors in cooperation and analogously study cellulose synthase trimers. We have demonstrated cellulose's propensity to self-associate, which likely leads to immediate cellulose crystallization in rosettes *in vivo*. Multiple cooperating BcsAB motors would likely display similar behavior by producing a microfibril. Comparing the microfibril's mechanical properties to those of a single cellulose strand may reveal information about the physical environment in biofilms and cell walls. Additionally, the hydrophobic and hydrogen bonding inside cellulose microfibrils as a function of the number of stack cellulose chains and as a function of crystallinity may be directly measured using our cellulose stretching techniques, offering new characterization parameters by which cellulose can be assessed. In addition to cooperation or multimer studies, experiments with different free-floating cellulose-binding polymers, such as xyloglucans or lignol multimers, and their comparison to experiments with cello-oligosaccharides may reveal information about the formation of complex cell-wall compositions. The healthcare, aquatic, and biofuels industries each can build off this work to advance their field.

The optical tweezers microscope designed and constructed as part of this dissertation will also enable future studies on carbohydrate molecular machinery to have higher resolution. Similar instrumental set-ups have been suggested before, but the methods proposed here promote high accuracy and flexible assay designs to benefit any assay, not just carbohydrate synthases. The use of a piezo tip-tilt mirror as the beam-steering device reduces the instrumental complications but poses minor challenges when navigating Labview programming because of hysteresis. Ultimately, the issues can be overcome, but other steering solutions, such as a lens placed on a 3-axis piezo stage, may combine simple instrumentation with easier operation. This optical tweezers instrument utilizes large, heavy optical tables and mounts to reduce pointing instability. To reduce intensity fluctuations in the detection system without using immediate feedback systems to

modulate laser power, a practical option is to search laser manufacturers for lasers with the lowest power stability % and intensity noise %. Once the laser is acquired, identifying the input current that yields the least power stability % and maintaining those settings are essential. The drift tracking system provides high spatial and temporal resolution so that slower molecular machinery, particularly cellulose machinery, can be monitored accurately. The tracking system can be used with other molecular motors or even to study ligand-substrate interactions, as it will increase resolution without the complexities of dual-trap assay construction. This system will see the greatest benefit at elevated temperatures where heating elements introduce thermal expansion and, therefore, drift. The addition of fluorescence capabilities on the instrument could also vastly expand the pool of potential experiments and applications. At minimum, this instrument is able to reproduce current single-trap assays and increase the throughput of data collection with simultaneous experiments.

Overall, the purpose of this dissertation is to develop or add to a molecular understanding of two of the most universal processes of life. Although the studies here intended to be comprehensive, exploring many aspects of cellulose, its synthesis and degradation, this work is by no means final. We have used a novel approach to answer questions posed by the greater community, and we leave more questions for future studies. We also detail instrumentation capable of answering some those questions. As we stand on the shoulders of giants, we provide mounts for others to see further.

APPENDIX

A. Protocols

A.1 Buffer recipes

1. Phosphate Buffer Solution (PBS), pH 7.4

To be used in bead washing, reagent suspension/dilution, assay washing steps (Chapter 2-4)

Materials:

NaCl – 800 mg

KCl – 20 mg

Na₂HPO₄ – 144 mg

KH₂PO₄ – 24 mg

Deionized H₂O – 100 mL total

(Tween-20 optional to make PBST) 10 µL

Nalgene 150 mL rapid-flow bottle top filter – 0.2 µm aPES membrane, 50 mm diameter, 45 mm neck (Thermo Scientific)

(a) Combine all reagents in 80 mL of deionized water in a beaker

(b) Adjust the pH to 7.4 using small amounts of KOH

(c) Add Deionized water to a final volume of 100 mL

(d) Filter buffer through the Nalgene vacuum filter

2. 50 mM Acetate Buffer Solution (ABS), pH 4.9

To be used in CBM assays (Chapter 2)

Materials:

Sodium acetate – 410 mg

Deionized H₂O – 100 mL total

Nalgene 150 mL rapid-flow bottle top filter – 0.2 µm aPES membrane, 50 mm diameter, 45 mm neck (Thermo Scientific)

(a) Combine sodium acetate in 80 mL of deionized water in a beaker

(b) Adjust the pH to 4.9 using small amounts of HCl

(c) Add Deionized water to a final volume of 100 mL

(d) Filter buffer through the Nalgene vacuum filter

3. 20 mM Tris-HCl Buffer, pH 7.0

To be used in BcsAB assays (Chapter 3)

Materials:

Tris-HCl – 315.2 mg
Deionized H₂O – 100 mL total
Nalgene 150 mL rapid-flow bottle top filter – 0.2 µm aPES membrane, 50 mm diameter, 45 mm neck (Thermo Scientific)

- (a) Combine Tris-HCl in 80 mL of deionized water in a beaker
- (b) Adjust the pH to 7.0 using small amounts of KOH
- (c) Add Deionized water to a final volume of 100 mL
- (d) Filter buffer through the Nalgene vacuum filter

4. 2x Incomplete BcsAB motility buffer, pH 7.5

To be used in BcsAB assays (Chapter 3)

Materials:

Glycerol – 2.4 mL
NaCl – 70.1 mg
NaH₂PO₄ – 82.8 mg
Cellobiose – 41.1 mg
Deionized H₂O – ~9.6 mL

- (a) Combine reagents, starting with glycerol, in 9 mL of deionized water in a 15 mL falcon tube
- (b) Mix thoroughly, the glycerol is viscous
- (c) Adjust the pH to 7.5 using small amounts of NaOH, mixing thoroughly after each small addition
- (d) Add Deionized water to a final volume of 12 mL

5. Complete BcsAB motility buffer

To be made fresh for each BcsAB assay (Chapter 3)

Materials:

2x Incomplete buffer – 20 µL
Cyclic-di-GMP – 4 µL of 300 µM solution
UDP-glucose – 2 µL of 100 mM solution
MgCl₂ – 2 µL of 400 mM solution
Deionized H₂O – 12 µL

- (a) Combine reagents in 0.6 mL Eppendorf tube
- (b) Mix thoroughly and store in 4°C until ready to use
- (c) Equilibrate to room temp before flowing
- (d) Discard if not used same-day

6. Mg²⁺ control BcsAB buffer

To be made fresh for each Mg²⁺ control BcsAB assay (Chapter 3)

Materials:

2x Incomplete buffer – 20 μ L
Cyclic-di-GMP – 4 μ L of 300 μ M solution
UDP-glucose – 2 μ L of 100 mM solution
EDTA – 8 μ L of 250 mM solution (made fresh daily)
Deionized H₂O – 6 μ L

- (a) Combine reagents in 0.6 mL Eppendorf tube
- (b) Mix thoroughly and store in 4°C until ready to use
- (c) Equilibrate to room temp before flowing
- (d) Discard if not used same-day

7. Fluorescent c-d-GMP BcsAB buffer

To be made fresh for each Mg²⁺ control BcsAB assay (Chapter 3)

Materials:

2x Incomplete buffer – 50 μ L
Cyclic-di-GMP – 9.9 μ L of 300 μ M solution (final 29.7 μ M)
Cyclic-di-GMP-DY547 (Biolog) 10 μ L of 3 μ L solution (final 300 nM)
UDP-glucose – 5 μ L of 100 mM solution
MgCl₂ – 5 μ L of 400 mM solution
Deionized H₂O – 20 μ L

- (a) Combine reagents in 0.6 mL Eppendorf tube
- (b) Mix thoroughly and store in 4°C until ready to use
- (c) Equilibrate to room temp before flowing
- (d) Discard if not used same-day

8. Cellotetraose BcsAB buffer

To be made fresh for each Mg²⁺ control BcsAB assay (Chapter 3)

Materials:

2x Incomplete buffer – 20 μ L
Cyclic-di-GMP – 4 μ L of 300 μ M solution
UDP-glucose – 2 μ L of 100 mM solution
MgCl₂ – 2 μ L of 400 mM solution
Cellotetraose – 12 μ L of 16.7 mM or 167 mM solution in Deionized H₂O (final 5 mM and 50 mM) respectively

- (a) Combine reagents in 0.6 mL Eppendorf tube
- (b) Mix thoroughly and store in 4°C until ready to use
- (c) Equilibrate to room temp before flowing
- (d) Discard if not used same-day

9. Cellohexaose BcsAB buffer

To be made fresh for each Mg²⁺ control BcsAB assay (Chapter 3)

Materials:

2x Incomplete buffer – 20 µL

Cyclic-di-GMP – 4 µL of 300 µM solution

UDP-glucose – 2 µL of 100 mM solution

MgCl₂ – 2 µL of 400 mM solution

Cellohexaose – 12 µL of 1.5 mg/mL solution in Deionized H₂O (0.454 mM) respectively

- (a) Combine reagents in 0.6 mL Eppendorf tube
- (b) Mix thoroughly and store in 4°C until ready to use
- (c) Equilibrate to room temp before flowing
- (d) Discard if not used same-day

10. 0.1 M MES Buffer, pH 4.5

To be used in cellulose aptamer bead preparation (Chapter 3)

Materials:

MES – 195.2 mg

Tween-20 – 10 µL

Deionized H₂O – 100 mL total

Nalgene 150 mL rapid-flow bottle top filter – 0.2 µm aPES membrane, 50 mm diameter, 45 mm neck (Thermo Scientific)

- (a) Combine reagents in 80 mL of deionized water in a beaker
- (b) Adjust the pH to 4.5 using small amounts of HCl
- (c) Add Deionized water to a final volume of 100 mL
- (d) Filter buffer through the Nalgene vacuum filter

11. 0.1 M Borate Buffer, pH 8.5

To be used in cellulose aptamer bead preparation (Chapter 3)

Materials:

Boric acid – 618 mg

Deionized H₂O – 100 mL total

Nalgene 150 mL rapid-flow bottle top filter – 0.2 μm aPES membrane, 50 mm diameter, 45 mm neck (Thermo Scientific)

- (a) Combine Boric acid in 80 mL of deionized water in a beaker
- (b) Adjust the pH to 8.5 using small amounts of NaOH
- (c) Add Deionized water to a final volume of 100 mL
- (d) Filter buffer through the Nalgene vacuum filter

A.2 DNA tethers

This protocol produces DNA tethers of varying lengths with various functional groups using an M18 plasmid and specific primers.

DNA tether creation and amplification

Materials:

M18 plasmid (Thermo Scientific)
5x GC Buffer (Thermo Scientific)
dNTPs (Thermo Scientific)
Forward and reverse primers (IDT, see below)
Phusion DNA polymerase (Thermo Scientific)
PCR 100 μL Eppendorf tubes
PCR machine
MinElute PCR Purification Kit (Qiagen)

Reverse Primers:

5' – *functional group* – TTG AAA TAC CGA CCG TGT GA – 3'

Forward Primer for desired lengths:

100 bp = 5' – *functional group* – TGT ATA ACG CAT ATG ATA CT – 3'
150 bp = 5' – *functional group* – TTC TCA ATT AAG CCC TAC TG – 3'
200 bp = 5' – *functional group* – TCG AAA ATG CCT CTG CCT AA – 3'
1010 bp = 5' – *functional group* – TAT TGC GTT TCC TCG GTT TC – 3'
3500 bp = 5' – *functional group* – AAT CCG CTT TGC TTC TGA CT – 3'

Functional groups used in this dissertation:

Biotin
Digoxigenin
Primary amine group

1. Combine the following and disperse into 10, 100 μL Eppendorf tubes
 - a. 25 μL of 20 μM forward primer
 - b. 25 μL of 20 μM reverse primer
 - c. 20 μL of 10 μM dNTPs
 - d. 5 μL of 50 ng/ μL M18 Plasmid

- e. 200 μ L of GC Buffer
- f. 10 μ L of Phusion DNA polymerase
- g. 715 μ L of deionized H₂O
2. Put in PCR machine and run "Phusion" pre-set program
3. Combine and purify the resulting DNA tether solutions using MinElute columns
4. Measure the concentration using NanoDrop's nucleic acid setting

DNA tether gel electrophoresis

This protocol is to ensure the PCR amplification reaction and purification yields the desired length and quality of DNA.

Materials:

10 mM TE Buffer, pH 7.5
 10x TBE buffer (Invitrogen 955155301)
 10x BlueJuice Gel Loading Buffer (Invitrogen 10816015)
 1kb dsDNA ladder mixture (Bayou biolabs L-201)
 Agarose (VWR EM-2010)
 SybrGreen 10,000x (molecular probes S7563)
 Gel Electrophoresis system (Owl EasyCast B1 Mini Gel Electrophoresis System)
 UV Lamp

1. Combine 60 mL 10x TBE Buffer with 540 mL deionized water to make 1x TBE
2. In a 250 mL Erlenmeyer flask combine 0.8 g agarose with 100 mL 1x TBE buffer and microwave for 2 minutes on high. Watch the flask and stop heating if solution begins to boil over, after a few seconds resume heating (repeat as necessary, but ensure the full 2 min of heating are complete otherwise agarose will not fully dissolve)
3. Allow agarose solution to cool for 4 minutes
4. Add 8 μ L of SybrGreen
5. Prepare electrophoresis chamber for gel pouring and align comb
6. Pour the agarose solution in the chamber and allow 30 minutes to cool
7. Rotate the chamber so that the combs are proximal to the cathod (black terminal)
8. Fill the electrophoresis apparatus with the remainder of the 1x TBE buffer (~500 mL)
9. Remove the comb and inspect the well walls
10. Combine for each PCR sample
 - a. 1.8 μ L PCR product
 - b. 16.2 μ L TE buffer
 - c. 2 μ L BlueJuice
11. Add 6 μ L of the DNA ladder mixture to a well
12. Place 16 μ L of the PCR sample/loading buffer into a well, repeat for each sample to be run
13. Replace the gel box cover and begin run at 110 V
14. Run until the marker lines (blue and yellow) are near the anode side of the gel (between 1.5 and 2.5 hours)
15. View bands on a gel imaging system (Alpha Innotech FluorChem 8900) or using a hand-held UV Lamp
16. Dispose of the gel in appropriate Biohazardous container

A.3 Anti-body splitting and conjugating to DNA

This protocol cleaves antibodies at their disulfide bonds to attach to DNA tethers using SMCC crosslinking.

Making Half Antibody (This dissertation uses Anti-His)

Materials:

Antibody

1mM EDTA (ethylenediaminetetraacetic acid) in PBST (2.92 mg per 10 ml)

MEA (2-mercaptoethylamine-HCl)

MBS6 Column

Centrifuge

Procedure

1. Mix 80 μ l of 1 mg/ml Anti-His with 20 μ l PBST/EDTA (Final concentration 0.8 mg/ml)
2. Mix 0.8 μ l of MEA with 100 μ l of Anti-His
3. Mix well, then incubate for 90 minutes at 37°C
4. Purify the half Anti-His from MEA, by 1-3 consecutive MBS6 columns
5. Measure concentration of half Anti-His, should be ~0.9 mg/ml
6. Run SDS Page protein gel to confirm weight is half that of full Antibody

Do SMCC Reaction in the same day. The Antibody recombines over night

SMCC Reaction

Materials:

Half Antibody ~0.9 mg/ml

Sulfo-SMCC

PBST/EDTA (Final concentration 0.8 mg/ml)

X-DNA-NH₂

MBS6 column (green ones, follow buffer replacement)

MBS30 column (orange ones, follow buffer replacement)

Centrifuge

Procedure

1. Dissolve 2mg of Sulfo-SMCC in 200 μ l of PBST/EDTA by heating at 75°C until fully dissolved
2. Add 6 μ l of sulfo-SMCC to 30 μ l of X-DNA-NH₂ (410 ng/ μ l)
3. Incubate 45 min at room temperature
4. Purify X-DNA-Sulfo-SMCC from unreacted sulfo-SMCC by 1-2 MBS6 column (measure concentration to make sure it doesn't fall too much)
5. Mix 54 μ l half Antibody (0.9 mg/ml) with 60 μ l X-DNA-sulfo-SMCC
6. Incubate over night at 4°C
7. Purify DNA using MBS30 column. Measure Concentration after.

A.4 CBM bead preparation

This protocol is for creating beads with single CBMs tethered to each.

Materials

PBS

BSA (albumin serum from Bovine)

Streptavidin-coated polystyrene beads 1 μm (Spherotech)

His-tagged GFP-CBM1 (or Y5A and Y31A CBM1 mutants)

Biotin-1010bp-anti-his fab DNA tether

Cup sonicator

Rotator

Centrifuge

Mix the following in 600 μL eppendorf tube

- 128 μL of PBS (4° door top shelf)
- 1 μL of a 10 mg/mL BSA solution in PBS
- 20 μL Streptavidin beads 1:50 dilution (4° top shelf)
- 8 μL of CBM 1:100 dilution (4° top shelf)
- 1 μL of biotin-1010bpDNA-AntiHisFab (-20° second shelf, box labeled Mark)

Rotate in Glass door fridge for 45 min

3 x (Centrifuge solution at 8.5 x1,000 g for 3 min

(draw out 130 μL of supernatant fluid (drawing from top of solution)

(Resuspend in 130 μL of ABS by pipetting up and down

(Sonicate 2 min at 20%

Store in 4°

A.5 Anti-Digoxigenin bead preparation

This protocol creates Anti-digoxigenin beads for the use in DNA stretching assays.

Materials

Protein G beads (Spherotech PGP-08-5)

Anti-Digoxigenin (Roche 11333089001)

PBS buffer

PBST buffer

DSS Crosslinker (Lifetechnologies)

Ethanolamine (Sigma)

Cup sonicator

Rotator

Centrifuge

1. Wash 25 μL of Protein G bead stock solution with 500 μL PBST by spinning down for 3 minutes a 10,000 rpm (repeat a total of three times).

2. Remove the supernatant and resuspend in 500 μ L PBST after the first 2 spin downs. Use 100 μ L of PBS for the final resuspension.
3. Sonicate for 3min at 30% (fill the cup sonicator with cold water, but do not add ice).
4. Add 80 μ L of 200 μ g/mL Antibody to the cleaned bead solution (make sure Anti-Dig bottle is not past the use-by date).
5. Mix for 1hr @ R.T. on a rotator.
6. Spin down for 2 minutes at 8.0 x1,000 g.
7. Remove supernatant and gently resuspend the beads with 500 μ L PBST (repeat wash a total of 3 times).
8. Resuspend in 475 μ L of PBST after the last spin down.
9. Prepare 100mM DSS crosslinker by adding 54 μ L DMSO to a pre-weighed 2mg tube of DSS).
10. Add 25 μ L of 100mM DSS to the bead solution in step 8 (final concentration of 5mM DSS in the tube).
11. Sonicate the tube for 2min @ 20% (fill the cup sonicator with cold water, but do not add ice).
12. React for 1hr @ R.T. on a rotator.
13. Quench the reaction by adding 250 μ L of 50 mM ethanolamine to the bead solution (to make 50mM ethanol amine, mix 2 μ L of ethanolamine with 658uL PBS).
14. Incubate for 30min @ R.T. on rotator.
15. Spin down for 2min at 8.0 x1,000 g.
16. Remove supernatant and gently resuspend beads with 500 μ L PBST (repeat wash a total of 3 times). Final resuspension is in 250 μ L PBST.
17. Store @4°C on rotator. Use beads within 2 months.

A.6 Coverslip KOH etching

This protocol is used to clean and etch coverslips for use in CBM assays and BcsAB assays.

Materials

4 Beakers 1 L
 Ethanol 200 proof
 KOH 100 g
 Teflon coverslip racks
 Sonicator

1. Dissolve 100 g KOH in 300 mL of ethanol in 1 of the beakers. Stir until completely dissolved, an hour or more. The solution may turn brown.
2. Put coverslips in the Teflon racks
3. Fill the 2nd beaker with 300 mL ethanol and the 3rd and 4th beakers with deionized water
4. Degas all four beakers in the sonicator for 5 min at the “degas” setting.
5. Submerge a rack of coverslips in the KOH beaker and sonicate for 5 min
6. Dip coverslips in the ethanol beaker until the ethanol runs off smoothly
7. Dip the same coverslips in one of the water beakers until the water runs off smoothly
8. Submerge the coverslips in the 2nd water beaker and sonicate for 5 min
9. Use a spray bottle to spray both sides of the coverslips with water very thoroughly with high pressure
10. Spray both sides of the coverslips with ethanol with power and thoroughly. The ethanol should run off smoothly.

11. Dry the rack in the oven at 90°C for at least 15 min.
12. Store at room temperature in closed containers

A.7 Coverslip surface passivation with PEG-silane

This protocol produces (poly)ethylene glycol (PEG) polymer brushes on the surfaces of glass coverslips. 1% of the PEG molecules on the surface have biotin covalently linked to the end of the chain. PEG coverslips are used in BcsAB TIRF assays and some DNA stretching assays.

Materials

mPEG-silane, MW 5000 (Laysan Bio)
biotin-PEG-silane MW 5000 (Laysan Bio)
Triethylamine (Sigma 90335)
Toluene (Sigma 244511)
Methanol (Sigma 179337)
KOH (Sigma 221473)
1.6 mL eppendorf tube
Sonicator

1. Remove triethylamine from the 4°C refrigerator and the PEG-silane jar (contains mPEG-silane and bio-PEG-silane from the -20°C freezer. Wrap both the triethylamine and PEG jar in aluminum foil and allow the reagents to equilibrate to room temperature. These reagents are moisture sensitive.
2. Place glass coverslips in the glass staining jar. Rinse twice and sonicate for 10 min with deionized water.
3. Repeat the twice rinse and sonication with methanol
4. Remove mPEG-silane and bio-PEG-silane from the peg jar. Weigh a 1.6 mL Eppendorf tube. Place approximately 297 mg mPEG-silane and 3 mg bio-PEG-silane (1%) in the Eppendorf tube. Reweigh the Eppendorf tube to ensure a total of 300 mg.
5. Rinse the coverslips twice with toluene. Poor 30 mL of toluene into a small beaker. Add 3.38 µL of triethylamine and the 300 mg of PEG mixture into the toluene beaker. Mix thoroughly and poor the solution into the glass staining jar with the coverslips.
6. Sonicate the reaction mixture for 30 minutes at 35°C
7. Wash twice with toluene, then multiple times with DI water until the coverslips are clean.
8. Dry the coverslips with Nitrogen and place individual coverslips in 50 mL Falcon tubes and wrap the caps with parafilm.
9. Store at -20°C

A.8 Cellulose aptamer bead preparation

There are two protocols for creating cellulose aptamer beads. The first is successful but cannot be used with PEG slides as it utilizes biotin-streptavidin interactions. The second covalently bonds the aptamer to the beads using EDC chemistry and is superior. These beads are used in all BcsAB motility and stretching experiments.

Protocol 1 using Streptavidin beads

Materials

PBS

Streptavidin-coated, 1.09 μm beads

Biotinylated cellulose aptamer (5'-bio-GCG GGG TTG GGC GGG TGG GTT CGC TGG GCA GGG GGC GAG TG -3')

0.6 mL Eppendorf tube

Cup sonicator

Centrifuge

1. Dilute streptavidin beads 1:50 from stock in PBS. Vortex and sonicate for 2 min at 20%
2. Dilute biotin-aptamer to 10 ng/ μL from stock with PBS
3. Combine the following reagents in the Eppendorf tube
 - a. 50 μL PBS
 - b. 25 μL of 1:50 diluted streptavidin beads
 - c. 25 μL of 10 ng/ μL biotinylated cellulose aptamer
4. Vortex and rotate at 4°C for 45 min
5. Wash beads 3x and remove unreacted components by centrifuging for 4 min at 8,000 g, discarding the supernatant, and resuspending in PBS.

Protocol 2 using carboxylate beads

Materials

Carboxylate polystyrene 1 μm beads

EDC crosslinker

PBS

Amine-cellulose DNA aptamer (5'-am-GCG GGG TTG GGC GGG TGG GTT CGC TGG GCA GGG GGC GAG TG -3') diluted to 1 μM in PBS (~1:100)

0.1 M MES buffer, pH 4.5

0.1 M borate buffer, pH 8.5

Ethanolamine

Rotator at room temperature and in 4°C

Cup sonicator

Centrifuge

1. Remove EDC crosslinker from the -20°C freezer to equilibrate to room temperature
2. Combine 10 μL of 1 μm carboxylate beads stock (2% w/v) with 190 μL MES buffer
3. Centrifuge for 2 min at 8,000 g, remove supernatant, resuspend in MES buffer and sonicate for 2 min at 40% after each resuspension (repeat 3x)
4. Add 200 μL of 2% w/v freshly made EDC solution in MES buffer (10 mg EDC in 500 μL MES)
5. Incubate at room temperature for 3 hours on the rotator
6. Centrifuge for 4 min at 8,000 g, remove supernatant, resuspend in 400 μL borate buffer, and sonicate 2 min at 40%. Repeat twice (three total). The beads do not pellet as easy in borate buffer and will stick to the far side of the Eppendorf tube from the center of the centrifuge. Drawing the supernatant from just under the surface and near the opposite side of the far side yields the best results.

7. Add 25 μL of the 1 μM amine-cellulose aptamer and rotate at room temperature for 1 hour, and then rotate overnight at 4°C.
8. Add 10 μL of 0.25 M ethanolamine in borate buffer (10 μL ethanolamine in 650 μL borate buffer) to stop the reaction
9. Incubate for 30 min on rotator at 4°C
10. Spin down (4 min at 8,000 g) and resuspend in 400 μL of PBS. Sonicate 2 min 40% after each resuspension. Repeat 3x.
11. Store at 4°C. Best if used within 3 months.

A.9 Cellulose Solutions

These solutions are used in CBM-cellulose rupture assays to prepare each substrate: filter paper cellulose, *Cladophora* cellulose I, and *Cladophora*-derived cellulose III. The main goal of these protocols is to create microfibrils small enough for single molecule studies while still maintaining microfibril integrity.

Filter paper cellulose solution

Materials

Whatman grade 1 filter paper
 Deionized water
 50 mM acetate buffer (pH 4.9)
 Tissue homogenizer
 1 mL micropipette
 Cup sonicator
 Vortex
 16-gauge syringe

1. Cut approximately 20-25 mg of Whatman Grade 1 filter paper (99% cellulose) into small pieces.
2. Place pieces into a tissue homogenizer, add a few drops of deionized water and use the homogenizers to mechanically break apart the filter paper for 15 minutes.
3. Scoop the resulting mixture into a 15 mL Falcon tube and add 10 mL of 50 mM sodium acetate buffer.
4. Pull apart and mix the cellulose by pulling the filter paper in and out of a 10 mL serological pipette or a 1 mL micropipette with the very end cut off of the pipette tip.
5. Sonicate the mixture in a cup sonicator for 2.5 minutes at 40%.
6. Vortex the solution for 10-20 seconds on high.
7. Mix again as in Step 4.
8. Repeat steps 5-7 three times (or more as necessary).
9. Pull a 1 mL sample from the larger stock and place in an Eppendorf tube. Mix the solution thoroughly by pulling the solution in and out of a 16-gauge needle.
10. Dilute a portion of this sample 50 times in 50 mM sodium acetate buffer in a new Eppendorf tube.
11. Sonicate the diluted sample for 2.5 minutes at 40%.
12. Store the samples at 4°C.

***Cladophora* cellulose I and III solutions**

Materials

Cellulose samples (*Cladophora* I or III) - Provided by Prof. Shishir Chundawat (Rutgers)

Deionized water

Cup sonicator

Vortex

16-gauge syringe

1. Weight out a 1 mg sample of the desired cellulose sample and add it to 1 mL of deionized water.
2. Sonicate the mixture for 2 minutes at 50% in a cup sonicator.
3. Vortex the solution for 15 seconds on high.
4. Pull the solution up and down using a 16-gauge syringe for 1-2 minutes.
5. Vortex the solution again for 15 seconds.
6. Repeat steps 2-5 three times.
7. Dilute the mixture 1:2 by mixing 500 μ L of the prepared mixture with 500 μ L deionized water.
8. Store at 4°C.

Before loading a slide, sonicate for 2 minutes at 50% in a cup sonicator and vortex for 15 seconds to further disperse the microfibrils.

A.10 CBM assay construction

This protocol creates an experiment flow cell to study CBM-cellulose bond rupture optical tweezers.

Materials

Cellulose solution (*Cladophora* I or III, or filter paper

KOH etched coverslip

BSA (Albumin Serum from Bovine)

ABS Acetate Buffer solution

CBM beads

Cup sonicator

1. Sonicate the 1:2 Diluted Cellulose Solution 4 min 40%
2. Prepare flow cell with KOH etched coverslip
3. Flow 20 μ L of Cellulose solution into flow cell. Use gravity to pull most solution through the flow cell
4. Dry the flow cell for 1 hour in the 95° furnace
5. Warm BSA to near room temp before opening. Make a 5 mg/mL solution of BSA with 1 mL of ABS and 5 mg of BSA.
6. Flow 20 μ L BSA solution into flow cell. Incubate for 15 min.
7. Sonicate CBM beads for 2 min at 25%
8. Flow 20 μ L CBM beads into flow cell.
9. Use vacuum to **slowly** suction solution through the flow cell (suctioning too quickly can rip cellulose off coverslip surface)

10. Seal flow cell with nail polish and take to microscope for data collection

A.11 BcsAB assay construction

This protocol is to construct an assay to study single-strand cellulose biosynthesis by BcsAB contained in His-tagged nanodiscs. Two protocols, conceptually the same, are included for both motility and stretching assays using optical tweezers and fluorescence studies using TIRF.

Optical tweezers BcsAB Assay protocol

Materials

Streptavidin diluted 1:100 to 0.01 mg/mL in PBS

Polystyrene beads 0.75 μm beads diluted 1:50 in PBS

KOH coverslip (See above), microscope slide, double-sided sticky tape

Casein

Biotinylated (anti)Penta-His antibody diluted 1:100 or 0.01 mg/mL in PBS (Qiagen 34440)

-Qiagen no longer supplies. Sigma has (anti)Penta-His antibody and Abcam has a great Lightening biotinylation kit, (Type B)

BcsAB purified and constrained in nanodiscs diluted to 600 pM in Tris-HCl buffer (Jochen group)
BSA

Cellulose aptamer beads (See above)

Incomplete synthesis buffer and respective components to make the complete synthesis buffer (See above)

Cup sonicator

Vortex

Table-top centrifuge

1. The day before experiments, create a 5 mg/mL solution of Casein in PBS and 1 mg/mL solution of Casein in PBS and dissolve the casein on the heat block overnight at 70°C
2. Day of experiments: start defrosting 0.01 Str aliquot and synthesis buffer components in 4°C. Pull BSA out of fridge to equilibrate to room temperature.
3. Create a flow cell with the microscope slide, KOH etched coverslip and double-sided sticky tape.
4. Sonicate the 1:50 dilution of 0.75 μm beads for 2 min at 25%
5. Add 1 μL of 0.75 μm polystyrene beads to 20 μL of Streptavidin 0.01 mg/mL. Vortex then centrifuge lightly to get rid of any air bubbles. Flow the mixture and incubate for 15 min
6. Filter the 5 mg/mL casein solution using a syringe filter. Flow 20 μL of the filtered casein solution and incubate for 30 min.
7. Move the BcsAB aliquot from the -80°C to 4°C to defrost
8. Flow 20 μL the 0.01 mg/mL biotinylated anti-His antibody solution and incubate for 15 min.
9. Add BSA to the 1 mg/mL casein solution so that the final concentration of BSA is 5 mg/mL. Vortex thoroughly to dissolve the BSA. Filter using a syringe filter.
10. Wash the flow cell with 60 μL of the BSA/Casein solution
11. Centrifuge the defrosted BcsAB aliquot lightly to eliminate air bubbles. Flow 20 μL of the BcsAB solution and incubate for 20 min.
12. Combine the Incomplete buffer with UDP-glucose, Mg^{2+} (or EDTA), cyclic-di-GMP, and deionized water to make the complete motility buffer solution. Exclude relevant components

- for control assays and include cellotetraose (final 5 mM or 50 mM) or cellohexaose (final 0.45 mM) for cello-oligosaccharide studies.
13. Wash the flow channel again with 60 μ L of the BSA/casein solution.
 14. Sonicate the cellulose aptamer beads for 2 min at 40% and flow 20 μ L the beads. Incubate for 15 min.
 15. Flow 40 μ L of the complete buffer solution. Seal off the flow cell and bring to the microscope for experiments.

TIRF BcsAB fluorescence assay

This protocol is mostly the same, except the use of a PEG slide and excluding casein incubation.

Materials

Streptavidin diluted 1:100 to 0.01 mg/mL in PBS

PEG coverslip (See above), microscope slide, double-sided sticky tape

Casein

Biotinylated (anti)Penta-His antibody diluted 1:100 or 0.01 mg/mL in PBS (Qiagen 34440)

-Qiagen no longer supplies. Sigma has (anti)Penta-His antibody and Abcam has a great Lightening biotinylation kit, (Type B)

BcsAB purified and constrained in nanodiscs diluted to 600 pM in Tris-HCl buffer (Jochen group)

BSA

Cellulose aptamer beads (See above)

Incomplete synthesis buffer and respective components to make the complete synthesis buffer (See above) Note the use of cyclic-di-GMP-DY547

Vortex

Table-top centrifuge

1. The day before experiments, create a 1 mg/mL solution of Casein in PBS and dissolve the casein on the heat block overnight at 70°C
2. Day of experiments: start defrosting 0.01 Str aliquot and synthesis buffer components in 4°C. Pull BSA out of fridge to equilibrate to room temperature.
3. Create a flow cell with the microscope slide, PEG coverslip, double-sided sticky tape.
4. Vortex then centrifuge the 20 μ L of Streptavidin 0.01 mg/mL aliquot lightly to get rid of any air bubbles. Flow the solution and incubate for 15 min
5. Add BSA to the 1 mg/mL casein solution so that the final concentration of BSA is 5 mg/mL. Vortex thoroughly to dissolve the BSA. Filter using a syringe filter.
6. Wash the flow cell with 100 μ L of the BSA/Casein solution
7. Move the BcsAB aliquot from the -80°C to 4°C to defrost
8. Flow 20 μ L the 0.01 mg/mL biotinylated anti-His antibody solution and incubate for 15 min.
9. Wash the flow cell with 100 μ L of the BSA/Casein solution
10. Centrifuge the defrosted BcsAB aliquot lightly to eliminate air bubbles. Flow 20 μ L of the BcsAB solution and incubate for 20 min.
11. Create 2 complete buffer solutions, one with cyclic-di-GMP-DY547 (300 nM) and one without.
12. Wash the flow channel again with 100 μ L of the BSA/casein solution.
13. Flow 40 μ L of the complete buffer solution with c-d-GMP-DY547 and incubate for 20 min.
14. Take the slide to the microscope, and directly before data acquisition, flow 100 μ L of complete synthesis buffer without c-d-GMP-DY547.

A.12 DNA tether assay construction

This protocol creates a flow cell with beads linked to the coverslip surface via a DNA tether, typically 3500 bp long. This assay is used in BcsAB studies as a control to distinguish cellulose rapid fluctuations from noise. DNA stretching and over-stretching is a great biological control for verifying optical tweezers position and stiffness calibrations. I have had great success using KOH etched coverslips and casein blocking buffer, but PEG coverslips work well too.

Materials

Anti-digoxigenin beads (diluted 1:100 from 0.25% in PBS)
Biotin-3500bp-dig DNA (~30 ng/ μ L, may need to dilute from stock in PBS)
Streptavidin (0.01 mg/mL)
PBS
PEG coverslip OR KOH etched coverslip
Casein (dissolved overnight in PBS at 5 mg/mL)
Microscope slide
Double-sided sticky tape
Cup sonicator

1. Create a flow cell with either a PEG coverslip or KOH etched coverslip
2. Flow 20 μ L of the 0.01 mg/mL streptavidin solution and incubate for 15 min
3. If using a KOH etched coverslip, flow 20 μ L of the 5 mg/mL casein solution and incubate for 15 min. If using a PEG coverslip, wash the channel with 60 μ L of Casein solution with no incubation required
4. Flow 20 μ L of the 30 ng/ μ L biotin-3500-dig DNA solution and incubate for 20 min
5. Sonicate the Anti-dig beads and flow 20 μ L
6. Seal the flow cell with nail polish and take to the microscope for measurements.